Synthesis, Characterization and Sinterability of Nanoceramics

By

Biranchi Muni Tripathi

CHEM 01 2013 04 016

Bhabha Atomic Research Centre, Mumbai

A thesis submitted to the
Board of Studies in Chemical Sciences

In partial fulfillment of requirements
For the Degree of

DOCTOR OF PHILOSOPHY

of

HOMI BHABHA NATIONAL INSTITUTE

July, 2020

Homi Bhabha National Institute[1]

Recommendations of the Viva Voce Committee

As members of the Viva Voce Committee, we certify that we have read the dissertation prepared by **Shri Biranchi Muni Tripathi** entitled **"Synthesis, Characterization and Sinterability of Nanoceramics"** and recommend that it may be accepted as fulfilling the thesis requirement for the award of Degree of Doctor of Philosophy.

Chairman : **Prof. G. K. Dey** Gautam Kumar Dey **Date: 2-11-2020**

Guide / Convener: **Prof. A. K. Tyagi** AKTyagi **Date: 2-11-2020**

Co-guide - (if any) **Date: 2-11-2020**

Examiner : **Prof. A. R. Kulkarni** ARKulkarni **Date: 2-11-2020**

Member : **Prof. S. K. Mukerjee** **Date: 2-11-2020**

Member : **Dr. V. Sudarsan** Sudarsan. V **Date: 2-11-2020**

Member: **Dr. T. K. Ghanty, Dean Academic** Tapan K Ghanty **Date: 2-11-2020**

Final approval and acceptance of this thesis is contingent upon the candidate's submission of the final copies of the thesis to HBNI.

I/We hereby certify that I/we have read this thesis prepared under my/our direction and recommend that it may be accepted as fulfilling the thesis requirement.

Date: 2/11/2020

Place: BARC, mumbai

AKTyagi
(Signature)
Guide

---

[1] This page is to be included only for final submission after successful completion of viva voce.

Version approved during the meeting of Standing Committee of Deans held during 29-30 Nov 2013

STATEMENT BY AUTHOR

This dissertation has been submitted in partial fulfilment of requirements for an advanced degree at Homi Bhabha National Institute (HBNI) and is deposited in the Library to be made available to borrowers under rules of the HBNI.

Brief quotations from this dissertation are allowable without special permission, provided that accurate acknowledgement of source is made. Requests for permission for extended quotation from or reproduction of this manuscript in whole or in part may be granted by the Competent Authority of HBNI when in his or her judgment the proposed use of the material is in the interests of scholarship. In all other instances, however, permission must be obtained from the author.

B. M. Tripathi

(Biranchi Muni Tripathi)

DECLARATION

I, hereby declare that the investigation presented in the thesis has been carried out by me. The work is original and has not been submitted earlier as a whole or in part for a degree / diploma at this or any other Institution / University.

B. M. Tripathi

(Biranchi Muni Tripathi)

List of publications arising from the thesis

Publications in Refereed Journals

A. Published

1. Monoclinic β-Li_2TiO_3 nanocrystalline particles employing novel urea assisted solid state route: Synthesis, characterization and sintering behavior
   Biranchi M. Tripathi, Trupti Mohanty, Deep Prakash, A. K.Tyagi, P. K. Sinha
   J. Nucl. Mater. 490 (2017) 167-173.

2. Combustion Synthesis of nanocrystalline lithium zirconate
   Biranchi Tripathi, Deep Prakash, A. K.Tyagi, P. K. Sinha
   Transactions of PMAI, 44(2) (2018) 51-55.

3. Glycine-nitrate solution combustion synthesis of lithium zirconate: Effect of fuel-to-oxidant ratio on phase, microstructure and sintering
   Biranchi M. Tripathi, Trupti Mohanty, Deep Prakash, A. K. Tyagi, P. K. Sinha
   J. Eur. Ceram. Soc. 40 (2020) 136-144.

B. **Accepted**

Nil

C. Communicated

1. Novel mixed fuel solution combustion synthesis of γ-$LiAlO_2$: effect of fuel ratio on phase, microstructure and sintering
   Biranchi M. Tripathi, P. K Patro, T. Mohanty, Deep Prakash, A. K. Tyagi, P. K. Sinha,
   Ceram. Int.

2. Anomalous phase transformation of Li_2TiO_3 during sintering in oxygen atmosphere: a dilatometry study
   Biranchi M. Tripathi, Jyothi Sharma, Deep Prakash, A. K. Tyagi
   J. Eur. Ceram. Soc.

Other publication (not included in thesis)

1. High pressure stability of lithium metatitanate and metazirconate: Insight from experiments & ab-initio calculations
   A. Chitnis, B. Chakraborty, **B. M. Tripathi**, A. K. Tyagi, Nandini Garg
   J. Nucl. Mater. 499 (2018) 334-343.

Publication in conference/symposium

1. Physico-chemical characterization of red mud produced during extraction of beryllium
   B. M. Tripathi, Deep Prakash and P.K. Sinha,
   International Conference on Powder Metallurgy & Particulate Materials, Jan 19–21 2015, Mumbai, India.

2. Development of an interactive web application using R Shiny open source software for impedance Measurement Data Analysis
   T. Mohanty, **Biranchi M Tripathi**, T. S. Mahata and P. K. Sinha,
   Conference on Electrochemistry in Advanced Materials, Corrosion and Radiopharmaceuticals, CEAMCR-2018.

B.M. Tripathi

(**Biranchi Muni Tripathi**)

ACKNOWLEDGEMENTS

I render my sincere thanks and deep sense of gratitude to my supervisor and mentor, Dr. A. K. Tyagi, Associate Director, Chemistry Group, for his constant encouragement, support, and invaluable guidance during work. His affectionate treatment and generosity made it viable to bring the present work from conception to worthy completion. He has been a constant source of inspiration for me. I extend my gratitude to Dr. D. Sathiyamoorthy, Ex-Head, PMD, for giving me motivation for this work. I am thankful to Shri P.K. Sinha, Ex-Head, PMD, for encouragement and support.

I wish to acknowledge the Doctoral Committee Chairman, Dr. G.K. Dey, and members Dr. S.K. Mukerjee, Dr. S. Kapoor, and Dr. V. Sudarsan for their critical analysis and valuable suggestions provided during the review presentations and pre-synopsis viva-voce. I am very thankful to Dr. T.K. Ghanty, Dean-Academic, HBNI, for giving useful suggestions during the pre-synopsis viva-voce.

I express my profound gratitude to Dr. Deep Prakash for useful discussions and constant encouragement. I am grateful to Smt. Trupti Mohanty for her assistance that I received impromptu and lavishly throughout the work of the dissertation. I specially thank Dr. P.K. Patro and Smt. Jyothi Sharma for assisting in the characterization of materials. The thanks are also due to Dr. T. Mahata, Dr. Amit Sinha, Dr. R. D. Purohit, Dr (Smt) S. R. Nair, Dr. R. K. Lenka, and all the colleagues of PMD for assisting at various stages of the work.

I sincerely thank my friends Shri K.V. Ravikanth, Dr. Jyoti Prakash, Dr. R. A. Jat and Dr. K. K. Yadav, for their selfless advice, moral support and constant positivity that enabled me to face the challenging times successfully.

I express my love and gratitude to my parents for inspiring me from all walks of life. I am indebted to my family for always motivating and supporting me. Thanks to my brothers, sister, mother-in-law, and father-in-law. I am grateful to my loving wife, Garima, to be with me sharing all the difficulties of my life without complaining. I sincerely appreciate her constant support and encouragement throughout the dissertation work. I express my immense love to my son, Anssh.

Finally, I thank all those I might have forgotten to mention, as the list is more of omission than inclusion. This dissertation would not have completed without any one of you.

Last but most important, I owe a deep sense of gratitude to the Almighty God (Parampita Parmeshwar) for his relentless blessings on me.

(Biranchi Muni Tripathi)

CONTENT

SYNOPSIS

Energy is acknowledged as a key input towards raising the standard of living of citizens of any country. Due to the continuous increase in the global population, better living standards, and expanding economies, the demands for all forms of energy will continue to rise. No single energy source and technology can fulfill the huge global energy demand expected in the coming decades as each of them has strengths and weaknesses. In this scenario, a mix of energy sources will be the most viable option to meet the challenges of energy security, sustainable development, and environmental protection.

Nuclear energy provides promising alternative energy options that can be generated from two processes viz. nuclear fission or nuclear fusion. In everyday life, we witness enormous and inexhaustible energy coming from the Sun which represents a spectacular example of fusion reaction in nature [1].

Fusion power is a potential major source of base-load electricity with attractive features: no greenhouse gas emission, abundant and word-wide distributed sources of fuels, no long-lived radioactive waste generation, and inherent safety features [2]. In fusion reactions, the specific energy is much higher as compared to any ordinary chemical reaction, like the burning of coal. Consequently, a fusion power plant needs only a very small quantity of fuel. Development and testing of the requisite materials and technology to build robust, reliable and economical fusion power stations undoubtedly represent one of the world's most ambitious research endeavors whose outcome could change the world's energy landscape providing a sustainable, secure, safe, affordable, inexhaustible and CO_2 free energy source to meet increasing global energy demand and combat climate change. International Thermonuclear Experimental Reactor (ITER) is a milestone project directed towards the development of commercial fusion energy based on the D-T fuel cycle. It aims to produce 500 MW of power by nuclear fusion of deuterium (D) and tritium (T) [3,4].

The operation of a commercial fusion power plant with the D-T fuel cycle requires an essentially continuous supply of deuterium and tritium into the reactor chamber. Deuterium is readily available as heavy water (D_2O), however, naturally occurring tritium is in-sufficient in quantity and concentration for use as a fuel. Moreover, tritium, being a radioactive substance with a short half-life (about 12.3 years), naturally decays with time. Therefore, large power D-T fusion devices must breed their own tritium from other sources. Tritium can be produced by irradiation of lithium with neutrons [5,6].

Li-based tritium breeding blanket is a key component of the D-T fusion reactor. Lithium-containing ceramics which mainly include Li_2TiO_3, Li_2ZrO_3, $LiAlO_2$, and Li_4SiO_4 have been considered as potential candidate tritium breeding materials owing to their promising thermophysical and thermochemical properties and inherent safety advantages [7]. Processing of tritium breeders based on Li ceramics broadly involves three steps: powder synthesis, consolidation/shaping, and sintering [7].

Sintering is invariably the final and extremely important step in the fabrication of Li containing tritium breeder materials with the designed microstructure irrespective of powder synthesis methods and shapes (pellet, pebble, bar, foam, etc.) [8]. Microstructural control involves the control of grain size, sintered density, and size and distribution of other phases including pores. The microstructure has a very crucial role in controlling tritium retention and release characteristics of ceramic breeders. The central theme in the processing of Li ceramic breeders is to enhance densification while simultaneously limiting the grain growth [7].

Li ceramics exhibit a tendency of Li sublimation and uncontrolled grain growth, at high sintering temperature [9–11]. Due to these factors, it is often quite challenging to achieve the required density and small grain size at the same time. The loss of Li has a detrimental effect on tritium breeding as the breeder in the blanket must have a high amount of lithium to achieve tritium self-sufficiency. The large grain size arising due to uncontrolled grain growth could dampen the tritium release process through the breeder microstructure. This would decrease the tritium breeding ratio and also allow accumulation of tritium inventory in breeders, which has a serious concern with regard to D-T fusion reactor safety.

This has led to concerted research efforts globally to explore and establish a suitable approach for enhancing sinterability of lithium ceramics so that these ceramics could be sintered at low temperature and/or time duration and thereby issue of Li sublimation and uncontrolled grain growth could be effectively avoided. Among the various approaches of improving sinterability, the one utilizing sub-micron to nanoscale powders could be an extremely effective approach. Nanocrystalline ceramic compacts often exhibit improved densification which is mainly due to the high surface area of these materials accompanied by large driving force for sintering. Moreover, the shortened diffusion distances and the increased grain boundary volume in nanoparticulate systems also enhance the densification kinetics. The other widely used alternative approaches, particularly, the addition of sintering aid and the use of aliovalent dopants have very limited scope in case of breeder application.

This is due to the condition of stringent chemical purity (i.e. nuclear grade) for breeder application which imposes serious restrictions on the addition of many foreign elements, particularly those which can act as a neutron absorber and can give rise to activation products upon neutron irradiation.

One of the goals of the present thesis was to improve the sinterability of Li ceramics without the use of any additive. The specific approach involving the use of fine Li ceramic powders has been investigated to improve sinterability and thereby reduce the sintering temperature/and or time of Li ceramics. This would help to avoid Li sublimation, reduce the average grain size, and decrease the cost of bulk production of tritium breeder material. Based on the literature, three potential candidate Li ceramic breeders; Li_2TiO_3, Li_2ZrO_3, and $LiAlO_2$ have been chosen for the investigation.

The work carried out in this thesis primarily consists of (a) synthesis of fine ceramic powders of Li_2TiO_3, Li_2ZrO_3 and $LiAlO_2$ by chemical methods, (b) characterization of as-synthesized and calcined powders and precursors by different techniques (c) consolidation of calcined powders to form powder compacts, (d) sintering behavior of powder compacts, (e) microstructure characterization of sintered compacts and (f) chemical analysis of sintered compacts to estimate Li sublimation.

The extensive work carried out in this thesis enables the establishment of an effective approach for the sinterability enhancement of Li ceramics by means of utilizing nanocrystalline/fine powders. This would augment the current processing method of a high performance sintered ceramic tritium breeder with tailored microstructure whose outcome would contribute significantly to the current state of knowledge about the development of ceramic tritium breeder materials and technology to build robust, reliable and economical fusion power stations. Such fusion power stations could change the world's energy landscape by providing a sustainable, secure, safe, affordable, inexhaustible, and CO_2 free energy source that would not only assist in fulfilling the global energy demand but also combat climate change.

The total work carried out in this thesis has been organized in seven chapters with further sub-chapters as and when required as outlined below.

Chapter 1: Introduction; Chapter 2: Experimental; Chapter 3: Synthesis, characterization, and sinterability of Li_2TiO_3; Chapter 4: Synthesis, characterization, and sinterability of Li_2ZrO_3; Chapter 5: Synthesis, characterization, and sinterability of $LiAlO_2$; Chapter 6: Novel beryllium oxide doped Li_2TiO_3 as tritium breeder; and Chapter 7: Conclusion and future scope

A brief description of each chapter is presented below.

Chapter 1: Introduction

This chapter deals with a brief introduction about the global energy demand and the role of nuclear fusion as source of energy. The need for tritium breeding for the fusion reactor based on the deuterium(D)-tritium(T) fuel cycle is addressed. The tritium breeding mechanism is presented. A brief overview of proposed candidate tritium breeder materials, their properties, and the need for lithium-containing ceramic as breeders are presented. The general scheme of processing of ceramic breeders involving sintering as a key process is presented. A brief description of the various aspects of sintering in general and the sintering of nanocrystalline ceramics is presented. The mechanism of tritium release from the sintered breeder compact in relation to the microstructure of the compact and sintering variables is explained. A brief account of critical issues in the sintering of lithium ceramics is presented, and gap areas from which the scope and objective of the present thesis is conceived, are outlined. A more detailed literature review is also incorporated in the individual chapters.

Chapter 2: Experimental

This chapter deals with the experimental techniques employed in the present investigation. A brief description of different synthesis techniques exploited for the preparation of nanocrystalline ceramic powder is presented. Among these techniques, the combustion synthesis (CS) technique, because of simplicity, less time-consuming, energy-effectiveness, and low cost has been adopted worldwide to synthesize nanomaterials, especially ceramic oxides and mixed-oxides [12]. The combustion synthesis method adopted in the present work for the preparation of Li ceramics is described in detail. The synthesized ceramics have been characterized by different techniques including thermal analysis, X-ray diffraction (XRD), scanning and transmission electron microscope (SEM/TEM), surface area analyzer, and inductively coupled plasma atomic emission spectroscopy (ICP-AES). The ceramic powder consolidation technique and the experimental methods used to investigate the sinterability of Li ceramic compact is described in this chapter. The uniaxial die pressing technique has been used to prepare ceramic powder compacts for the investigation of sintering behavior. The non-isothermal sintering behavior of ceramic compacts has been investigated by using a thermo-mechanical analyzer (TMA) and for isothermal sintering, the muffle furnace has been used. The density of the sintered ceramic compact has been measured by the Archimedes' method. The microstructure of the sintered compact has been investigated by SEM. The electrochemical characterization of the sintered compact has been carried out by the AC impedance measurement technique. The basic principle and working of the different characterization techniques have been presented in this chapter.

Chapter 3: Synthesis, characterization, and sinterability of Li_2TiO_3

This chapter deals with the work performed on the synthesis, characterization, and sintering behavior of Li_2TiO_3. The phase diagram, crystal structure, and a brief overview of the prior studies on the processing of Li_2TiO_3 are presented in this chapter. The experimental procedure adopted for synthesis, characterization, powder consolidation, and sintering of Li_2TiO_3 is discussed. The synthesis of Li_2TiO_3 powder was carried out by a solid-state combustion method which utilizes urea as fuel. A detailed discussion of the experimental results of various investigations on Li_2TiO_3 is depicted in this chapter. The TG/DTA analysis of a small quantity of CS reaction mixture was carried out in a flowing air atmosphere which showed continuous weight loss up to 750ºC.

Based on thermal analysis, the calcination temperature of the reaction mixture was selected in the range of 600-800°C for the synthesis of Li_2TiO_3. The XRD patterns of Li_2TiO_3 confirm the formation of single-phase monoclinic well crystalline Li_2TiO_3 powder at temperature (600-700ºC). The crystallite size calculated invoking the Scherrer's relation revealed nanocrystalline particles of Li_2TiO_3. The SEM analysis revealed the formation of fine particles of Li_2TiO_3 with soft-agglomeration. As revealed by density measurement and SEM microstructure analysis, the Li_2TiO_3 powder compact exhibited excellent sinterability characterized by high relative density (~98%) with small grain size (2-3μm) when isothermally sintered at a temperature as low as <1000ºC. The ICP-AES analysis revealed that the Li/Ti mole ratio in sintered compact was very close to the stoichiometry of Li_2TiO_3 which confirms no loss of Li occurred during the sintering process. The impedance analysis revealed enhanced ionic diffusion in the sintered compact. The observed microstructure of sintered Li_2TiO_3 compact with intact Li content is consistent with the optimal requirement generally envisaged for tritium breeding application in fusion reactors.

Chapter 4: Synthesis, characterization, and sinterability of Li_2ZrO_3

This chapter deals with the work carried out on the synthesis, characterization, and sintering behavior of Li_2ZrO_3. The phase diagram, crystal structure, and a brief outline of the prior studies on the processing of Li_2ZrO_3 are described in this chapter. The experimental procedure adopted for synthesis, characterization, powder consolidation, and sintering of Li_2ZrO_3 is discussed. The synthesis of Li_2ZrO_3 powder was performed via the solution combustion route by exploiting glycine as fuel. The experimental results of various investigations on Li_2ZrO_3 are discussed in detail. The exothermic heat energies and adiabatic flame temperature of possible combustion reactions with different fuel-to-oxidant (φ) ratios were theoretically calculated using standard thermodynamic data of the reactants and products. The reaction temperature for different φ was also measured experimentally. The thermochemical analysis revealed that the fuel-to-oxidant ratio has a significant influence on the mode of combustion, phase composition, and morphology of Li_2ZrO_3 powders. The adiabatic temperature and amount of released gases increase with φ. However, interestingly the measured maximum reaction temperature was observed to decrease with increasing φ. The XRD patterns revealed the presence of a metastable tetragonal phase in minor quantities along with the equilibrium monoclinic phase of Li_2ZrO_3. The Li_2ZrO_3 powder needed to be calcined at 800°C to synthesize a pure monoclinic phase. The crystallite size calculation by using Scherrer's relation revealed the nanocrystalline nature of Li_2ZrO_3 particles. The particle size as measured by laser particle size analyzer was observed to be considerably larger than crystallite size which indicated agglomeration of Li_2ZrO_3 particles. The SEM image of the powder indicated the soft-agglomeration of Li_2ZrO_3 particles. The dilatometric analysis revealed preferable sintering temperature for Li_2ZrO_3 compact is in the range of 800-1000°C. The isothermal sintering followed by density measurement using Archimedes' method revealed that the relative density of Li_2ZrO_3 powder compact was around 90% at sintering temperature of 950°C and almost full densification was achieved at 1000°C. The grain size in the compact sintered at 1000°C was observed in the range of 1-2μm. This clearly shows the remarkable sinterability of Li_2ZrO_3 powder compact. Further increase of sintering temperature to 1050°C is observed to be disadvantageous as it resulted in abnormal grain growth with a large number of closed pores. Moreover, it was revealed by ICP-AES analysis that Li content was intact during the sintering process. The enhanced sinterability would reduce the processing temperature and/or time of Li_2ZrO_3 as a tritium breeder which would facilitate optimal density and small grain size at the same time without loss of Li due to sublimation.

Chapter 5: Synthesis, characterization, and sinterability of $LiAlO_2$

This chapter deals with the work carried out on the synthesis, characterization, and sintering behavior of $LiAlO_2$. The phase diagram, crystal structure, and a brief description of the prior studies on the processing of $LiAlO_2$ is presented in this chapter. The experimental procedure adopted for synthesis, characterization, powder consolidation, and sintering of $LiAlO_2$ is described. The synthesis of $LiAlO_2$ powder was carried out by a solution combustion route using citric acid and glycine as mixed fuel with varying fuel ratios. The experimental results of various investigations on $LiAlO_2$ are elaborated in detail in this chapter. The exothermic heat energy and adiabatic flame temperature of possible combustion reactions with different fuel compositions were theoretically calculated using standard thermodynamic data of the reactants and products. The reaction temperature for different fuel compositions was also measured experimentally. The thermochemical analysis revealed that fuel composition has considerable effect in determining the mode of combustion, phase composition, and morphology of $LiAlO_2$ powders. It was observed that there is no considerable variation in the adiabatic temperature with the change in fuel composition, however, interestingly the measured maximum reaction temperature was observed to increase with increasing glycine content in the fuel mixture. The XRD patterns revealed that well crystalline γ-$LiAlO_2$ phase was obtained directly from the combustion reaction preferably at fuel compositions with higher glycine content. However, after calcination at 700ºC, powders resulting from all combustion reactions tend to crystallize into pure phase γ-$LiAlO_2$. The crystallite size calculation by using Scherrer's relation revealed the nanocrystalline nature of γ-$LiAlO_2$ particles. The γ-$LiAlO_2$ powder synthesized by single citric acid fuel has shown the highest loss on ignition and that synthesized using single glycine fuel has shown the least. The SEM images revealed that $LiAlO_2$ powder consists of irregular flake shape soft-agglomerated particles with large variation in particle size (4-20μm). The dilatometric analysis revealed, sintering of γ-$LiAlO_2$ compact commences at a temperature of around 800-850°C and maximum shrinkage was realized at 1000-1050°C. The isothermal sintering followed by density measurement using Archimedes' method revealed that the relative density of $LiAlO_2$ powder compact was around 85% at sintering temperature as low as 850ºC which sharply increased to about 92% at 900°C and almost full densification (97-98%) was observed at 950-1000ºC. The grain size in the compact sintered at temperature of 900 and 950°C was observed in the range of 2-4μm. This clearly demonstrates the remarkable sinterability of

$LiAlO_2$ compact. Further increase of sintering temperature to 1050°C was observed to be disadvantageous as it resulted in microstructure with considerably large grain size. Additionally, the ICP-AES analysis revealed that Li content was preserved during the sintering process. The improved sinterability would reduce the processing temperature and/or time of $LiAlO_2$ based tritium breeder which would facilitate to achieve desired microstructure with optimal densification and small grain size without loss of Li as envisaged for tritium breeder application in a fusion reactor.

Chapter 6: Novel beryllium oxide doped Li_2TiO_3 as tritium breeder

This chapter deals with the work carried out on the synthesis, characterization, and sintering behavior of beryllium oxide (BeO) doped Li_2TiO_3. A brief description of the properties of beryllium oxide and its advantages as a dopant for Li_2TiO_3 is presented in this chapter. The necessary precautions that need to be taken while handling beryllium compounds are briefly narrated. The experimental procedure adopted for synthesis, characterization, powder consolidation, and sintering of BeO doped Li_2TiO_3 is described. The synthesis of BeO doped Li_2TiO_3 powder was carried out by urea assisted solid-state combustion method. The experimental results of various investigations on BeO doped Li_2TiO_3 are elaborated in detail in this chapter. The XRD patterns revealed the formation of the monoclinic phase of Li_2TiO_3 and the incorporation of Be^{2+} into the crystal lattice. The TEM image of Li_2TiO_3 powders disclosed a broad particle size distribution. The dilatometric analysis revealed excellent sinterability of an un-doped Li_2TiO_3 powder compact characterized by remarkably low sintering onset temperature in the O_2 atmosphere. Increasing sintering temperature resulted in an anomalous monoclinic-to-cubic phase transformation at a temperature significantly lower than the usual transformation temperature. The suppression of this phenomenon was observed in BeO doped Li_2TiO_3. The sinterability of Li_2TiO_3 powder compact was augmented after doping with a small amount of BeO. Reduction in sintering temperature has a vital role in controlling Li sublimation and uncontrolled grain growth during the fabrication of advanced tritium breeder materials.

Chapter 7: Conclusion and future scope

In this chapter major findings and highlights of our studies on Li_2TiO_3, Li_2ZrO_3, and $LiAlO_2$ ceramics have been summarized. The presented results on combustion synthesis of fine/nanocrystalline powders of these ceramics have provided relevant new information that would further augment the current synthesis practices in terms of phase purity, powder yield, control over the loss of Li, powder agglomeration, and scalability. The results on sintering behavior would serve as a guide to the utilization of the fine/nanocrystalline powders in the processing of high-performance ceramic tritium breeders with designed microstructure (i.e., optimum density and small grain size) and better control over the Li loss. The initial results on synthesis and sintering behavior of BeO doped Li_2TiO_3 as an advanced tritium breeder have opened up a new area of research which due to the neutron multiplication ability of Be could facilitate the realization of desired tritium breeding ratio. In addition to the studied ceramics, the extensive work presented in this thesis would also serve as a guide in general to augment the ongoing research on the synthesis and sintering process of the various new Li containing ceramics which have not gained enough maturity yet.

References

[1] D. Clery, A Piece of the Sun: The Quest for Fusion Energy, Overlook Duckworth, 2013.

[2] R. Toschi, Nuclear fusion, an energy source, Fusion Eng. Des. 36 (1997) 1–8.

[3] R. Aymar, - Overview of the ITER Project, in: T. Haruyama, T. Mitsui, K.B.T.-P. of the S.I.C.E.C.C.M.C. Yamafuji (Eds.), Elsevier Science, Oxford, 1997: pp. 53–59.

[4] N. Holtkamp, Overview of the Status of the ITER Project, Fusion Power Assoc. Annu.

Meet. Symp. (2010) 1–85.

[5] T. Tanabe, Tritium: Fuel of fusion reactors, Springer Japan 2017.

[6] T. Tanabe, Tritium fuel cycle in ITER and DEMO: Issues in handling large amount of fuel, J. Nucl. Mater. 438 (2013) S19–S26.

[7] N. Roux, C. Johnson, K. Noda, Properties and performance of tritium breeding ceramics, J. Nucl. Mater. 191–194 (1992) 15–22.

[8] Z. Wen, X. Wu, X. Xu, J. Lin, Z. Gu, Research on the preparation of ceramic tritium breeders in SICCAS, Fusion Eng. Des. 85 (2010) 1551–1555.

[9] T. Hoshino, M. Yasumoto, K. Tsuchiya, K. Hayashi, Vapor species evolved from Li_2TiO_3 heated at high temperature under various conditions, Fusion Eng. Des. 81 (2006) 555–559.

[10] T. Hoshino, H. Kawamura, M. Dokiya, Y. Takahashi, T. Terai, M. Yamawaki, Non-stoichiometry of Li_2TiO_3 under hydrogen atmosphere conditions, J. Nucl. Mater. 329–333 (2004) 1300–1304.

[11] T. Hoshino, M. Dokiya, T. Terai, Y. Takahashi, M. Yamawaki, Non-stoichiometry and its effect on thermal properties of Li_2TiO_3, Fusion Eng. Des. 61–62 (2002) 353–360.

[12] F. Deganello, A.K. Tyagi, Solution combustion synthesis, energy and environment: Best parameters for better materials, Prog. Cryst. Growth Charact. Mater. 64 (2018) 23–61.

LIST OF FIGURES

LIST OF TABLES

Thesis Highlights

❑ The pure phase nanocrystalline Li_2TiO_3, Li_2ZrO_3, and $LiAlO_2$ powders were synthesized and characterized by various techniques.

❑ The pellet-shaped green compacts of Li_2TiO_3, Li_2ZrO_3, and $LiAlO_2$ with desired dimensions were made by consolidating the synthesized powders employing the isostatic hydraulic pressing method.

❑ The sintering behaviour of the Li_2TiO_3, Li_2ZrO_3, and $LiAlO_2$ green pellets, analysed by dilatometry, revealed the sintering temperature regimes of these ceramics.

❑ The isothermal sintering (conducted based on dilatometry data) disclosed the effect of sintering temperature on densification of Li_2TiO_3, Li_2ZrO_3, and $LiAlO_2$ green pellets and also established the appropriate sintering temperature of these ceramic tritium breeders.

❑ The high densification of Li_2TiO_3, Li_2ZrO_3, and $LiAlO_2$ green pellets observed at relatively low sintering temperature and short duration, indicated improved sinterability of these ceramic tritium breeders.

❑ Reduction in sintering temperature and time play a vital role in circumventing Li sublimation and uncontrolled grain growth during production of advance ceramic tritium breeder materials.

❑ The enhanced sinterability resulted in fine grain-sized microstructure with the uniform grain morphology in sintered Li_2TiO_3, Li_2ZrO_3, and $LiAlO_2$ pellets as confirmed by the SEM images of the fracture surface of the sintered pellets.

❑ The isothermal sintering of Li_2TiO_3 pellet at a temperature as low as 850°C resulted in a relative density close to 90%, which often considered sufficient for tritium breeder application. Further, an increase in sintering temperature to 950-1000°C resulted in a high relative density (~98%) of Li_2TiO_3 compact.

- The SEM images of the fracture surface depicted uniform grain morphology and small grain size (2-3 μm) in Li_2TiO_3 pellet sintered at 900 and 950°C. Increasing the sintering temperature above 950°C resulted in rapid grain growth without significant improvement in densification of the Li_2TiO_3 compact.
- The impedance analysis of sintered Li_2TiO_3 pellet at different temperatures revealed significant improvement in Li conductivity resulting from a decrease in grain and grain boundary resistance and thereby accelerating the intragranular and grain boundary diffusion processes. The improved Li conductivity indicated better tritium release property of sintered Li_2TiO_3 compact.
- The dilatometry analysis of Li_2ZrO_3 pellet revealed the onset of sintering at significantly low temperature (850-900°C) with peak around 1000°C.
- The isothermal sintering of Li_2ZrO_3 pellet at a temperature of 950°C resulted in a relative density of around 90%. Further, an increase in sintering temperature to 1000°C produced nearly full densification (97-98%) of the pellet.
- The SEM images of the fracture surface depicted uniform grain morphology and small grain size (1-2 μm) in Li_2ZrO_3 pellet sintered at 1000°C. Increasing the sintering temperature above 1000°C produced a rapid grain growth with a large number of the closed pores without significant improvement in densification of the pellet.
- The dilatometry analysis of $LiAlO_2$ pellet revealed the onset of sintering at significantly low temperature (800-900°C) with peak around 1000°C.
- The isothermal sintering of $LiAlO_2$ pellet at a temperature of 900°C produced a relative density close to 93%. Further, an increase in sintering temperature to 950-1000°C resulted in nearly full densification (97-98%) of the pellet.

- The SEM images of the fracture surface depicted uniform grain morphology and grain size of around 2-4μm in $LiAlO_2$ pellet sintered at 900 and 950°C. Further, an increase in sintering temperature above 950°C resulted in a rapid grain growth with large number of the closed pores without significant improvement in densification of the pellet.
- The chemical analysis by ICP-AES revealed Li content in the synthesized powders and the sintered Li_2TiO_3, Li_2ZrO_3, and $LiAlO_2$ pellets nearly close to the stoichiometric value, which confirmed no significant loss of Li during the synthesis of powders as well as sintering of the pellets.
- A novel BeO doped Li_2TiO_3 ceramic tritium breeder was synthesized by the solid-state combustion method employing urea as a fuel. The XRD analysis revealed doping of BeO in Li_2TiO_3.
- The pellet-shaped green compact of BeO doped Li_2TiO_3 was made by isostatic hydraulic pressing technique.
- The dilatometry analysis revealed, improvement in densification of Li_2TiO_3 pellet after BeO doping in comparison to the undoped sample.
- The dilatometry analysis revealed an anomalous monoclinic-to-cubic phase transformation in undoped Li_2TiO_3 at a sintering temperature of around 970°C, whereas the usual phase transformation temperature has been reported in the range of 1150-1250°C.
- The doping of BeO resulted in the suppression of the monoclinic-to-cubic phase transformation in Li_2TiO_3.
- The Li_2TiO_3, Li_2ZrO_3, and $LiAlO_2$ compacts prepared utilizing the fine ceramic powders synthesized in this work have achieved the desired densification (relative

density: 85-90%) with small grain size (1-4 μm) at the sintering temperature < 1000°C without loss of Li.

Chapter 1

Introduction

1.1 Background

1.1.1 Global energy demand: Role of thermonuclear fusion

Energy is recognized as an essential stimulus for fostering the standard of living of citizens of any country. Moreover, the economic growth of a nation will have important implications for the energy demand. In view of this, development of a sustainable energy economy is absolutely necessary for the economic welfare of any nation. The demands for all forms of energy will continue to rise as a consequence of continuously increasing global population, improved living standards and expanding economies. The developing countries like India, China, Brazil are major contributors to rising energy demand, where due to anticipated fast urbanization and industrialization, large-scale electrical energy will be required (Figure 1.1) [1–3]. The huge global energy demand expected in the coming decades can not be fulfilled by single energy source and technology. Each energy source has strengths and weaknesses. For instance, over reliance on fossil fuels is impractical and inconceivable due to the depletion of fossil fuels resources [4]. Moreover, excessive use of fossil fuels will lead to emission of greenhouse gases in large quantities which in turn has been identified as a major culprit of global warming [5]. Due to irreversible detrimental effects on the environment, global warming has been considered a serious concern over the years. The other renewable energy options including solar, wind and hydro energy, due to very low energy density and strong dependency on specific geographical locations, have limited scope [5]. Hydrogen is another promising energy option which is actively evaluated as a portable and environment benign energy carrier for domestic and commercial/industrial applications [5]. In this scenario, a mix of energy sources will be the most viable option to meet the challenges of energy security, sustainable development and environmental protection.

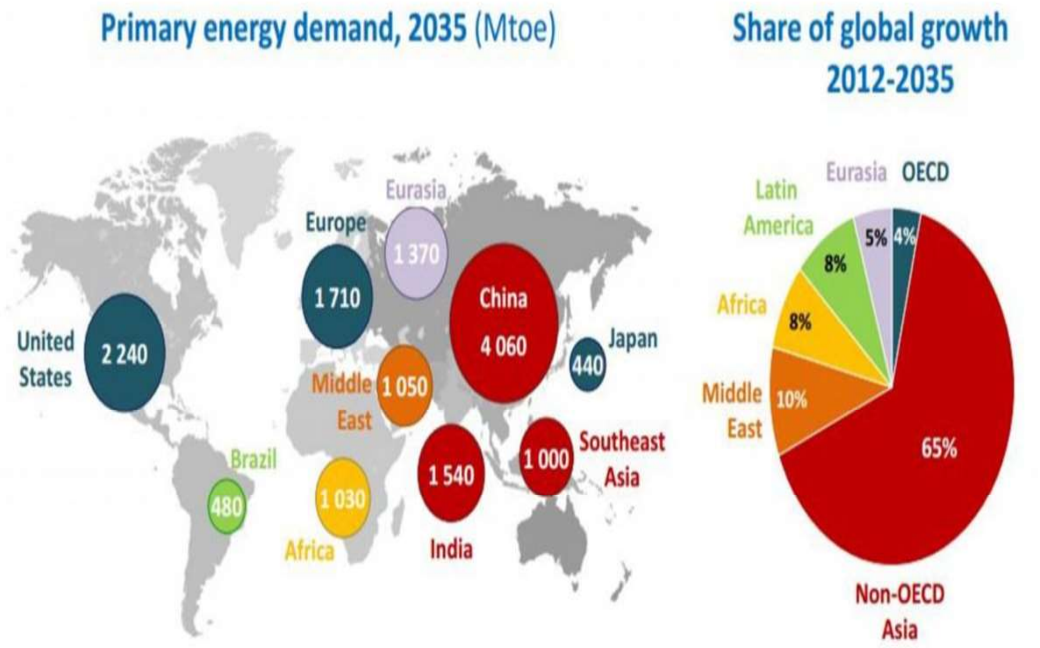

Figure 1.1 World energy consumption with estimation of world population [1]

Nuclear energy provides a promising alternative energy options which relies on nuclear reactions accompanied by release of energy. In nuclear reactions enormous energy is released in comparison to combustion of fossil fuels or other conventional energy resources. Nuclear energy can be generated from two processes viz. nuclear fission or nuclear fusion. Although nuclear fission is promising, however, high capital investment, high-level radioactive waste management and public acceptance are some of the major deterrent factors to its continued application [6–9].

Fusion power is a potential major source of base-load electricity with many attractive features. It does not involve greenhouse gas emission as the only by-products of fusion reactions are small amounts of inert helium gas that will not add to atmospheric pollution. The fuel resources for generation of fusion energy are abundant and word-wide distributed as the deuterium can be extracted from water and tritium is produced from lithium (Li) which is found in the earth's crust. In nuclear fusion, there is no long-lived radioactive waste generation, and only structural materials become radioactive which will be safe to recycle or dispose of by the conventional methods within 100 years. The fusion reactors have inherent safety features which is associated with the utilization of only a small amount of fuel in fusion devices that implies a large-scale nuclear accident is completely ruled out [8,10]. The specific energy (energy per unit mass of the fuel) of fusion reactions is much higher as compared to any ordinary chemical reaction, like burning of coal. Consequently, a fusion power plant only needs a very small quantity of fuel [9]. The nuclear fusion is not a chain reaction that means any perturbations from the optimum conditions to sustain the reaction will lead to immediate shut-down of the fusion reaction. In fusion power plants, as the total amount of fuel in the vessel is nominal (only a few grams), in case of any accidental scenario, once the fuel supply is interrupted, the fusion reaction stops within seconds without any difficulty [9,10].

The availability of Li is very important for generation of fusion energy at large scale. The worldwide identified reserves of Li in 2011 were estimated by the US Geological Survey as 13 million tonnes. About half the world's known Li reserves are located in Bolivia's Uyuni Desert with 5.4 million tonnes of Li. The deposits of lithium are found in the Andes mountain range. The Chile is the leading Li producer, followed by Argentina. The Li extraction from ocean sea is the last important fuel source which is uniformly distributed worldwide [11–13].

Tritium, an intermediate fuel for the fusion reaction, is a radioactive substance with a short half-life (about 12.3 years) [14].

Techniques and expertise to safely handle tritium already exist. The fusion power plants are constructed in compliance with appropriate laws and regulations to ensure a safe handling of the tritium [14,15]. Moreover, the stable helium-3 (^{3}He) produced as a by-product of tritium decays is a very expensive isotope which has many useful applications such as medical medicine for the lung and for slow-neutron detectors. Thus, fusion economy would provide a substantial new resource of ^{3}He [14,15].

The products of the fusion process (helium and neutrons) are not radioactive, the structural materials of the vessel are prone to be activated by interaction with neutrons. Due to this reason, the design of new low-activation materials (e.g. austenitic stainless or ferritic steels, ceramics such as SiC with restrictions on alloying elements and impurities) for fusion reactors is an important and active part of the international fusion research [16–20]. By use of such materials, the impact of induced radioactivity can be greatly minimized.

Nowadays experiments on fusion reactions always require the input of far more energy than released by the fusion reactions. Hence, the actual challenge is not to produce fusion reaction, but to turn fusion into an energy source that generates more energy than it consumes [10]. Development and testing of the requisite materials and technology to build robust, reliable and economical fusion power stations undoubtedly represents one of the world's most ambitious research endeavours. The outcome of this research could change the world's energy landscape providing a sustainable, secure, safe, affordable, inexhaustible and CO_2 free energy source to meet increasing global energy demand and combat climate change.

In everyday life, we witness enormous and inexhaustible energy coming from the Sun. The energy radiating from the Sun represents a spectacular example of fusion reaction in nature. The source of energy coming from the Sun is a process of nuclear fusion of hydrogen nuclei bound together by strong gravitational force in a chain of reactions to produce helium [10,21].

1.1.2 Nuclear fusion as energy source

In nuclear fusion, light nuclei are brought intimately together to a distance comparable to their size to form heavier ones. In this process, a small mass difference between the initial and the final reaction products termed as "mass defect" arises that converted into equivalent amount energy invoking Einstein's famous mass-energy relationship $E=mc^2$, where c is the speed of light and m is the mass defect. As the speed of light is a large number, the energy equivalent to a small quantity of mass defect is quite large. For example, some of the fusion reactions of interest with respective value of energy released (Q value) are given below (**Table 1.1**) [14].

Table 1.1 Some of the fusion reactions of interest [14]

$D + T \rightarrow \alpha + n$	$Q = 17.59$ MeV	(R1)
$D + D \rightarrow T + p$	$Q = 4.04$ MeV	(R2)
$\rightarrow {}^3He + n$	$Q = 3.27$ MeV	(R3)
$\rightarrow \alpha + \gamma$	$Q = 23.85$ MeV	(R4)
$T + T \rightarrow \alpha + 2n$	$Q = 11.33$ MeV	(R5)
$D + {}^3He \rightarrow \alpha + p$	$Q = 18.35$ MeV	(R6)
${}^3He + {}^3He \rightarrow \alpha + 2p$	$Q = 12.86$ MeV	(R7)
$p + {}^6Li \rightarrow \alpha + {}^3He$	$Q = 4.02$ MeV	(R8)
$p + {}^7Li \rightarrow 2\alpha$	$Q = 17.35$ MeV	(R9)
$p + {}^{11}B \rightarrow 3\alpha$	$Q = 8.68$ MeV	(R10)

For the occurrence of a fusion reaction the, the fusing nuclei need to be imparted the sufficient kinetic energy to circumvent the repulsive electrostatic barrier (Coulomb barrier). The cross-section of a fusion reaction is used to express the probability of its successful occurrence. Fusion reactivity is defined as average cross sections (σ) times the relative speed (v) of the reacting nuclei. The fusion reactivity as a function of temperature for the three most probable fusion reactions is depicted in **Figure 1.2** [14].

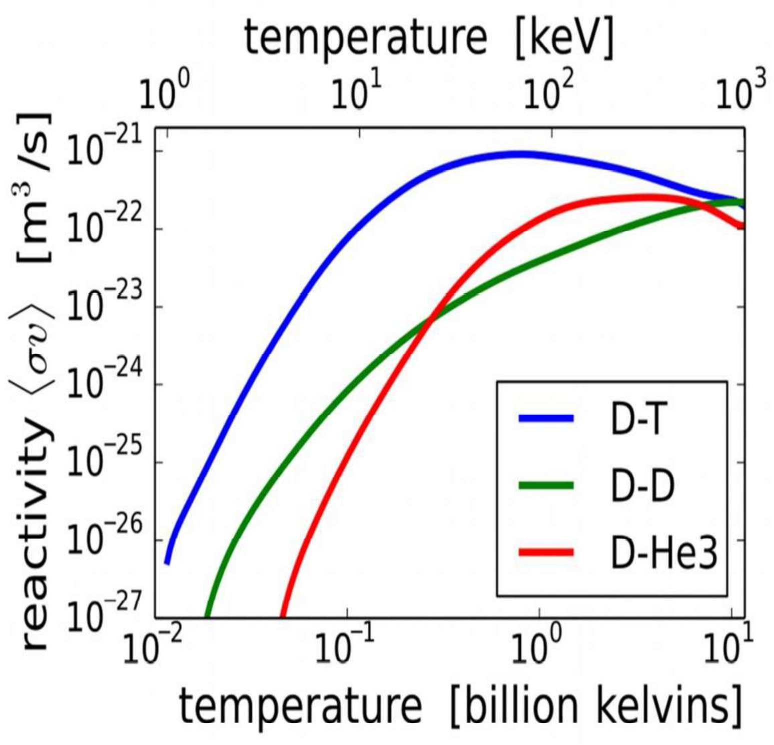

Figure 1.2 Plot of the fusion reactivity as a function of temperature [22]

The fusion of elements with higher charges takes place with an increasingly lower probability and requires higher temperatures/kinetic energy. It is because with an increase in electrical charge, the fusing nuclei have to experience an increasingly more repulsive Coulomb barrier. The rate of fusion reaction increases sharply with temperature until the attainment of maximum and subsequently drops off gradually (**Figure 1.2**).

The D-T fusion rate maximizes at a lower temperature (~70 keV/or 700 million kelvins) with higher reactivity value than other reactions. Because of these reasons, D-T fusion has been the reaction of choice to date for fusion energy. In order to realize D-T fusion, the fuel comprising of these gases must be heated to temperature arpund 20keV or 20×10^7 °C. At such extremely high temperatures, the fuel turns into a plasma.

The fusion of deuterium and a tritium nucleus produces a helium nucleus and a neutron with release of 17.6 MeV of energy (**Figure 1.3**). The alpha particle carries 20% (3.5 MeV), and the neutron 80% (14.1 MeV) of the total energy [10,14].

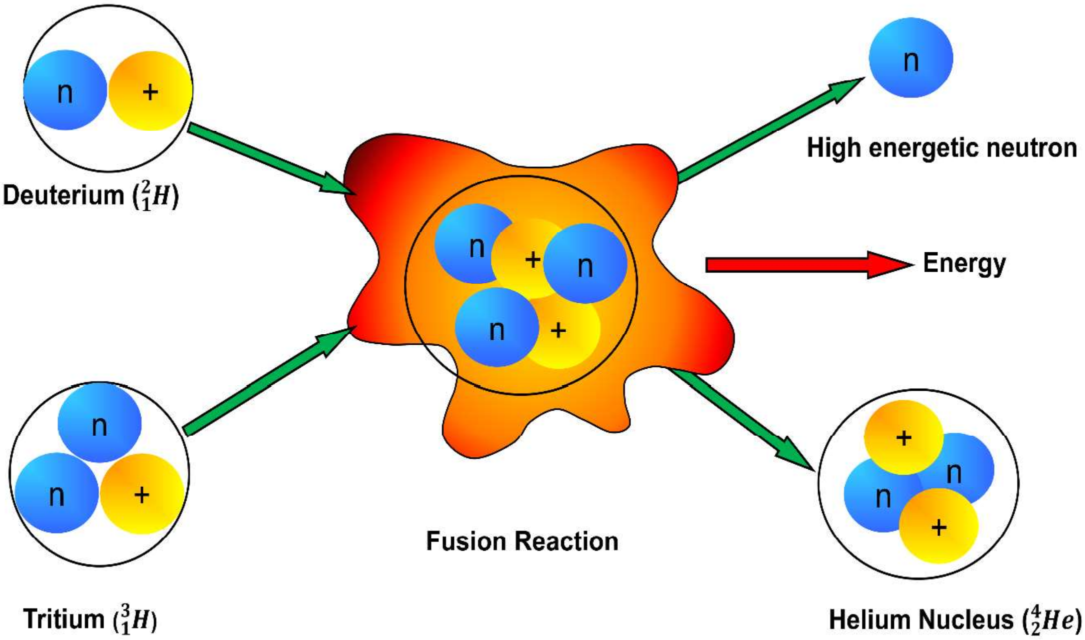

Figure 1.3 D-T fusion reaction-schematic [10,14]

In fusion reactor, the energy of neutron will be dissipated as heat followed by into the electricity. The positively charged alpha particle is entrapped by the magnetic field, and its energy can be utilized for the plasma heating. For a self-sustaining fusion reaction, initially, an external source of energy with minimal thermal loss is required to raise the plasma temperature over 100 million Kelvin [10,14]. However, the fraction of heating power contributed by the alpha particles towards total power required for the plasma heating increases with increase in the rate of fusion reaction. Therefore, at some point called ignition, the heating power provided by the alpha particles itself becomes adequate to sustain the D-T fusion. The isolation of the hot plasma from the walls of the reactor is essential to protect the structural materials at such a high temperature. This can be achieved through different confinement techniques, and the one such technique is the magnetic confinement. In magnetic confinement, a strong magnetic field is applied to confine the motion of alpha particles into a circular trajectory away from the reactor walls by creating a magnetic cage [10,23].

To generate more energy from D-T magnetic confinement fusion reaction than the input energy, the Lawson's criterion developed by John D. Lawson (a Physicist at the UK Atomic Energy Establishment at Harwell) in 1955 need to be satisfied. The Lawson criterion was derived by equating the alpha particle heat to the rate at which energy is lost from the plasma. This criterion is expressed as triple product of plasma temperature (T), density (n), and confinement time (τ): $nT\tau_E > 3x10^{21}$ keVm^{-3}s^{-1} [24]. According to this criterion, a minimum temperature (ideal ignition temperature) needs to be exceeded for the D-T fusion reaction to serve as an energy source. Additionally, a trade-off exists between the required plasma density (n) and the confinement time (τ), and accordingly a higher plasma density allows lower confinement time and vice versa. The Lawson criterion comprised a scientific Holy Grail for researchers working in the area of fusion energy [7].

1.1.3 Achieving Fusion energy: Fusion reactor

To harness energy from nuclear fusion many attempts have been made to mimic thermonuclear action of the sun and the stars and develop fusion power stations, which will utilize dissipated neutrons energy for generating electricity. The conceptual design of a fusion power station is similar to a contemporary thermal power stations [25]. The dissipated heat generated due to slowing down of neutrons in the blanket material surrounding the reactor, will be converted into steam and steam will be further used to drive turbines and generate the electrical power (**Figure 1.4**).

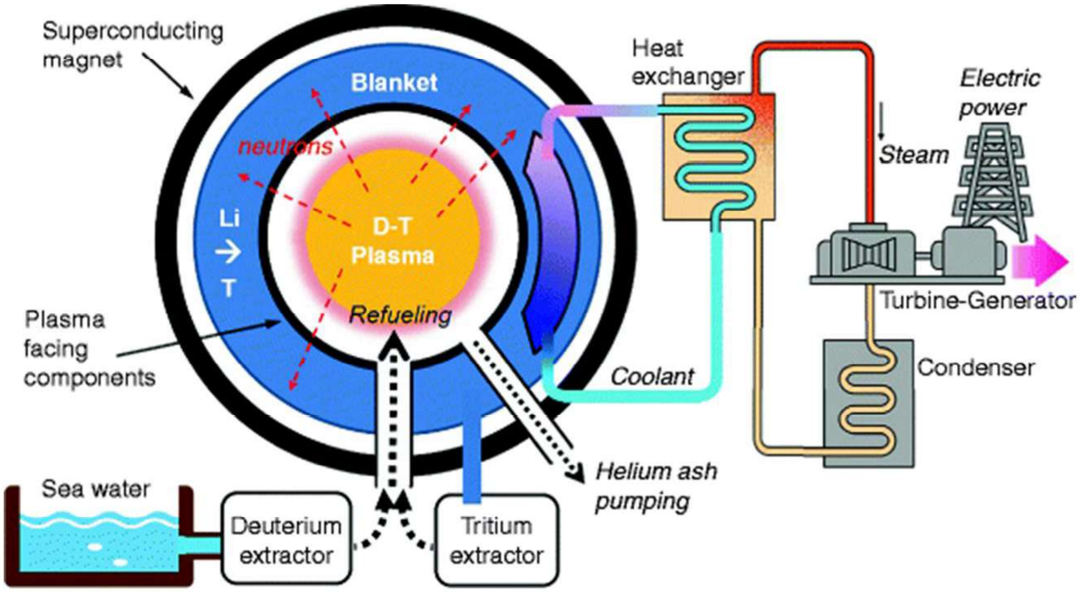

Figure 1.4 Conceptual schematic of a D-T nuclear fusion power plant [25] (Reproduced with the permission from Springer)

The achievement of extreme plasma conditions is the most challenging for the occurrence of fusion reaction in the reactor. Two different confinement approaches, the inertial and magnetic, have been investigated widely for this purpose [10,23]. In the inertial confinement approach, a small pellet containing frozen D-T fuels is rapidly heated by flash-irradiation with several extremely intense laser beams, and thereby to attain the necessary plasma conditions for fusion without allowing sufficient time to escape. The magnetic-confinement concept utilizes a strong magnetic field to control the plasma. The ignition conditions required for the two fusion concepts are a bit different. For inertial-confinement fusion, the time is shorter (n↑ and τ↓). However, for magnetic-confinement, plasma, density is quite low (n↓ and τ↑). Therefore, both concepts utilize different plasma pressure versus time [10,23]. Until now, none of these concepts have successfully achieved nuclear fusion in a sustainable and controlled way and thereby able to produce energy on a commercial scale. However, controlled fusion reactions have been successfully demonstrated on a small scale, and the feasibility of power generation through nuclear fusion has been verified. The best demonstration was achieved in 1997 by the Joint European Torus (JET) reactor (in Culham, UK), which produced a fusion power output of 16 MW from an input power of 24 MW (i.e. conversion gain Q=0.65) [10,23,25]. The National Ignition Facility (NIF) at the Lawrence Livermore National Laboratory in California, USA, is conducting experiments and testing the inertial fusion employing larger laser facility. The NIF Laser Fusion reactor first went live in June 2009, is the only reactor till now that have exceeded breakeven performance. In 2013, it achieved a conversion gain factor of 1.4, but with the much lower output power than that of a magnetic-confinement device Tokamak [10,23]. Although quite good improvements in the plasma profiles and magnetic control have been made that influence the confinement, but still a long way to go for building a commercial fusion power station.

1.1.4 International Thermonuclear Experimental Reactor (ITER)

ITER, means The Way in Latin. The ITER project is directed towards the development of commercial fusion energy [26–28]. Its programmatic objective, as defined in the ITER EDA Agreement, is *to demonstrate the scientific and technological feasibility of fusion energy for peaceful purposes* [29]. The participants countries in this mega project are: China, the European Union, India, Japan, South Korea, Russia, and the United States of America (**Figure 1.5**) [30]. ITER will be the first thermonuclear fusion device which aims to produce net energy by sustaining fusion for long periods. ITER will also provide an opportunity to test the integrated technologies, materials, and physics regimes necessary for the development of commercial fusion power reactors. The ITER project site is located at Cadarache in the southern France.

Figure 1.5 Countries participating in the ITER project [30]

The ITER Tokamak cutaway is shown in **Figure 1.6** [31]. The ITER primarily has been designed to achieve the following objectives [29];

- Demonstrate release of 500 MW of fusion power from 50 MW of input power (i.e. energy gain factor Q=10) for up to 500 seconds.
- Demonstrate integrated operation of technologies for a fusion power plant.
- Demonstrate the feasibility of heating a large volume of deuterium-tritium plasma and sustain fusion reaction through internal heating.
- Demonstrate endurance of candidate fusion reactor materials against irradiation by energetic neutrons and radiations, high thermal stresses, and intense interactions with D and T.
- Demonstrate the feasibility of tritium breeding within the vacuum vessel.

- Demonstrate the safety characteristics of a fusion device.

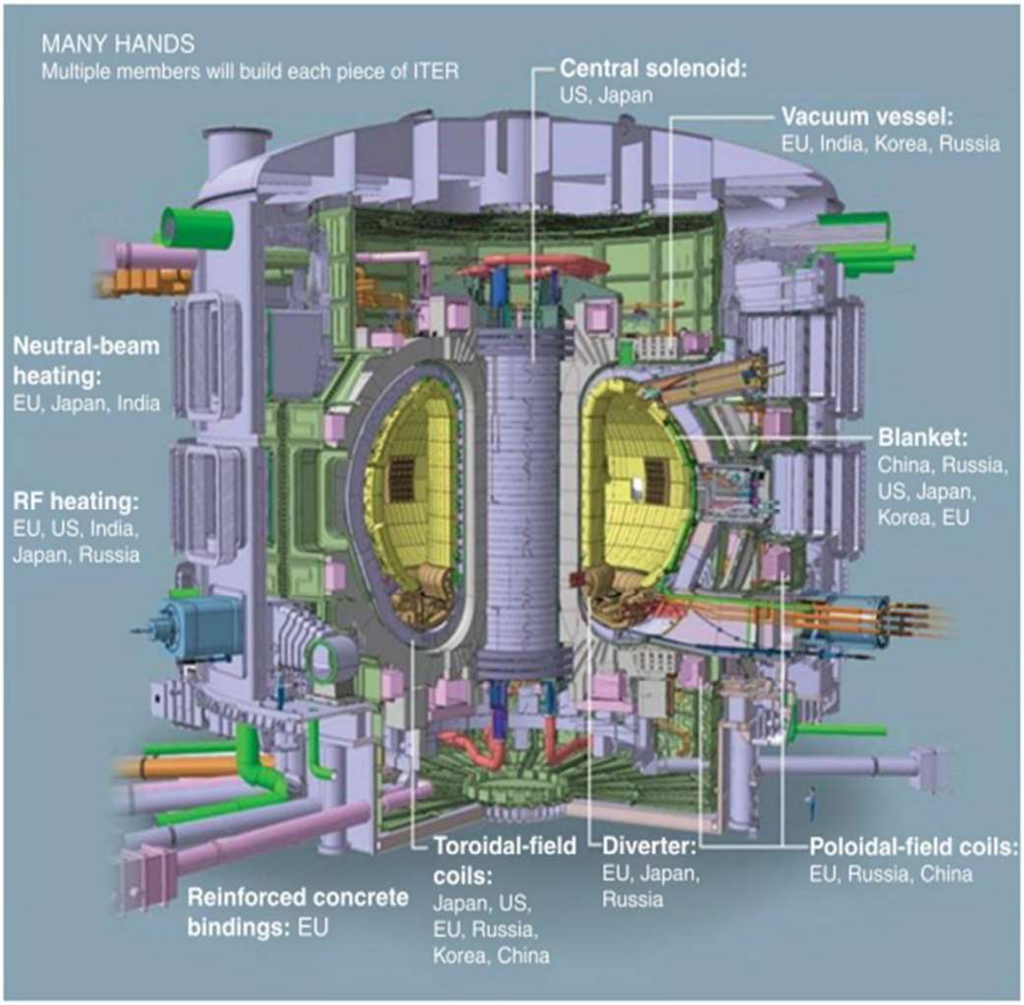

Figure 1.6 A cutaway view of ITER Tokamak [31] **(Reproduced with the permission from Springer)**

1.1.5 Tritium breeding requirement for fusion reactor

For the operation of a commercial fusion power plant based on D-T fuel cycle, an uninterrupted supply of fuels (D and T) required to be maintained into the reactor core. Although adequate quantity of deuterium is naturally available as heavy water (D_2O), however, quantity as well as concentration of naturally occurring tritium is in-sufficient for use as a fuel [32,33]. Hydrogen composed of three naturally occurring isotopes, namely ^1H

(protium or H), ^{2}H (deuterium or D) and ^{3}H (tritium or T), is the most abundant element in the solar system, around 91% of all the atoms are hydrogen [14]. Among hydrogen isotopes, H is the most abundant in nature. The natural abundance of other isotopes, D and T are 0.0156 atom% (156 ppm) and 1TU (1 atom per 10^{18} atoms of hydrogen), respectively [14]. In earth's atmosphere tritium is produced by interaction of cosmic radiation with nitrogen and oxygen nuclei via $^{14}N(n, T)^{12}C$ and $^{16}O(n, T)^{14}N$ reactions, respectively [14]. The transfer of tritium to the oceans by the hydrological system is assumed equivalent to the total estimated tritium production rate of 0.4 kg/year [34,35]. The other sources of tritium mostly include various nuclear reactions such as ternary fission of heavy nuclei like ^{235}U, ^{238}U, ^{239}Pu and ^{241}Pu etc. in the nuclear fuel, neutron reaction with D present in the coolant/moderator via D(n, γ)T reaction [14,32,33]. In addition to extremely low natural abundance, tritium is also exhausted owing to its radioactive nature. It undergoes beta decay with half-life of 12.3 years. The reaction of tritium decay written as [14];

$$ {}_{1}^{3}H \rightarrow {}_{2}^{3}He + \beta^{-} + \bar{\vartheta} \qquad Q=18.6 \text{ keV} $$

where, β^{-} is a beta particle and $\bar{\vartheta}$ is an antineutrino. The maximum energy of beta particle is 18.6 keV and the average energy is 5.7 keV.

The estimated tritium consumption in commercial D-T fusion reactor is high (55.8 kg per 1000 MW fusion power per year). According to this projection, if ITER were to run at 1000 MW fusion power with 10% availability, the global tritium supply would be exhausted by 2025 [32,33,36,37]. Therefore, high power D-T fusion devices must breed their tritium from other sources.

1.2 Solid tritium breeder materials

1.2.1 Tritium breeding concept

Lithium, by irradiation of neutrons, can be used to produce tritium. Natural lithium is composed of two stable isotopes viz. ^{6}Li and ^{7}Li with isotopic composition of 7.4% and 92.6% respectively [14,36,38,39]. The isotopes of lithium, because of low nuclear binding energy per nucleon, are used to produce tritium by the following nuclear reactions [10,14]:

$$^{6}_{3}Li + \, ^{1}_{0}n \rightarrow \, ^{3}_{1}H + \, ^{4}_{2}He + 4.78\ MeV$$

$$^{7}_{3}Li + \, ^{1}_{0}n \rightarrow \, ^{3}_{1}H + \, ^{4}_{2}He + \, ^{1}_{0}n - 2.47\ MeV$$

The tritium production cross-section as a function of neutron energy for above reactions are depicted in **Figure 1.7** [40,41]. The reaction of ^{6}Li isotope with neutron is exoergic and has a high cross-section for low energy neutrons. In contrast, the reaction of ^{7}Li is a threshold reaction (endoergic) that requires an incident neutron energy over 2.47 MeV. Moreover, because of the Coulomb barrier, the cross section this reaction is considerably low above the threshold energy (2.5 MeV). Therefore, ^{6}Li enrichment of the selected tritium breeding material is always required to achieve target tritium breeder ratio and thereby tritium self-sufficiency. The effective ^{6}Li density can be increased to any desired value through the use of isotope enrichment process. However, the neutrons with energy of 14 MeV generated from the primary fusion reaction can promptly cause ^{7}Li reaction and the decelerated neutron can produce another tritium atom by the ^{6}Li reaction. Therefore, two tritium atoms can be produced from single neutrons. Neutron multipliers such as beryllium (Be) can compensate for parasitic losses of neutrons in structural components of the reactor and thereby improve tritium breeding ratio. Beryllium serves as neutron multiplier via (n,2n) reaction as written below;

$${}_{4}^{9}Be + {}_{0}^{1}n\ (> 2MeV) \rightarrow 2\ {}_{2}^{4}He + 2\,{}_{0}^{1}n - 1.67\ MeV$$

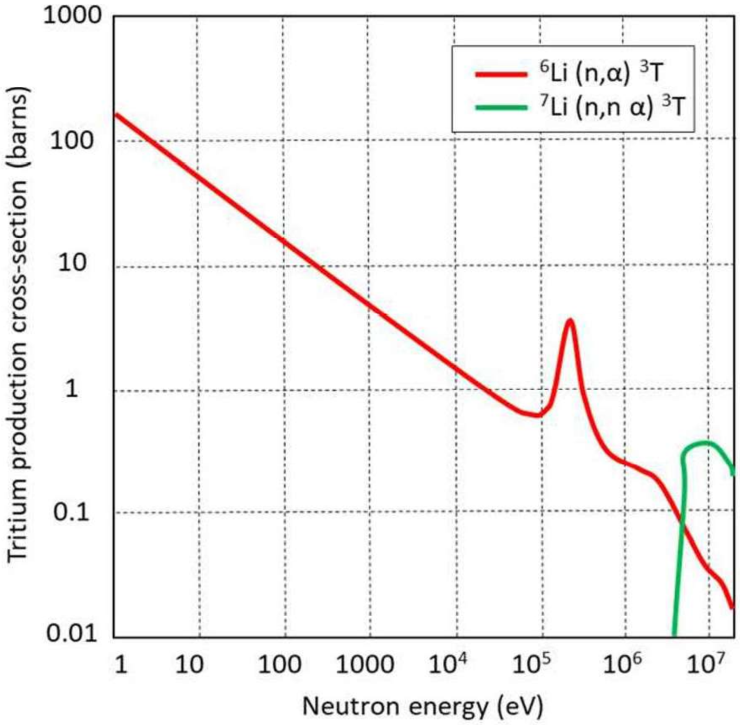

Figure 1.7 Tritium production cross-section as function of neutron energy [40,41]

1.2.2 Lithium ceramics: Candidate tritium breeder

Li-based tritium breeding blanket is a critical component of the magnetic-confinement based D-T fusion reactor. The various chemical forms of Li is utilized in different breeding blanket concepts. The breeding blanket serves two functions: breeding tritium and converting the energy into sensible heat. Principal requirements fulfilled by the breeder material are [36,39]:

- Breed and release tritium,
- Possess physical and chemical stability at high temperature,
- Display compatibility with other blanket components, and
- Exhibit adequate irradiation behaviour.

From the sole consideration of tritium breeding, the best breeder material would be the one containing highest lithium atom density. Moreover, the composition of breeder materials must include elements having the lowest neutron absorption cross-sections. In principle, metallic Li can also be used for tritium breeding. In fact, metallic Li and Li-Pb molten alloy can offer the highest tritium breeding ratios (TBR). However, in the molten state, metallic Li is violently reactive in the presence of air or water that can lead to fire hazard in off-normal or accidental scenarios. Moreover, since the molten metals are electrically conducting, it often poses difficulties in pumping molten metals at high rates across the existing strong magnetic field [36,39,42,43]. In order to circumvent these problems, the alternative blanket concepts utilizing Li-based ceramics solid tritium breeders has been developed. Lithium-containing ceramics mainly include Li_2TiO_3, Li_2ZrO_3, $LiAlO_2$ and Li_4SiO_4 that have been considered as potential candidate tritium breeding materials owing to promising thermo-physical and thermo-chemical properties and inherent safety advantages [36,38,39][44,45]. Some of the relevant characteristics of these ceramics have been presented in **Table 1.2** [14]. Each of these ceramics has advantages and disadvantages for breeder applications. These ceramics have different Li atom density that can be compensated by ^{6}Li-enrichment. In addition to these ceramics, numerous other Li containing ceramics that can result in improved tritium breeding ratio, have been continuously investigated [44]. Although Li_2O, due to the high Li atom density is the only ceramic that may achieve the desired tritium breeding ratio without the use of a neutron multiplier, however, strong moisture sensitivity (hygroscopic nature), corrosive property, and evidence of irradiation induced swelling are some of its serious disadvantages [36,45]. Therefore, it is not suitable for the application of a tritium breeder. Although Li_2TiO_3 and Li_4SiO_4 have been preferred choice as breeding blanket material for ITER DEMO, however, Li_2ZrO_3 and $LiAlO_2$ have superior mechanical properties, irradiation behaviour and compatibility with other structural components which can be advantageous for application in high power commercial fusion reactors [38,46–48].

Table 1.2 Properties of candidate Li-based ceramic tritium breeders [14]

Properties	Preferable	Li_2O	Li_2TiO_3	Li_2ZrO_3	Li_4SiO_4	γ-$LiAlO_2$
Melting point [K]	Higher	1692	1808	1888	1523	1883
Density [g/cm^3]	Lower	2.02	3.43	4.15	2.21	2.55
Li density [g/cm^3]	Higher	0.94	0.43	0.38	0.51	0.27
Thermal conductivity at 500°C [W/m/°C]	Higher	4.7	1.8	0.75	2.4	2.4
Thermal expansion at 500°C, [dL/L$_0$ %]	Smaller	1.25	0.8	0.50	1.15	0.54
Reactivity with water	Lower	High	Stable	Stable	Low	Low
Tritium retention time at 400°C [h]	Shorter	8.0	2.0	1.1	7.0	50
Swelling [dV/V$_0$ %]	Lower	7.0	-	<0.7	1.7	<0.5
Activated products by neutron absorption	Less	$^{16}O(n, p)$:7 s	$^{46}Ti(n,p)$:84 d $^{47}Ti(n,p)$:3.4 d $^{48}Ti(n,p)$:1.8 d	$^{90}Zr(n,p)$:64 h $^{91}Zr(n,p)$:57 d $^{94}Zr(n,2n)$:106 y $^{96}Zr(n,2n)$:64 d	$^{28}Si(n,2n)$:4 s $^{29}Si(n,p)$:6 m $^{30}Si(n, \alpha)$:9 m	$^{27}Al(n,2n)$:6 s $^{27}Al(n,p)$:9.5 m $^{27}Al(n,\alpha)$:15 h

Processing of tritium breeder based on Li ceramics broadly involves three steps (i) powder synthesis, (ii) powder consolidation/shaping, and (iii) sintering [36].

Sintering is invariably the final and an important processing step of Li-containing tritium breeding materials irrespective of powder synthesis methods and shape of the consolidated powder (pellet, pebble, bar, foam etc.). The general scheme of processing of sintered tritium breeders is depicted in **Figure 1.8**. Processing has a critical role in determining the microstructure of the breeder and thereby tritium recovery and control.

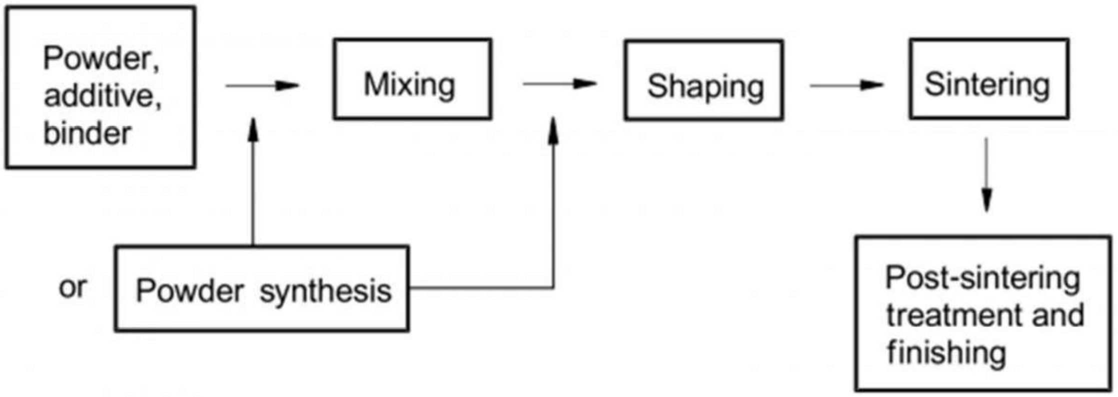

Figure 1.8 General processing scheme for preparation of ceramic breeder

1.3 Sintering

Sintering is a process of bonding individual powder particles into a coherent, predominantly solid structure by the application of heat. Heat enables the mass transport phenomena that often occur on the atomic scale leading to inter-particle bonding that results in improved strength and lower system energy [49–51].

Sintering processes can be of two types: solid state sintering and liquid phase sintering [52,53]. In solid state sintering, the powder compact is densified completely in a solid state at the sintering temperature. However, liquid phase sintering occurs in the presence of a liquid phase in the powder compact during sintering [52]. In general, compared with solid state sintering, liquid phase sintering allows easy control of microstructure and higher densification rate with concomitant reduction in processing cost. However, it often degrades some important properties, for example, mechanical properties [52,53]. The liquid phase sintering of solids requires addition of low melting point compounds or low temperature glass forming constituents commonly referred as sintering aid in the solid prior to sintering [52,53].

The driving force of sintering is the reduction of the total interfacial energy by the reduction of surface area of the powder. The total interfacial energy of a powder compact is expressed as γA, where γ is the specific surface (interface) energy, and A, the total surface (interface) area of the compact. The reduction of the total interfacial energy can be expressed as [49,52,54]

$$\Delta(\gamma A) = \Delta\gamma A + \gamma\Delta A$$

The reduction of total interfacial energy of the powder compact can proceed by two often competing processes, densification ($\Delta\gamma$) and grain-coarsening/growth (ΔA) as schematically shown in **Figure 1.9**. For solid state sintering, $\Delta\gamma$ is related to the replacement of solid/vapour interfaces (surface) by solid/solid interfaces.

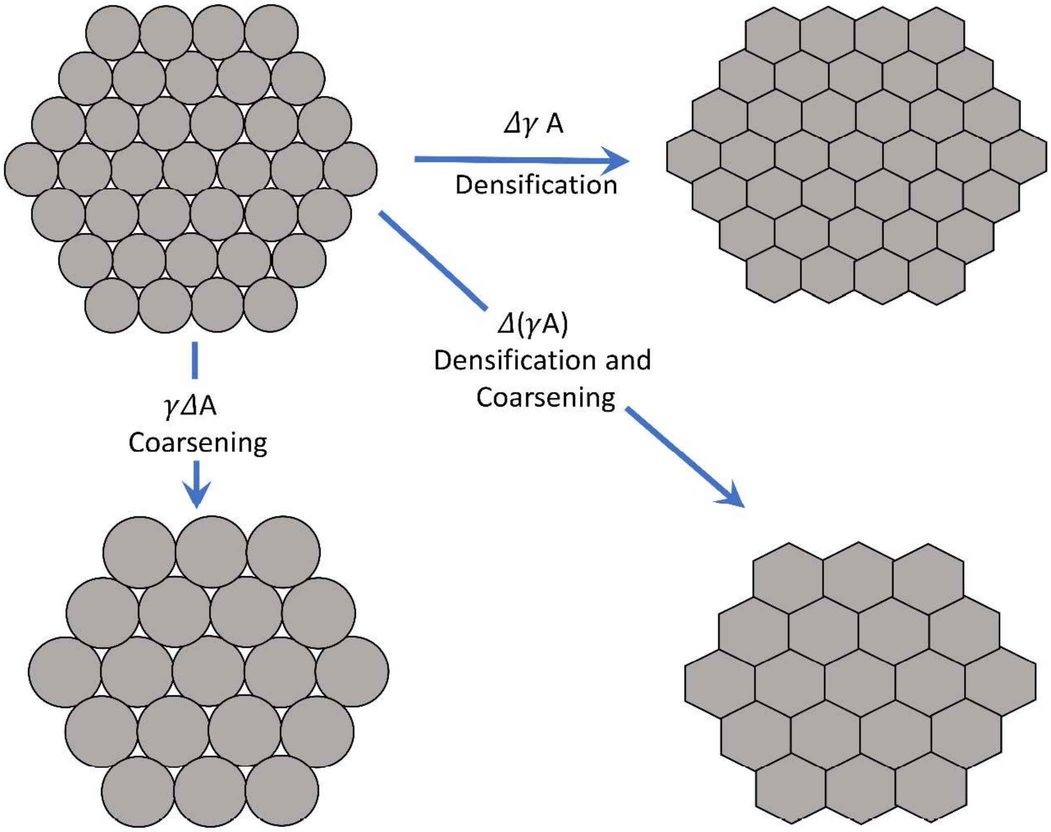

Figure 1.9 Schematic demonstration of phenomena occurring during sintering [52,54]

The major variables determining sinterability and the sintered microstructure of a powder compact can be divided into two categories: material variables and process variables (**Figure 1.10**). The material variables include chemical composition of powder compact, powder size, powder shape, powder size distribution, degree of powder agglomeration, etc. The other variables involved in sintering are mostly thermodynamic variables, such as temperature, time, atmosphere, pressure, heating and cooling rate [50,52–54].

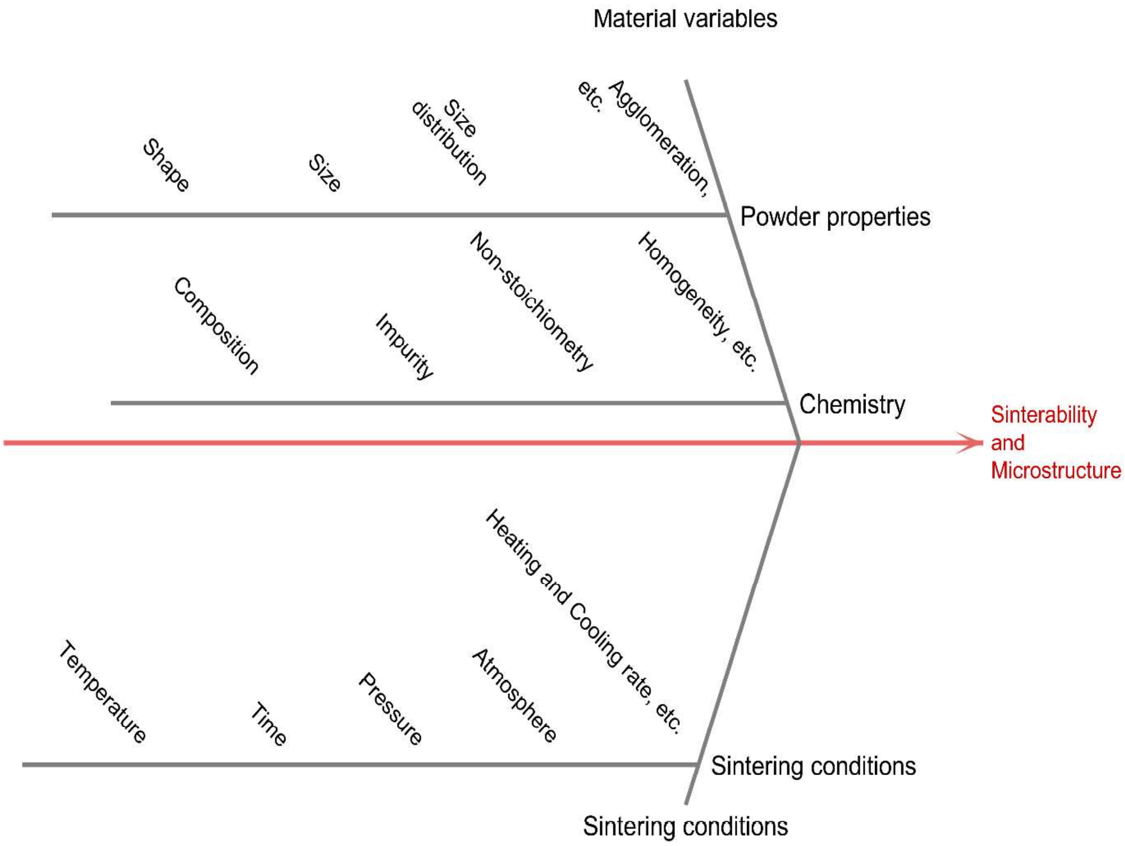

Figure 1.10 Sintering variables: Factors and effects

Solid state sintering is usually divided into three overlapping stages: (a) initial stage, (b) intermediate stage, and (c) final stage [49,52,54].

The typical densification curve of a compact through these stages over sintering time at fixed temperature is schematically depicted in **Figure 1.11** [55]. The initial stage is characterized by the formation of interparticle necks and its contribution to compact shrinkage is limited to a maximum of around 2–3%. During the intermediate stage, substantial densification, up to about 93% of the relative density, takes place and pores are still interconnected. The final stage of densification involves formation of isolated pores [52,54].

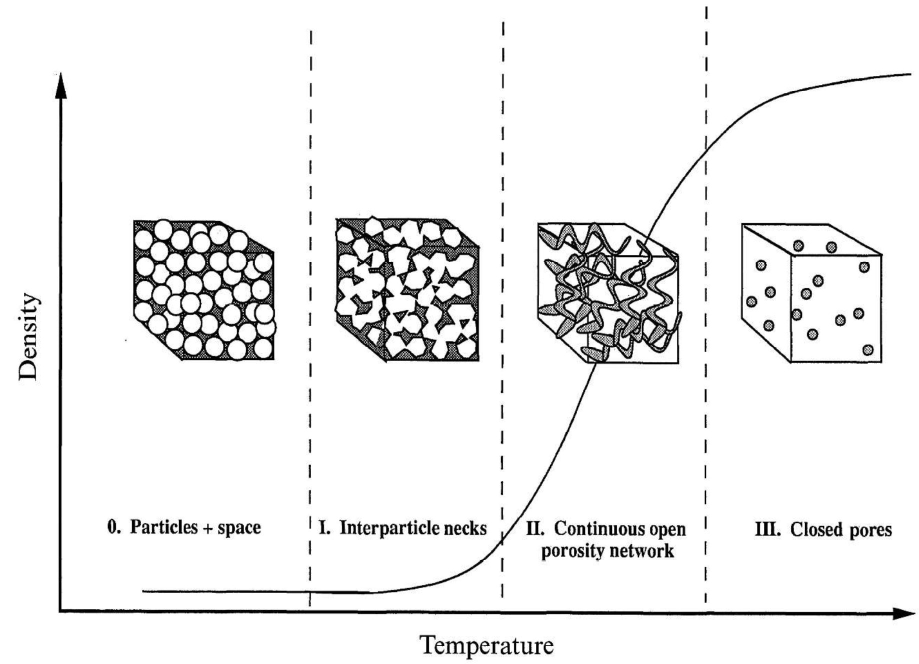

Figure 1.11 Schematic density as a function of temperature [55] (Reproduced with the permission from Taylor and Francis)

The average grain size of polycrystalline materials increases with the annealing time. The phenomenon of grain growth is important not only in sintering but also in other materials processes [53,54]. Phenomenologically, the grain growth can be divided into two types: normal and abnormal (sometimes also called exaggerated) grain growth. Normal grain growth is characterized by a simple and invariable distribution of relative grain sizes with annealing time. In abnormal grain growth, some (or a few) large grains grow unusually quickly in a matrix of fine grains with a very slow growth rate. In terms of microstructure, the normal grain growth exhibits unimodal grain size distribution, and the abnormal grain growth the bimodal grain size distribution [50–54].

1.3.1 Sintering of nanocrystalline ceramics

Nanocrystalline is a term used to describe an exciting class of crystalline materials with a particle or grain size less than 100 nm [56]. Usually, the conventional materials including both bulk (e.g., steel or concrete) and powdered (e.g., sugar and sand), typically have grain sizes on the orders of microns to millimeters. As a result of decreasing the particle or grain size to the nanometer regime, the specific surface area (i.e., surface area per unit mass) and grain boundary volume of these materials are greatly increased. This in turn can have a large effect on the properties of the materials. **Figure 1.12** shows the change in surface area and grain boundary volume fraction as the particle or grain size of a material is decreased [57].

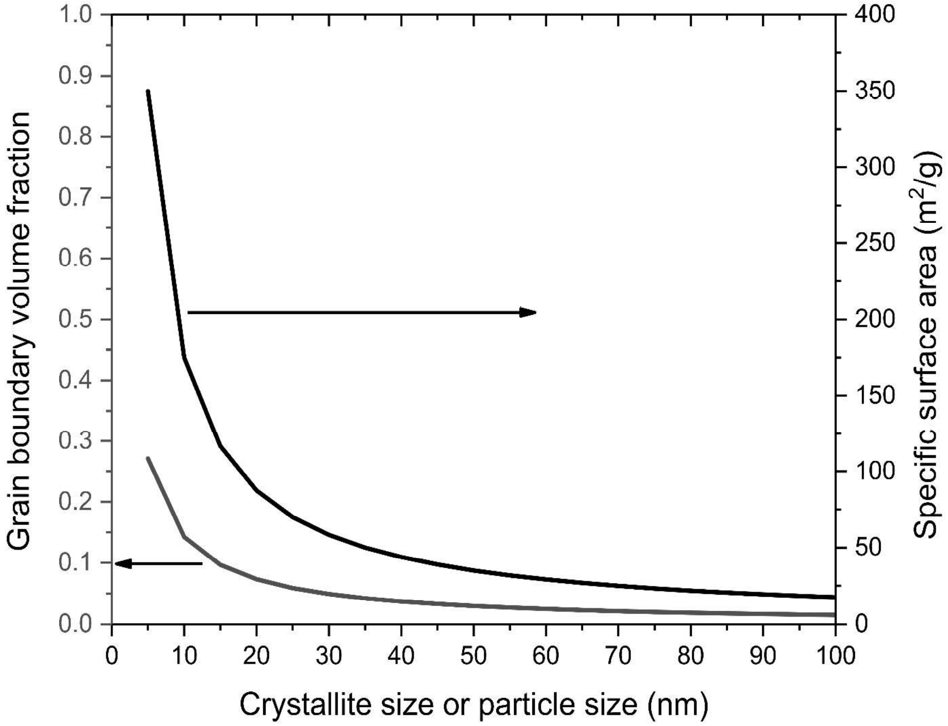

Figure 1.12 Grain boundary volume fraction and surface area as a function of crystallite size or particle size

The surface area was calculated for dense monodisperse spherical Li_2TiO_3 particles and the grain boundary volume fraction was calculated assuming a grain boundary thickness equals to 0.5 nm. Due to difference in structure or chemistry from the bulk, the nanocrystalline materials behave differently from their microcrystalline form. Additionally, the quantum confinement effects rather than interfacial effects can also affect the properties of the nanocrystalline material. The quantum confinement effects mainly dominates the electronic properties (as observed in quantum dots and wires), magnetic properties (such as superparamagnetism observed in small ferromagnetic and ferrimagnetic nanoparticles or giant magnetoresistance observed in thin films composed of alternating ferromagnetic and nonmagnetic layers), and optical properties (such as shift in the absorption edge) [56,58–61]. These differences between the bulk and nanocrystalline forms along with the associated potential applications have engendered numerous research programs on nanocrystalline materials around the world.

Most of the current research on nanocrystalline ceramics have been directed towards the development of high value-added engineered systems whereby the material is designed at the nanometer scale to optimize specific properties for catalytic, electronic, optical, magnetic or nuclear applications. The design of such ceramic systems mainly relies on improved densification rate of nanoparticulate compacts. In addition, the production of nanoparticles for fabrication of bulk ceramic components is also of much interest. The goal of such research is to (i) understand, optimize, scale-up and reduce the costs of nanoparticle synthesis (ii) produce materials that can be densified at lower temperatures, and (iii) enhance the properties or lower the cost of specialized products. The improved densification of nanoscale powder compacts is partly due to the high surface areas (i.e., large driving force for sintering), the shortened diffusion lengths and the increased grain boundary volume. These effects can be explained by a generalized densification rate equation given below [55].

$$\frac{d\rho}{dt} = \frac{1}{G^{n}} exp\left(\frac{-E_a}{RT}\right)$$

According to this equation the rate of densification/sintering (dρ/dt) is inversely proportional to the n^th^ power of grain size (G). The value of n depends on which mechanism dominates the sintering process. If the surface diffusion is dominating the n = 3, and in case of grain boundary diffusion is dominant mechanism the value of n = 4. This implies that sintering temperature and/or time duration necessary to attain required density could be drastically reduced by decreasing the particle size. For example, if the particle size is decreased by a factor of 10, the sintering rate could increase by a factor of 1000 or more. Therefore, sintering temperature and time necessary to attain desired density could be drastically reduced (**Figure 1.13)** [55].

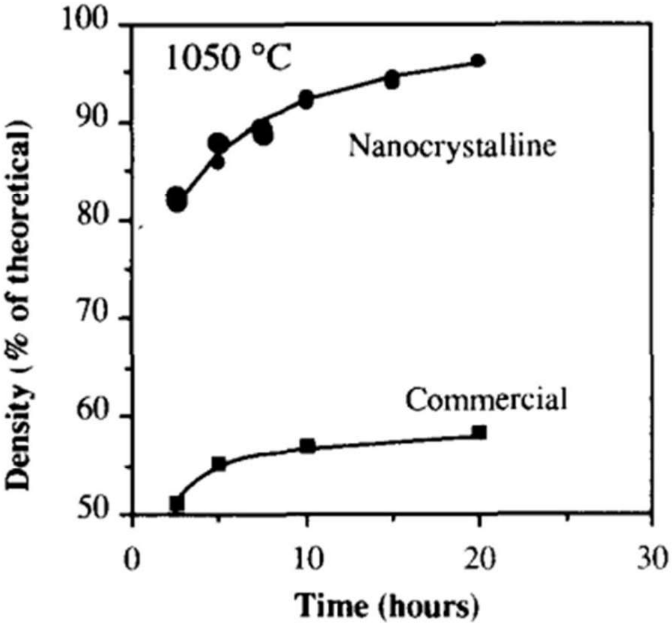

Figure 1.13 Density of nanocrystalline versus commercial (Tosoh TZ-3Y) ZrO_2 3mol% Y_2O_3 as a function of holding time when isothermally sintered at 1050°C [55] (Reproduced with the permission from Taylor and Francis)

However, there are some issues in compaction and sintering of nanoscale ceramic powders which mainly arise because considerable agglomeration of nanoscale powders under the influence of Van der Waals attraction forces. The agglomeration often takes place during the synthesis, handling and particularly drying. Agglomeration leads to two types of pores in the green body (the powder compacts prior to sintering); inter-agglomerate pores and smaller inter-crystalline pores within the agglomerate; as shown in **Figure 1.14** [55]. The removal of the inter-agglomerate pores generally requires high sintering temperatures that also encourages fast grain growth which makes it challenging to maintain nanoscale grain size in sintered component. The removal of agglomeration and thereby achieve dense packing free from cracks, pores, and density gradients in the green powder compact is of concern in consolidation of nanoscale ceramic powders [62]. The uniformity particle packing is an effective means of achieving higher densification of the green body during the sintering.

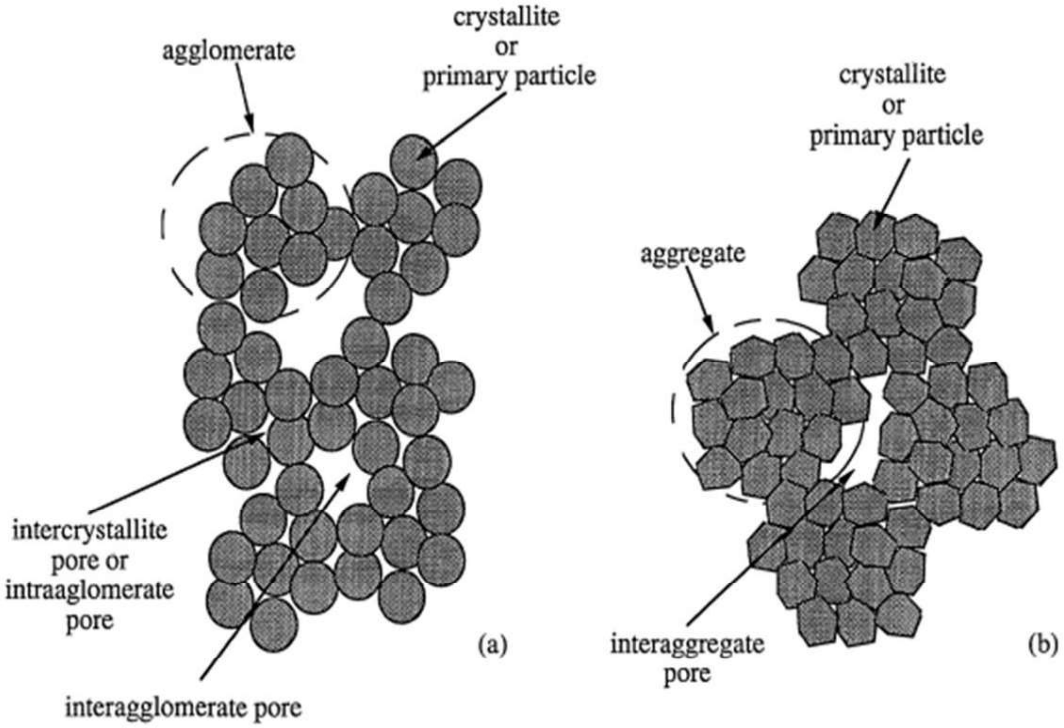

Figure 1.14 Schematic illustration of (a) agglomerate and (b) aggregate [55] (Reproduced with the permission from Elsevier)

1.3.2 Sintering of Li ceramics

Sintering of Li ceramic is of prime importance, in general, to produce sintered tritium breeder materials with desired microstructure in reproducible manner by controlling the sintering variables. The microstructure of sintered tritium breeder is comprised of density, grain size, porosity and distribution of other phases. Microstructure of breeder has very crucial role in controlling tritium retention and release characteristics of ceramic breeder. Tritium recovery and control, requires understanding of transport and retention of tritium within the breeder. Firstly, tritium generated from nuclear transmutation of Li by neutron capture is transported to the grain boundary by intragranular (lattice) diffusion within the grains. The bulk diffusion and trapping of tritium within the grains are affected by the neutron and radiation-induced defects. Subsequently, tritium diffuses along the existing grain boundary pathways between the adjacent grains to the solid/gas interface (open and closed porosity). The fraction of closed porosity provides another means to build up inventory in the material. At the surface, various processes take place involving isotope exchange with hydrogen (H_2) and water (H_2O) leading to desorption of tritium in chemical forms of HT and HTO, respectively. Further, the tritium-bearing species (HT, HTO and T_2O) are transported through the interconnected pores and enter the flow of the purge gas. The assessment of tritium retention in the breeder requires knowledge of rate determining steps and the most relevant operation as well as microstructural parameters that facilitate the tritium release. The involved tritium transport mechanisms in single sintered ceramic breeder pebble is schematically depicted in **Figure 1.15** [63–65]. In summary, the entire transport mechanisms of bred tritium can be divided into the following steps: intragranular diffusion; grain boundary diffusion; surface adsorption/desorption; pore diffusion and purge flow convection (**Figure 1.15**) [63,65–68]. The microstructure is an important factor affecting several steps of tritium transport mechanisms, particularly intragranular diffusion, grain boundary diffusion and pore diffusion in sintered ceramic breeders. Particularly, grain size is an important parameter affecting the tritium release properties of tritium breeding ceramics. The out-of-pile tritium annealing studies on sintered Li ceramic pebbles have shown that tritium release can be accelerated by decreasing grain size [69–74]. It is because the activation energy for intragranular diffusion is higher as compared to grain boundary diffusion. Annealing studies and in-pile tests clearly demonstrated that, in case of small grained microstructure, tritium release is faster compared to large grained [71,75–80].

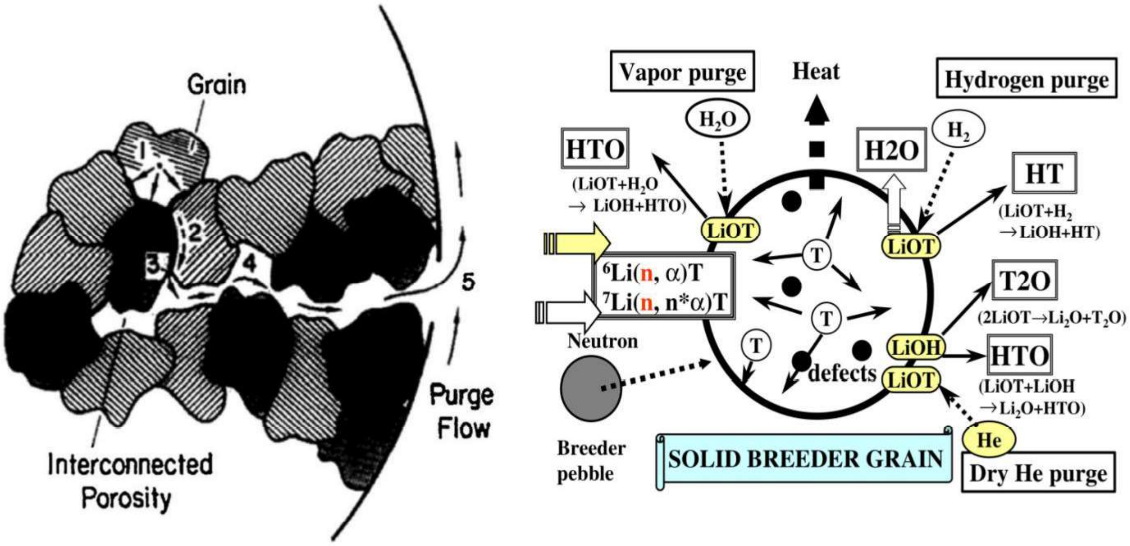

Figure 1.15 Schematic diagram of the tritium transport mechanism in the ceramic breeder (1: intragranular diffusion, 2: grain-boundary diffusion, 3,4: pore diffusion and 5: purge flow convection [63–65] (Reproduced with the permission from Elsevier)

The tritium retention (i.e., residence time) in sintered Li ceramic with large grain size is much longer than with small grain size. Moreover, microstructure has a significant effect on mechanical properties of the breeder. The mechanical properties and radiation resistance can be augmented by increasing density and decreasing grain size which can alleviate the swelling, embrittlement and fragmentation of Li ceramic breeders under intense thermal and radiation fields in fusion reactor environments [81–88]. In summary, the central theme in the processing of Li ceramic breeders is to enhance densification while simultaneously limiting the grain growth. The typical preferable microstructure of breeders consisted of relative density in the range of 85-90%, grain size of about 2-5μ or even smaller, interconnected porosity (10-15%) [89–94].

1.3.3 Critical issues in sintering of Li ceramics

Li ceramics exhibit a tendency of Li sublimation and uncontrolled grain growth, particularly, when sintering temperature exceeds 1000°C [95–101]. Due to these factors, it is often quite challenging to achieve required density and small grain size at the same time. The loss of Li has a detrimental effect on tritium breeding as the breeder in the blanket must have a high amount of lithium to achieve tritium self-sufficiency. The large grain size arising due to uncontrolled grain growth could dampen the tritium release process through the breeder microstructure. It would decrease tritium breeding ratio and also allow accumulation of tritium inventory in breeders, which has serious concern with regard to D-T fusion reactor safety.

1.4 Motivation and objective of present work

Sinterability enhancement of Li ceramics has drawn much attention among scientists that have spawned numerous research programs around the world. The goal of such concerted research is to explore and establish suitable approaches to circumvent the critical issue of Li sublimation and uncontrolled grain growth that occurs during the sintering of Li ceramics. Numerous prior works report on the sintering of Li ceramics. However, the sintering parameters in the literature severely lacked consistency, for instance, a considerably broad range of sintering temperatures (850-1400°C) and time (2-10h) have been reported [102–111]. But the final sintering parameters have not been established yet.

There are many methods for improving the sinterability of ceramic powders. The widely used methods are the use of fine (sub-micron to nanoscale) powders, the addition of sintering aids, and aliovalent doping.

Among these methods, the one utilizing sub-micron to nanoscale powders could be the most useful approach for Li ceramics. The other methods, (addition of sintering aid and aliovalent doping), have limited scope for Li-based ceramic tritium breeders. It is due to the condition of stringent chemical purity (nuclear grade) for application as the tritium breeders that imposes restrictions on the addition of many foreign elements, particularly those which can act as a neutron absorber or give rise to activation products upon neutron irradiation.

One of the goals of the present thesis is to improve sinterability of Li ceramics without additives. With no use of additives, detrimental effects associated with the neutron absorption by impurities or activation of impurities by interaction with neutrons will minimize. The specific approach investigated was the use of fine Li ceramic powders to improve sinterability and thereby reduce the sintering temperature/and or time of Li ceramics. It would help to avoid Li sublimation, reduce the average grain size, and decrease cost of bulk production of tritium breeder material. Based on the literature, three potential candidate Li ceramic breeders; Li_2TiO_3, Li_2ZrO_3 and $LiAlO_2$ with relatively high melting points (**Table 1.2**) that is very close to each other, have been chosen for the investigation. Sintering of these ceramics often require high temperature to achieve desired microstructure for improved tritium breeding performance. The work carried out in this thesis primarily consists of (a) synthesis of fine ceramic powders of Li_2TiO_3, Li_2ZrO_3 and $LiAlO_2$ by chemical methods, (b) characterisation of as-synthesized and calcined powders and precursors by different techniques (c) consolidation of calcined powders to form powder compacts, (d) sintering behaviour of powder compacts, (e) microstructure characterization of sintered compacts and (f) chemical analysis of sintered compacts to estimate Li sublimation.

The extensive work carried out in this thesis enables the establishment of an effective method for the sinterability enhancement of Li ceramics by utilizing fine powders. It would augment the current processing method of a high performance sintered ceramic tritium breeder with a tailored microstructure that can achieve the targeted tritium breeding ratio and thereby tritium self-sufficiency. The outcome of this thesis would contribute significantly to the current state of knowledge about the development of ceramic tritium breeder materials and technology to build robust, reliable, and economical fusion power stations. Such fusion power stations could change the world's energy landscape by providing a sustainable, secure, safe, affordable, inexhaustible, and CO_2 free energy source that would not only assist in fulfilling the global energy demand but also combat climate change.

Chapter 2

Experimental

2.1 Experimental methods

2.1.1 Synthesis of nanocrystalline ceramic powders

Nanocrystalline oxides and non-oxide ceramic powders are synthesized by many different methods that can be broadly categorized as wet-chemical synthesis, combustion synthesis, attrition, and gas-phase reaction techniques [56]. Wet-chemical synthesis techniques encompass precipitation/co-precipitation, hydrolysis condensation reactions, followed by calcination, hydrothermal method, etc. Combustion synthesis techniques include flash pyrolysis of oxidizer/fuel mixtures, flame pyrolysis, and rapid evaporation techniques whereby the particles are formed very rapidly as the reactants undergo fast heating. The attrition techniques utilize mechanical energy to obtain a nanocrystalline structure from typically microcrystalline starting materials. These techniques have been used mostly for the preparation of nanocrystalline and amorphous metallic systems. The gas-phase techniques, such as plasma reactions, evaporation-condensation reactions, and sputtering, usually rely on the homogeneous condensation of particles in the gas phase to produce the desired nanocrystals.

Each of these techniques has some advantages and disadvantages, and they are used in different applications depending on the composition, quantity, and purity that need to be produced. In this thesis, two variants of combustion synthesis techniques; solid-state combustion and solution combustion synthesis have been adopted to synthesize Li ceramic powders.

2.1.2 Combustion synthesis of Li ceramics

Combustion synthesis (CS) technique, because of simplicity, less time-consuming, energy - effectiveness, and low cost has been adopted worldwide to synthesize nanomaterials, especially ceramic oxides and mixed-oxides [112–114]. Based on the physical nature of the reactants and also reaction media, CS can be classified as self-propagating high temperature synthesis (SHS) and solution combustion synthesis (SCS). The reactants in conventional SHS are all in the solid-state, typically in the form of a compact. However, in SCS, the reactants are mixed in an aqueous solution that ensures the molecular-level mixing of the reactants. The typical combustion synthesis flow sheet is depicted in **Figure 2.1**.

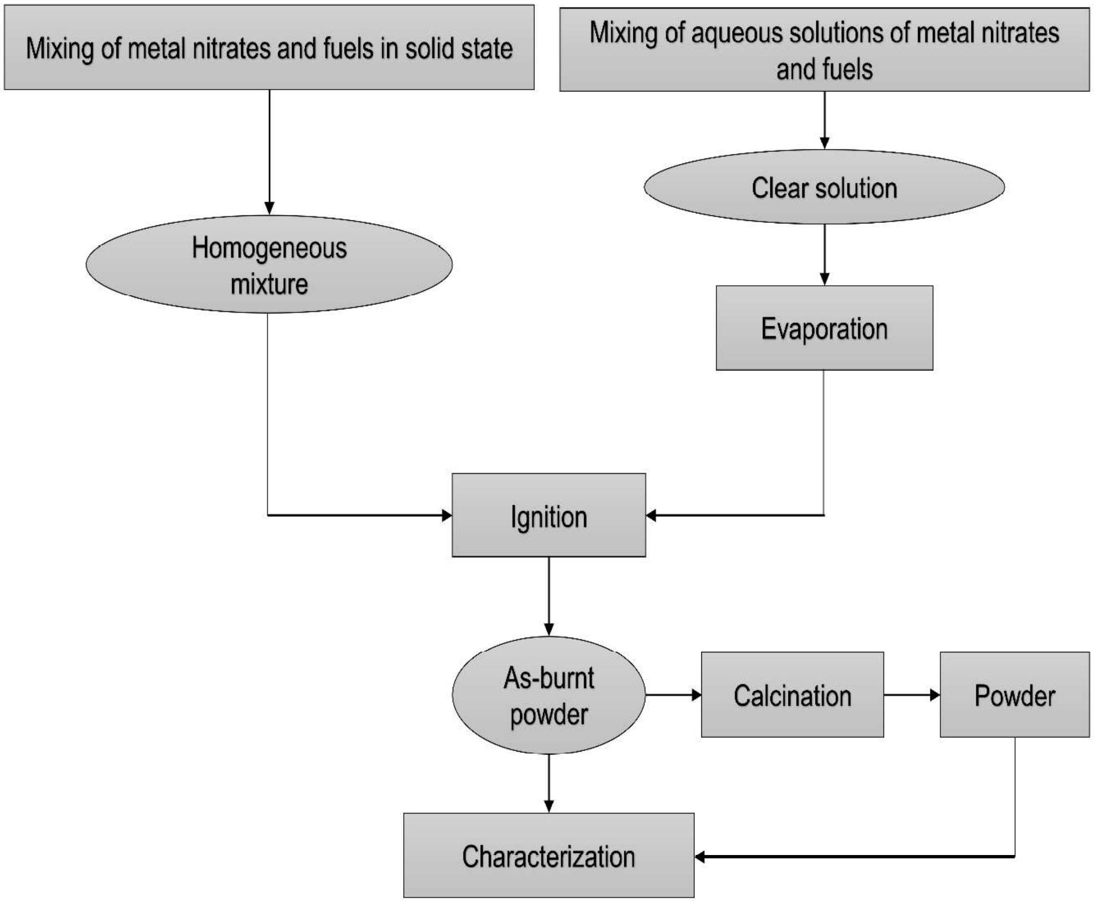

Figure 2.1 Typical Li ceramic powder synthesis process flow sheet

The CS procedure relies on a self-sustained exothermic reaction among thoroughly mixed reactants consisted of an oxidizer and an organic fuel. The driving force for the formation of crystalline structure is derived from internal chemical energy. In conventional material fabrication routes, continuous energy input is required to form crystalline structure. However, the temperature input for CS is not high, as it is required just to trigger the combustion reaction, and subsequently, a high-temperature wave, propagates through the reaction mixture resulting in a powdered product. Metal nitrates are commonly used oxidizers because they are water- soluble. Various water-soluble organic compounds containing large quantities of C and H are used as fuels, which facilitate the liberation of exothermic heat by combustion. The hydroxy-carboxylic acids as citric acid: $(HOOC)CH_2C(OH)(COOH)CH_2(COOH)$, amino acids such as glycine: NH_2CH_2COOH, and urea: NH_2CONH_2 are some of the commonly used fuels [112]. In addition to providing heat, fuels also bind with metal ions to form chelate complex compounds. It helps to achieve a more homogeneous mixing without segregation at a later stage that is quite beneficial for producing complex and multi-component oxides. Glycine forms very stable chelate complex compounds with metal ions because it has two strong complex-forming functional groups (amino- and carboxyl-). The selection of fuels is primarily based on its heat content (exothermicity), complex-forming ability and ease of availability. In a typical SCS procedure, stoichiometric amounts of the metal nitrate and organic fuel are well-mixed in solution. Subsequently, the reaction mixture is dehydrated, ignited, and brought to combustion. During the onset of the combustion reaction a highly exothermic propagating wave is generated which promotes the product crystallinity. The expulsion of a large volume of noxious gases results in finely dispersed, porous solid particles of high purity. The short reaction times hinder particle growth and thereby facilitate formation of nano-sized material of large surface area.

In SCS, the fuel/oxidizer ratio and pH value of the solution are key parameters which control to certain extent the phase, morphology, particle size and surface area of the powders. The propellant chemistry theory is usually invoked to calculate the oxidizer to fuel (O/F) ratio expressed as [112,115]:

$$\varphi_e = \frac{\sum(\mathit{coefficient\ of\ oxidizing\ elements\ in\ specific\ formula}) \times (\mathit{valency})}{(-1)\sum(\mathit{coefficient\ of\ reducing\ elements\ in\ specific\ formula}) \times (\mathit{valency})}$$

In a given SCS reaction mixture, $\varphi_e = 1$ means a stoichiometric state, in which atmospheric oxygen is not needed for complete oxidation of the fuel. $\varphi_e > 1$ and $\varphi_e < 1$ indicate a fuel-lean and fuel-rich condition, respectively. When $\varphi_e = 1$, the combustion is intense and complete, which releases maximum exothermic heat. In determining φ_e (also called equivalence ratio), the valence numbers for the oxidizing and reducing elements are determined similarly as the oxidation number for chemists. For reducing elements C and H, the valence numbers are +4 and +1 respectively, while for an oxidizing element like O, the valence number is -2. Many of the metals represented as M^+, M^{2+}, and M^{3+} have valence numbers +1, +2, and +3, respectively [115]. The powder properties can also be tailored by utilizing a mixture of fuels, instead of a single fuel (as in conventional SCS).

The advantages of SCS can be summarized as follows: (a) time and energy-efficient (b) the use of simple equipment with inexpensive raw materials (c) a molecular level mixing of the raw materials, and (d) tuneable composition of the products.

In this thesis, CS reaction mixtures utilized urea as a fuel for synthesis of Li_2TiO_3. The SCS reaction mixtures exploited glycine as a fuel for the synthesis of Li_2ZrO_3 and mixed fuel containing glycine and citric acid for the synthesis of $LiAlO_2$.

2.2 Characterization techniques

Several characterization techniques were utilized for the characterization of precursor, synthesized ceramic (Li_2TiO_3, Li_2ZrO_3, and $LiAlO_2$) powders and sintered microstructure of compacts derived from consolidation and sintering of powders. The brief description of the characterization techniques used is as follows.

2.2.1 Thermal analysis

Thermal analysis is used to describe a group of techniques that include thermogravimetric analysis (TGA), differential thermal analysis/differential scanning calorimetry (DTA/DSC), Thermomechanical analysis (TMA), etc. In general, these techniques were used to investigate one (or more) property of a sample while the sample is subjected to a controlled temperature program. The temperature program may take many forms, e.g. sample may be subjected to a constant heating (or cooling) rate (dynamic mode) or may be held at a constant temperature (isothermal mode), a "modulated temperature program" may be used where a sinusoidal or other alteration is superimposed onto the underlying heating rate, to simulate special processes, a step-wise or complex program may also be used. In the present work, three thermal techniques namely TGA, DTA/DSC, and TMA have been used.

2.2.1.1 TGA and DTA/DSC

TGA is a technique in which the mass change of a substance is measured as a function of temperature or time while the substance is subjected to a controlled temperature program. This technique can be exploited to investigate any physical or chemical process that involves mass loss or mass gain of the substance, for instance, evaporation, sublimation, oxidation, thermal decomposition, etc. There are, of course, many processes that do not accompany any mass change e.g., phase transition, congruent melting etc. These processes can not be detected by this technique. TGA experiments can be performed either under a heating ramp (dynamic mode) or a constant test temperature (isothermal mode) program. TGA also has provisions to conduct experiments in different atmospheres by gas switching, which enables the study of precursor decomposition/calcination or volatilization under inert, oxidizing, or reducing conditions. The basic instrumentation of a commercial TG system includes: a precision balance, a programmable furnace, atmosphere control, and a recorder and/or a computer with loaded software for data processing [116].

DTA and DSC are allied techniques that are used to measure temperature and energy changes that occur while a sample is heated, cooled or held isothermally alongside an inert reference. The physical or chemical processes that essentially do not involve any mass change e.g., melting, glass-transition, phase transformation, and a range of more complex events, may be detected by these techniques. The practical distinction between DTA and DSC is in the nature of the signal obtained from the equipment. In the case of a DTA, it is proportional to the temperature difference established between the sample and an inert reference, due to underlying exothermic or endothermic events when both are subjected to the same temperature program. In DSC, the signal is proportional to the difference in thermal power between the sample and reference, usually measured in units of mW or mJ/s which is the flow of energy into or out of the sample in unit time. This enables users to undertake quantitative measurement of several useful material properties such as heat capacity, enthalpies of reactions, transitions and transformations, purity, kinetic parameters, vapour pressure, thermal conductivity, etc. Most differential scanning calorimeters, depending on their operating principle, can be categorized into two groups: power compensation or heat flux. Power compensation DSC has two small identical furnaces, one for the sample and other for the reference. The sample and reference both are heated at a pre-programmed heating (or cooling) rate, and in the event of a temperature difference arising between the sample and reference, power compensations are applied to either furnace as required to maintain the temperature at the program value. The differential thermal power is the source of the instrument signal. The difference in energy flowing into the sample furnace is compared to the inert reference and plotted as a function of temperature or time. This design measures the flow of energy directly in mW or mJ/s. The fundamental equation of DSC is given below [116].

DSC signal (W/g) = Heat Capacity (J/(K. g) × Scanning Rate (K/s)

$dH/dt = dH/dT \times dT/dt$

Heat flux DSC has a single furnace with a temperature sensor (or multiple sensors) for each of the sample and reference pans located within the same furnace. Sample and reference are heated in the furnace at the pre-programmed heating (or cooling) rate and when transitions in the sample are encountered a temperature difference is created between sample and reference which is measured as a signal [116].

The design principle of DTA is similar to heat flux DSC, except that the temperature difference remains as a microvolt signal and is not converted to a heat flow equivalent. This was the original instrument approach used before quantitative energy measurements were established using DSC.

In present work, thermo-gravimetric analysis of CS reaction mixture, used for the synthesis of Li_2TiO_3 powder, was carried out in a flowing air atmosphere on a TG-DSC instrument (SETARAM make: SETSYS EVOLUTION) to study its thermal decomposition behaviour. The experiments were carried out in a flowing air atmosphere in a platinum crucible at a heating rate of 10°C/min. The mass loss as a function of temperature was recorded up to 1000°C and the DSC curve was recorded alongside the TG curve to observe phase change and the nature of decomposition.

2.2.1.2 Thermomechanical analysis (TMA)

Thermomechanical Analysis (TMA) is defined as a technique where the change in dimensions (length or volume) due to expansion or contraction of the sample is measured as a function of temperature under a constant negligible mechanical load [117]. It is a powerful tool that can provide valuable insight into thermal expansion, sintering steps, glass-transition, softening, composition, phase changes, structure, etc., which can occur in a wide class of materials. Particularly, TMA is a very useful technique which provides a convenient method to follow material behaviour precisely during the sintering process under a constant rate of heating. The basic instrumentation of a commercial TMA system includes a linear variable differential transducer (LVDT) which is an electromechanical transducer sensor, a load cell, a programmable furnace, atmosphere control, and a recorder and/or a computer with loaded software for data processing [117].

In the present work, TMA (SETARAM make: SETSYS EVOLUTION) has been exploited to study the sintering behaviour of Li_2TiO_3, Li_2ZrO_3, and $LiAlO_2$.

2.2.2 X-Ray diffraction (XRD)

X-ray diffraction is a non-destructive technique to characterize solid-state crystalline materials. This technique can provide valuable insight into the phase composition of materials and crystallographic information of different phases. In X-ray diffraction, monochromatic X-rays, electromagnetic radiation, whose wavelength is of the order of inter-atomic spacing, are elastically scattered by the electron cloud of the atoms in a crystal. The scattered X-rays are completely in-phase provided the path difference between them is equal to an integer multiple of the wavelength of the X-ray (λ). In this condition, the phenomenon of constructive interference increases the net intensity of the scattered X-ray. Similarly, out-of-phase X-rays undergo destructive interference which reduces the intensity of the scattered

X-ray. As a consequence of an alteration in the intensity of the scattered X-rays, a diffraction pattern is generated which is considered as a fingerprint of the crystalline materials. The diffraction pattern is directly related to the lattice parameters of the crystalline sample. The classical Bragg's law, a fundamental relation of X-ray diffraction, links the possibility of constructive interference to the inter-planar separations [118].

Bragg's law: $n\lambda = 2d \, \mathrm{Sin}\theta$

where n is the integer, λ is the wavelength of X-ray, 2θ is the angle between the incident beam and diffraction plane and d is the interplanar spacing for a particular set of planes with Miller indices (hkl).

All X-ray measurements in this thesis were performed by utilizing: i) the INEL CPS powder diffractometer equipped with curved position-sensitive detector and Cu Kα radiation (λ= 1.5406Å), and (ii) a theta–2theta geometry diffractometer (Make: PROTO AXRD,) with NaI(Tl) scintillation detector and Cu Kα radiation (λ = 1.5406Å). Silicon single crystal and lanthanum hexaboride (LaB_6) supplied by the manufacturer was used as a standard for calibration and correction of instrumental broadening. The samples were ground into fine powders and homogenised by a mortar and pestle before the powder diffraction pattern was recorded. The room temperature powder XRD patterns were recorded in the 2θ range of 15-75° with a step of 0.02° and 3 seconds per step counting time.

2.2.3 Scanning and Transmission Electron Microscope (SEM/TEM)

Interaction of electrons with matter evolves various interesting phenomena that contain information about the sample's surface topography and composition. These phenomena are well understood and have been extensively used in the field of materials characterization. As the electrons can be focused to micron or submicron size, it is well suited for analysing submicron-sized regions or features in materials. When a high- energy primary electron beam strikes the atom of a specimen, a variety of interactions take place which produces different types of electrons and photons. The various electron-matter interactions include: a) Elastic scattering of electrons by atomic nuclei which results in the generation of back-scattered electrons (BSE), b) Inelastic scattering of electrons by sample atoms which produces low-energy secondary electrons, c) Inelastic scattering of electrons by sample atoms might also result in the generation of characteristic and Bremsstrahlung background X-rays from lower sample depths, d) Inelastic scattering might also produce Auger electrons emitted from the atoms near the sample surface, and e) Electrons may get transmitted from the sample provided it is thin [119] .

The order of relative energies of the generated particles is as follows: Auger electrons < SE < BSE < X-rays. [119] All these interactions have a wealth of information about the sample. Dedicated instruments have been developed to exploit these signals for the characterization of the materials. For example, backscattered electrons, secondary electrons, and transmitted electrons provide information about the microstructure of the sample; Auger electrons, ejected electrons, and X-rays have energies specific to the element and therefore, give information about the chemical identification and composition of the sample. The probability of elastic scattering increases with Z^2 and hence BSEs are useful for generating images based on Z-contrast. Scanning Electron Microscope (SEM), a type of electron microscope, produces images of a sample by scanning it with a focused beam of electrons which provides useful information about the sample's surface topography and composition. The focused beam of electrons is generally scanned in a raster scan pattern and the signals emitted from the surface, primarily secondary electrons, are collected. Thereafter, the beam's position is combined with the detected signal to produce an image. The principal images produced in the SEM can be categorized into three types: secondary electron images, backscattered electron images, and elemental X-ray maps. Transmission electron microscope (TEM) utilizes transmitted electrons to reveal the microstructure of thin samples. In this thesis, all electron microscopy images were captured using a scanning electron microscope (SEM, SERON INC South Korea, Model ATS 2100 and SEM, Carl-Zeiss, Germany) and Transmission electron microscope (TEM, Model: Jeol 2000 FX). For SEM analysis, a powder sample was dispersed in acetone using an ultrasonic bath to form a suspension. A drop of this suspension was dispensed and spread on an adhesive carbon tape adhered on an aluminium stub. Carbon tape is conventionally used in SEM for conduction purposes. Acetone was evaporated from the carbon tape leaving behind the dispersed powder. Similarly, a sample was prepared for TEM by spreading a drop of suspension on a copper grid. To avoid charging due to the insulating nature, the dispersed powder on the carbon tape and copper grid was coated with gold using a D.C. sputtering unit before microscopy analysis

2.2.4 Surface area analysis technique

The surface area is best described as the external surface area of a solid object including surface attributable to pores. The surface area of ceramic powders has an important role in various stages of different ceramic processing methods, for example, it is one among the driving forces for the sintering of powder compacts. Gas adsorption method continues to be the most widely used procedure for evaluating the surface area of porous and finely-divided materials with a distinct advantage as many classical models for particle measurement and characterization fail to consider porosity [120]. In this method, the specific surface area of a sample (i.e. surface area per unit mass) is determined by physical adsorption of a gas on the surface of the solid and by calculating the amount of adsorbate gas corresponding to a monomolecular layer coverage on the surface and from which surface area can be calculated by invoking Brunauer–Emmett–Teller (BET) principle [121]. As the physical adsorption results from relatively weak forces (van der Waals forces) between the adsorbate gas molecules and the adsorbent surface of the sample, the surface area determination is usually conducted at the liquid nitrogen temperature. In a typical surface area determination procedure, nitrogen gas is passed over the sample with pressure, gas molecules are allowed to adsorb on the powder surface and the volume of gas absorbed at different pressures is recorded. Using this data, the volume of gas adsorbed at STP to produce an apparent monolayer on the sample surface (i.e. volume of a monolayer) in millilitres is calculated with the help of B.E.T. equation. The specific surface area (SSA) can then be derived from the relation given below [121].

$$SSA = \frac{V_m . N_A . a}{\mathrm{m}. 22{,}400}$$

where N_A is Avogadro constant (6.022×10^{23} mol^{-1}), a is the effective cross-sectional area of one adsorbate molecule in square metres (0.162 nm^2 for nitrogen and 0.195 nm^2 for krypton), m is mass of test sample in grams and volume occupied by 1 mole of the adsorbate gas at STP is 22,400 ml. In this thesis, the specific surface area of the powder was measured using a surface area analyser (Sorptomatic 1990, Thermo Fisher Scientific, Italy).

2.2.5 Inductively Coupled Plasma-Atomic Emission Spectroscopy

Inductively coupled plasma atomic emission spectroscopy (ICP-AES) is an emission spectrophotometric technique that relies upon the interaction of molecules with electromagnetic radiation [122,123]. The working principle of ICP-AES is based on the fact that, as the excited electrons return to the ground state after excitation by high-temperature Argon Plasma, they emit energy at a given wavelength. Each element emits energy at specific wavelengths unique to its atomic character. The energy transfer by electrons during the emission process depends upon the electronic configuration of the orbital and is inversely proportional to the wavelength of the electromagnetic radiation,

$$E = hc/ \lambda$$

(where h is Planck's constant, c the velocity of light and λ is wavelength). Consequently, the wavelength of light emitted is also unique. Each element emits energy at multiple wavelengths, however, in the ICP-AES technique, either a single or a very few wavelengths of a given element is commonly selected for the analysis purpose. The intensity of the emission line at the chosen wavelength is proportional to the amount (concentration) of that element in the sample. Therefore, qualitative and quantitative multi-element analysis of a given sample relative to a reference standard can be performed by determining characteristic spectral wavelengths emitted by the sample along with their intensities. The wavelength ranges from the upper part of the vacuum ultraviolet (160 nm) to the limit of visible light (800 nm) are typically used in the AES measurements. This limits the use of borosilicate glass to fabricate optical lenses and prisms as it absorbs light below 310 nm and therefore, alternatively quartz glasses are used for this purpose. Also, oxygen in air absorbs light below 200 nm, therefore optical paths are either fully evacuated or filled with a non-absorbing gas such as Argon during the elemental analysis. In the present thesis, ICP-AES (Horiba, Germany) has been used for elemental analysis of the samples. For elemental analysis, all the samples were dissolved by the microwave digestion method, utilizing aqua-regia as a digestion medium.

2.3 Powder consolidation and sintering behaviour

Powder consolidation is a ceramic processing method which is used to form ceramic green bodies starting from (i) a dry ceramic powder, (ii) a suspension of ceramic powders in a solvent solution, or (iii) a paste of ceramic powder in a limited amount of solvent solution [53,124]. Two types of dry pressing methods are generally used for the consolidation of dry ceramic powders at room temperature: isostatic and die pressing. In isostatic pressing, the powder is encapsulated in a deformable, leak-proof membrane (often a rubber mold) and after vibrating or tapping to give uniform particle packing density distribution, immersed in a pressurized liquid. The pressing action takes place when the fluid is placed under hydrostatic pressure. With isostatic pressing, the pressure is evenly distributed over all the surface of the green body inside the rubber mold. In die pressing, the powder is allowed to flow into a hardened steel mold and pressed by a die with pressing action to be either uniaxial or biaxial, depending on the type of press. Wet consolidation techniques involving a suspension of ceramic powder include slip casting, filter pressing, tape casting, sedimentation casting, and centrifugal casting, etc. Extrusion and injection molding techniques are used for the consolidation of ceramic pastes. Osmotic consolidation is another effective technique that is used for the consolidation of relatively more concentrated suspensions of nanometer-scale ceramic powders. In this technique, the powder suspension contained within a semipermeable membrane is placed within a concentrated polymer solution. The semipermeable membrane only allows the liquid but not the ceramic particles to pass through and as the chemical potential of the liquid is much higher inside the membrane, therefore the solvent from the particle suspension passes through the membrane. The osmotic potential which has units of stress, acts similar to mechanical stress, pushing the particles inside the membrane yielding relatively dense green bodies. In all wet consolidation techniques, the rheology of ceramic suspension is the most important parameter which needs to be carefully controlled so the suspension has the desirable properties needed for green body fabrication. Each of these techniques has a number of advantages and disadvantages, and they are used in different applications depending on the shape, quantity, and purity that need to be produced. The uniaxial die pressing technique is the simplest and most commonly used compaction method. This method has the capability of making rather complex shapes via novel die and press design, and large-scale production at an affordable cost. In this thesis, the uniaxial die pressing technique has been used for the consolidation of Li ceramic powders. The typical consolidation and sintering process flow sheet are presented in **Figure 2.2**. Compaction of the powder was carried out by a motor-driven electrical uniaxial hydraulic press at final compaction pressure around 300MPa. After holding for a short period of time under pressure, the pressing action is decreased and the press is used to eject the green body from the press. Steel dies with tungsten carbide lining were utilized for the pressing operation.

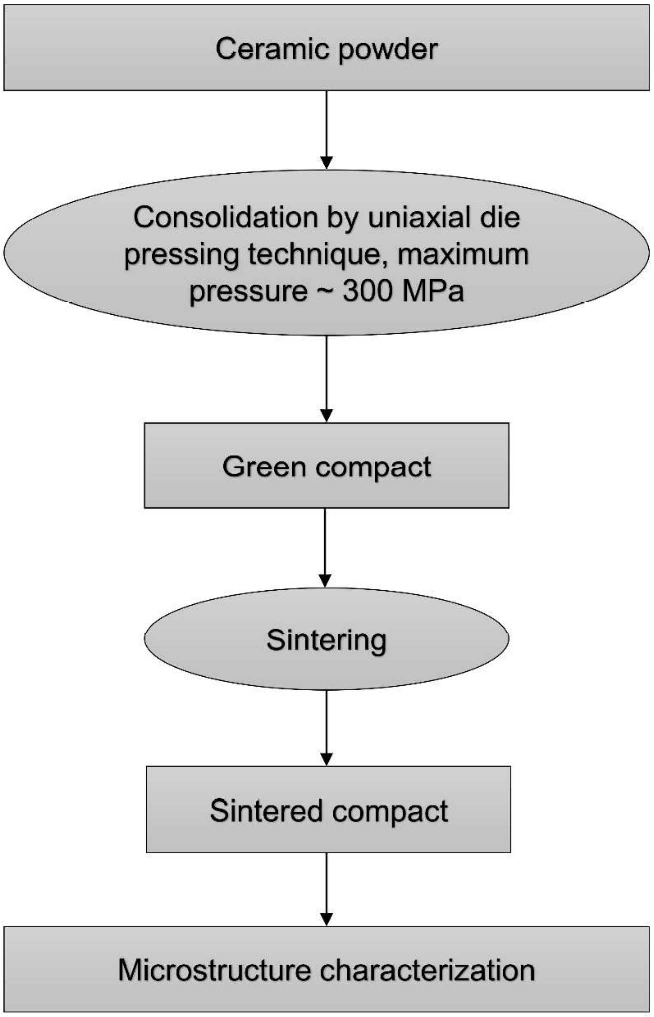

Figure 2.2 Typical Li ceramic powder consolidation and sintering process flow sheet

In order to avoid density gradients within the green compacts arising due to die wall friction, the die-wall was lubricated with a dilute stearic acid solution. Pellets of different diameter were prepared for studying the sintering behaviour. Sintering behaviour of pellet-shaped green compacts of Li_2TiO_3, Li_2ZrO_3 and $LiAlO_2$ powders were investigated under both, non-isothermal and isothermal conditions. The non-isothermal study was conducted by means of measuring shrinkage as a function of temperature under a given temperature ramp (°C/min) in the air using TMA. For TMA, pellets of 8 mm diameter and 3-4 mm thickness/height were fabricated by compacting Li_2TiO_3, Li_2ZrO_3, and $LiAlO_2$ ceramic powders. The isothermal study was performed by heating the green compacts at fixed sintering temperatures for a constant time duration in a muffle furnace (Make: Nabertherm, Germany). For this, pellets of 10 mm diameter and 2-3 mm thickness/height were fabricated by compacting Li_2TiO_3, Li_2ZrO_3, and $LiAlO_2$ ceramic powders without use of any binder. Sintering of these pellets was performed at a fixed temperature for constant dwell time in the air.

2.4 Characterization of sintered materials

2.4.1 Microstructure characterization

The microstructure characterization of sintered pellets of Li_2TiO_3, Li_2ZrO_3, and $LiAlO_2$ was performed by SEM. The SEM micrographs of the sintered pellets were captured on the fracture surfaces. In a typical procedure, a tiny piece of the fractured pellet was mounted on an alumina stub with the help of a double-sided adhesive carbon tape sandwiched between the alumina stub and the fractured piece. The samples were sputter-coated with gold using a DC sputtering unit to prevent charging due to a lack of electrical conductivity of the samples. The coated samples were then used for capturing SEM micrographs. The density of the sintered samples was measured at room temperature by Archimedes' method using water/ or ethyl alcohol as an immersion medium. The volumetric shrinkage was calculated by measuring the change in dimensions of the pellets before and after sintering.

2.4.2 AC Impedance Spectroscopy

Impedance spectroscopy technique is used to characterize the electrical conductivity/electrical charge transport behaviour of the material which may reflect some characteristic features of the microstructure as well as ionic diffusion performance of sintered ceramics [125,126]. In some of the studies, a strong correlation between the tritium diffusion behaviour and lithium-ion diffusion performance of the solid breeder materials has already been established [127–131]. Moreover, due to neutron irradiation, the temperature of the breeder will increase which therefore affects the tritium diffusion process. Impedance spectroscopy technique can serve as an indirect method to anticipate tritium diffusion behaviour derived from electrochemical impedance data of solid breeder material at variable temperatures. This method is simple, convenient, and economic and it avoids the expensive in-pile experiments. In this thesis, the electrical characterization of Li_2TiO_3 was investigated by the AC impedance spectroscopy technique. Impedance measurements were performed in an Electrochemical workstation (Model CHI 760D) in the frequency range from 1MHz to 100 Hz. In a typical procedure for the impedance measurement, the sintered pellet after polishing both sides near to flatness, and cleaning in an ultrasonic bath, was coated with frit free platinum conductive paste (Make: M/s ELTECKS Corporation, Bangalore). The coating was allowed to dry at room temperature or sometimes under an IR lamp. Subsequently, the coating was baked at 1000ºC for about one hour to remove the organic binders (used to make the platinum paste) and to make a uniform continuous electrically conducting layer. The conductivity of the surface platinum layer was verified by a multimeter. Alternatively, the sintered pellet can also be uniformly sputtered coated with a thin layer of gold to ensure proper electrical contact with the platinum electrode for the impedance measurements.

A number of studies performed on Li-based ceramics using these techniques will be discussed in subsequent chapters.

Chapter 3

Synthesis, characterization, and sinterability of Li_2TiO_3

The work reported in this chapter has been published as follows:

Monoclinic β-Li_2TiO_3 nanocrystalline particles employing novel urea assisted solid state route: Synthesis, characterization and sintering behavior

Biranchi M. Tripathi, Trupti Mohanty, Deep Prakash, A. K. Tyagi, P. K. Sinha,

J. Nucl. Mater. 490 (2017) 167-173.

3.1 Introduction

The phase diagram reveals four ternary oxides (Li_4TiO_4, Li_2TiO_3, $Li_4Ti_5O_{12}$), and the high-temperature phase $Li_2Ti_3O_7$ exist in binary Li_2O-TiO_2 system [132,133]. The phase diagram is depicted in **Figure 3.1** [133].

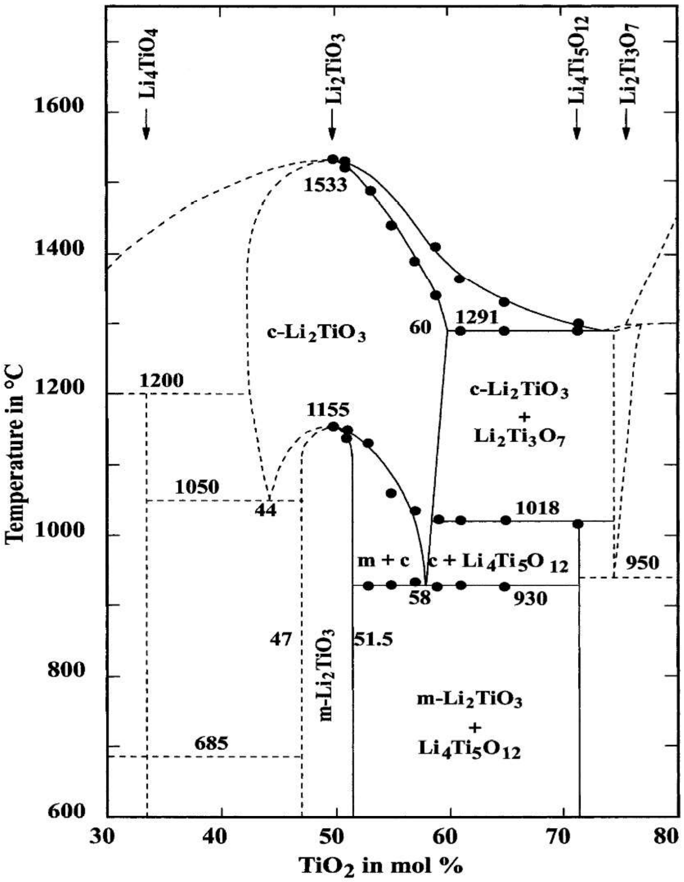

Figure 3.1 Phase diagram of Li_2O-TiO_2 system [133] (Reproduced with the permission from Elsevier)

There are three allotropic modifications of the phase Li_2TiO_3: α, β, and γ. The α-modification is metastable. Upon heating at temperature higher than 300°C, the α-phase monotropically transforms to β-phase. The low-temperature β-phase has narrow homogeneity range, and a monoclinic crystal structure. It crystallises in the Li_2SnO_3-type structure with the space group

C2/c (No. 15), Z=8, and the lattice parameters: a = 504.1 pm, b = 880.6 pm, c = 972.7 pm and β = 100.08°. The high temperature γ-phase crystallises in the NaCl-type structure (Z = 4/3). The γ-phase has cubic crystal structure with the room temperature lattice parameter a = 415.05 pm [128,132–134].

Recently, β-Li_2TiO_3 has drawn considerable attention as a very useful ceramic owing to its practical industrial applications, especially in the area of energy production, energy conversion, and energy storage [135–141]. In view of its reasonably good tritium release property at relatively low temperatures, low activation performance and good thermal as well as chemical stability, Li_2TiO_3 in sintered compact form has been reckoned as a promising candidate for tritium breeding materials in nuclear fusion reactors. It is used in a double-layer cathode material for molten carbonate fuel cells [142]. In the field of rechargeable Li ion batteries, Li_2TiO_3 has been successfully utilized as a stabilizer for the high capacity cathode materials [138,139].

Particularly for tritium breeding application, the sintered β-Li_2TiO_3 compact with fine-grained microstructure and the relative density close to 90% is required for achieving targeted tritium breeding performance. However, the evaporative loss of Li and fast grain-growth at high sintering temperature poses serious limitation on developing the desired microstructure [98,101].

Many prior studies have described viable methods of synthesizing Li_2TiO_3 ceramic powders. Recently, sinterability enhancement of Li_2TiO_3 powders by synthesizing submicron to nanoscale Li_2TiO_3 powders has drawn much attention to decrease the sintering temperature of Li_2TiO_3 compact. Solid state reaction method has been widely used to synthesize Li_2TiO_3 powders in which Li_2CO_3 and TiO_2 are used as precursors. The solid-state reaction was usually carried out by heating stoichiometric mixture of the precursors in temperature 750-

800°C for 5-10h duration [86,102,106][143,144]. Sometimes, temperature as high as 900-1100°C and time duration 10h to several days has also been reported for synthesis of Li_2TiO_3 powder by solid-state method [143–145]. The large-scale synthesis of Li_2TiO_3 powder by solid-state method often requires high synthesis temperature, prolonged reaction, and intermittent ball milling. The high synthesis temperature often results in formation of hard particle aggregates with large particle size leading to poor sinterability of the as-synthesized powders. Because of poor sinterability of the powders, the sintered compact with low density is obtained even at higher sintering temperatures. Moreover, high sintering temperature facilitates the rapid grain growth leading to large grain size. Many alternative wet chemical methods such as sol–gel, hydrothermal, solution combustion synthesis, and the polymer solution method have been developed to circumvent these issues [109,145–148]. The solution combustion synthesis method is very useful method to synthesize nanoscale ceramic powders. The Li_2TiO_3 powders synthesized by the solution combustion method have shown improved sinterability [149–151]. For wet chemical synthesis of titanate-based ceramics, the precursor containing titanium need to be water soluble. The commonly used Ti-precursors, for example, $TiCl_4$, $Ti(C_6H_6O_7)_2$, $Ti(OC_3H_7)_4$, $TiO(NO_3)_2$, are difficult to handle and expensive. It increases the overall cost of large-scale production of tritium breeders [152]. Moreover, some of the issues such as control of vigorous chemical reactions, and generation of liquid waste need to be addressed to scale-up the wet chemical methods for large-scale production of tritium breeders.

The present chapter focuses on a new urea assisted solid state combustion method for synthesizing nanocrystalline Li_2TiO_3 ceramic powders. This method is an improved variant of commonly used solid-state synthesis method in which urea is added as a fuel along with the precursors (Li_2CO_3 and TiO_2) for the synthesis of Li_2TiO_3. The selection of urea as a fuel is due to its high heat of combustion, and less carbon content. The less carbon content in urea minimizes the residual carbon in as-synthesized Li_2TiO_3 powder compared to other commonly used fuels (citric acid and glycine). The present method has advantages of solid-state synthesis method as well as wet chemical methods. Therefore, the present method is a potential alternative for the production of tritium breeder materials at large scale. Some of the attractive features of this method are: i) phase pure powder ii) small particle size of the powder iii) no hard particle aggregates (although soft agglomerates are formed) iv) improved powder sinterability v) higher density of sintered compact with small grain size at low sintering temperature (as desired for good tritium release from Li_2TiO_3 vi) No need of extensive ball milling due to soft agglomeration of particles, and vii) short reaction time relatively low synthesis temperature (both of which are beneficial to reduce the large scale production cost of tritium breeders).

3.2 Experimental procedure

3.2.1 Synthesis of Li_2TiO_3 powders

Lithium carbonate: Li_2CO_3 (purity: 99%, Prabhat Chemicals Private Limited, India) and hydrous titanium oxide: $TiO_2.xH_2O$ (x=0.6) (purity: 99%, Indian Rare Earths Limited, India) were used as precursors for the synthesis of lithium titanate (Li_2TiO_3). Urea (purity: 99%, Sigma-Aldrich, India) was utilized as fuel. Li_2TiO_3 powders were synthesized by the reaction scheme as follows:

$$Li_2CO_3(s) + TiO_2(s) + xNH_2CONH_2(s) + (3x/2)\,O_2(g)$$
$$= Li_2TiO_3(s) + (1+x)\,CO_2(g) + x\,N_2(g) + 2xH_2O(g)$$

The CS reaction mixtures were prepared by thoroughly blending the stoichiometric proportion of Li_2CO_3 and TiO_2 along with varying urea content (x=25, 50, 75 and 100 wt %) utilizing the pestle and mortar, and ethyl alcohol as medium. Mixture was labelled based on their urea proportion as LT-25, LT-50, LT-75 and LT-100. After drying the mixtures on hot plate, the dried powders (LT-25, LT-50, LT-75 and LT-100) were placed inside a muffle furnace (Nabertherm, Germany) and calcined at different temperatures; 600, 700 and 800ºC, for fixed time duration of 2 hours with constant heating rate (5ºC/min) in static air environment. The synthesis flow sheet is depicted in **Figure 3.2**.

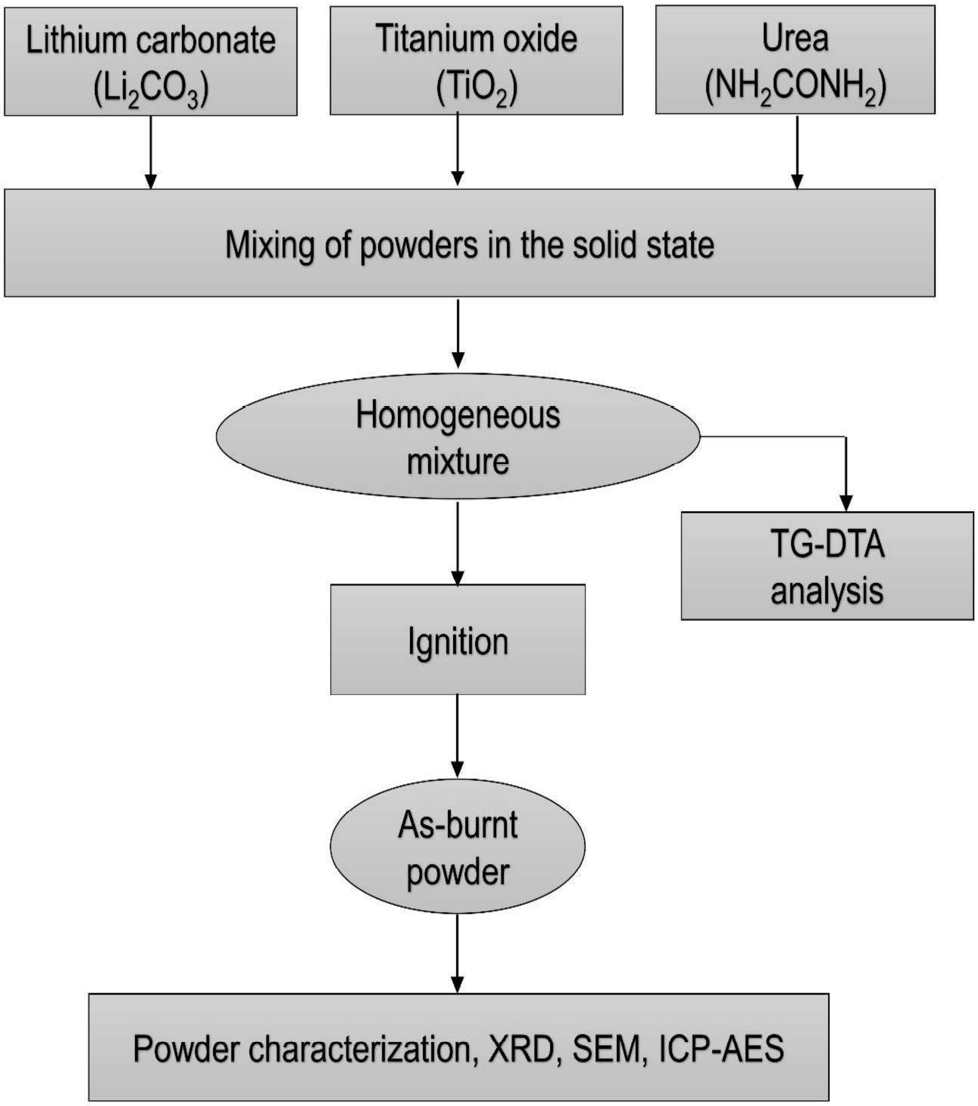

Figure 3.2 Li_2TiO_3 synthesis process flow sheet

3.2.2 Consolidation and sintering of Li_2TiO_3 powder

Compaction of Li_2TiO_3 powder was carried out by a uniaxial hydraulic press to form pellet shaped green compacts without using a binder. The cylindrical steel die with tungsten carbide lining was used for the pressing operation. The flow sheet of consolidation and sintering is presented in **Figure 3.3**.

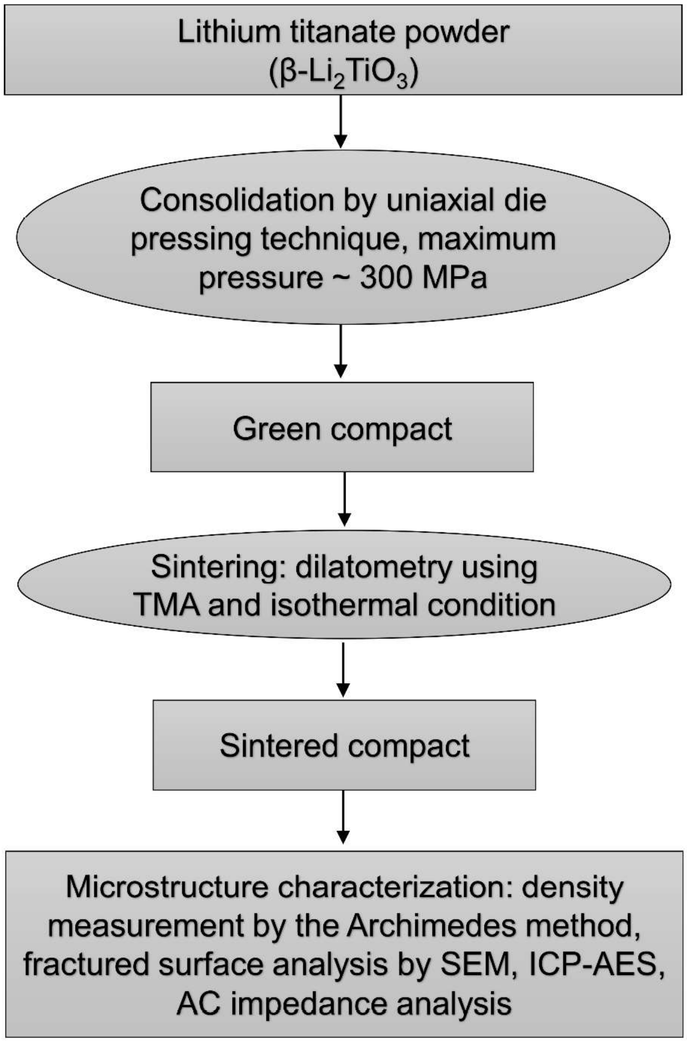

Figure 3.3 Li_2TiO_3 consolidation and sintering process flow sheet

The die wall was lubricated with dilute stearic acid solution to minimise the wall friction and thereby avoid density gradients within Li_2TiO_3 green pellets. The compaction pressure was applied around 300MPa. Sintering behaviour of Li_2TiO_3 green pellets was investigated under both, non-isothermal and isothermal conditions. In non-isothermal sintering study, Li_2TiO_3 pellets of the required size i.e. 8 mm diameter and 3-4 mm thickness/height were prepared and geometrical shrinkage of these pellets was measured up to 1200°C under a given temperature ramp (5, and 10°C/min) in flowing air using TMA. For performing isothermal study, Li_2TiO_3 pellets of 10 mm diameter and 3 mm height were prepared and these pellets were sintered at fixed temperatures ranging from 800-1000°C for constant duration (2h) with heating rate of 5°C/min in a muffle furnace (Make: Nabertherm, Germany) in static air.

3.2.3 Characterization

The phase of as-synthesized powders was analysed by XRD. For recording diffraction patterns, Inel diffractometer equipped with Ni filtered Cu-Kα radiation (λ=1.54056 Å) source was exploited.

Scanning electron microscopy (SEM) (Make: Seron, Korea) operating at 20kV accelerating voltage was used to characterize the microstructures of as-synthesized powders and sintered pellets.

Thermogravimetry and differential thermal analysis (TG/DTA) analysis was carried out using a Setaram TG/ DTA model.

Inductively coupled plasma atomic emission spectroscopy (ICP-AES, Horiba, Germany) was used for determination of chemical composition of the powder. Prior to the ICP-AES measurement, powder was dissolved in aqua-regia as medium.

The Archimedes method was exploited to determine the relative density of the sintered samples. The relative density was measured at room temperature using water as an immersion medium.

For electrical characterization of sintered Li_2TiO_3, the electrochemical impedance spectroscopy (EIS) technique was used. The impedance measurements were carried out in the frequency range of 1MHz to 100 Hz using Electrochemical workstation (Model: CHI 760D. In order to make proper electrical contact with the platinum electrode, the surface of sintered Li_2TiO_3 pellet was uniformly coated with a thin layer of gold by sputter coating technique before the impedance measurement. The electrical continuity of the gold coating was verified by a multimeter. The impedance measurements were carried out in the temperature range of 500-700°C at an interval of 50°C. The temperature was controlled by a microprocessor. Sample temperature was measured with an accuracy of ±1°C by a K-type thermocouple located in proximity of the sample. Sample was equilibrated for 20-30 min at each temperature before recording the impedance data.

3.3 Results and discussion

3.3.1 Thermal (TG/DTA) analysis

The thermal analysis of a small portion of CS reaction mixture, LT-25 and LT-50, was carried out in a flowing air atmosphere. The results of thermal analysis are shown in **Figure 3.4**. A continuous weight loss was observed in both the mixtures (LT-25 and LT-50) up to 750°C with no weight change further. The weight loss is due to step-wise decomposition of urea in different temperature ranges. The intermediate products of urea decomposition are not thermally stable as indicated by the continuous weight loss with no perfect plateau in TG pattern. The heat changes accompanying decomposition reactions are depicted in DTA pattern (**Figure 3.4)**.

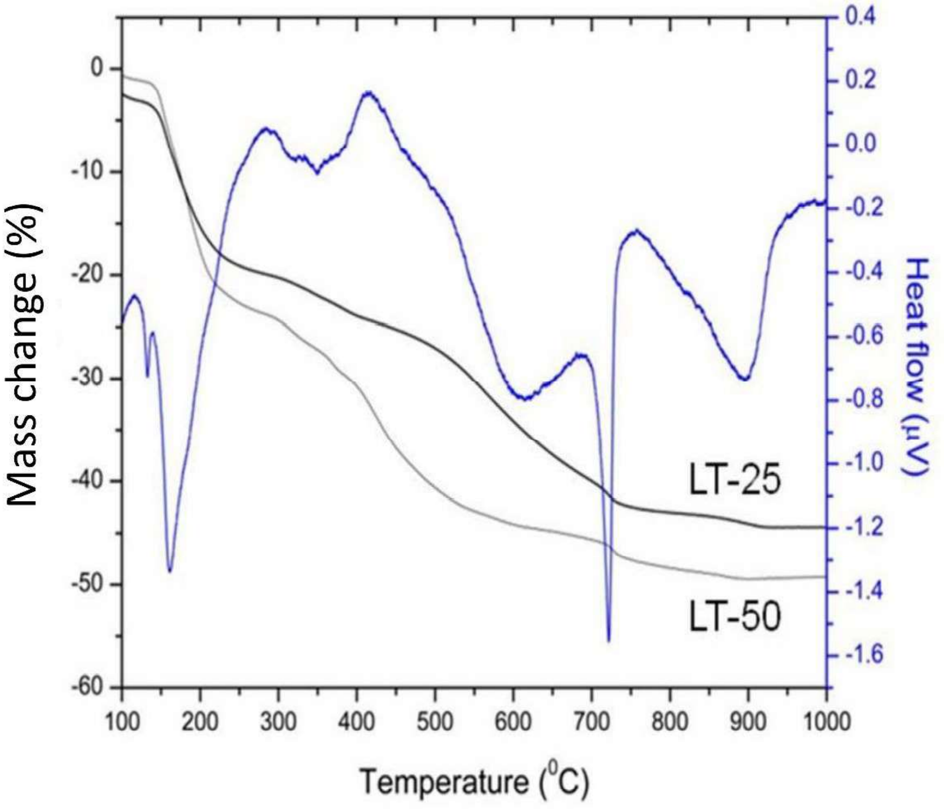

Figure 3.4 TG/DTA pattern of CS reaction mixture with 25 and 50 wt% urea

In DTA curve, a prominent endothermic peak was observed around 700-750°C, which is due to the melting of Li_2CO_3. This endothermic peak is also accompanied by weight loss, as shown in the TG curve, which indicates decomposition of molten Li_2CO_3. Interestingly, the DTA curve does not contain a clear exothermic peak expected from combustion of urea in air. It may be due considerable broadening of DTA peaks with shift of baseline that might obscure the expected exothermic peak of urea combustion. The DTA peak broadening and shift of baseline can be attributed to the occurrence of multiple decomposition reactions in overlapping stages (as evident from the sloping plateau in TG curve).

3.3.2 Phase analysis and crystallite size

Based on the TG analysis, the temperature of 600, 700 and 800°C were chosen for the calcination of CS reaction mixtures (LT-25, LT-50, LT-75, and LT-100). The formation of the desired monoclinic phase of Li_2TiO_3 was monitored by the XRD analysis of the calcined powders. The XRD patterns of calcined powders are shown in **Figure 3.5**.

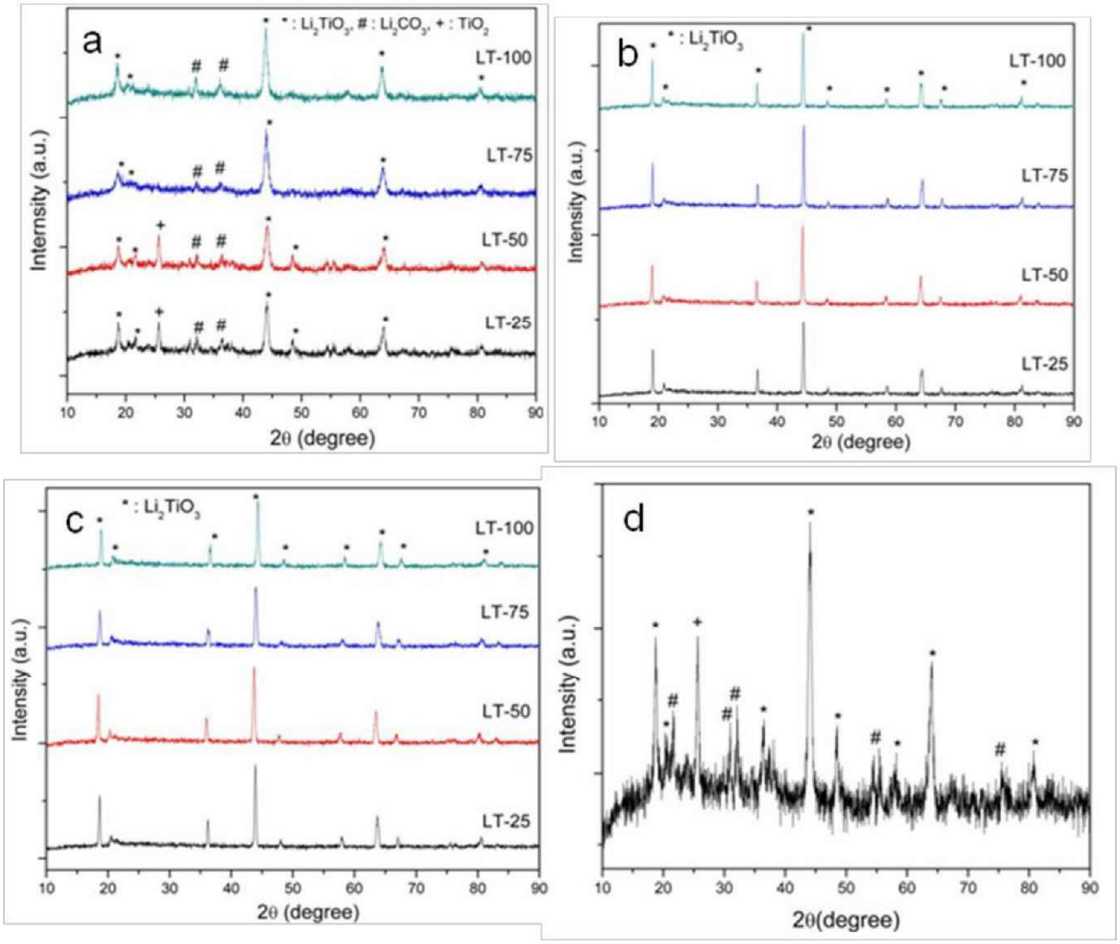

Figure 3.5 XRD patterns of Li_2TiO_3 a) 600°C b) 700°C c) 800°C d) solid state route without urea at 1000°C

The XRD analysis (**Figure 3.5**) revealed that mixtures calcined at 600°C produced monoclinic Li_2TiO_3 phase as major phase irrespective of their urea contents. However, presence of minor quantity of unreacted Li_2CO_3 and TiO_2 was also observed in the powder at this temperature. It indicates need for further optimization of synthesis parameters. It is noteworthy at this point that synthesis of monoclinic Li_2TiO_3 phase by the conventional solid-state reaction method often requires temperature of around 900-1100°C. Therefore, it is evident that one of the effects of urea addition is the reduction of synthesis temperature of monoclinic Li_2TiO_3 phase. It can be due to the release of incipient exothermic heat (by the combustion reaction of urea in presence of air atmosphere) and its homogeneous distribution throughout the reaction mixture. Both of these factors alleviate synthesis of monoclinic Li_2TiO_3 phase at relatively lower temperature. Increasing calcination temperature of the mixture up to 700°C eliminated the traces of unreacted components and resulted in pure monoclinic Li_2TiO_3 phase. Upon further raising calcination temperature of the mixture at 800°C, the XRD pattern of the as-synthesized powder did not reveal any apparent modification with regard to the phase purity of Li_2TiO_3.

From the XRD peak broadening measured in terms of the full width at half maximum (FWHM), the crystallite size of Li_2TiO_3 was calculated. Before the crystallite calculation, the instrumental contribution to XRD peak broadening was obtained from FWHM of the XRD peak of the standard LaB_6 sample and it was used to obtain the instrument corrected broadening (β_{hkl}) of the XRD peaks of Li_2TiO_3 by the relation [153]:

$$\beta^2_{hkl} = [(\beta^2)_{measured} - (\beta^2)_{instrumental}$$

Scherrer's equation was used to calculate the average crystallite size (D) of Li_2TiO_3 as follows:

$$D = (K\lambda / \beta_{hkl} \cos\theta)$$

where, λ is the wavelength of radiation (1.54056 Å for Cu-Kα radiation), K = 0.94 (a constant), β_{hkl} is FWHM of XRD peak, and θ is the peak position.

The effect of percentage urea content in the reaction mixture on the crystallite size of Li_2TiO_3 at each calcination temperatures (600, 700 and 800°C) is shown in **Figure 3.6**.

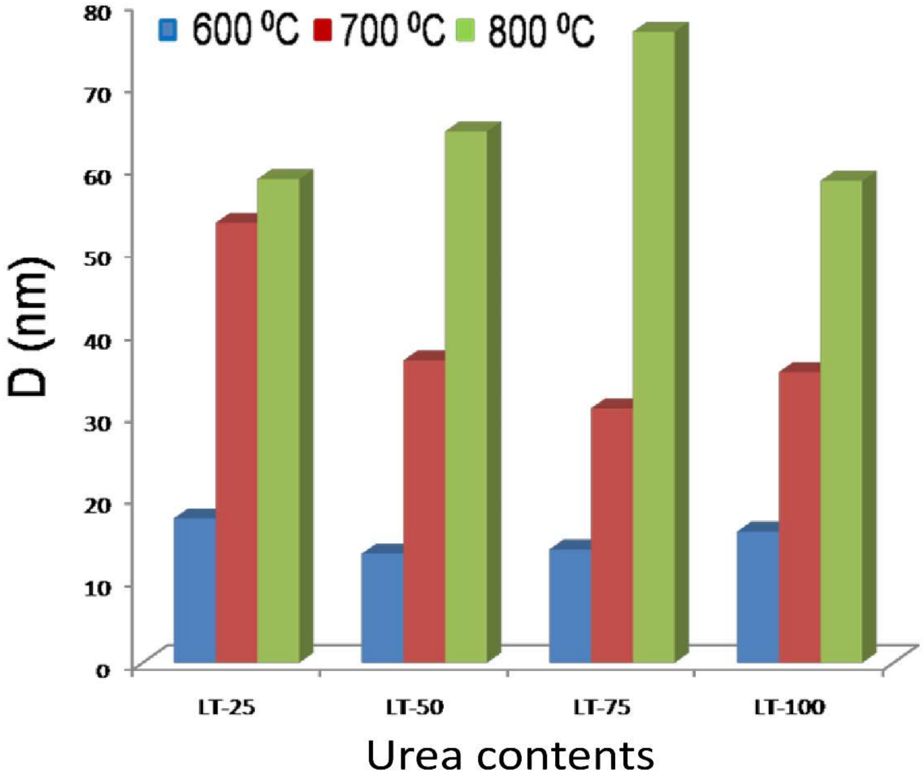

Figure 3.6 Variation in crystallite size of Li_2TiO_3 with temperature and urea content

The crystallite sizes of Li_2TiO_3 synthesized at calcination temperatures of 600°C and different urea contents (25, 50, 75, and 100 wt%) were calculated to be in the range of 14-20 nm. The crystallite sizes at 700 and 800°C, and different urea contents were calculated to be in the range of, 30-55 nm and 60-80 nm, respectively. The crystallite size increased with calcination temperature, which is an obvious effect indication coarsening of Li_2TiO_3 particles with increase of calcination temperature. Although the increase in the percentage of urea in the mixture increases the exothermic heat of combustion, however the crystallite sizes did not affect significantly as evident from **Figure 3.6**. It is due to simultaneous release of large volume of the combustion gases with increase in urea content, which rapidly dissipate the heat by the convective process and thereby limits the coarsening of Li_2TiO_3 crystallites.

3.3.3 Powder morphology

The morphology of Li_2TiO_3 powders synthesized by the calcination of reaction mixtures, comprised of different urea contents, at temperature of 700°C is pictured in **Figure 3.7**.

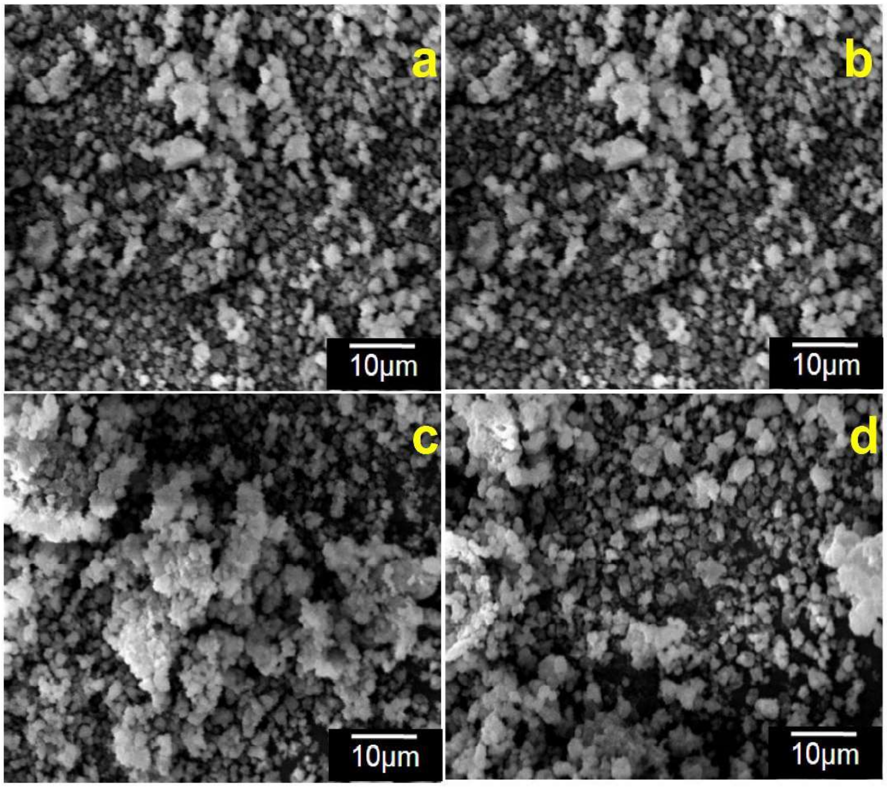

Figure 3.7 SEM images of of Li_2TiO_3 powder clacined at 700 °C a) LT-25 b) LT-50 c) LT-75 d) LT-100

The particle size of the powder is in the narrow range of 2-5μm, which considerably larger than the crystallite size. It indicates significant agglomeration of synthesized powder particles. The agglomeration is generally soft in nature, and the agglomerated particles are comprised of nanoscale primary particles of Li_2TiO_3 as evident from **Figure 3.7**. It is noteworthy at this juncture that powder synthesized by the conventional solid-state reaction method often produces hard-aggregates of particles with considerably large in size as compared to the present method, and it is due to relatively high synthesis temperature and long reaction time. The powders with such morphology often exhibit inferior sinterability. The addition of urea as a fuel in the reaction mixture, due to reduction of the reaction temperature (as discussed in Section 3.3.2), only allows the formation of soft-agglomerated particles. Moreover, the gases released alleviate diminishing the inter-particle contact and decreases the extent of agglomeration of Li_2TiO_3 particles. Therefore, relatively small size agglomerates are formed.

3.3.4 Chemical analysis (Li/Ti ratio) and colour observation

The chemical analysis of Li_2TiO_3 powder synthesized by calcination of the reaction mixtures with different urea compositions (LT-25, LT-50, LT-75 and LT-100) at 700°C was carried out by ICP-AES analysis and Li/Ti mole ratio of the samples was determined. The Li/Ti mole ratio was calculated to be around 1.98 in all the samples, which is in good agreement with the value for stoichiometric Li_2TiO_3. It indicates that Li was not lost by evaporation during the synthesis of Li_2TiO_3 by the proposed method. It is worth mentioning at this point that evaporative loss of Li is a matter of concern for Li-based ceramic tritium breeding materials, and it is because Li breeds the tritium. The Li-evaporation from Li_2TiO_3 was prevented due to fast removal of the exothermic heat by the release of gases.

The colour of Li_2TiO_3 powders (LT-25, LT-50, LT-75 and LT-100) was visually examined, and difference in colour is observed. It indicates that percentage of urea in the reaction mixture affects the colour of the synthesized Li_2TiO_3 powder. The colour of Li_2TiO_3 powder synthesized by calcination of reaction mixture containing 25 wt% urea (LT-25) is off-white. The colour of Li_2TiO_3 powder synthesized by calcination of reaction mixture containing increasingly more percentages of urea i.e. LT-50 (50 wt%), LT-75 (75 wt%), and LT-100 (100 wt%) turned somewhat brown. Generally, colour of transition metal compounds changes due to the change in valence state of transition metal ions with the experimental conditions. The transition metal ions often have vacant d-orbitals, which allow acquiring variable valence state. The off-white or brown colour is probably due to the reduction of some of the Ti^{4+} (d^0 system) to Ti^{3+} (d^1 system) by urea [133].

3.3.5 Sintering and microstructure of fractured surface of Li_2TiO_3 pellets

In order to study the sintering behaviour, the volumetric shrinkage of the sintered pellets of Li_2TiO_3 was calculated from the measurement of the change in dimensions of the pellet before and after the sintering. The density of sintered pellets was determined by Archimedes method. **Figure 3.8** shows the effect of sintering temperature on the relative density and volumetric shrinkage of the sintered pellets. Increasing the sintering temperature increases relative density of the pellets. The pellet achieves relative density of more than 90% at significantly low temperature (850ºC). The relative density increases to around 98% at temperature of 950ºC. It clearly shows that Li_2TiO_3 powder synthesized by the present method has very good sinterability. The variation of percentage volumetric shrinkage with the sintering temperature is also observed to be in accordance with the relative density. The large volumetric shrinkage of around 30% at sintering temperature of 900°C is due to the presence of more porosity in the green pellets.

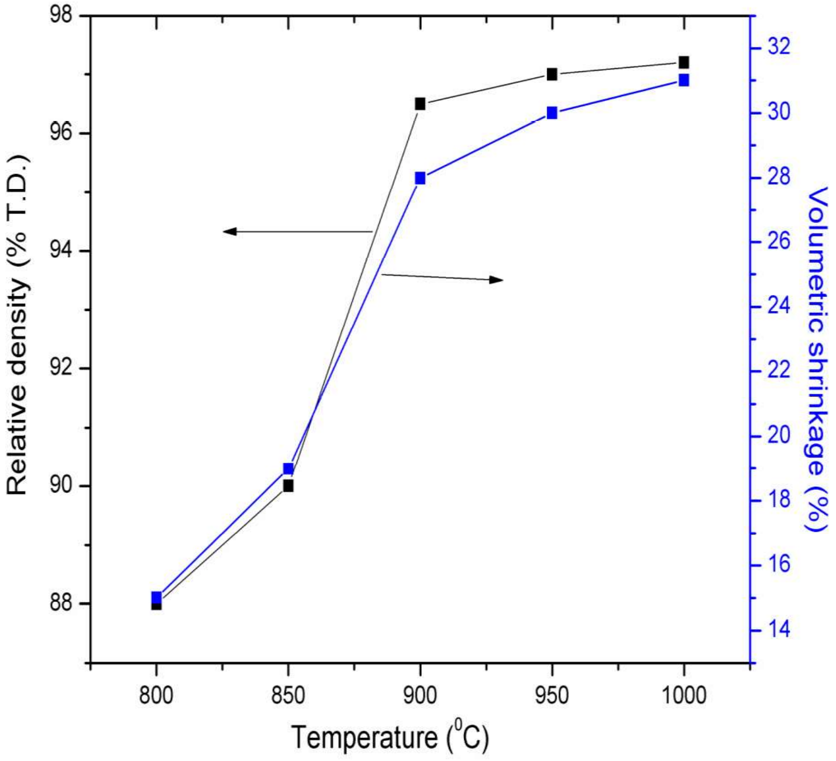

Figure 3.8 Effect of sintering temperature on relative density and volumetric shrinkage of Li_2TiO_3 pellet

In order to reveal the microstructural characteristics, the SEM images of the fracture surface of sintered Li_2TiO_3 pellets was captured. The microstructure is shown in **Figure 3.9**. The SEM images demonstrate uniform grain morphology of sintered Li_2TiO_3 pellets, which rules out presence of any secondary phase. This result is in complete agreement with the XRD analysis which also confirmed formation of pure monoclinic Li_2TiO_3 phase (**Figure 3.5**). The microstructure of pellet sintered at 850°C displays characteristics of agglomerated sintering. The grain boundaries are not clearly demarcated at this temperature. However, the microstructure at sintering temperature of 900 and 950°C displays evident polyhedral grains and grain boundaries with grain size of 2-3μm, which indicates good sintering of the pellet. The grain size increased rapidly on further increasing the sintering temperature up to 1000°C, however, the relative density of the pellet does not improve significantly.

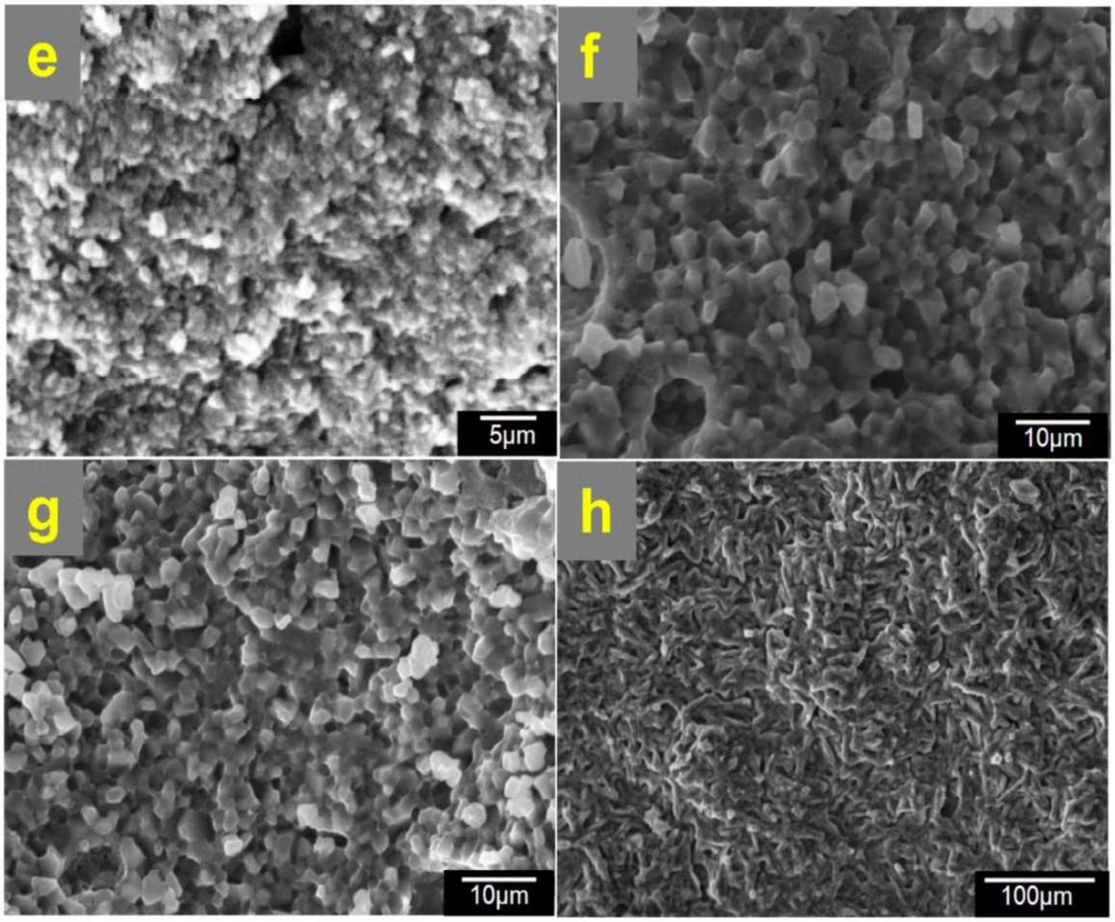

Figure 3.9 SEM images of fractured surface of Li_2TiO_3 sintered at e) 850°C f) 900°C g) 950°C and h) 1000°C

3.3.6 Investigation of electrical properties

Tritium release from sintered Li-based ceramic breeder is correlated with its Li ion diffusion performance, and often higher the Li ion conductivity better is the tritium release behaviour [154–156]. Therefore, analysis of Li ion conductivity might indirectly reflect tritium release performance of Li_2TiO_3. In the fusion reactor blanket, temperature of Li_2TiO_3 increases due to neutron irradiation which might affect tritium diffusion from the blanket. The effect of temperature on tritium diffusion might be correlated with Li ion conductivity of Li_2TiO_3 at variable temperatures. Therefore, measurement and analysis of electrochemical impedance might be quite useful to predict tritium diffusion behaviour of solid breeder materials at different temperatures. This method, due to simplicity, convenience and cost-effectiveness can be an alternative to the expensive in-pile experiments for predicting tritium diffusion behaviour of Li-based solid tritium breeders. **Figure 3.10** shows impedance plot (Nyquist plot) of sintered Li_2TiO_3 (sintering temperature of 950°C) at different temperatures.

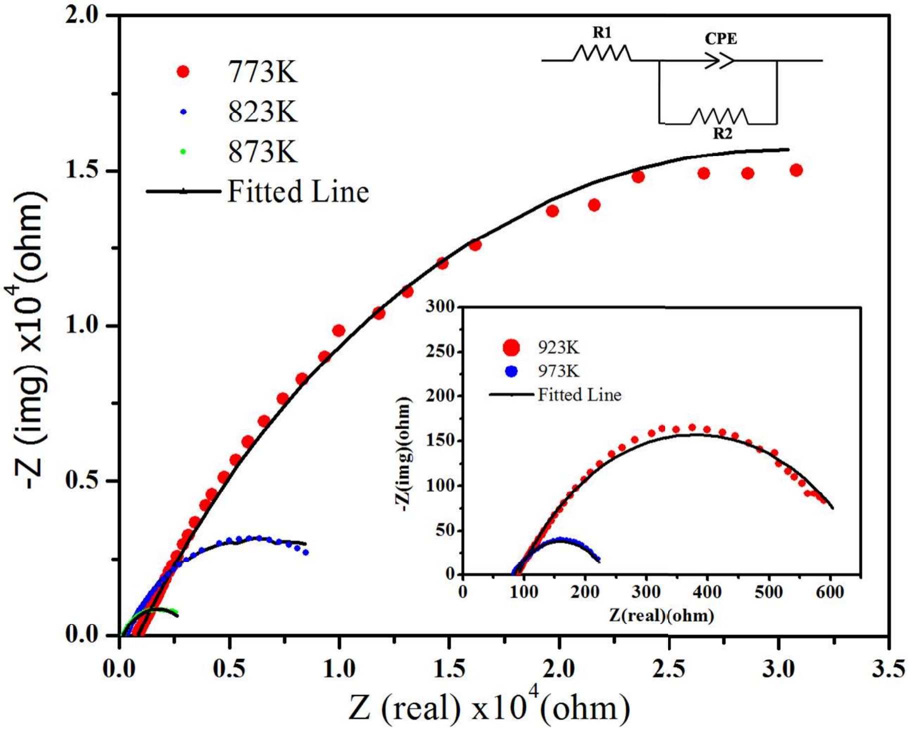

Figure 3.10 Complex impedance (Nyquist) plots for Li_2TiO_3 at different temperatures

Almost linear response of impedance at low temperature (<500°C) indicates the insulating behaviour of the sample. The linear response gradually turns to semicircle with increasing temperature, which indicates conducting behaviour of the sample at higher temperature. A single semi-circular arc at temperatures 550°C and 600°C indicates bulk electrical properties of Li_2TiO_3. A second semi-circular arc emerges at temperatures 650°C and 700°C as depicted **Figure 3.10** (inset graph), which is due to contribution of grain boundary to the impedance of

Li_2TiO_3 at higher temperature. The intercept of semi-circular arc on the real axis decreases with increasing temperature. It indicates that bulk resistance of Li_2TiO_3 decreases with increasing temperature. **Figure 3.11** shows variation of real and imaginary components of impedance as a function of frequency at different temperatures on double logarithmic scale. The magnitude of Z(real) decreases with increase of temperature, which indicates reduction of resistances including grain, grain boundaries and interface. It may be due to some temperature assisted electric or ionic relaxation processes. The observed impedance values of Li_2TiO_3 are considerably lower than the previously measured values [154,156]. Therefore, microstructure of sintered Li_2TiO_3 promotes the ionic diffusion process, which is advantageous for tritium extraction.

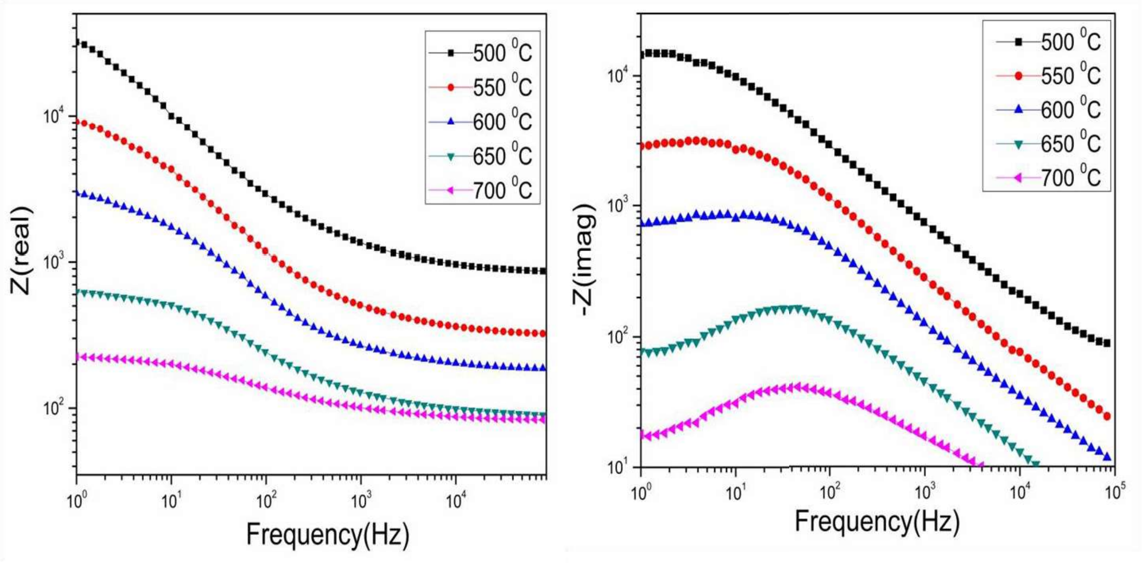

Figure 3.11 Frequency dependences of the real part i.e. Z(real) and imaginary part i.e. Z(imag) at various temperatures

The microstructural characteristics (grain size, grain boundary volume fraction, grain boundary thickness, distribution of secondary phases etc.) and the defect chemistry (oxygen vacancies, non-stoichiometry and impurities etc.) significantly affect diffusion of Li^+ ion in Li_2TiO_3 [128,157]. The grain boundary diffusion of Li^+ ion is often faster than lattice diffusion [130,158]. Therefore, Li^+ ion conductivity increases with decrease in grain size and increase in grain boundary volume fraction. This is a prominent effect in nanoscale Li_2TiO_3. At the temperatures of 650°C and 700°C, the Z(real) decreases at low frequencies, but merges at higher frequencies. It may be due to the space charge polarization in the sample. The Z(imag) curve as a function of frequency at different temperatures depicts broad and low intensity peaks (**Figure 3.11**). The peak frequency shifts to a higher side with increasing temperature and the relaxation occurs over several decades of frequency. It may be due to some temperature dependent electrical relaxation phenomena in the material.

3.4 Summary

The addition of urea as fuel allows the synthesis well-crystalline pure monoclinic phase of Li_2TiO_3 at relatively low temperature (600-700°C) and short duration (2h) by the solid-state method. The percentage of urea in the solid-state reaction mixture has a significant effect on the microstructure of as-synthesized Li_2TiO_3 powder. Due to reduction in synthesis temperature and time the present urea assisted solid state synthesis method produces soft-agglomerated powders with relatively small size. The agglomeration can be eliminated conveniently. The pellets of as-synthesized Li_2TiO_3 powder achieve high relative density (~ 98%) with small grain size (2-3μm) at sintering temperature of <1000°C that shows excellent sinterability of the Li_2TiO_3 powder. The sintered Li_2TiO_3 pellet exhibited improved Li ion conductivity which is advantageous for tritium release from Li_2TiO_3. The proposed method can provide a simple, and cost-effective alternative for large scale production of highly sinterable nanocrystalline Li_2TiO_3 powder.

This chapter demonstrated enhanced sinterability of Li_2TiO_3 ceramic compact through the utilization of nanocrystalline/fine powders. The Li_2ZrO_3, due to neutron multiplication ability of Zr, is unique among the candidate Li-based ceramic tritium breeders. The neutron multiplication property of Zr can enhance the tritium breeding ratio of the blanket. The sinterability improvement of Li_2ZrO_3 powder compact (which often require higher sintering temperature than Li_2TiO_3) can be quite useful to produce sintered Li_2ZrO_3 ceramic components with desired densification and microstructure for tritium breeding application.

In view of this, study on sinterability enhancement of the Li_2ZrO_3 ceramic compact through the utilization of nanocrystalline/fine powder has been undertaken which will be discussed in the next chapter.

Chapter 4

Synthesis, characterization, and sinterability of Li_2ZrO_3

The work reported in this chapter has been published as follows:

i) Combustion Synthesis of nanocrystalline lithium zirconate"

Biranchi Tripathi, Deep Prakash, A. K. Tyagi, P. K. Sinha, Transactions of PMAI 44(2) (2018) 51-55.

ii) Glycine-nitrate solution combustion synthesis of lithium zirconate: Effect of fuel-to-oxidant ratio on phase, microstructure and sintering

Biranchi M. Tripathi, Trupti Mohanty, Deep Prakash, A. K. Tyagi, P. K. Sinha,

J. Eur. Ceram. Soc. 40 (2020) 136-144.

4.1 Introduction

Several compounds in Li_2O-ZrO_2 system (e.g., Li_8ZrO_6, $Li_6Zr_2O_7$ and Li_2ZrO_3) has been considered for tritium breeding. Lithium metazirconate (Li_2ZrO_3) has been considered for numerous applications including anode in lithium ion batteries as well as a coating for anodes and cathodes and solid sorbent for CO_2 sequestration [159–168]. The phase diagram of Li_2O-ZrO_2 system is presented in **Figure 4.1** [169].

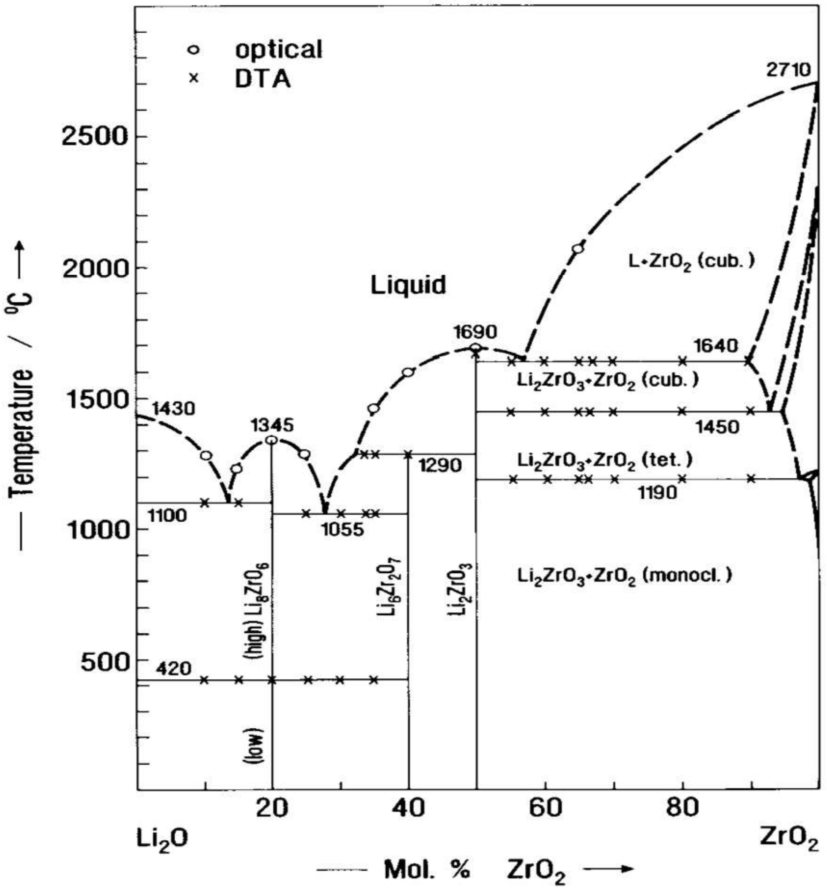

Figure 4.1 Phase diagram of Li_2O-ZrO_2 system [169] **(Reproduced with the permission from Elsevier)**

The Li_2ZrO_3 has monoclinic crystal structure within the C2/c space group (No. 15), Z=4. The lattice parameters are: a = 542.2 pm, b = 902.2 pm and c = 541.9 pm, and β = 112.709° [168–171]. It crystallizes in NaCl-type structure in which the oxygen anions, as well as the cations, form a distorted cubic close-packed network [170]. Particularly, Li_2ZrO_3 have recently drawn much attention as candidate ceramic tritium breeder in thermonuclear fusion reactors. The lithium density in Li_2ZrO_3 is sufficiently high and zirconium which acts as a neutron multiplier, can further enhance the tritium breeding [48,85,87][88,172–177]. Preliminary studies have showed that thermal stability and tritium residence times of Li_2ZrO_3 compares favourably to other prospective breeder materials. However, the activation of Zr under neutron irradiation in fusion reactor might be disadvantageous. The Li_2ZrO_3 is required in sintered compact shape (pellet, pebble or bar) tritium for breeding in fusion reactor. The microstructural features of the sintered compact including the relative density, grain size, and porosity are controlling parameters for release and retention behaviour of the breeder. The preferable microstructure generally comprises of small grain size, and the relative density of 90%. However, poor sinterability, evaporative loss of Li, and rapid grain growth at high sintering temperature are some of the major limitations in achieving the desired microstructural characteristics of sintered Li_2ZrO_3 compacts. Because of these limitations sintering of Li_2ZrO_3 powder compacts with tailored microstructural characteristics is often quite challenging. The one of the possible ways to enhance sinterability of Li_2ZrO_3 is synthesis and utilization of nanocrystalline powders for processing of breeders. The improved sinterability and thereby reduction in sintering temperature of nanocrystalline powder compacts compared to bulk counterpart is due to high surface area, increased grain boundary volume fraction, and the shorter diffusion pathways. The low sintering temperature facilitates acquiring high relative density with small grain size in sintered compact.

Conventionally, Li_2ZrO_3 powder has been synthesized by solid-state reaction method by utilizing Li_2CO_3 and ZrO_2 as precursors. The solid-state method often requires a high synthesis temperature and longer reaction time (from many hours to days), which often leads to poor sinterability of as-synthesized powders [48,85,96][159,178,179]. Recently, improvement in sinterability of Li_2ZrO_3 powder by synthesizing submicron to nanoscale particles has drawn much attention. To synthesizing nanoscale Li_2ZrO_3 powders, many wet chemical methods including solution combustion synthesis (SCS), hydrothermal, sol–gel, and polymer solution method have been developed [160,163,165][167,180–182].

The SCS is quick and energy efficient method, which is widely used for the preparation of nanoscale ceramic powders. Recently, SCS has drawn attention to synthesize and thereby improve sinterability of Li-based ceramic tritium breeders. The SCS relies on high exothermic heat generated by the redox reaction between metal nitrates and organic fuel. For ignition of the reaction, the mixed precursor solution is heated at relatively low temperatures, and after ignition the reaction is self-propagated yielding the desired ceramic powders.

In this chapter, a systematic study on the solution combustion synthesis of nanocrystalline/fine Li_2ZrO_3 ceramic powders utilizing glycine as organic fuel has been presented. The effect of fuel-to-oxidizer ratio (φ=0.5–1.25) on synthesis condition, phase purity and microstructure of powder, and the thermochemistry of combustion reactions is systematically investigated. The sinerability of as-synthesized Li_2ZrO_3 powders was investigated by dilatometry analysis and also under isothermal conditions. The advantages of SCS method is discussed with respect to the powder characteristics, sintering behaviour, and the microstructure of sintered compact.

4.2 Experimental procedure

4.2.1 Synthesis of Li_2ZrO_3 powders

Lithium nitrate: $LiNO_3$ (purity: AR grade, Prabhat Chemicals Private Limited, India), zirconium oxynitrate: $ZrO(NO_3)_2$ (purity: AR grade, Prabhat Chemicals Private Limited, India) were used as precursors for the synthesis of lithium zirconate (Li_2ZrO_3). Glycine (purity: AR grade, Prabhat Chemicals Private Limited, India) was utilized as fuel. All reagents were used as received without further purifications. The stock solutions were prepared by dissolving $LiNO_3$ and $ZrO(NO_3)_2$ in deionised water. According to the stoichiometry, the required volume of the stock solutions was mixed properly. In order to prepare the SCS reaction mixtures, varying amounts of glycine were separately added in the mixed nitrate solution so as to maintain the desired fuel-to-oxidizer ratios (φ). The resulting transparent SCS solutions were heated on a hot plate at temperature of 90°C. For the measurement of combustion temperature, a K-type thermocouple was properly placed inside the reaction vessel. The solution temperature was raised to ~200°C after the solutions turned viscous. It was observed that combustion was ignited within a few minutes and self-propagated. At the end of combustion reaction, a friable and voluminous powder was obtained. Flow sheet of the synthesis process is shown in **Figure 4.2**. The time elapsed from the ignition of combustion reaction until its completion was noted carefully for each combustion reaction. The general equation for the combustion reactions can be expressed as:

$$2LiNO_3\,(aq.) + ZrO(NO_3)_2\,(aq.) + 2.22\varphi\; C_2H_5NO_2\,(aq.) + 5(\varphi - 1)\; O_2\,(g)$$

$$= Li_2ZrO_3\,(c) + 4.44\varphi\; CO_2\,(g) + (2+1.11\varphi)\; N_2\,(g) + 5.55\varphi\; H_2O\,(g)$$

In order to delineate the effect of fuel-to-oxidizer ratios (φ) on mode of combustion, thermodynamic aspects, and powder properties, φ was varied as 0.5, 0.75, 1.0 and 1.25, in the present work. The unreacted reactants or residual carbonaceous material might be present in the as-synthesized powders. Therefore, the as-synthesized powders were further calcined at temperature of 600-800°C in a muffle furnace (Nabertherm, Germany) in static air. In addition to removal of residual materials, heat treatment facilitates the formation of desired crystalline phase of Li_2ZrO_3.

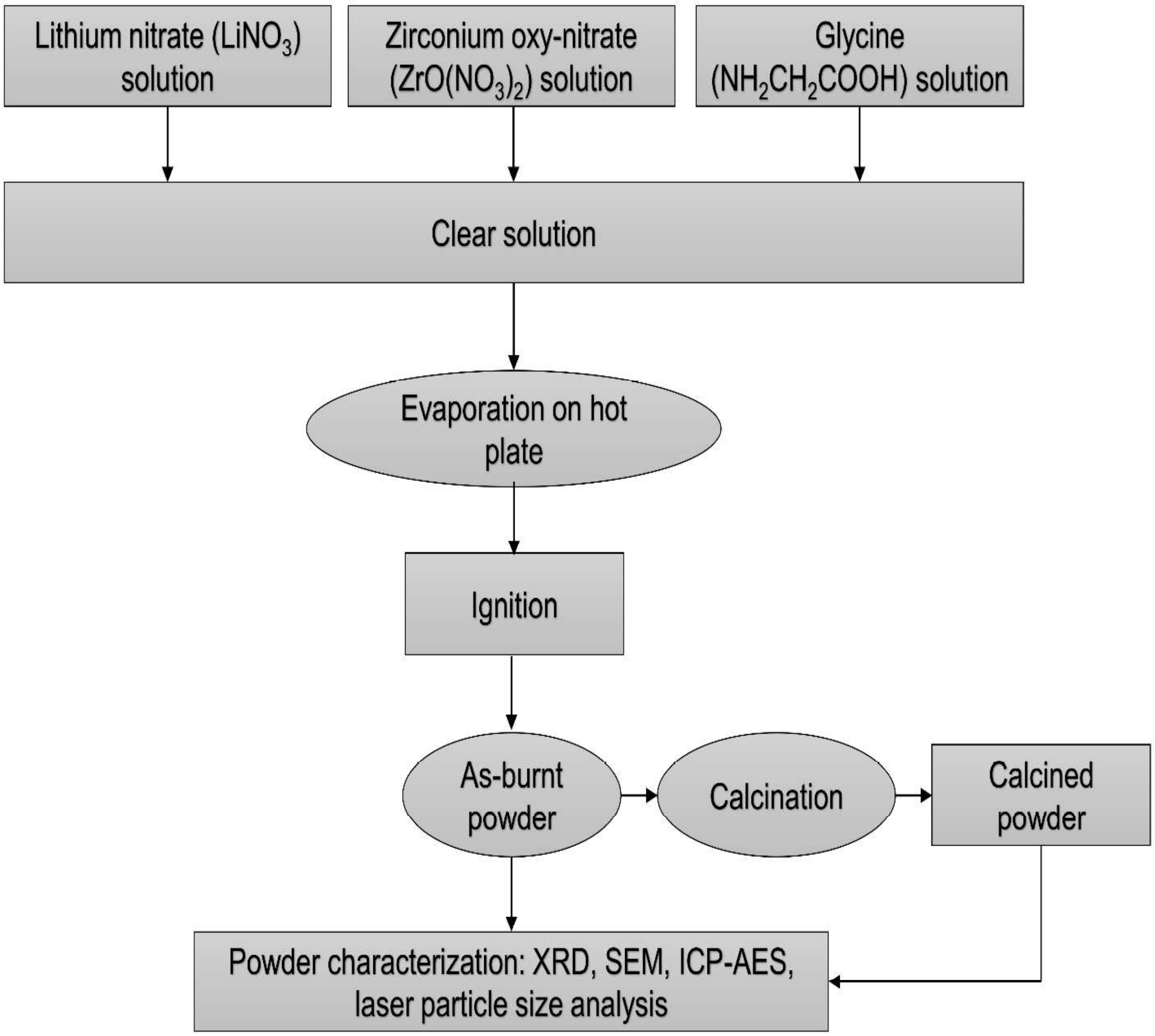

Figure 4.2 Li_2ZrO_3 synthesis process flow sheet

4.2.2 Consolidation and sintering of Li_2ZrO_3 powders

The Li_2ZrO_3 powders were compacted to form pellet shape green compacts without addition of binder. The compaction was performed by a uniaxial hydraulic press using a cylindrical steel die with tungsten carbide lining for the pressing operation. The flow sheet of consolidation and sintering is presented in **Figure 4.3**.

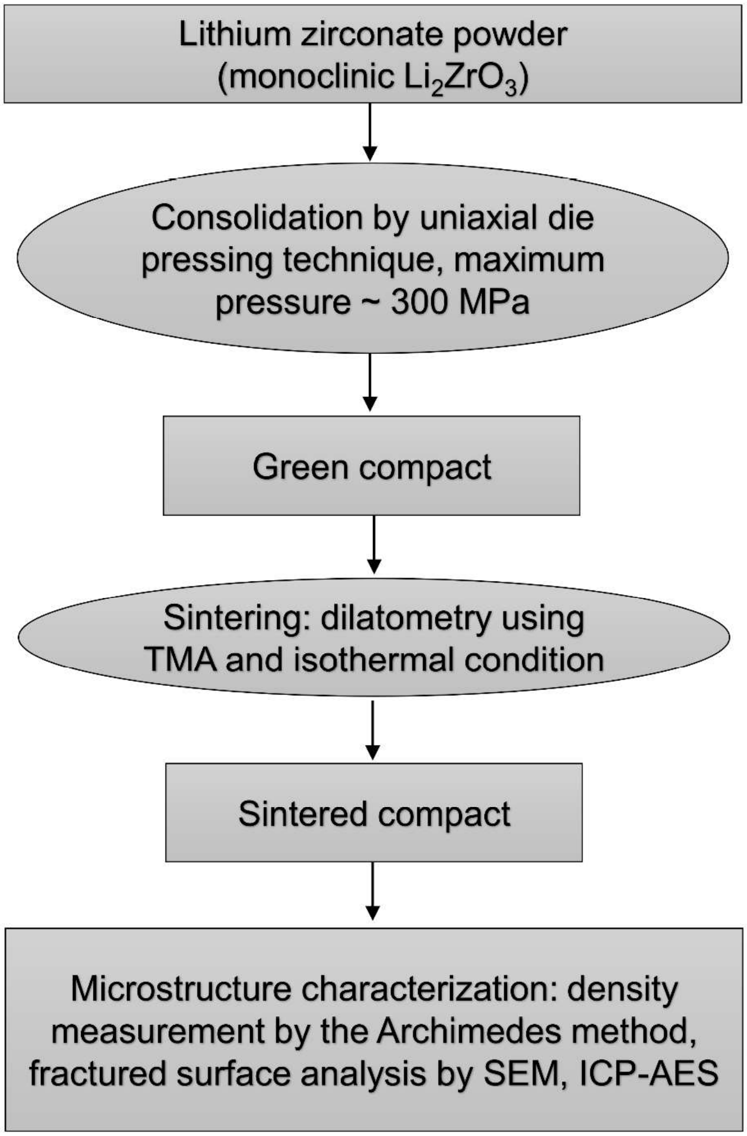

Figure 4.3 Li_2ZrO_3 powder consolidation and sintering process flow sheet

Before compaction, the die wall was lubricated using a dilute stearic acid solution to minimise the wall friction and thereby avoid density gradients within Li_2ZrO_3 green pellets. The final compaction pressure was applied around 300 MPa. Sintering behaviour of Li_2ZrO_3 green pellets were investigated under both, non-isothermal and isothermal conditions. For non-isothermal sintering study, Li_2ZrO_3 pellets of the required size (8 mm diameter and around 4 mm height) were prepared. The geometrical shrinkage of these pellets was measured, up to 1200°C under a given temperature ramp (5, and 10°C/min) in flowing air, using TMA. For performing isothermal sintering experiments, Li_2ZrO_3 pellets (size: 10 mm diameter and 3 mm height) were prepared. These pellets were sintered at fixed temperatures in the range of 800-1000°C with heating rate of 5°C/min for constant time duration (2h) in a muffle furnace (Make: Nabertherm, Germany) in static air.

4.2.3 Characterization

The phase of as-synthesized powders was analysed by XRD. Inel diffractometer equipped with Ni filtered Cu-Kα radiation (λ=1.54056 Å) source was exploited for recording the diffraction patterns.

Laser diffraction particle size analyser (Make: CILAS, France) was utilized for the measurement of particle size of the as-synthesized powders.

Scanning electron microscopy (SEM) (Make: Seron, Korea) operating at 20kV accelerating voltage was used to characterize the microstructures of as-synthesized powders and sintered pellets.

Inductively coupled plasma atomic emission spectroscopy (ICP-AES) (Make: Horiba, Germany) was used for the chemical analysis and determination of Li-content of sintered pellets. The pellets were dissolved in the aqua-regia as medium for the chemical analysis.

Archimedes' method was used to measure the relative density of the sintered pellets at room temperature. The volumetric shrinkage was calculated by measuring change in dimensions of the sintered pellets before and after sintering.

4.3 Results and discussion

4.3.1 Thermodynamic aspects and mode of combustion

The combustion reaction for different fuel-to-oxidizer ratios can be written as follows:

$$2LiNO_3(aq.) + ZrO(NO_3)_2(aq.) + 1.11\ C_2H_5NO_2(aq.)$$
$$= Li_2ZrO_3(s) + 2.22CO_2(g) + 2.555N_2(g) + 2.775H_2O(g) + 2.5O_2\ (g) \quad (\varphi = 0.5)$$

$$2LiNO_3(aq.) + ZrO(NO_3)_2(aq.) + 1.665\ C_2H_5NO_2(aq.)$$
$$= Li_2ZrO_3(s) + 3.33CO_2(g) + 2.832N_2(g) + 4.162H_2O(g) + 1.25O_2(g) \quad (\varphi = 0.75)$$

$$2LiNO_3(aq.) + ZrO(NO_3)_2(aq.) + 2.22C_2H_5NO_2(aq.)$$
$$= Li_2ZrO_3(c) + 4.44CO_2(g) + 3.11N_2(g) + 5.55H_2O(g) \quad (\varphi = 1)$$

$$2LiNO_3(aq.) + ZrO(NO_3)_2(aq.) + 2.775C_2H_5NO_2(aq.) + 1.25O_2(g)$$
$$= Li_2ZrO_3(c) + 5.55CO_2(g) + 3.387N_2(g) + 6.937H_2O(g) \quad (\varphi = 1.25)$$

In the above reactions, $\varphi = 1$, $\varphi > 1$ and $\varphi < 1$ corresponds to stoichiometric, fuel-rich, and fuel-lean conditions, respectively. In case of $\varphi = 1$, complete oxidation of glycine does not involve atmospheric oxygen, while in case of $\varphi > 1$, the oxidation of excess glycine requires atmospheric oxygen.

The standard enthalpy of combustion and the adiabatic temperature were calculated using the existing thermodynamic data. The amount of gases released was also calculated for the combustion reactions. The thermodynamic relations used for the calculation of enthalpy and adiabatic temperature of reactions are as follows:

$$\Delta_r H^0_{298} = \sum n(\Delta_f H^0_{298})_{product} - \sum n(\Delta_f H^0_{298})_{reactant}$$

$$\Delta_r H^0_{298} = \int_{298}^{T_{ad}} \sum (n\ c_p)_{products}\ dT$$

where, $\Delta_r H^0_{298}$, c_p, T_{ad} and n are the standard enthalpy of reaction, the heat capacity at constant pressure, the adiabatic temperature and the number of moles, respectively. In calculation of theoretical adiabatic temperature following assumptions were made: i) completion of the combustion reactions ii) oxidation of excess fuel by atmospheric oxygen, and iii) no heat loss by conduction, convection or radiation. The variation of the standard enthalpy of reaction with the fuel-to-oxidant ratio is shown in **Figure 4.4**.

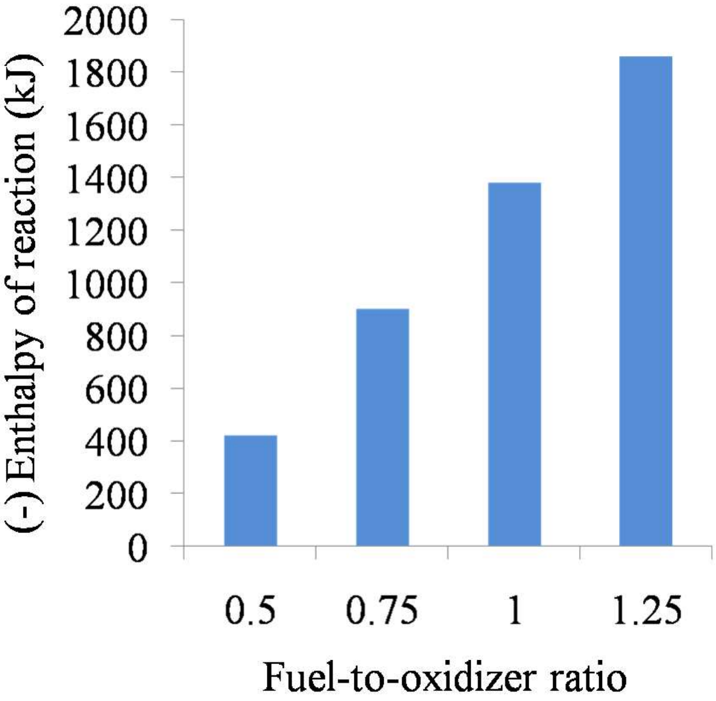

Figure 4.4 Effect of fuel-to-oxidizer ratio on standard enthalpy of reaction

The large negative standard enthalpy values imply highly exothermic nature of the combustion reactions. The exothermic heat of combustion increases with the increase in φ. The dependence of calculated adiabatic temperature and the measured temperature on the fuel-to-oxidant ratio are depicted in **Figure 4.5**.

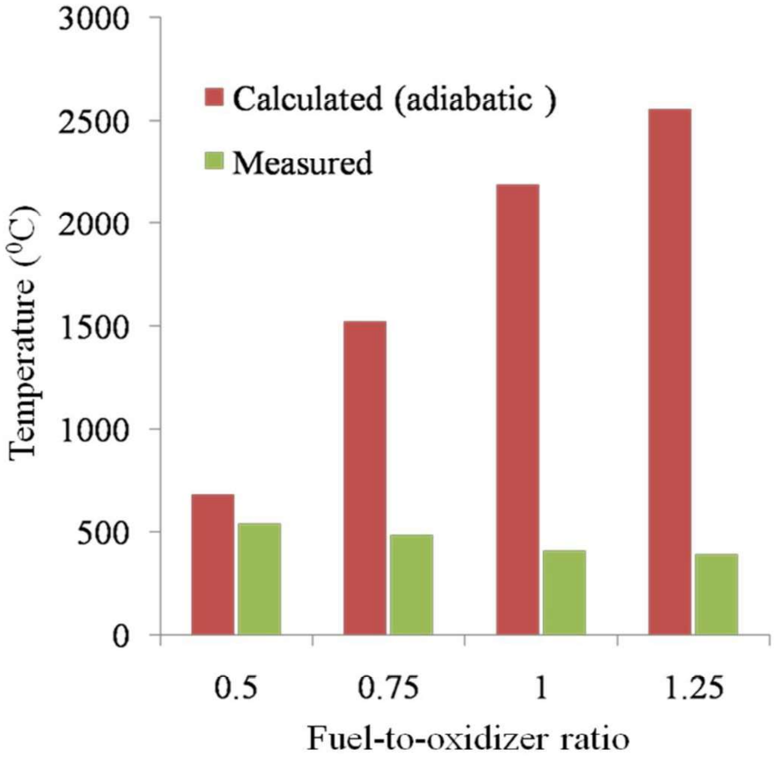

Figure 4.5 Effect of fuel-to-oxidizer ratio on calculated and measured temperature

The highest adiabatic temperature (2554°C) is produced from the reaction (φ =1.25) while the lowest (680°C) from the reaction (φ = 0.5). This result is consistent with corresponding enthalpy values of the reactions.

On the other hand, the actual maximum temperature measured for each combustion reactions are much lower than the adiabatic temperature. It is due to release of large volume of gases in the combustion process, which dissipate heat very quickly by the convective process. Therefore, it largely affects the actual temperature. As shown in **Figure 4.6**, the amount of gases (moles) increases with ϕ, and release of gases in case of fuel-rich system are approximately twice of the fuel-lean system. Therefore, the difference between the adiabatic and actual temperature is initially somewhat less but gradually increases with increasing φ. Moreover, in contrast to adiabatic temperature, the actual temperature decreases with increasing φ.

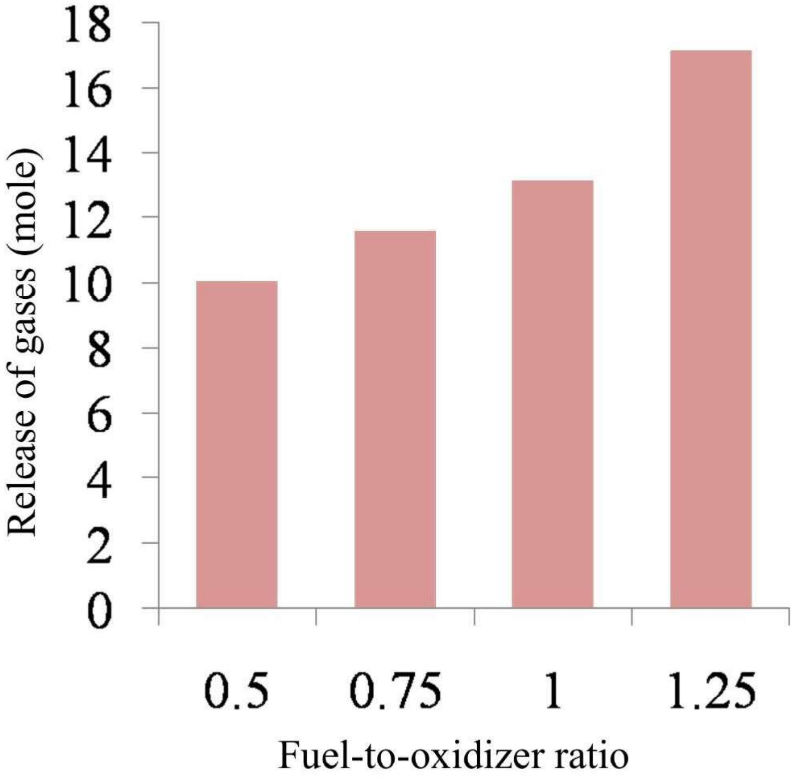

Figure 4.6 Effect of fuel-to-oxidizer ratio on amount of gases released

This trend of actual temperature with increasing φ cannot be only due to the convective loss of exothermic heat by the releasing gases but also due to the switch in the mode of combustion reaction with change of φ. The switch in the mode of combustion was visually observed for each combustion reactions and results are summarized in **Table 4.1**.

Table 4.1 Mode of combustion at different fuel to oxidant ratio

φ	Mode of combustion	Duration of combustion reaction (s)	Colour of powder
0.5	VCS	12	White
0.75	VCS	15	White
1	VCS	5	White
1.25	SHS-Volcanic eruption	20	White

It is worth mentioning at this juncture that in case of φ≤1, the atmospheric oxygen is not needed for the completion of the redox reactions between glycine and nitrates, however, in case of φ>1, the atmospheric oxygen is necessarily required. But slow diffusion of oxygen into the reaction mass might result in deprivation of oxygen leading to incomplete combustion of glycine in case of φ>1. It is clearly violating one of the assumptions for adiabatic heat calculation that excess glycine completely oxidizes by the atmospheric oxygen. Therefore, a plausible explanation for large difference between the adiabatic and the actual temperature (in case of φ>1) would be due to incomplete oxidation of glycine in addition to convective heat loss by the escaping gases. As given in **Table 4.1**, the mode of combustion reaction depends on φ. The VCS mode of combustion was observed for φ = 0.5, 0.75 and 1, which is characterized by a very violent reaction. In case of φ = 1.25, comparatively moderate reaction was observed due to switch in combustion mode to SHS. Interestingly, a white colour powder was obtained even for φ >1, however, Zhou et al. obtained grey colour powder while using citric acid fuel [150]. It is because, unlike citric acid (Zhou et al.) [150], the excess glycine (in case of φ>1) decomposes without generating carbon (C). It is to be noted that grey colour of the powder is due to the carbon impurity. The decomposition of excess glycine can be expressed by the following chemical reaction:

$$2C_2H_5NO_2(s) + 4.5\ O_2(g) = 4CO_2(g) + N_2(g) + 5H_2O(g)$$

The standard Gibbs free energy and enthalpy for above reaction is calculated as -237 and -206 Kcal/mol. Therefore, from the thermodynamics point of view, the above reaction is feasible and highly exothermic.

4.3.2 Phase composition and crystallite size

The XRD pattern (**Figure 4.7**) revealed the formation of mixture of two crystallographic phases of Li_2ZrO_3 in the powder calcined at 700 and 750°C irrespective of the fuel-to-oxidizer ratios. The assigned XRD peaks of the as-synthesized powders match well with the standard patterns of the monoclinic and tetragonal phases of Li_2ZrO_3 (JCPDS Card No. 033-0843 and 041-0324). The peaks of tetragonal phase are not observed in the XRD pattern of powder calcined at 600°C, which might be due to the amorphous nature. The formation of metastable phase is commonly observed in SCS method. It is due to the extremely fast kinetics of the combustions reactions which allows the exothermic energy (generated from the combustion) to turn-off very quickly before the formation of equilibrium (or stable) phase. Also, in the present case the formation of metastable tetragonal phase is consistent with the extremely fast nature of the combustion reaction (**Table 4.1**). The time of completion of the combustion reactions is within 5-20 sec (**Table 4.1**). The XRD peaks of tetragonal phase have very low intensity, which indicates the formation of minor quantity of tetragonal phase in the powder.

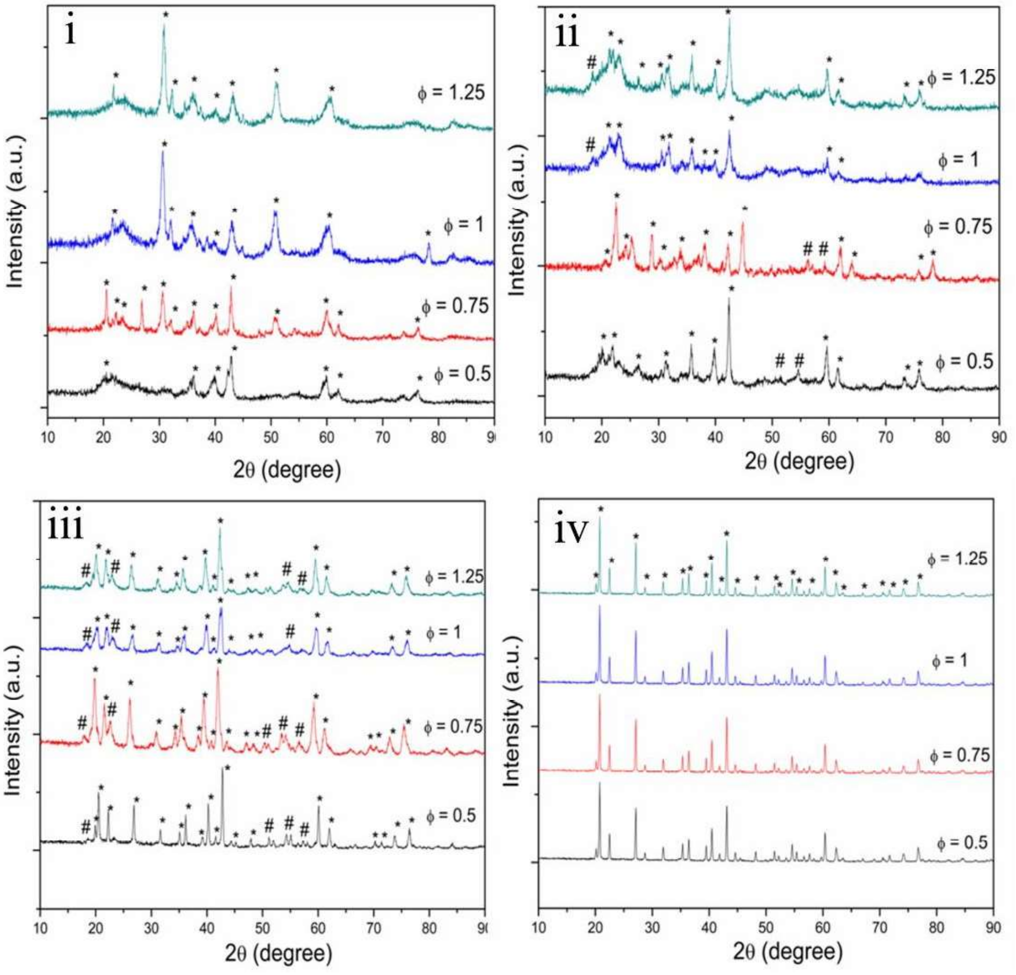

Figure 4.7 XRD pattern of Li_2ZrO_3 powder synthesized at varying fuel-to-oxidizer ratios and temperatures (* = Monoclinic phase, # = Tetragonal phase) i) 600°C ii) 700°C iii) 750°C iv) 800°C

The well crystalline monoclinic Li_2ZrO_3 phase was synthesized after annealing the powder at 800°C as confirmed by the XRD pattern (**Figure 4.7**) of the powder. Moreover, any unreacted component or impurity phases are not observed in XRD pattern, which indicates that enough exothermic heat was produced in the combustion reactions for the formation of Li_2ZrO_3. This result is somewhat different from the work of Zhou et al. [150] which showed presence of unreacted $LiNO_3$ and TiO_2 in as-synthesized Li_2TiO_3 powder while citric acid was used as the fuel.

The crystallite size of Li_2ZrO_3 was calculated from the FWHM of the XRD peaks. Before the crystallite calculation, the instrumental contribution to XRD peak broadening was obtained from the XRD peak of the standard LaB_6 sample, and it was used to obtain the instrument corrected broadening (β_{hkl}) of the XRD peaks of Li_2ZrO_3. The corrected FWHM (β_{hkl}) was calculated using the following relations:

$$(\beta^2)_{hkl} = [(\beta^2)_{measured} - (\beta^2)_{instrumental}$$

Scherrer's equation was used to calculate the average crystallite size (D) of Li_2ZrO_3 as follows:

$$D = (0.9\,\lambda / \beta_{hkl} \cos\theta)$$

where, λ is the wavelength of radiation (1.54056 Å for Cu-Kα radiation), β_{hkl} is FWHM of XRD peak, and θ is the peak position.

The crystallite size of Li_2ZrO_3 powder synthesized under fuel-lean, stoichiometric and fuel-rich conditions, and calcined at 800°C are depicted in **Figure 4.8**. The crystallite size first decreases with increase in fuel-to-oxidizer ratio from φ = 0.5 (40 nm) to 0.75(32 nm) and then to 1 (18 nm), and then increases somewhat at φ =1.25 with the crystallite size of 25 nm. Decrease in crystallite size up to φ equals to 1 is consistent with increase in the actual temperature of the combustion reaction (**Figure 4.5**). However, slight increase of crystallite at φ =1.25 may be due to switch in combustion mode from VCS to SHS. In SHS mode, time duration of combustion reaction is relatively longer as given in **Table 4.1**, which allows crystallites to grow larger. Therefore, many competing factors including the temperature, volume of gases released, and the mode of the combustion lead to the observed dependence of crystallite size on fuel-to-oxidizer ratio.

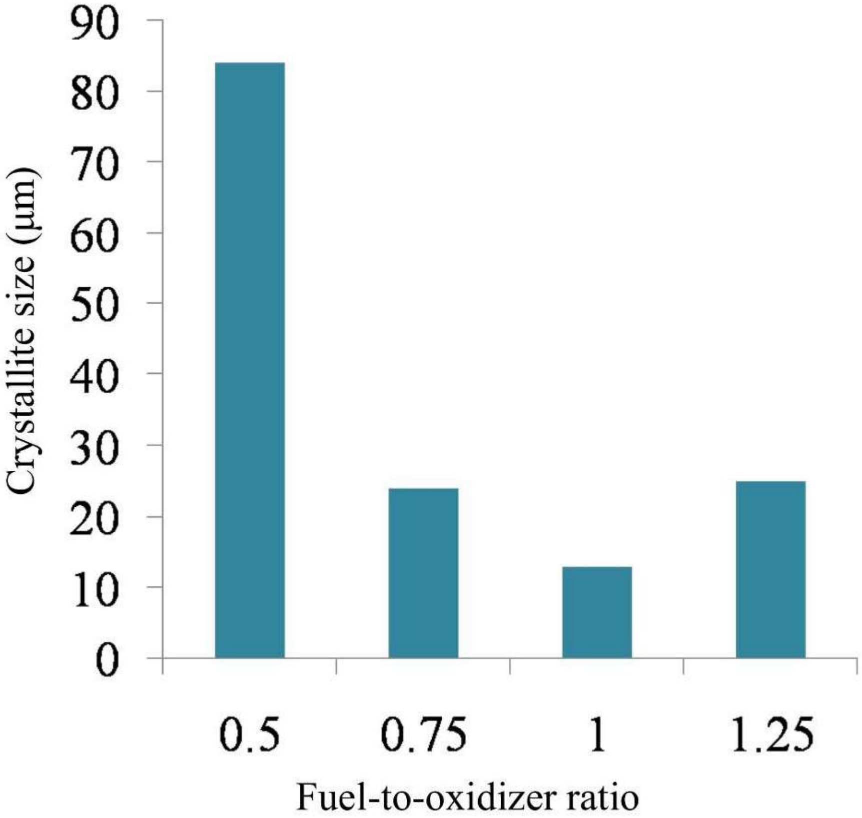

Figure 4.8 Effect of fuel-to-oxidizer ratio on crystallite size of Li_2ZrO_3

4.3.3 Powder morphology

Mean particle size (measured by laser diffraction method) of Li_2ZrO_3 powder synthesized at fuel-lean, stoichiometric and fuel-rich conditions, and subsequently calcined at 800°C and 1000°C is shown in **Figure 4.9**. The mean particle size is observed to be considerably larger than the crystallite size (**Figure 4.8**), irrespective of the fuel-to-oxidizer ratios. It is due to the high surface area of the combustion derived fine Li_2ZrO_3 powders leading to agglomeration of the particles under the influence of available exothermic heat of the combustion.

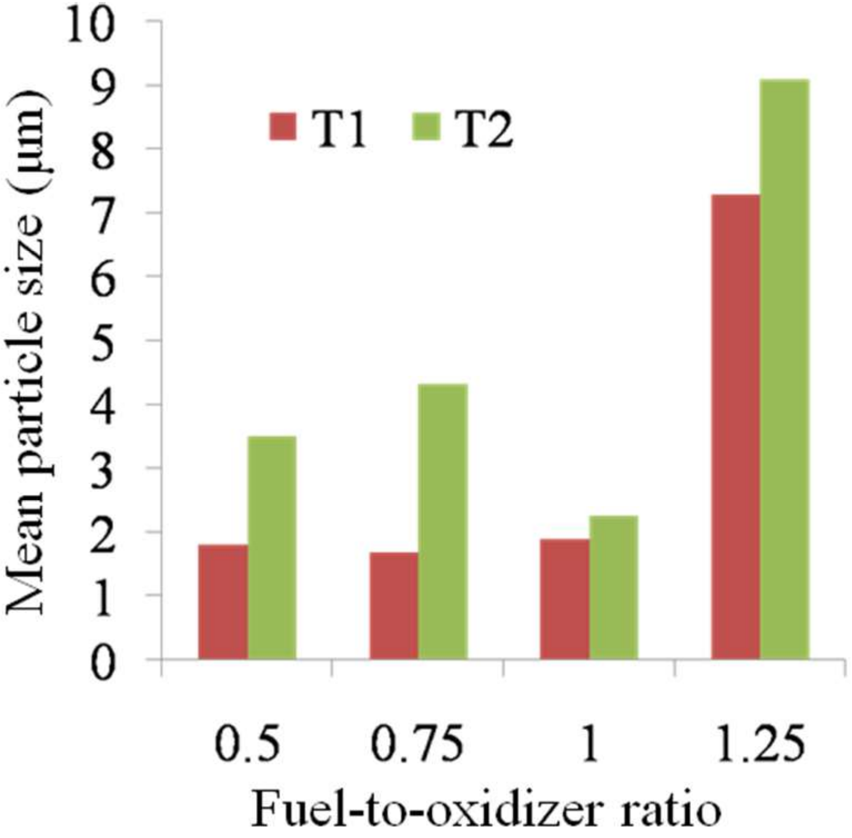

Figure 4.9 Effect of fuel-to-oxidizer ratio on mean particle size of Li_2ZrO_3 powder (T1 = 800°C, T2 = 1000°C)

As the reaction temperature varies with the fuel-to-oxidizer ratios (**Figure 4.5**), the extent of agglomeration and thereby mean particle size also varies with the fuel-to-oxidizer ratios (**Figure 4.9**). The small particle size of powder calcined at higher temperature (1000°C) as compare to 800°C is obvious. The agglomerate size and its nature (hard or soft) have bearing on the green density, and thereby sinterability of the powder compact. Generally, large sized hard powder aggregates result in poor sinterability of the compact. Therefore, the fuel-to-oxidizer ratio needs to be optimized to avoid the formation of hard particle aggregates.

The SEM micrographs of Li_2ZrO_3 powder synthesized at different fuel-to-oxidizer ratios, and subsequently calcined at 800°C are shown in **Figure 4.10**.

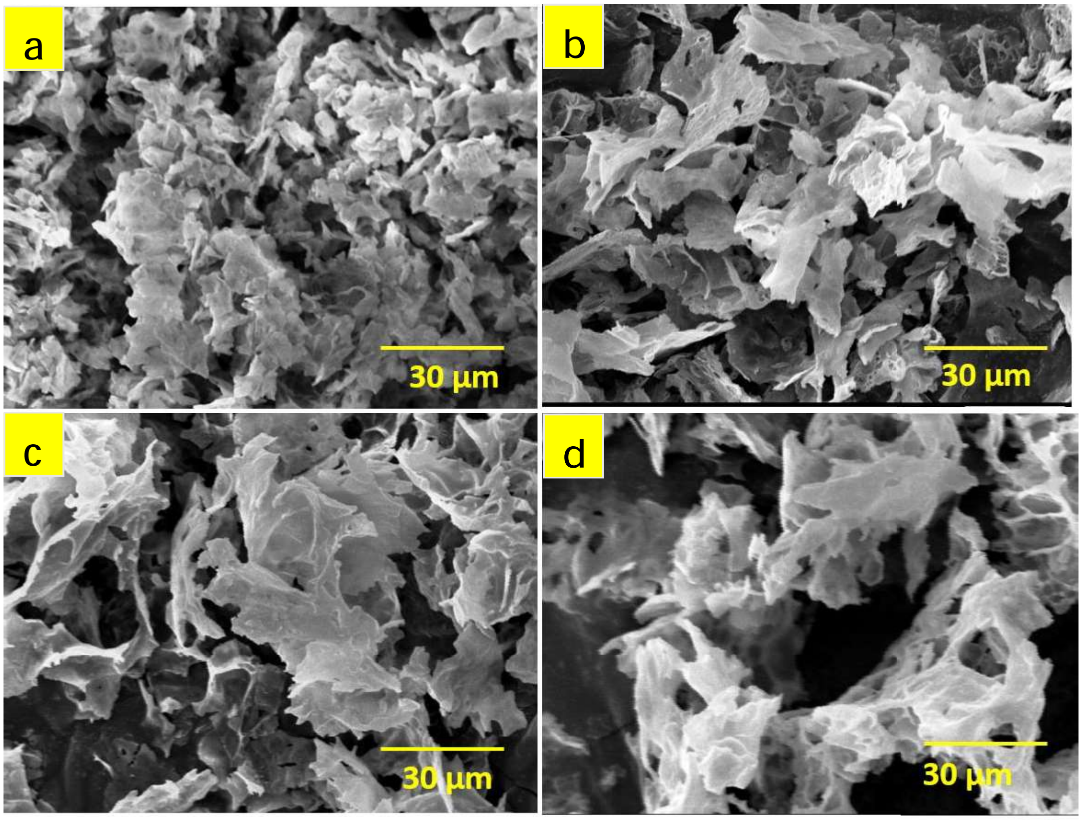

Figure 4.10 SEM images of of Li_2ZrO_3 powder clacined at 800°C and fuel-to-oxidizer ratio a=0.5, b=0.75, c=1, d=1.25

The powder exhibits morphology comprising of agglomerated flake shape particles with very broad size range (5-30 µm), which is in good agreement with the laser particle size data (**Figure 4.9**). The morphological variations in the powder synthesized at different fuel-to-oxidizer ratios is due to the difference in reaction temperature. The poor thermal conductivity of Li_2ZrO_3, poor inter-particle connectivity, and formation of large voids are additional contributing factors to the temperature variations within the powder. Due to the release of large volume of gases, the synthesized powder is highly porous and voluminous. The formation of large size gas channels is clearly visible in the fuel-rich composition (**Figure 4.10 d**). The agglomerated Li_2ZrO_3 powders comprised of very fine primary particles (**Figure 4.10)**. It is worth to be mentioned at this juncture that conventional solid-state synthesis method, due to high temperature (> 1000°C), prolonged reaction, and moderate gaseous release, often results in large size hard Li_2ZrO_3 powder aggregates, which lead to extremely poor sinterability of the powder compact. However, in present SCS method, despite the high adiabatic temperature, the formation of hard particle aggregates is prevented due to extremely short reaction time, and quick dissipation of heat by large volume of releasing gases via convective process. The soft particle agglomerates, due to very weak inter-particle bonding, easily disintegrate into the primary particles by pestle-mortar or modertae ultrasonication, and therefore do not deteriorate the green density and thereby sinterability of the powder compact.

4.3.4 Chemical analysis (Li/Zr ratio) and residual Li_2O content

The estimated mean value of Li/Zr mole ratio (1.975 ± 0.006) in Li_2ZrO_3 powder synthesized at different fuel-to-oxidizer ratios (φ = 0.5, 0.75, 1 and 1.25), and subsequently calcined at 1000°C, is consistent with the stoichiometric value (i.e. 2). Therefore, it confirms that no evaporative loss of Li occurred from as-synthesized Li_2ZrO_3 by the present SCS method. It is worth to mention that evaporative loss of Li from tritium breeders is of concern because it has direct bearing on the tritium breeding ratio. Despite the high heat of combustion reaction, the loss of Li is prevented because of the transient nature of the reaction and fast dissipation of heat by large volume of the releasing gases. The residual Li_2O in the as-synthesized Li_2ZrO_3 powder at different fuel-to-oxidizer ratios, and subsequently calcined at 800°C was determined for by a simple pH measurement method. In this method, a known quantity (50 mg) of Li_2ZrO_3 powder was suspended in fixed volume of distilled water and ultrasonicated for constant duration (15 min) at the room temperature. It was assumed that residual Li_2O dissolves completely into water due to high solubility, and therefore, increases the pH of the resulting solution. The residual Li_2O content was determined from measuring the increase in the solution pH. The dissolution reaction can be expressed as given below.

$Li_2O(s) + H_2O\ (l) = 2\ LiOH\ (aq.)$

To confirm that Li_2ZrO_3 was not hydroxylated in water, one of the samples was kept overnight in water under the identical conditions, and thereafter the sample was filtered, dried, and its XRD pattern was recorded as depicted in **Figure 4.11**.

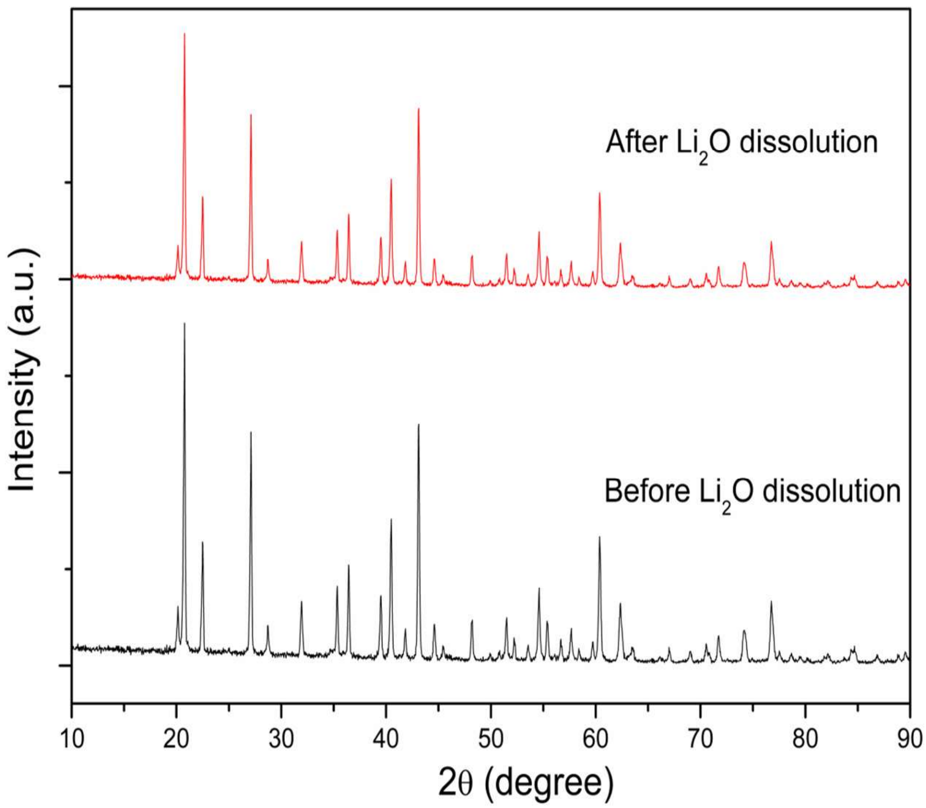

Figure 4.11 XRD pattern of Li_2ZrO_3 before and after dissolution

The comparison of the XRD pattern of Li_2ZrO_3 before and after dissolution confirmed no hydroxylation in water.

The quantity of residual Li_2O in the as-synthesized Li_2ZrO_3 powder is in the range 155-469 (μg/g) as presented in **Figure 4.12**. Such small quantities are often difficult to observe by XRD method, and therefore, Li_2O peaks were possibly not detected in the XRD pattern (**Figure 4.7**).

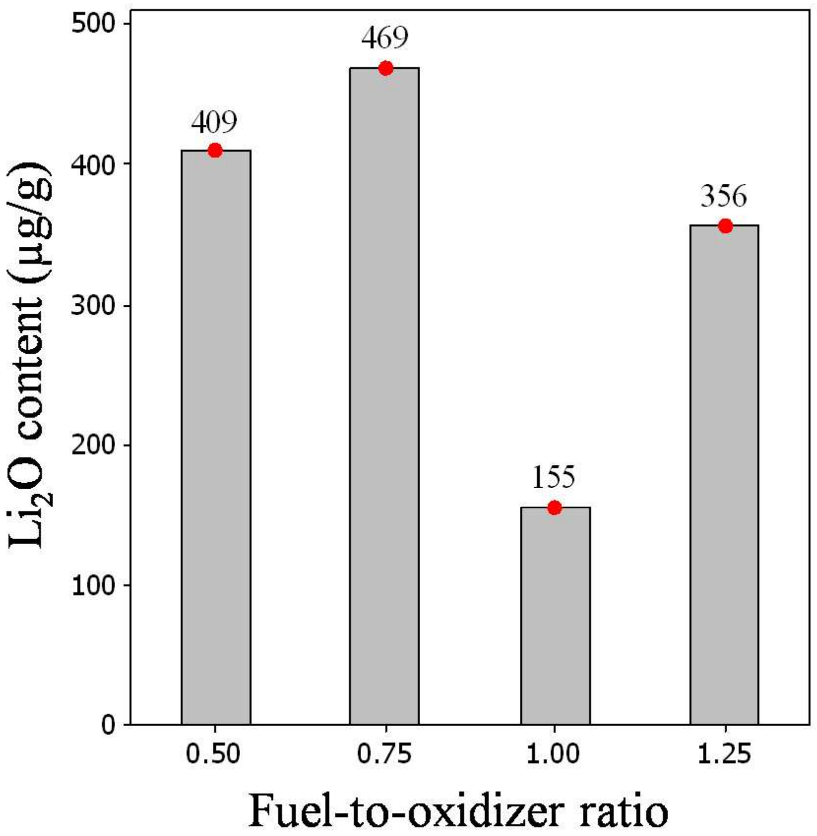

Figure 4.12 Li_2O content in Li_2ZrO_3 powder annealed at 800°C for different fuel-to-oxidizer ratio

The residual Li_2O was originated from the thermal decomposition of $LiNO_3$ in the combustion process, and its quantity depends on many factors including reaction temperature, volume of gases, and the mode of combustion. Therefore, the residual Li_2O content in as-synthesized Li_2ZrO_3 powder varies with the fuel-to-oxidizer ratios (**Figure 4.12**). It is worth emphasizing that tritium breeding performance of Li_2ZrO_3 is affected by the presence of residual Li_2O in Li_2ZrO_3. Tritiated water vapours are one of the chemical forms in which the bred tritium purges out of the tritium breeder by thermal desorption. The residual Li_2O chemically reacts with the tritiated water vapours to form tritiated lithium hydroxide and thereby chemically traps tritium within the breeder. To recover tritium from the tritiated lithium hydroxide a separate high temperature (> 1000°C) decomposition process is needed which is not compatible with the current TBM configuration. Therefore, fuel-to-oxidizer ratio need to be optimized such that synthesized Li_2ZrO_3 powder should be free from the residual Li_2O.

4.3.5 Sintering behavior of Li_2ZrO_3

Representative dilatometry curve of Li_2ZrO_3 pellet (8mm diameter and 3-4mm thickness) at different heating rates (5, 10 and 15°C/min) up to 1200°C is shown in **Figure 4.13**. It indicates percentage shrinkage of the pellet expressed as dL/L_0 (%) with increasing temperature where Lo is initial length. Intense shrinkage (~15%) of the pellet was observed in temperature ranging from around 850 to 1000°C at a heating of 5°C/min. It is due to the dominance of the sintering mechanisms over the intrinsic thermal expansion of the pellet resulting in densification of the pellet. Intense shrinkage observed is consistent with large amount of porosity present in the green pellet. The onset of sintering step was observed at around 850°C as distinctly depicted in inset derivative plot (**Figure 4.13**) which suggests excellent sinterability of Li_2ZrO_3 powder synthesized by present method. Apparently, increasing the heating rate shifted the onset of initial sintering to higher temperature (**Figure 4.13**) which is related to kinetic aspect of sintering. In fact, at low heating rates, the pellet is exposed to heating for a longer duration and consequently underwent more shrinkage until reaching a specific temperature. During the final step (>1000-1200°C) only a modest shrinkage around 1-2% was observed. In this step, instead of densification, the grain growth mechanism might be dominant.

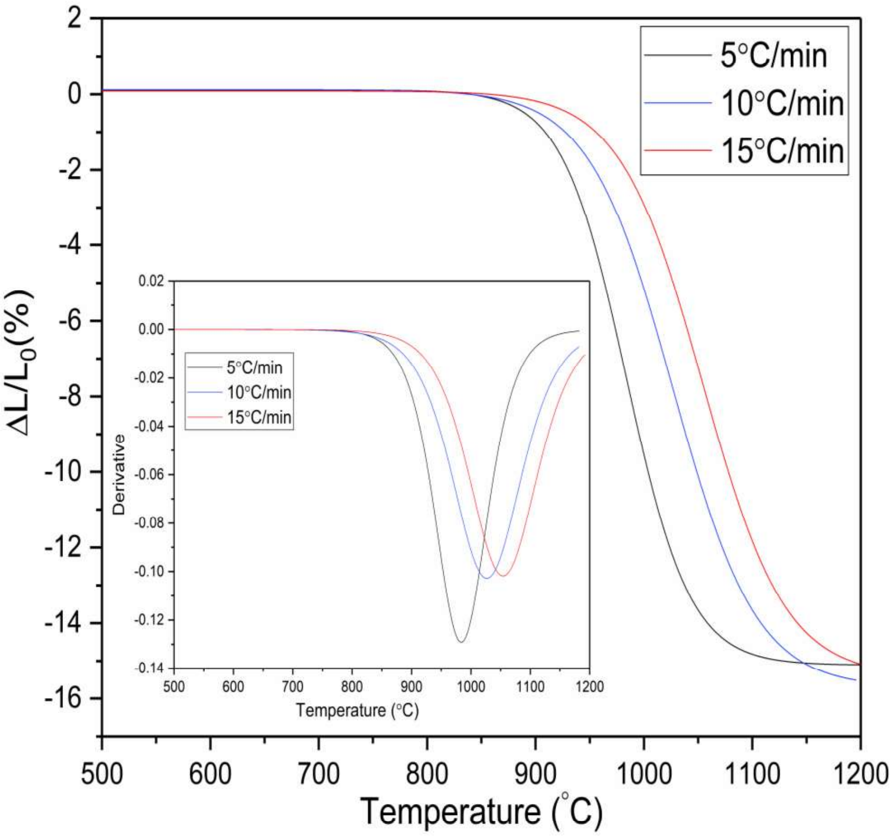

Figure 4.13 Dilatometry curve of Li_2ZrO_3 pellet at heating rate of 5, 10 and 15°C/min

For more insight on sintering process, isothermal sintering of Li_2ZrO_3 pellets was conducted. For this, Li_2ZrO_3 powders synthesized at stoichiometric fuel-to-oxidizer ratio (φ =1) and calcined at 800°C were compacted to form pellets of desired dimension (10mm diameter x 3 mm height). The pellets were sintered at different sintering temperatures ranging from 900-1100°C and constant sintering time (2h). The rate of heating was kept constant (10°C/min). The volumetric shrinkage of the pellets was determined at each sintering temperature from measured difference in pellet dimensions before and after sintering. The relative density of the sintered Li_2ZrO_3 pellets at each sintering temperature was determined by Archimedes' water displacement method.

The plot of relative density and volumetric shrinkage of sintered Li_2ZrO_3 pellet as a function of sintering temperature is presented in **Figure 4.14**.

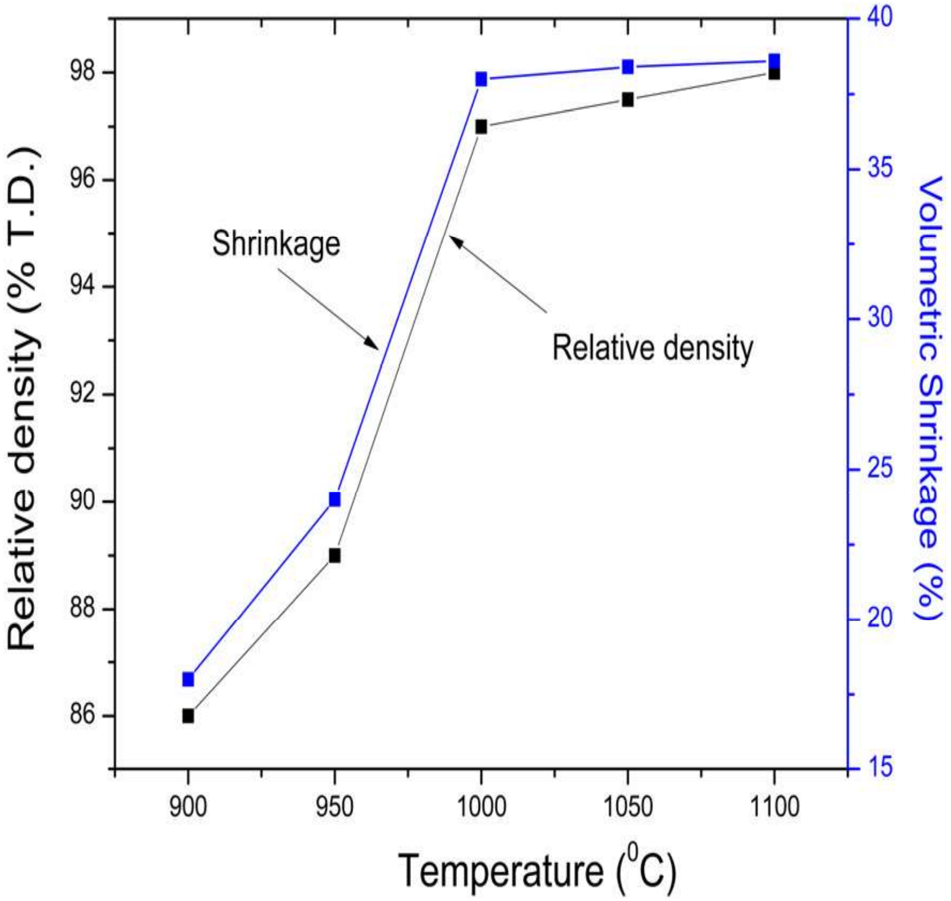

Figure 4.14 Effect of sintering temperature on relative density and volumetric shrinkage of Li_2ZrO_3 pellet

The relative density of the sintered pellets increases with the sintering temperature. The optimum relative density for tritium breeding purpose that is generally about 90%, is achieved at temperature as low as 950°C. Additionally, at such as low sintering temperature (below 1000°C), evaporative loss of Li might be insignificant. The relative density sharply increases to about 98% at sintering temperature of 1000°C. Further increasing the sintering temperature to 1050 and 1100°C does not improve the relative density significantly (**Figure 4.14**). Jean-Daniel Lulewicz et al. synthesized Li_2ZrO_3 powder by the solid-state method and fabricated sintered pebbles with relative density about 70% at sintering temperature of about 1200°C [85]. It shows that the Li_2ZrO_3 powder synthesized by the present method has significantly improved sinterability as compared to the conventional solid-state method. The densification behaviour of Li_2ZrO_3 pellets at different sintering temperatures can be correlated with the kinetics of two competing sintering processes, the densification and the grain-growth. The densification is likely to be a dominant process at sintering temperature of up to 1000°C, which results in fast increase in the relative density Li_2ZrO_3 pellet. However, at further higher sintering temperature, the grain growth is likely to be a dominant process, which results in grain coarsening without significant improvement in the relative density of the pellets. The volumetric shrinkage (%) curve of the pellets is consistent with the densification curve. The large volumetric shrinkage of the pellets is consistent with the more porosity present in the green pellets.

To reveal the microstructural characteristics, SEM images of fracture surface of sintered Li_2ZrO_3 pellets at different sintering temperatures (900, 950, 1000 and 1050°C) was captured as shown in **Figure 4.15**. The uniform grain morphology, as evident from the SEM images, confirms the phase purity of the of sintered Li_2ZrO_3 pellets. It is in complete agreement with the XRD result (**Figure 4.7**) confirming the formation of pure monoclinic Li_2ZrO_3 at annealing temperature of 800°C annealing. The microstructure of the pellets exhibits the agglomerated sintering at sintering temperatures of 900 and 950°C with no clear demarcation of the grain boundaries (**Figure 4.15 i-j**). However, microstructure at sintering temperature of 1000°C is comprised of evident polyhedral grains with grain size of 1-2μm and grain boundaries as shown in **Figure 4.15 k**. It shows good sintering of pellet at sintering temperature of 1000°C. Further increasing the sintering temperature to 1050°C results in rapid grain growth with large number of closed porosity (**Figure 4.15 l**). The microstructural evolution as a function of sintering temperature is consistent with the densification curve of

Li_2ZrO_3 pellet (**Figure 4.14**). The densification mechanism dominates grain growth at the sintering temperature of 1000°C, which results in microstructure with high relative density and small grain size (**Figure 4.15 k**). At sintering temperature of higher than 1000°C, the grain growth mechanism dominates the densification process leading to coarse-grained microstructure (**Figure 4.15 l**) with no significant improvement in the relative density of the pellet (**Figure 4.14**).

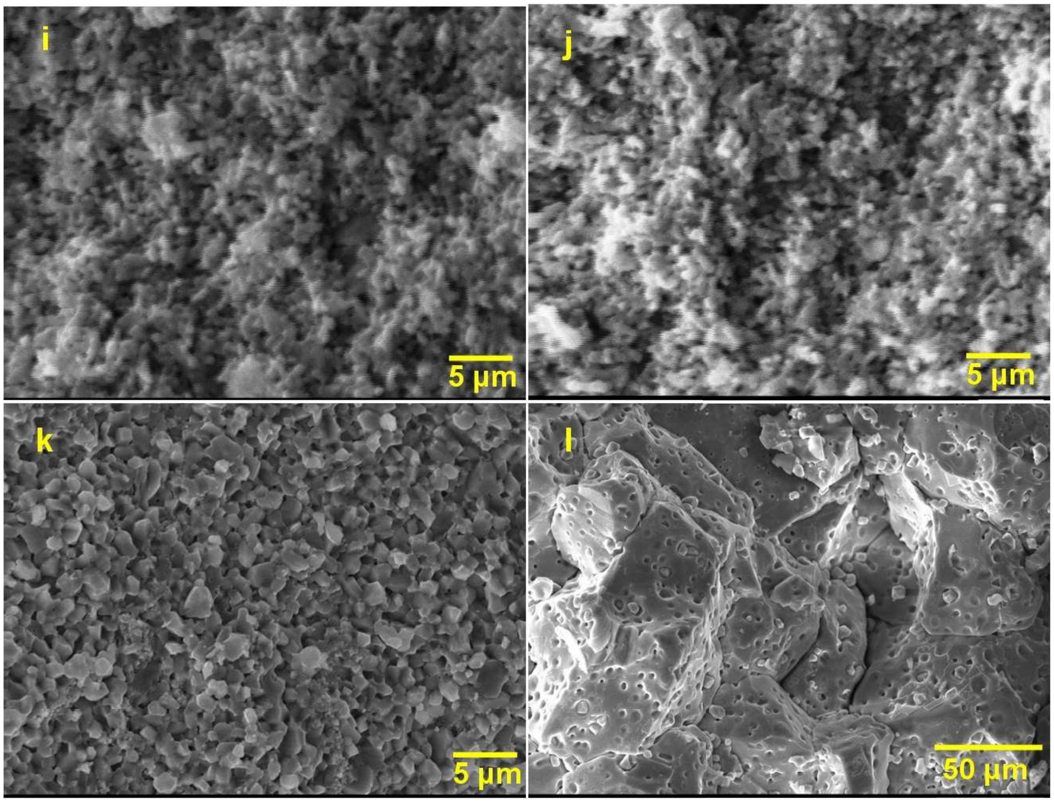

Figure 4.15 SEM images of fractured surface of Li_2ZrO_3 sintered at i) 900°C j) 950°C k) 1000°C and l) 1050°C

4.3.6 Post sintering characterizations of Li_2ZrO_3

The chemical analysis of sintered Li_2ZrO_3 pellets was carried out following the procedure already described in the Section 4.3.4 to determine the Li/Zr mole ratio. In Li_2ZrO_3 pellets sintered at 900-1100°C for 2 h duration, the estimated mean Li/Zr mole ratio (1.975 ± 0.006) is consistent with the stoichiometric ratio (i.e. 2). It confirms that no evaporative loss of Li took place during sintering of the Li_2ZrO_3 pellets. The XRD patterns of sintered Li_2ZrO_3 at different sintering temperatures is shown in **Figure 4.16**. The XRD pattern remains unchanged after the sintering except modest variation in relative peak intensities. The variation of peak intensity might be due to improved crystallinity at higher sintering temperatures.

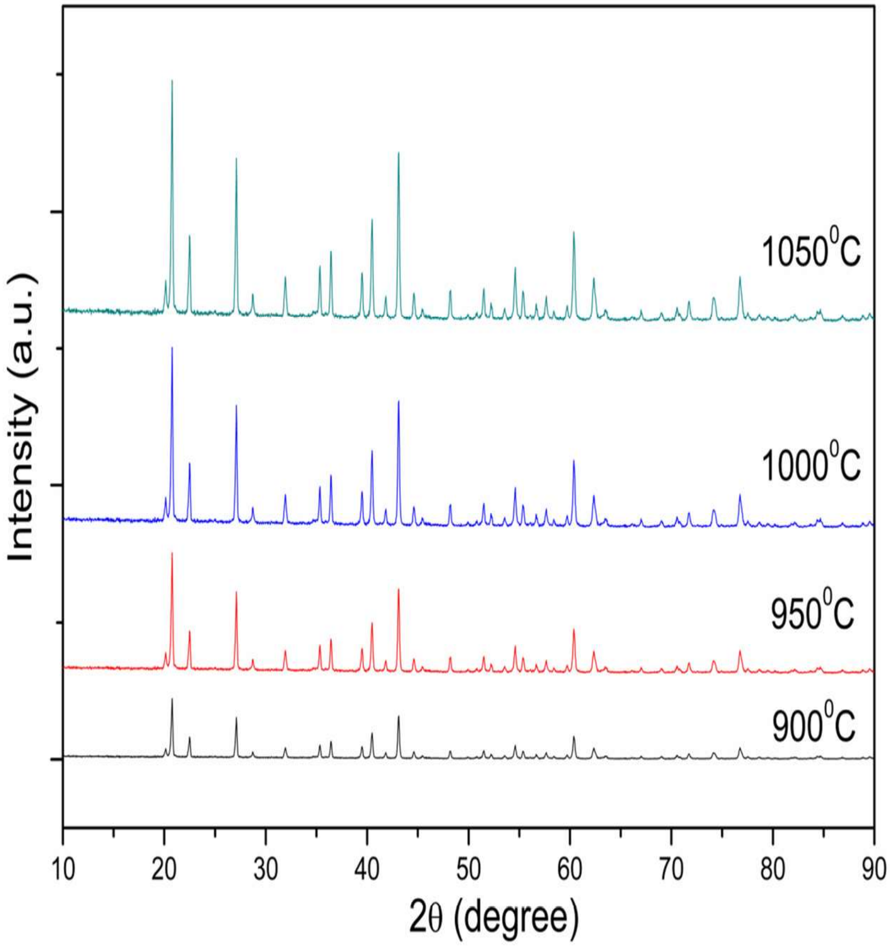

Figure 4.16 XRD patterns of Li_2ZrO_3 pellets after sintering

4.4 Summary

In this chapter the solution combustion synthesis of nanocrystalline Li_2ZrO_3 powders using glycine as fuel was accomplished. The fuel-to-oxidizer ratio (φ) significantly affected the mode of combustion, phase composition, and microstructure of Li_2ZrO_3 powders. The Thermochemical analysis of combustion reactions demonstrated that adiabatic temperature and the volume of gases increases with φ. However, the actual reaction temperature decreases with increasing φ due to the fast dissipation of heat by the evolving gases. Moreover, the mode of combustion switches from VCS to SHS-volcanic eruption at higher φ. The as-synthesized powders (directly from the combustion reaction) are comprised of minor quantity of metastable tetragonal phase along with the stable monoclinic phase of Li_2ZrO_3, irrespective of the fuel-to-oxidizer ratios. However, pure monoclinic Li_2ZrO_3 with good crystallinity was obtained after calcination of the powders at temperature of 800ºC. The crystallite size of Li_2ZrO_3 is in the range of 18-40 nm depending on φ. The agglomeration of Li_2ZrO_3 powders results in considerably large particle size than the crystallite size. Powder morphology comprised of micrometric agglomerated irregular flake shape particles. In Li_2ZrO_3 powders, the residual Li_2O was determined to be in the range 155-469 µg/g. The Li_2ZrO_3 pellets demonstrated excellent sinterability. The pellets achieved a relative sintered density of about 90% at sintering temperature of as low as 950°C. Nearly full densification of pellets is achieved at sintering temperature of 1000°C with small grain size (1-2µm). The higher sintering temperature (1050°C) results in rapid grain growth with large number of closed pores.

The present work establishes that solution combustion synthesis is an efficient method to produce fine Li_2ZrO_3 powder with excellent sinterability which will facilitate circumventing the critical issues such as Li-evaporation and grain growth. Another Li-based ceramic, $LiAlO_2$, owing to excellent structural and mechanical stability, can be capable of reliably withstanding severe operational conditions. Therefore, $LiAlO_2$ might be a favourable material of choice for tritium breeder application in high power commercial fusion reactors. Additionally, due to these favourable properties, $LiAlO_2$ is a leading ceramic material for application in commercial light water reactor as tritium-producing burnable absorber rods (TPBARs). The sinterability enhancement of $LiAlO_2$ powder can be very useful to produce sintered $LiAlO_2$ ceramic components with desired densification and microstructure for these applications.

In view of this, study on synthesis of fine $LiAlO_2$ powder with improved sinterability has been undertaken in this thesis which will be presented in the next chapter.

Chapter 5

Synthesis, characterization, and sinterability of $LiAlO_2$

The work reported in this chapter has been communicated as follows:

Novel mixed fuel solution combustion synthesis of γ-$LiAlO_2$: effect of fuel ratio on phase, microstructure and sintering

Biranchi M. Tripathi, P. K Patro, T. Mohanty, Deep Prakash, A. K. Tyagi, P. K. Sinha,

Ceram. Int.

5.1 Introduction

Main interest in lithium aluminate ($LiAlO_2$) is due to its numerous practical applications: as a coating material for Li lithium-conducting electrodes, as an additive in composite Li electrolytes, as a template for epitaxial growth of III−V semiconductors, as a membrane material for molten-carbonate fuel cells and as a candidate material for tritium breeder or fusion reactors [183–194]. Although six polymorphs of $LiAlO_2$ have been announced so far, however, only three modifications which are referred to in the literature as α-phase, β-phase, and γ-phase have been synthesized and their structures have been thoroughly established using diffraction technique [188,195–204]. The α-$LiAlO_2$ has a hexagonal structure. The density of α-phase (3.401 g cm^{-3}) is the highest among the three phases. Therefore, this phase is the most stable at high pressure [200,205]. The β-$LiAlO_2$ has an orthorhombic crystal structure with density of 2.61 g cm^{-3} [196]. The γ-$LiAlO_2$ is preferred for various applications because it is the most stable phase among all polymorphs, under ambient conditions. Therefore, α-$LiAlO_2$ and β-$LiAlO_2$ phases transform into γ-$LiAlO_2$ at temperature above 750°C [196]. The γ-$LiAlO_2$ has a tetragonal crystal structure with the space group $P4_12_12$ (No.92), Z=4, and the lattice parameters: a = 522.4 pm, and c = 629.7 pm [196]. The phase diagram of Li_2O-Al_2O_3 system is shown in **Figure 5.1** [169]. γ-$LiAlO_2$ has excellent chemical, structural and mechanical stability against intense thermal and radiation (neutron and gamma) field in fusion reactor environment as well as good tritium breeding performance which makes it one of the most promising tritium breeder ceramic especially for off-line tritium breeding application [172,206–211]. For tritium breeding purpose, sintered γ-$LiAlO_2$ compact (pellet or pebble) is preferred. It is well documented that density and microstructure of sintered lithium ceramics are important parameters that have great influence on diffusivity and release process of bred tritium from crystal grain.

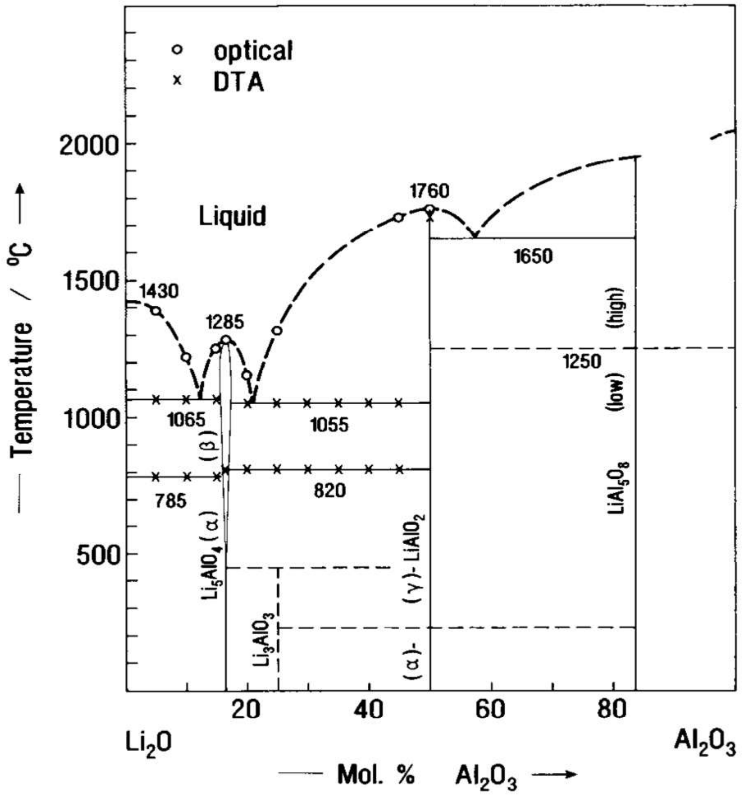

Figure 5.1 Phase diagram of Li_2O-Al_2O_3 system [169] (Reproduced with the permission from Elsevier)

Furthermore, it was found that tritium release rate from lithium ceramics with small grain size was much faster than that of ceramics with large grain size and with same open porosity. It was also observed that lithium ceramics with relative sintered density in the range of 85-90% exhibited optimal thermo-physical and mechanical properties. Fabricating lithium ceramics compliant with these physical and microstructural properties is quite challenging. This is primarily because lithium ceramics inherit poor sinterability and are prone to Li-sublimation and rapid grain growth when subjected to high temperature either during powder preparation or sintering. Recently, synthesis of nanocrystalline lithium ceramic powders have drawn much attention which can enable to sinter these ceramics possibly at low temperature and in short time duration and thereby overcome these problems. The reduction of sintering temperature and time will facilitate the fabrication of lithium ceramic components with optimal densification and fine-grained microstructure.

Early methods of γ-$LiAlO_2$ powder preparation are mainly based on solid state reaction between alumina (Al_2O_3) and lithium-containing compounds such as lithium carbonate (Li_2CO_3), lithium hydroxide (LiOH), lithium oxide (Li_2O) etc [111,193,207–220]. This method involves multiple cycles of high temperature calcination (>1000°C) for several hours and intermittent grinding of powder which often results hard agglomerated and bigger size particles. Meanwhile, Li sublimation due to high-temperature calcination and also contamination of powder with grinding media cannot be avoided. Therefore, phase pure γ-$LiAlO_2$ powder with controlled particle size is difficult to synthesize. These factors collectively lead to poor sinterability of synthesized powder and thereby put serious limitations on fabrication of γ-$LiAlO_2$ tritium breeder material with optimal densification and small grain size. The present-day methods of preparing γ-$LiAlO_2$ powder mainly include wet chemical methods such as alkoxide hydrolysis, co-precipitation, sol–gel, spray drying and hydrothermal process [221–228]. Although fine (sub-micron to nanoscale) γ-$LiAlO_2$ powders with enhanced sinterability were prepared by these methods, however, these methods involve sophisticated techniques, time consuming procedures and costly organometallic precursors which are not cost effective and deterrent to reproducibility and reliability of the final powder.

Solution combustion synthesis (SCS) is an innovative and promising method for preparation of sub-micron to nanoscale ceramic powder. It is very rapid chemical process which relies on highly exothermic redox reaction between metal nitrates and organic fuel. Initially combustion reaction is ignited by heating mixed nitrate and fuel solution at relatively low temperatures and afterwards it evolves in self-propagated manner to yield the desired product. For instance, fine Li_2TiO_3 and Li_2ZrO_3 powders were prepared by SCS method using citric acid and glycine as fuels respectively and desired nitrates as oxidizing agents. These powders exhibited very good sinterability. However, systematic study on preparation of γ-$LiAlO_2$ powders by SCS method and its sintering behaviour has been seldom reported.

This chapter focuses on a novel mixed fuel vis-à-vis conventional single fuel solution combustion synthesis of nanocrystalline γ-$LiAlO_2$ powders utilizing citric acid and glycine as organic fuel. The outstanding benefits of mixed fuel SCS approach over conventional single fuel approach as well as other synthesis methods are discussed in relation to powder properties, sintering behaviour, microstructure and thermochemical aspects.

5.2 Experimental procedure

5.2.1 Synthesis of $LiAlO_2$ powders

Lithium nitrate: $LiNO_3$ (purity: AR grade, Prabhat Chemicals Private Limited, India), aluminium nitrate nonahydrate: $Al(NO_3)_3.9H_2O$ (purity: AR grade, Sigma-Aldrich, India) were used as precursors for the synthesis of lithium aluminate ($LiAlO_2$). Glycine (purity: AR grade, Prabhat Chemicals Private Limited, India) and citric acid (purity: AR grade, Sigma-Aldrich, India) were exploited as fuels. All reagents were used as received without further purifications. The stock solutions were prepared by dissolving $LiNO_3$ and $Al(NO_3)_3$ in deionised water. Required volume of the stock solutions were taken in the stoichiometric proportion and thoroughly-mixed. The SCS reaction mixtures were prepared by separately adding glycine and citric acid in the mixed nitrate solution. The fuel compositions i.e. ratio of citric acid-to-glycine ratios were varied while maintaining stoichiometric O/F ratio. The studied fuel compositions are given in **Table 5.1**.

Table 5.1 Fuel compositions of different combustion reactions

Combustion reaction	**Fuel composition (mol %)**	
	Citric acid	Glycine
R1	100	0
R2	50	50
R3	40	60
R4	30	70
R5	20	80
R6	10	90
R7	0	100

Resulting transparent solution was transferred to a preheated hot plate at 90°C and dried until most of the water was evaporated and a viscous gel was formed. At this point, the temperature of the hot plate was increased to ~200°C and within a few minutes combustion was ignited and self-propagated until completion. The K-type thermocouple was appropriately placed for temperature measurement of combustion reactions. A friable and voluminous powder was obtained at the end of combustion reaction. The time elapsed from ignition until the end of combustion reaction was carefully noted. For calcination, the as-synthesized powders were transferred into muffle furnaces (Nabertherm, Germany) and heated in temperature range 550-700°C in a static air environment so as to augment the phase formation and remove residual carbonaceous materials. The process flow sheet of synthesis is outlined in **Figure 5.2**.

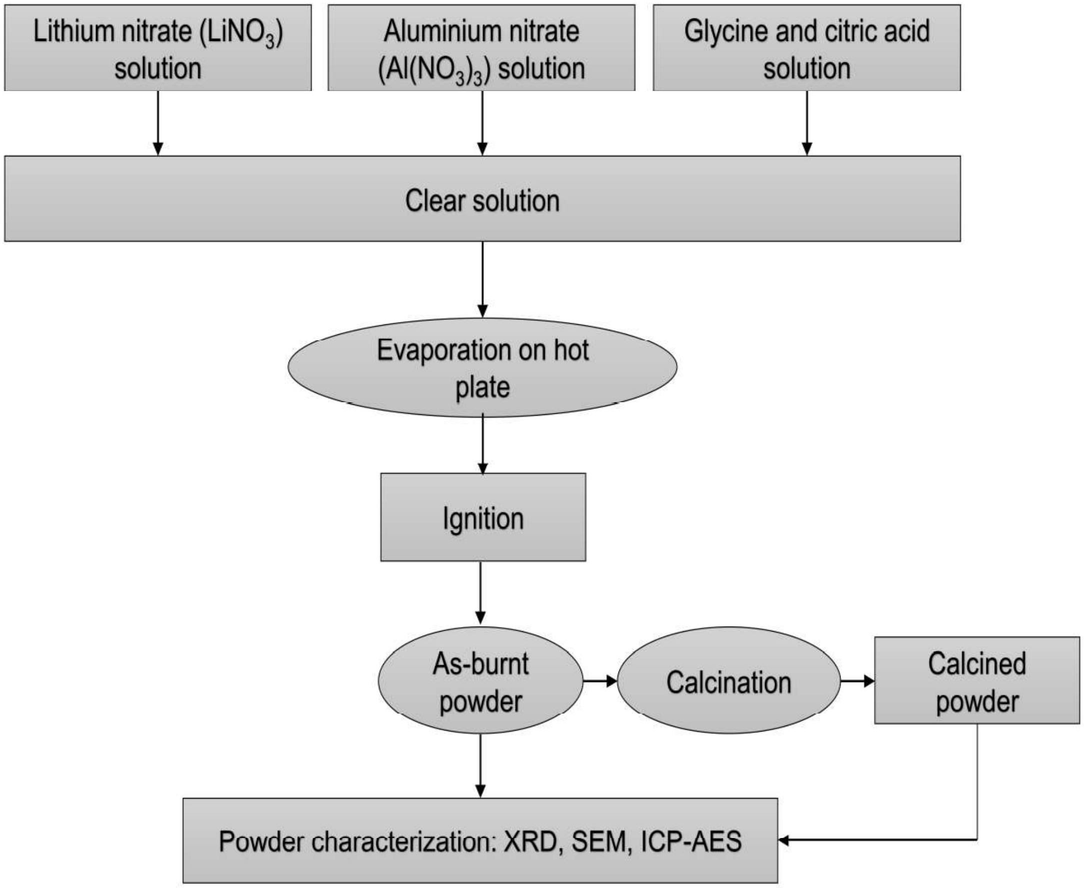

Figure 5.2 $LiAlO_2$ powder synthesis process flow sheet

5.2.2 Compaction and sintering of γ-$LiAlO_2$ powders

Compaction of γ-$LiAlO_2$ powder, to prepare pellet shaped green compacts, was performed by a uniaxial hydraulic press without use of binder. The consolidation and sintering process flow sheet is presented in **Figure 5.3**. The sintering behaviour of γ-$LiAlO_2$ pellets was studied under both, non-isothermal and isothermal conditions. Non-isothermal sintering study was conducted by preparing γ-$LiAlO_2$ pellets of the required size i.e. 8 mm diameter and around 4 mm height and measuring geometrical shrinkage of these pellets up to 1200°C under a given temperature ramp (5 and 10°C/min) in flowing air using TMA. For performing isothermal sintering experiments, the pellets of dimensions 10mm diameter and 2-3mm thickness were prepared in similar manner and these pellets were sintered in a Muffle Furnace (Nabertherm, Germany) at fixed temperatures ranging from 800-1100°C with heating rate of 10°C/min and constant dwell time (2h) in static air.

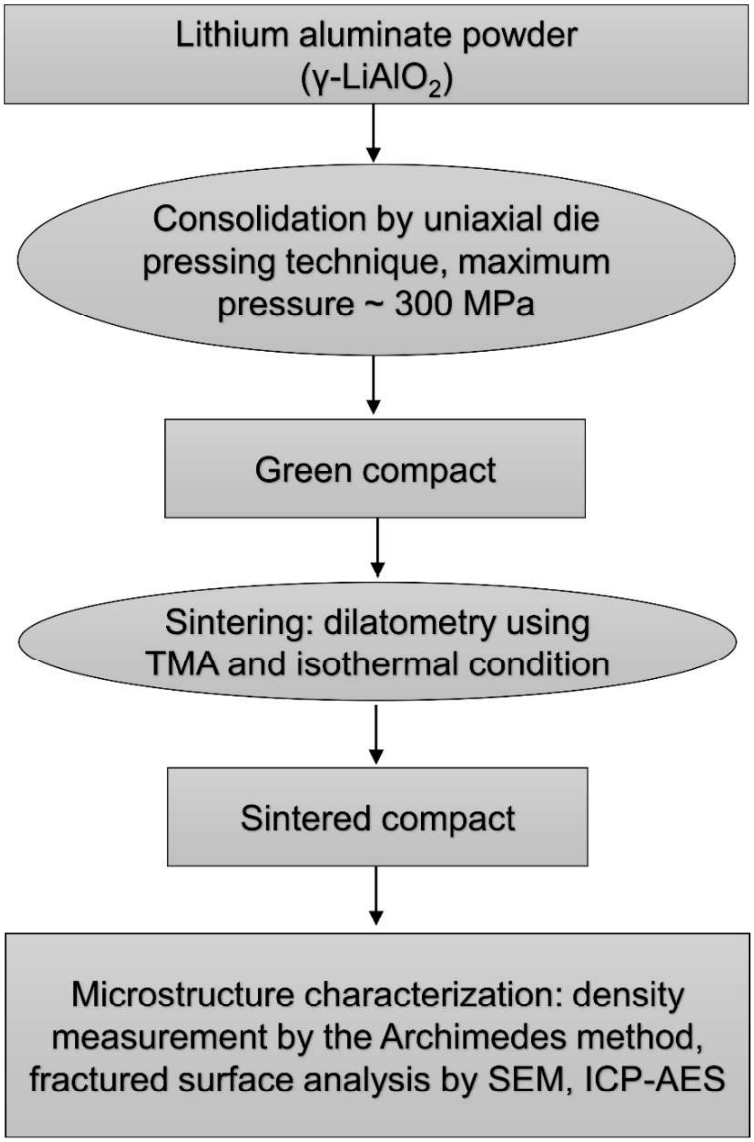

Figure 5.3 $LiAlO_2$ powder consolidation and sintering process flow sheet

5.2.3 Characterization

Powder XRD patterns of $LiAlO_2$ were recorded on a diffractometer (Proto AXRD, Canada) using Cu-Kα radiation (λ=1.54056 Å) as X-ray source.

A scanning electron microscope (SEM, Carl Zeiss, Germany), operating at 20kV accelerating voltage was used to study morphology of powder samples and microstructure of sintered pellets. The powder samples and pellets were sputter-coated with gold to prevent charging due to lack of electrical conductivity of the samples.

The density of sintered $LiAlO_2$ pellets was measured at room temperature by Archimedes' method. The volumetric shrinkage of pellets was calculated by measuring change in dimensions of the pellet before and after sintering.

5.3 Results and discussion

5.3.1 Thermochemical analysis and mode of combustion

The fuel composition was varied according to the plan given in **Table 5.1**. The fuel composition was varied such that stoichiometric value of fuel-to-oxidant ratio was maintained for all fuel compositions (equivalence ratio = 1). The equivalence ratio was derived from total oxidizing and reducing valency of reactants invoking basic principal of propellant chemistry. The combustion reaction corresponding to each fuel composition can be expressed as:

$$LiNO_3(aq.) + Al(NO_3)_3.9H_2O\ (aq.) + (10/9)\ C_6H_8O_7(aq.)$$
$$= LiAlO_2(s) + (60/9)\ CO_2(g) + 2N_2(g) + (94/9)\ H_2O(g) \qquad (R1)$$

$$LiNO_3(aq.) + Al(NO_3)_3.9H_2O(aq.) + (20/27)\ C_6H_8O_7(aq.) + (20/27)\ C_2H_5NO_2(aq.)$$
$$= LiAlO_2(s) + (160/27)\ CO_2(g) + (64/27)\ N_2(g) + (292/27)\ H_2O(g) \qquad (R2)$$

$LiNO_3$ + $Al(NO_3)_3.9H_2O$(aq.) + (80/126) $C_6H_8O_7$(aq.) + (120/126) $C_2H_5NO_2$(aq.)
= $LiAlO_2$(s) + (720/126) CO_2(g) + (312/126) N_2(g) + (1376/126) H_2O(g) (R3)

$LiNO_3$ + $Al(NO_3)_3.9H_2O$(aq.) + (60/117) $C_6H_8O_7$(aq.) + (140/117) $C_2H_5NO_2$(aq.)
= $LiAlO_2$(s) + (640/117) CO_2(g) + (304/117) N_2(g) + (1292/117) H_2O(g) (R4)

$LiNO_3$(aq.) + $Al(NO_3)_3.9H_2O$(aq.) + (10/27) $C_6H_8O_7$(aq.) + (40/27) $C_2H_5NO_2$(aq.)
= $LiAlO_2$(s) + (140/27) CO_2(g) + (74/27) N_2(g) + (302/27) H_2O(g) (R5)

$LiNO_3$(aq.) + $Al(NO_3)_3.9H_2O$(aq.) + (20/99) $C_6H_8O_7$(aq.) + (180/99) $C_2H_5NO_2$(aq.)
= $LiAlO_2$(s) + (480/99) CO_2(g) + (288/99) N_2(g) + (1124/99) H_2O(g) (R6)

$LiNO_3$(aq.) + $Al(NO_3)_3.9H_2O$(aq.) + (20/9) $C_2H_5NO_2$(aq.)
= $LiAlO_2$(s) + (40/9) CO_2(g) + (28/9) N_2(g) + (104/9) H_2O(g) (R7)

In the above reactions, R1 and R7 represent single fuel condition containing citric acid and glycine as fuels respectively. The reactions R2-R6 represent mixed fuel (citric acid + glycine) conditions with different fuel composition as given in **Table 5.1**. Since stoichiometric fuel-to-oxidizer ratio was maintained for all reactions (R1-R7), therefore for thermochemical calculations, it was assumed that fuels were completely oxidized without need of atmospheric oxygen. The standard thermodynamic data available in literature were used for all thermochemical calculations. The standard Gibbs free energy, standard enthalpy and adiabatic temperature of combustion reactions (R1-R7) were calculated according to the following thermochemical relations:

$$\Delta_r H^0_{298} = \sum n(\Delta_f H^0_{298})_{product} - \sum n(\Delta_f H^0_{298})_{reactant}$$

$$\Delta_r H^0_{298} = \int_{298}^{T_{ad}} \sum (n\ c_p)_{products}\ dT$$

$$\Delta_r G^0_{298} = \Delta_r H^0_{298} - T\ \Delta_r S^0_{298}$$

where, $\Delta_r G^0_{298}$, $\Delta_r H^0_{298}$, $\Delta_r S^0_{298}$ c_p, T_{ad} and n are the standard Gibbs free energy of reaction, standard enthalpy of reaction, standard entropy of reaction, the heat capacity at constant pressure, the adiabatic temperature and number of moles respectively. For calculation of theoretical adiabatic temperature, it was assumed that all reactions (R1-R7) were complete, the left-over fuels were oxidized by atmospheric oxygen and exothermic heat of reaction is not dissipated either by conduction, convection or radiation.

The effect of fuel composition on the standard Gibbs free energy and enthalpy of reactions is depicted in **Figure 5.4**. It was observed that, the Gibbs free energy and enthalpy of each reaction (R1-R7) are highly negative which indicates that combustion reactions for selected range of fuel composition are thermodynamically feasible and highly exothermic in nature. The highest exothermic heat (-1290 kJ/mol) was observed for reaction R1 in case of single fuel citric acid and the lowest (-1228 kJ/mol) observed for reaction R7 in case of single glycine fuel (**Figure 5.4)**. In case of mixed fuel compositions i.e. for reactions R2-R6, an intermediate value of exothermic heat was observed. **Figure 5.4** shows that on successive addition of glycine in compensation of citric acid, the exothermic heat was gradually decreased which is an obvious trend because as discussed above, combustion enthalpy of glycine (reaction R7) is lower than that of citric acid (reaction R1).

The adiabatic reaction temperature was calculated from enthalpy of reaction using the above thermochemical relation and also, the actual reaction temperature was measured according to the procedure given in the Section 5.2.1.

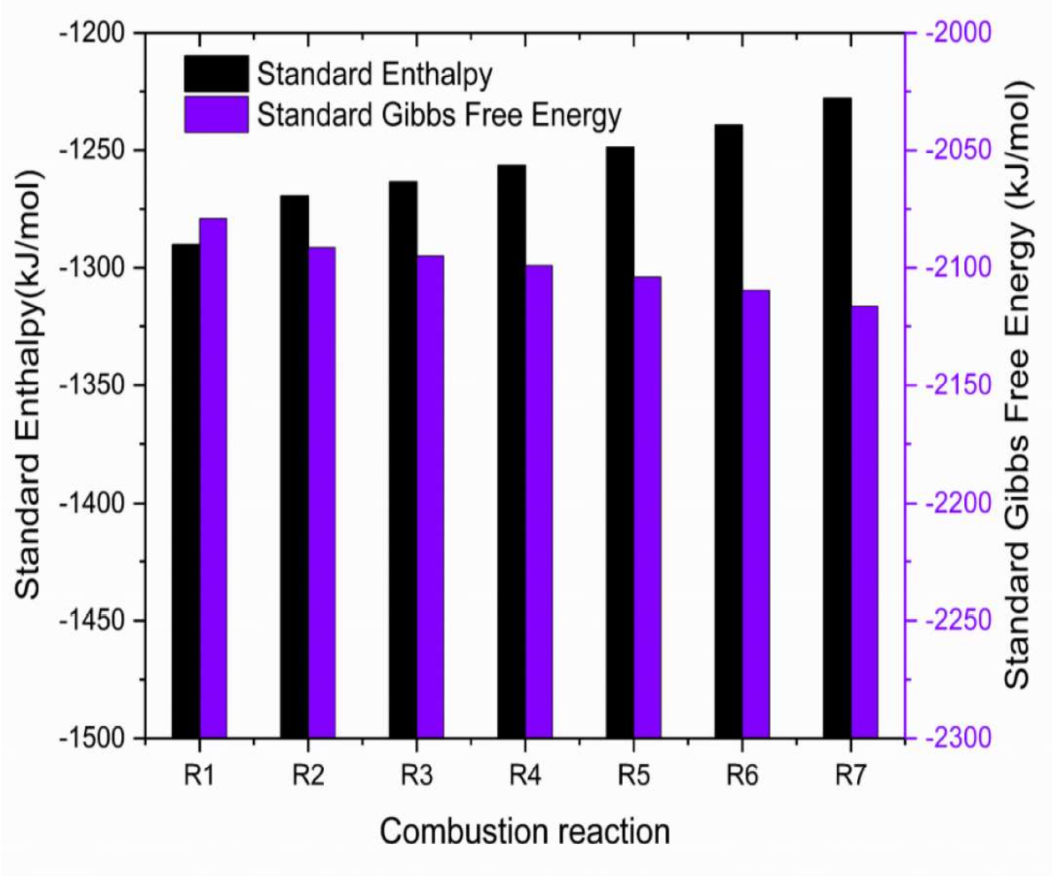

Figure 5.4 Effect of fuel composition on standard enthalpy and the Gibbs free energy of reaction

A comparison of adiabatic and actual temperature for different combustion reactions is shown in **Figure 5.5**. Evidently, due to the compensation effect, there is no significant variation in the adiabatic temperature of the combustion reactions with different fuel compositions. Interestingly, the actual reaction temperature was observed much lower than the adiabatic temperature for every reaction (R1-R7). Moreover, the actual temperature was found to increase on successive addition of glycine in place of citric acid. This is because the amine functional group in glycine not only facilitate the complex formation with metal cation but also decomposes at higher temperature to release ammonia gas (NH_3). The redox reaction between $NH_3(g)$ and oxides of nitrogen (NO_x) releases exothermic heat which increases the measured temperature and as the fraction of glycine increases the measured temperature also increases which facilitate the formation of the crystalline γ-$LiAlO_2$ powder. The redox reaction can be expressed as follows:

$$4xNH_3(g) + 10NO_x(g) = (5+2x)\ N_2(g) + 6x\ H_2O(g) + 2x\ O_2(g)$$

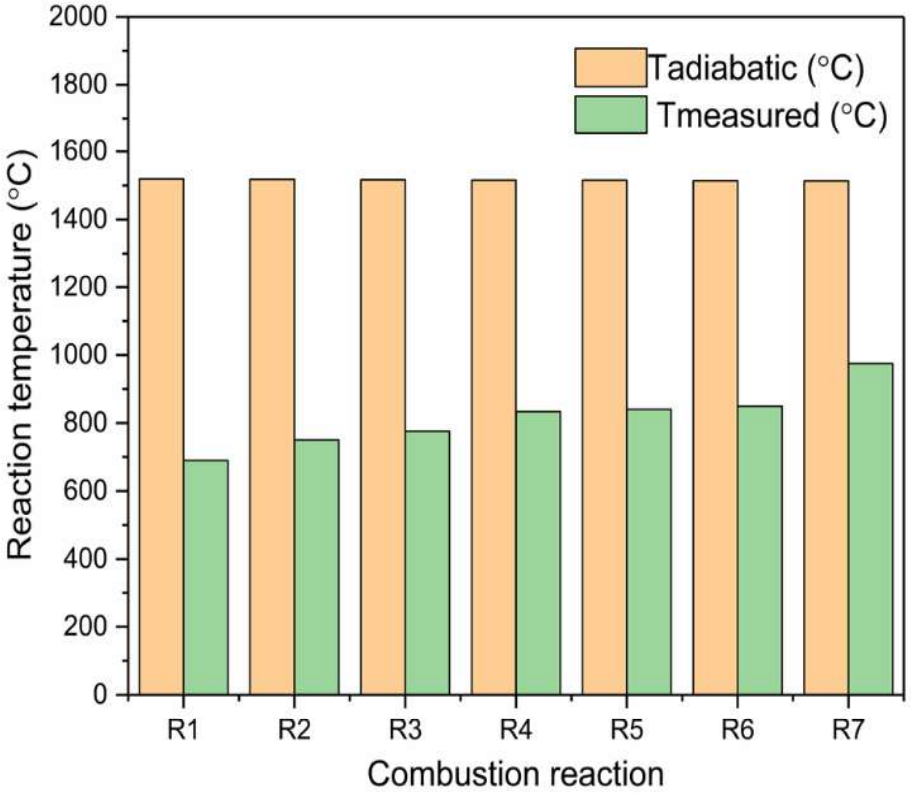

Figure 5.5 Effect of fuel composition on calculated adiabatic and measured reaction temperature

From the thermodynamics point of view, the above reactions are highly exothermic. Difference between calculated adiabatic and actual reaction temperature has been commonly observed in solution combustion synthesis which has been attributed to convective dissipation of heat caused by large amount of releasing gases in combustion process that affect the temperature to a large extent. In present case, since stoichiometric fuel-to-oxidizer ratio was maintained, the total moles of gases released in each reaction (R1-R7) remain same. However, the number of moles of individual gases (H_2O, CO_2 and N_2) differ for each reaction (R1-R7) as shown in **Figure 5.6**. Since the convective heat transfer also depend on physical properties of gases, therefore it can be anticipated quite reasonably that this factor causes variation in actual temperature with fuel composition (**Figure 5.5**).

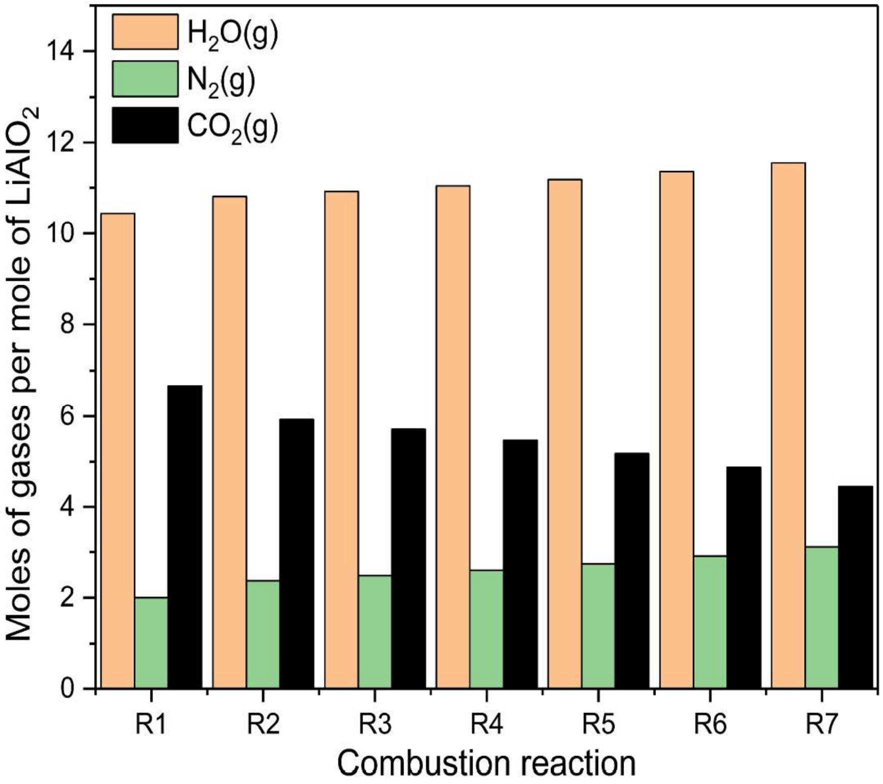

Figure 5.6 Effect of fuel composition on moles of gases released

Moreover, the gap between adiabatic and actual temperature is quite large (**Figure 5.5**). This tendency can not be solely designated to amount and physical properties of gases released during the reaction but also to the switch in mode of combustion reaction in relation to fuel composition which affect flow pattern of gases and thereby convective heat dissipation process. The mode of combustion was visually observed for each reaction (R1-R7) and results are summarized in **Table 5.2**. In case of citric acid as single fuel (reaction R1), volume combustion mode of combustion (VCS) was realized with slow smoldering of reaction mixture for longer duration (30s).

Table 5.2 Mode of combustion reaction at different fuel compositions

Combustion reaction	Mode of combustion	Duration of combustion (s)	Colour of powder
R1	VCS-Smoldering	30	Black
R2	VCS	20	Black
R3	VCS	15	Black
R4	VCS	12	Black
R5	SHS-controlled	10	Black
R6	SHS-eruption	5	Black
R7	SHS-eruption	<5	White

Proper combustion of citric acid was not observed, which may be due to early thermal decomposition of nitrates prior to participation in combustion process as a result the reaction mixture becomes fuel-rich and combustion of excess fuel (citric acid) requires O_2(g) from the atmosphere. However, combustion of excess citric acid did not complete due to slow diffusion of O_2(g) in reagent mass. Instead, excess citric acid thermally decomposed as follows:

$$C_6H_8O_7(s) = 4H_2O(g) + 6C(s) + 1.5O_2(g)$$

Thermodynamic calculation showed that above reaction is feasible when temperature exceeds 506°C which is much lower than the adiabatic temperature of reaction R1. The carbonization of citric acid (reaction R9) further decreases the combustion temperature. The carbonization of citric acid was also reported in combustion synthesis of Li_2TiO_3 using citric acid as fuel. In case of mixed fuels (R2-R4), the combustion reactions switch to rapid volume combustion (VCS) mode and also due to less fraction of citric acid (**Table 5.2**), rise in measured reaction temperature was observed (**Figure 5.5**). As citric acid content in the mixed fuel was further decreased in case of R5 and R6, the combustion switches to very fast self-propagating mode which is often associated with higher reaction temperature. The combustion reaction with fuel composition equal to 100% glycine (R7) proceeds via violent SHS-eruption mode (**Table 5.2**) with highest measured temperature (**Figure 5.5**) and combustion was seized in <5s (Table 2). The carbonization of citric acid yields free carbon which imparts black colour to powders synthesized from combustion reactions R1-R6 as evident from **Table 5.2**. The reaction R7 with single fuel glycine yielded white colour powder (**Table 5.2**) because unlike citric acid, glycine did not carbonize and also have highest measured temperature. This tendency has been reported in solution combustion synthesis of ceramic powder using glycine as fuel.

5.3.2 Analysis of phase formation

Powder XRD patterns of $LiAlO_2$ synthesized by combustion reactions with different fuel compositions (R1-R7) before calcination are shown in **Figure 5.7 a**. XRD pattern of $LiAlO_2$ powder synthesized via reaction R1 exhibits very low intensity broad peaks although some of the peak positions match with standard γ-$LiAlO_2$ phase. It indicates that γ-$LiAlO_2$ phase was not well crystallized via combustion with single citric acid fuel suggesting actual reaction temperature was not sufficient for crystallization of γ-$LiAlO_2$ phase. This result is consistent with observed lowest measured temperature of reaction R1 (**Figure 5.5**) as discussed in Section 5.3.1. Combustion reactions with mixed fuel (citric acid + glycine) compositions (R2-R6), due to higher reaction temperature (**Figure 5.5**), produced crystalline γ-$LiAlO_2$ phase as evident from sharp and good intensity XRD peaks with matching peak positions as depicted in **Figure 5.7 a**. XRD pattern shows that combustion reaction with single glycine fuel (R7), due to the highest reaction temperature also produced well crystalline γ-$LiAlO_2$ phase.

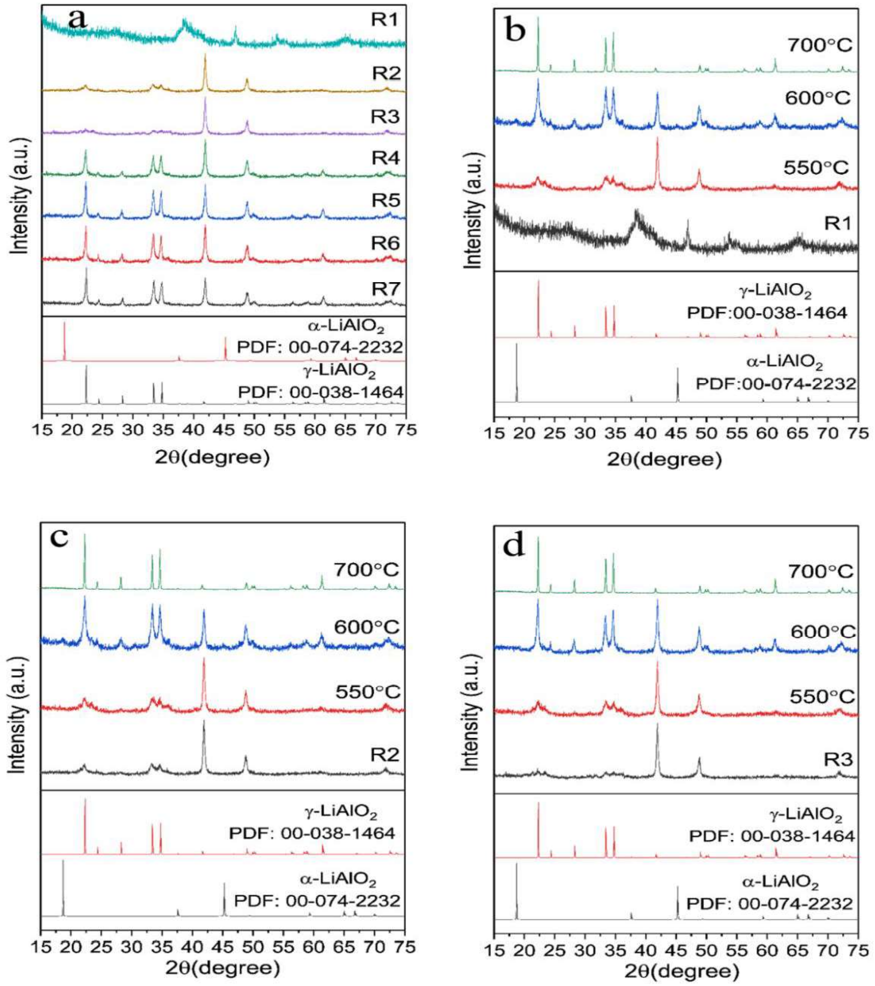

Figure 5.7 XRD pattern of $LiAlO_2$ powder synthesized using R1-R7 fuel compositions before calcination (a) and R1-R3 fuel compositions after calcination (b-d)

However, this reaction is extremely violent in nature which is difficult to control. Consequently, large quantity of powder is lost in stream of gases emanating from combustion reaction leading to very low yield of the product. On the other hand, it was observed that mixed fuel combustion reactions were moderate and controllable. The mixed fuel approach has definite advantage over single fuel as it produced well crystalline γ-$LiAlO_2$ phase without high temperature calcination and combustion reactions were controllable. This result is very interesting because many research on synthesis of $LiAlO_2$ indicated that γ-$LiAlO_2$ phase was obtained after high temperature (900-1000°C) calcination and before calcination often mixture of α, β and γ polymorphs of $LiAlO_2$ was obtained. Moreover, since with mixed fuel compositions, high temperature calcination is not needed for crystallization of γ-$LiAlO_2$ phase therefore, Li sublimation can be effectively avoided which is extremely important for tritium breeding purpose. It can be noticed in XRD pattern (**Figure 5.7 a**), one of the peak ($2\theta = 41.6°$) has abnormally high intensity in case of γ-$LiAlO_2$ synthesized via each mixed fuel reactions (R2-R6) as well as single glycine fuel, which indicates preferred growth of coherently diffracting crystallite domain in this direction instead of perfectly random orientation. The preferred growth may be due to formation of sterically constrained complex through bi-dentate chelation of metal ions via amino ($-NH_2$) and carboxylate (-COOH) groups of glycine which compels crystallite domain to grow in particular direction during crystallization of γ-$LiAlO_2$.

XRD patterns after calcination of γ-$LiAlO_2$ at different temperatures in the range 550-700°C are shown in **Figure 5.7 b-d** and **Figure 5.8 e-h**. Any significant modification was not detected in the XRD pattern after calcination at 550 and 600°C except minor variation in relative peak intensities for each fuel compositions. However, after calcination at 700°C sharp improvement in crystallinity of γ-$LiAlO_2$ powder was observed for each fuel composition. Unusual intensity of peak ($2\theta = 41.6°$) reverted back to normal as evident from

Figure 5.7 b-d and **Figure 5.8 e-h** which suggests that, the molecules of $LiAlO_2$ relaxed to equilibrium γ-crystal structure after annealing at 700°C through a thermally activated process.

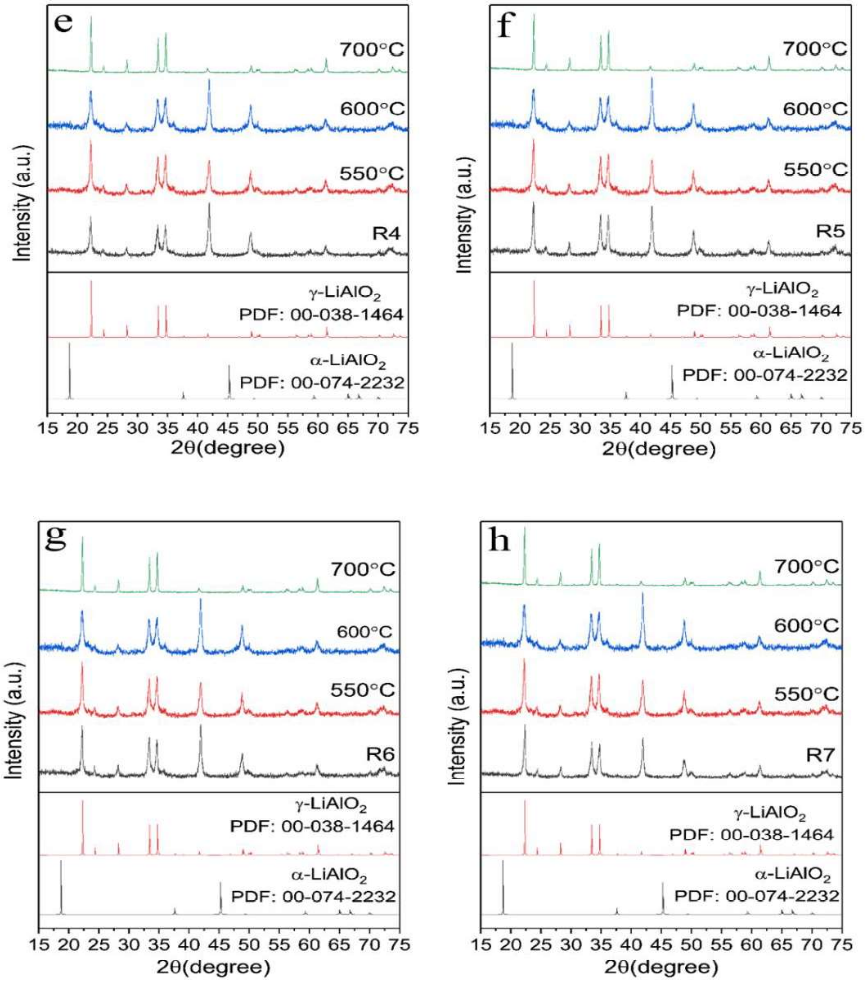

Figure 5.8 XRD pattern of $LiAlO_2$ powder synthesized using R4-R7 fuel composition after calcination (e-h)

Although, combustion reactions are highly exothermic (**Figure 5.4**), due to the short reaction time (<5-30s) (**Table 5.2**), the equilibrium γ-crystal structure of $LiAlO_2$ could not be formed by the reaction itself. Therefore, $LiAlO_2$ powder needed further annealing for extended period of time at appropriate temperature. Because of this reason, sometimes metastable phases have also been observed as impurity along with γ-phase in combustion synthesis of $LiAlO_2$

powders. However, in proposed method no impurity phases were observed. This indicates that exothermic heat of combustion reactions (R2-R7) was adequate for conversion of precursor into γ-$LiAlO_2$ phase.

5.3.3 Crystallite size analysis

The average crystallite size of $LiAlO_2$ was calculated from the XRD peak broadening (FWHM) using Scherrer's equation according to the detailed procedure described in Section 4.3.2 of the previous chapter. The mean crystallite sizes of synthesized $LiAlO_2$ before and after calcination in temperature range 550-700°C for different fuel compositions are given in **Table 5.3**. The mean crystallite sizes for uncalcined $LiAlO_2$ and after calcination at 550 and 600°C were found in narrow range of 17-27nm (**Table 5.3**). The mean crystallite size of γ-$LiAlO_2$ close to 49nm was observed after calcination at 700°C (**Table 5.3**).

Table 5.3 Mean crystallite size of γ-$LiAlO_2$

Combustion reaction	Mean crystallite size (nm)			
	Un-calcined	Calcined (550°C)	Calcined (600°)	Calcined (700°C)
R1	17.3	17.4	20.2	48.8
R2	18.4	18.6	21.6	48.9
R3	20.3	20.7	23.6	48.0
R4	22.2	22.8	24.3	48.3
R5	24.3	24.7	25.3	48.7
R6	24.8	25.3	26.2	49.0
R7	25.6	25.8	26.6	48.8

The comparison of crystallite sizes of uncalcined and calcined $LiAlO_2$ for different combustion reactions are shown in **Figure 5.9.** It is observed that crystallite size of $LiAlO_2$ after calcination at 550°C remained nearly unchanged and increased slightly after increasing the calcination temperature to 600°C. The crystallite size remarkably increased after calcination of $LiAlO_2$ at 700°C which indicates growth of crystallite through a thermally activated mechanism at this temperature.

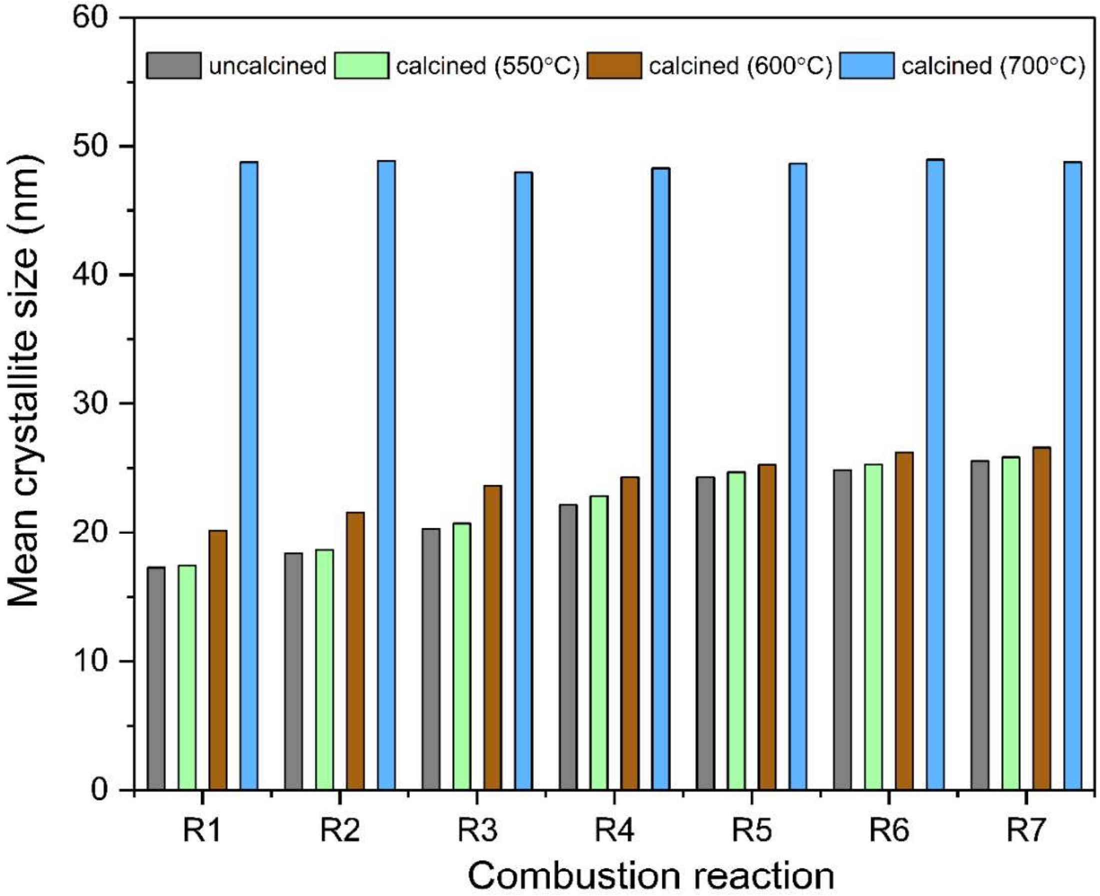

Figure 5.9 Effect of fuel composition and calcination temperature on crystallite size

5.3.4 Powder morphology

SEM images of $LiAlO_2$ particles synthesized by combustion reactions R1-R7 with different fuel compositions and after calcination at 700°C are depicted in **Figure 5.10**.

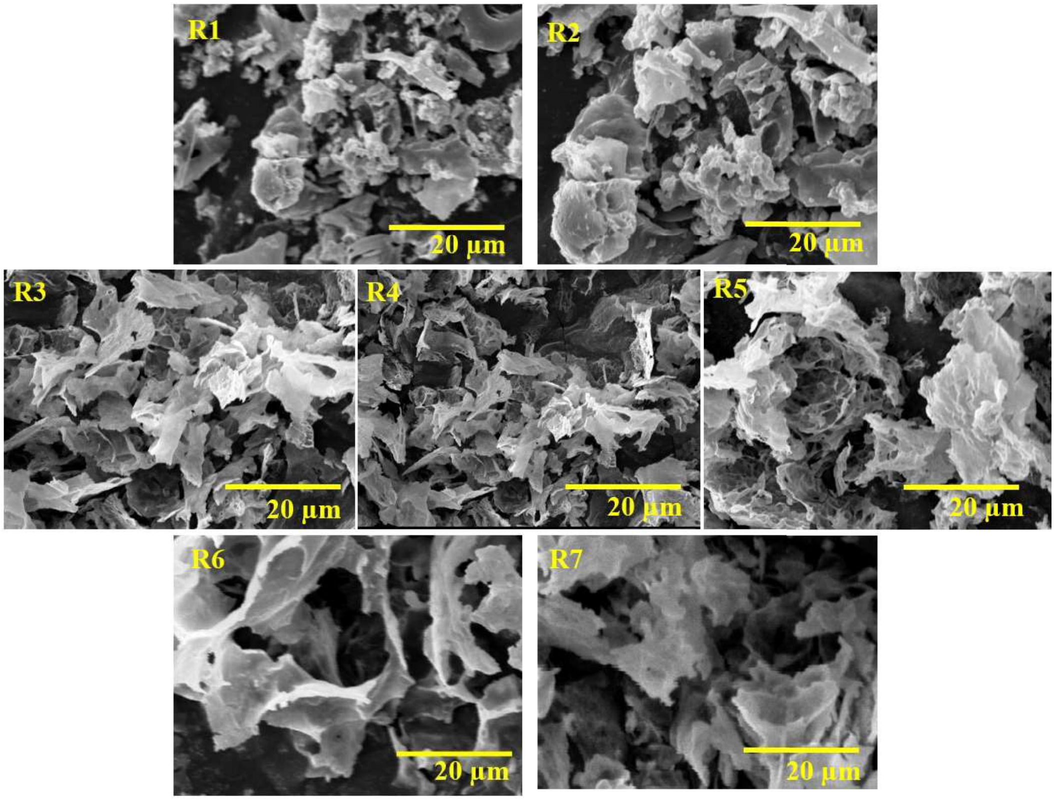

Figure 5.10 SEM images of $LiAlO_2$ powder synthesized using different fuel composition (R1-R7) after calcination at 700°C

$LiAlO_2$ powder consists of non-uniform size and irregular flake shape particles. Large variation in particle size (4-20µm) was observed as evident from **Figure 5.10**. This kind of powder morphology has been observed quite often in solution combustion synthesis of ceramic powder which is attributed to temperature difference arising either because of change in fuel composition or fuel-to-oxidizer ratio. In present case, difference in reaction temperature is caused by varying fuel composition (**Figure 5.5**). Moreover, poor thermal conductivity of $LiAlO_2$, short inter-particle connectivity and presence of voids develop temperature variation across different regions within the powder which contribute to morphological variations in $LiAlO_2$ powder. **Figure 5.10** demonstrate that powder is highly porous, voluminous in nature and large size gas channels are also visible in R6 and R7 due to release of large quantity of gases during the combustion process. Irrespective of fuel composition, the particle sizes were much larger than the crystallite size (**Figure 5.9**) estimated by XRD method indicating agglomeration of fine $LiAlO_2$ particles which can be assigned to large exothermic heat produced by combustion reactions as discussed in thermochemical analysis of combustion reactions. Although adiabatic temperature of combustion reactions (**Figure 5.5**) is very high, the reaction time is extremely short (**Table 5.2**) and heat is quickly dissipated via convective process by release of large quantity of gases (**Figure 5.6**), this allows only transient exposure of $LiAlO_2$ particles to high temperature. Consequently, soft agglomeration of $LiAlO_2$ particles is favoured over the formation of hard particle aggregates. The soft-agglomerated powder consists of large number of very fine $LiAlO_2$ primary particles as evident from **Figure 5.10**. It would be worth mentioning that in case of conventional solid-state-route, because of high temperature (> 1000°C) calcination, longer reaction time and modest gaseous release, often large size and hard-agglomerated $LiAlO_2$ powder was obtained. The large size and hard-agglomerated particles have deleterious effect on sinterability of powder. The soft-agglomerated particles of $LiAlO_2$ powder, due to very weak inter-particle bonding, can be easily disintegrated into primary particles with the help of pestle-mortar or mild ultra-sonication without need of high energy sophisticated milling and therefore do not deteriorate sinterability of powder.

5.3.5 Analysis of loss-on-ignition and Li/Al ratio

The γ-$LiAlO_2$ powders synthesized by combustion reactions with different fuel compositions (R1-R7) were subjected to loss-on-ignition test which determines content of total carbonaceous substances in powders. Carbon is considered an impurity of serious concern in nuclear materials due to activation problem. The test was carried out by heating the powders in temperature range 700-1000°C in steps of 100°C in a muffle furnace in air. The percentage loss-on-ignition was calculated from difference in weight of the samples measured before and after calcination. The percentage loss-on-ignition was observed constant in this temperature range which indicates that complete oxidation of the carbonaceous substances occurred at 700°C. However, percentage loss-on-ignition was found to vary with fuel composition as shown in **Figure 5.11**.

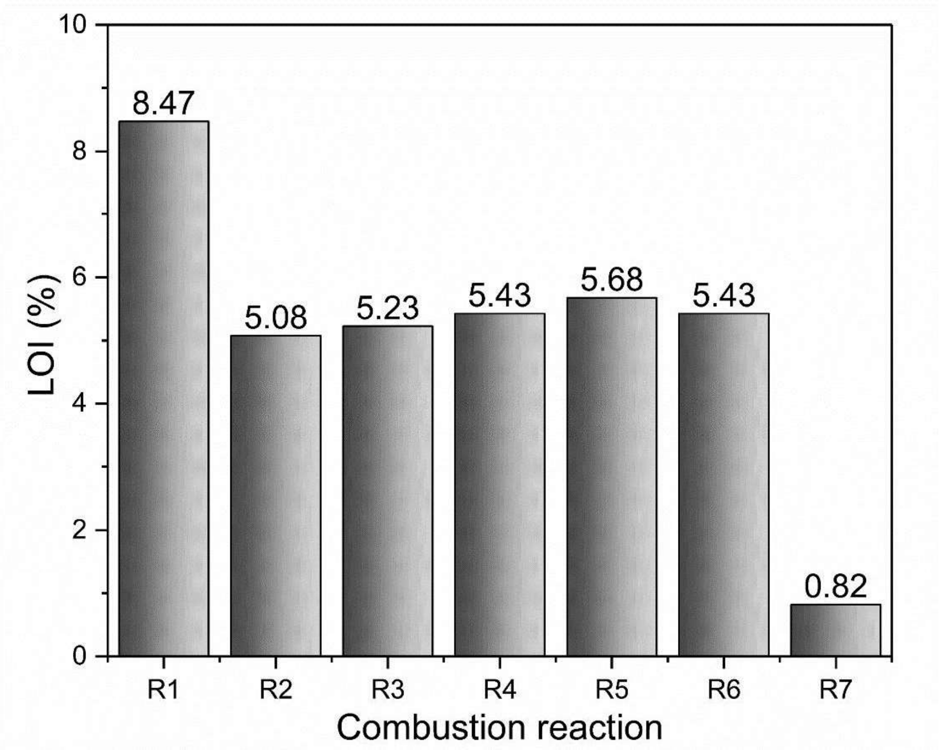

Figure 5.11 Loss on ignition (wt.%) from powder synthesized using different fuel compositions (R1-R7)

The highest percentage loss-on-ignition (8.47%) was observed in the sample synthesized with citric acid single fuel (R1) which is due to carbonization of citric acid and low combustion temperature (**Figure 5.5**) as evident from thermochemical analysis of the combustion reaction. Powder synthesized with glycine single fuel (R7), showed the lowest percentage loss-on-ignition (0.82%) which is due to high combustion temperature and also unlike citric acid, glycine does not carbonize yielding free carbon. In case of mixed fuel compositions (R2-R6), the percentage loss-on-ignition was observed in narrow range 5-6% which can be assigned to synergistic effect of reaction temperature and mode of combustion.

The Li/Al mole ratio in $LiAlO_2$ powder synthesized with different fuel compositions was determined after calcination at 1000°C by Inductively Coupled Plasma Atomic Emission Spectroscopy (ICP-AES). For chemical analysis, the sample was dissolved in aqua-regia. The Li/Al mole ratio was estimated equal to 0.987 ± 0.004 which is consistent with Li/Al mole ratio in stoichiometric $LiAlO_2$. It is evident from this result that Li sublimation did not occur during synthesis of $LiAlO_2$ powder by the employed method. It is to be noted that, despite highly exothermic combustion reaction (**Figure 5.4**), the Li sublimation is restrained due to transient reaction (**Table 5.2**) and fast convective dissipation of heat by large amount of evolving gases (**Figure 5.6**). It is worth mentioning that Li is source of tritium for fusion reactors and therefore its loss due to sublimation at high temperature is of serious concern in breeder materials development.

5.3.6 Sintering behavior of γ-$LiAlO_2$ powder

The representative dilatometry curve of γ-$LiAlO_2$ pellet (8mm diameter and 4mm thickness) at heating rates of 5 and 10°C/min up to 1200°C is shown in **Figure 5.12** which indicates percentage change in length of the pellet expressed as dL/L_0 (%) with increasing temperature where Lo is initial length. The pellet for dilatometry was fabricated using powder synthesized via combustion reaction with mixed fuel composition R4 (citric acid 30% + glycine 70%) after calcination at 700°C.

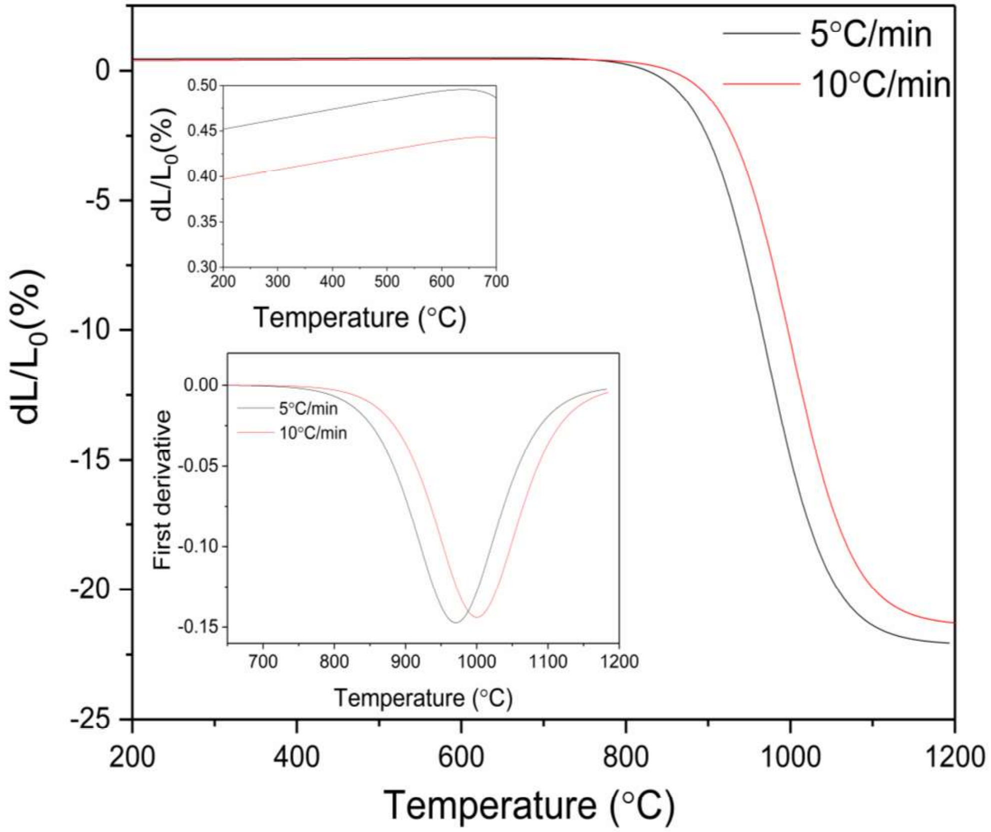

Figure 5.12 Dilatometry curve of $LiAlO_2$ pellet at heating rate of 5 and 10°C/min

Dilatometry curve shows three distinct steps of percentage change in length of the pellet. In the first step lying between 200-600°C, linear thermal expansion of pellet up to around 0.5% was observed as shown in enlarged inset graph which is attributed to intrinsic thermal expansion of γ-$LiAlO_2$. In the second step ranging from 700 to about 1000°C, large shrinkage up to 20% was noted. In this step, sintering mechanisms dominate over intrinsic thermal expansion, as a result pellet shrinks and densification takes place. Intense shrinkage observed in second step is consistent with large amount of porosity present in synthesized powder as evident from the powder morphology shown in SEM images (**Figure 5.10**). The onset of sintering step was observed at around 800°C as distinctly depicted in inset derivative plot (**Figure 5.12**) which suggests excellent sinterability of γ-$LiAlO_2$ powder synthesized by mixed fuel approach. Apparently, increasing the heating rate from 5 to 10°C/min shifted the onset of initial sintering to higher temperature (**Figure 5.12**) which is related to kinetic aspect of sintering. In fact, at low heating rates, the pellet is exposed to heating for a longer duration and consequently underwent more shrinkage until reaching a specific temperature. During the final step (1020-1200°C) modest shrinkage around 2% was observed. Instead of densification, the grain growth mechanism might be dominant in final step. For more insight on sintering process, isothermal sintering of γ-$LiAlO_2$ pellet (10mm diameter and 2mm thickness) was carried out in temperature span 800-1100°C at a heating rate of 10°C/min with constant dwell time (2h) in air. The volumetric shrinkage was calculated from the measured geometrical dimensions of pellets before and after sintering at different temperatures. The density of sintered $LiAlO_2$ pellets was determined by Archimedes' method. The relative sintered density and volumetric shrinkage of $LiAlO_2$ pellet at different sintering temperature is shown in **Figure 5.13**. The density was found to increase with sintering temperature as depicted in **Figure 5.13**. The relative density around 93% was observed at temperature as low as 900ºC. The optimal relative density for tritium breeding purpose is often recommended in the range 85- 90%. In present case, the optimal density was obtained at sintering temperature in the range 850-900°C as evident from **Figure 5.13**. Apparently, 97-98% relative density was observed at sintering temperature in the range 950- 1000ºC which entails γ-$LiAlO_2$ powder synthesized by the present method has excellent sinterability. Beyond this temperature, significant improvement in relative density was not observed (**Figure 5.13**) which is in good agreement with dilatometry result (**Figure 5.12**). It is to be noted that many earlier works have reported sintering of γ-$LiAlO_2$ require high temperature, often in the range 1200-1400°C for 4-10h duration with relative density 70-85% which has been assigned to poor sinterability of synthesized powder. During sintering at such a high temperature, Li sublimation cannot be avoided. However, γ-$LiAlO_2$ powder synthesized by present method can be remarkably sintered at temperature <1000°C with optimal relative density.

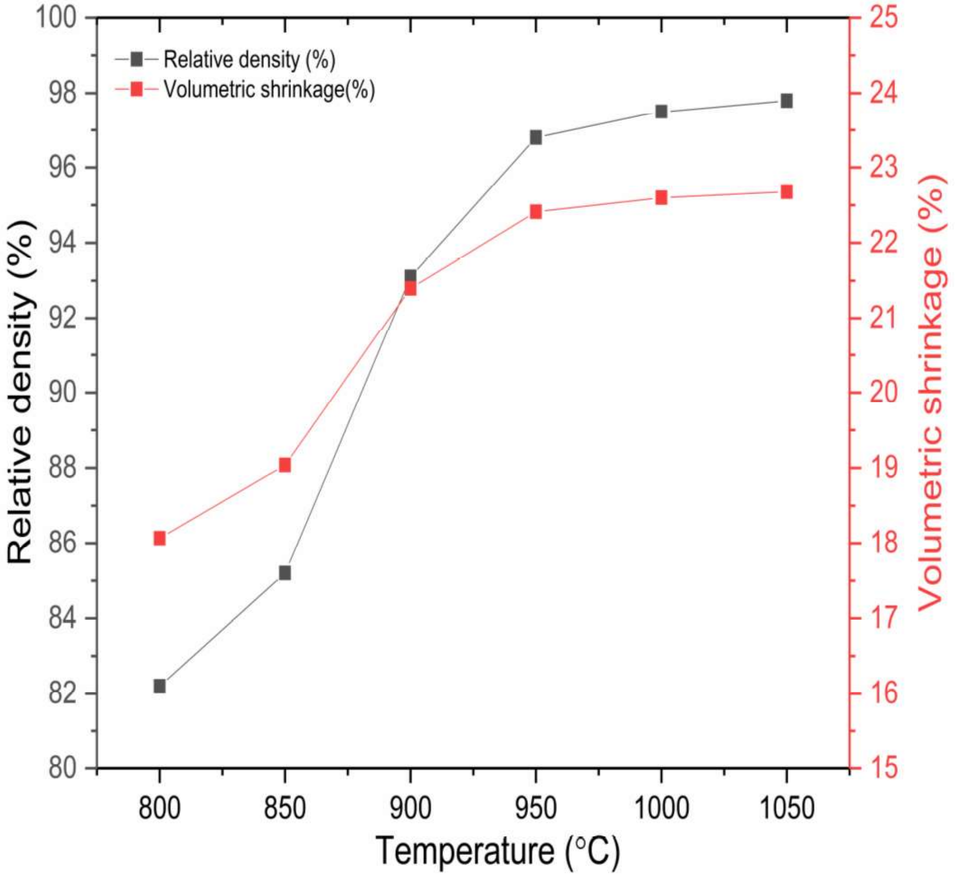

Figure 5.13 Effect of sintering temperature on relative density and volumetric shrinkage of $LiAlO_2$ pellet

Moreover, in this temperature regime problems associated with Li sublimation and uncontrolled grain growth can be effectively avoided during fabrication of tritium breeder ceramic by powder metallurgy route. The sintering behaviour of γ-$LiAlO_2$ as depicted in **Figure 5.13** can be explained in terms of two competing thermally activated kinetic processes viz., densification and grain growth. The densification is dominant sintering process in temperature range 850-950°C and beyond this temperature grain growth dominates the sintering process resulting grain size enlargement without substantial improvement in relative density. The percentage volumetric shrinkage was observed varying in accordance with relative density as a function of sintering temperature (**Figure 5.13**). The large volumetric shrinkage around 23% was observed which is due to large fraction of porosity initially present in green pellets. SEM images depicting fracture surface microstructure of γ-$LiAlO_2$ pellets sintered at temperature in range 800-1100°C are shown in **Figure 5.14**.

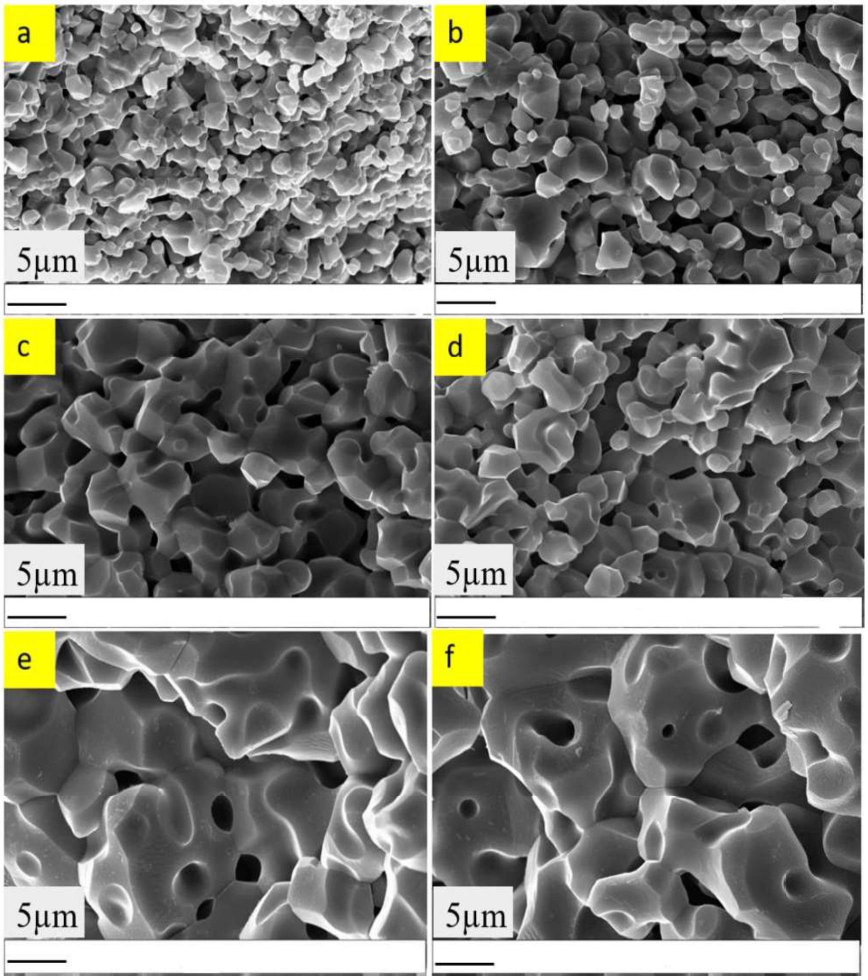

Figure 5.14 SEM images of fractured surface of $LiAlO_2$ sintered at a) 800°C b) 850°C c) 900°C d) 950°C e) 1000°C f) 1050°C

The SEM images demonstrate that pellets have uniform grain morphology which is in agreement with XRD results confirming phase purity of $LiAlO_2$ (**Figure 5.7, Figure 5.8**). As evident from **Figure 5.14 (a-c)**, the pellets sintered at 800, 850 and 900°C exhibited microstructure resembling intermediate stage of sintering characterized by large particle-to-particle contact area, continuous pore channels and relative density 80-94% (**Figure 5.13**). In this stage, apparently densification process dominates over grain growth and consequently, microstructure comprised of high density and small grain size (2-4µm) was evolved. This kind of microstructure is considered good from tritium breeding point of view because it consists of short tritium diffusion pathways and interconnected pores, both of which facilitate removal of bred tritium from the grains. In case of pellets sintered at 950, 1000 and 1050°C microstructure resembling final stage of sintering characterized by elimination of pore channels, formation of isolated pores and increase of relative density to 95-98% (**Figure 5.13**) was observed as depicted in **Figure 5.14 (d-f)**. In this stage, grain growth is clearly a dominant sintering mechanism which manifests large size grains (10-15µm), closed pores and modest improvement in relative density (**Figure 5.13**). This type of microstructure is not considered good from tritium breeding point of view, because due to long diffusion pathways and isolated pores the bred tritium either remains trapped or needs high temperature beyond practical limits for removal from the grains. The development of microstructure as a function of sintering temperature is in complete agreement with the densification curve (**Figure 5.13**).

5.3.7 Chemical analysis (Li/Al ratio) and phase analysis of $LiAlO_2$

Chemical analysis of $LiAlO_2$ pellets was carried out after sintering according to the procedure already described in Section 5.3.5 and Li/Al mole ratio was determined. The mean value of Li/Al mole ratio was estimated equal to 0.989 ± 0.003 after sintering in temperature range 800-1100°C for 2 h duration which is in good agreement with Li/Al mole ratio in stoichiometric $LiAlO_2$ (i.e. 1). This result confirms that any significant loss of lithium did not occur by sublimation during sintering of $LiAlO_2$ pellets. **Figure 5.15** shows XRD patterns of $LiAlO_2$ pellets after sintering at different temperatures. Except minor variation in relative peak intensities which is due to variation in crystallinity of sample with temperature, any noteworthy modification in XRD pattern of the pellets was not observed after sintering which indicates good phase stability of γ-$LiAlO_2$.

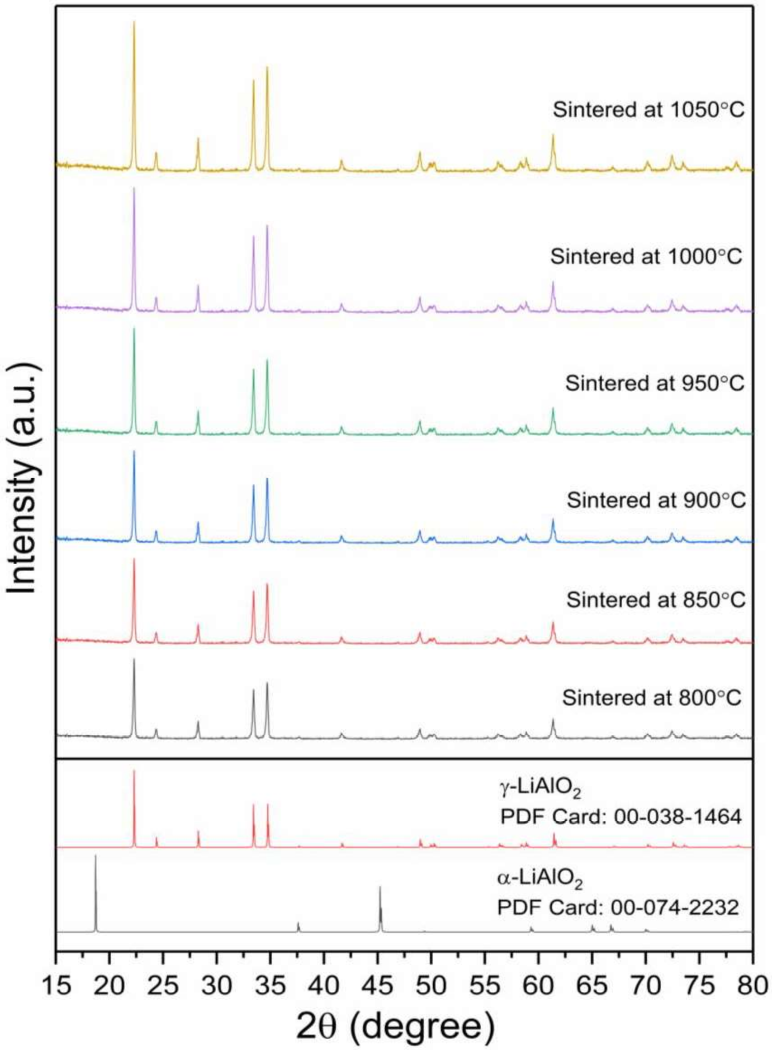

Figure 5.15 XRD pattern of $LiAlO_2$ pellets after sintering

5.4 Summary

Mixed fuel vis-à-vis conventional single fuel solution combustion synthesis of nanocrystalline γ-$LiAlO_2$ powders is investigated in this work utilizing citric acid and glycine as organic fuel. Thermochemical analysis revealed that combustion reactions are highly exothermic. The calculated adiabatic temperature decreases with increasing glycine fraction in mixed fuel composition and at high glycine fraction, mode of combustion switches from VCS to SHS. Contrary to adiabatic temperature, the measured reaction temperature increases with increasing glycine fraction in mixed fuel composition due to interactive effect of various parameters on adiabatic temperature, the parameters include mode of combustion, carbonization of citric acid and convective heat transfer by releasing combustion gases. Pure phase and well crystalline γ-$LiAlO_2$ powder were obtained after calcination at 700°C for all the fuel compositions. However, in case of mixed fuel approach well crystalline γ-$LiAlO_2$ phase was obtained even before high temperature calcination. Moreover, mixed fuel approach has advantage over single fuel in terms of better control over combustion reaction and more powder yield. The mean crystallite size γ-$LiAlO_2$ increases with increasing glycine fraction in mixed fuel. The crystallite size in narrow range of 17-27nm was found for γ-$LiAlO_2$ before calcination. After calcination at 550 and 600°C, any significant change in crystallite size was not observed, however, after calcination at 700°C, mean crystallite size increases sharply to around 49nm. The γ-$LiAlO_2$ powder synthesized by single citric acid fuel has shown the highest loss on ignition (8.47%) and powder synthesized using single glycine fuel has shown the least (0.82%). The mixed fuel compositions have shown loss on ignition in range 5-6%. Morphology of $LiAlO_2$ powder consists of irregular flake shape soft-agglomerated particles with large variation in particle size (4-20μm). The γ-$LiAlO_2$ powders synthesized by given mixed fuel approach presented remarkably enhanced sinterability which is characterized by optimal relative density (85-90%) with small grain size (2-4μm) at unprecedented low sintering temperature (800-900°C) and almost full densification at 1000°C. Sintering beyond 1050°C found disadvantageous because it causes abnormal grain growth with large number of closed isolated pores. The fine γ-$LiAlO_2$ powder synthesized by the employed solution combustion method exhibited excellent sinterability characterized by low sintering temperature and time duration. This will facilitate circumventing the critical issue of Li sublimation and uncontrolled grain growth which makes the fabrication of high-performance tritium breeder materials by powder metallurgy route challenging.

As described earlier in Chapter 1, due to the nuclear grade purity of breeders, the addition of many alloying elements as dopants or sintering aids in Li-based ceramics breeders is strictly prohibited. However, beryllium oxide (BeO), due to neutron multiplication properties with negligible neutron absorption and excellent thermophysical characteristics, is quite promising as a dopant or the sintering aid.

In view of this, the next chapter deals with the synthesis and sintering behaviour of BeO doped Li_2TiO_3.

Chapter 6

Novel beryllium oxide doped Li_2TiO_3 as tritium breeder

The work reported in this chapter has been communicated as follows:

Anomalous phase transformation of Li_2TiO_3 during sintering in oxygen atmosphere: a dilatometry study

Biranchi M. Tripathi, Jyothi Sharma, Deep Prakash, A. K. Tyagi

J. Eur. Ceram. Soc.

6.1 Introduction

The fusion reactor blanket development is an important aspect in designing D-T fusion power reactors. The one of the blanket's function is to breed sufficient tritium and other is to maximize the blanket heat deposition per D–T fusion neutron. Preferably, a blanket design having tritium breeding ratio greater than 1.0 is necessary to achieve tritium self-sufficiency [229,230]. In addition to tritium breeders, almost all blanket concepts need a neutron multiplier also to achieve adequate tritium breeding. The breeder and multiplier materials can either be a homogenous mixer, composite, solid solution, eutectic mixture or reside in separate zones. Beryllium (Be) and lead (Pb) have been considered as potential candidate neutron multiplier materials for fusion reactor blanket [44,229,231]. The comparison of neutron multiplication cross-section of Be and Pb as a function of the neutron energy is depicted in **Figure 6.1** [232]. Owing to the sufficient neutron multiplication with low threshold energy, negligible neutron absorption and large energy multiplication, Be is preferred as neutron multiplier [231,233]. However, limited resources of beryllium and its toxicity have serious concern [234–237]. Beryllium in the form of metal and intermetallic compounds (with Ti, V, Zr, etc.) are being investigated for a solid neutron multiplier [44]. BeO, due to an appreciable fast neutron multiplication cross-section, low neutron absorption cross section, low neutron moderation, high thermal conductivity, good strength, and good compatibility with the structural materials can be another potential candidate neutron multiplier material [235]. However, BeO has been rarely investigated as the neutron multiplier material.

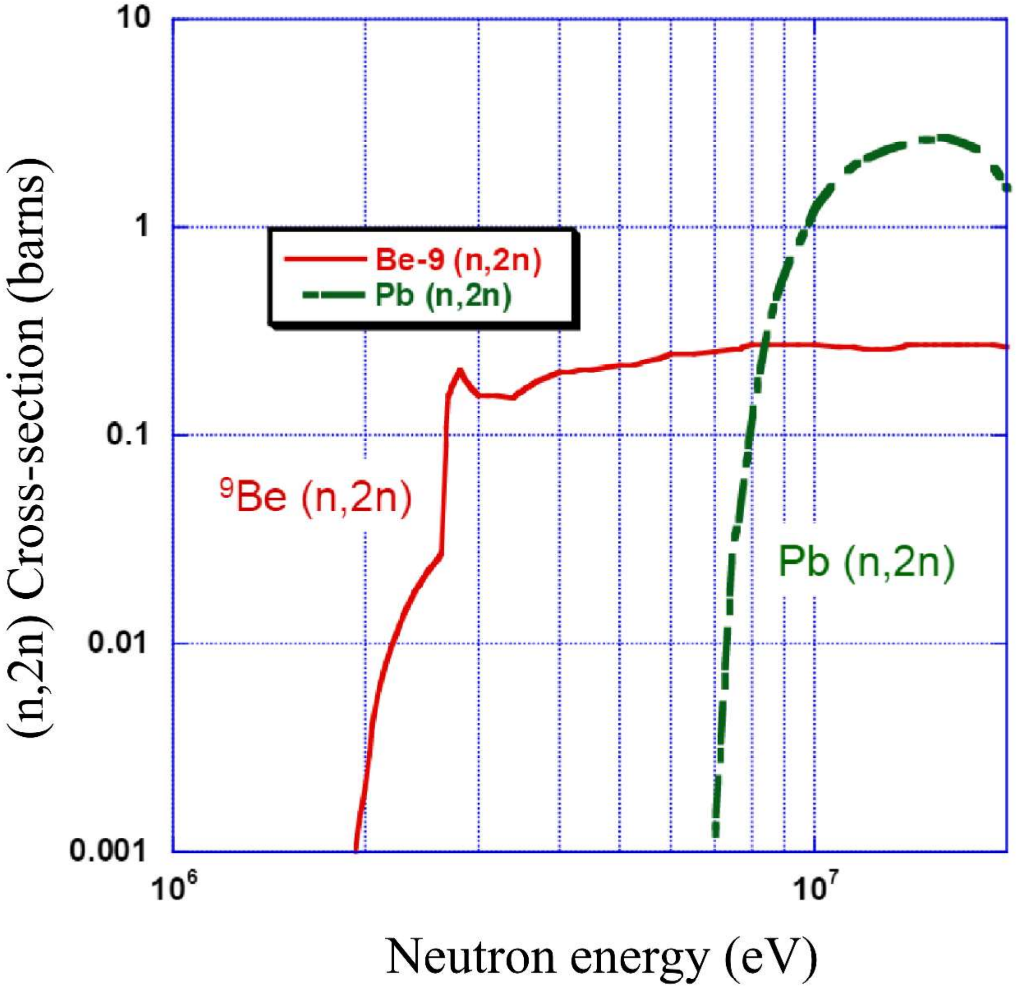

Figure 6.1 Neutron multiplication cross-section vs. neutron energy [232]

Due to high thermal conductivity of BeO, a mixture of BeO and Li-based ceramic tritium breeders will enhance thermal conductivity of the blanket and facilitate an easy blanket heat removal. Earlier, our group had reported study on BeO-Li_2TiO_3 composite as novel blanket material for fusion reactor [104,236]. However, no study has been performed on BeO doped Li_2TiO_3. The present chapter deals with synthesis of BeO doped Li_2TiO_3 powder and study its sintering behaviour employing dilatometry analysis.

6.2 Experimental procedure

6.2.1 Synthesis of BeO doped Li_2TiO_3 powder

Synthesis of Li_2TiO_3 with and without BeO doping was carried out by a urea assisted solid state method according to the procedure elaborated in our previous studies. The synthesis process flow sheet is presented in **Figure 6.2**.

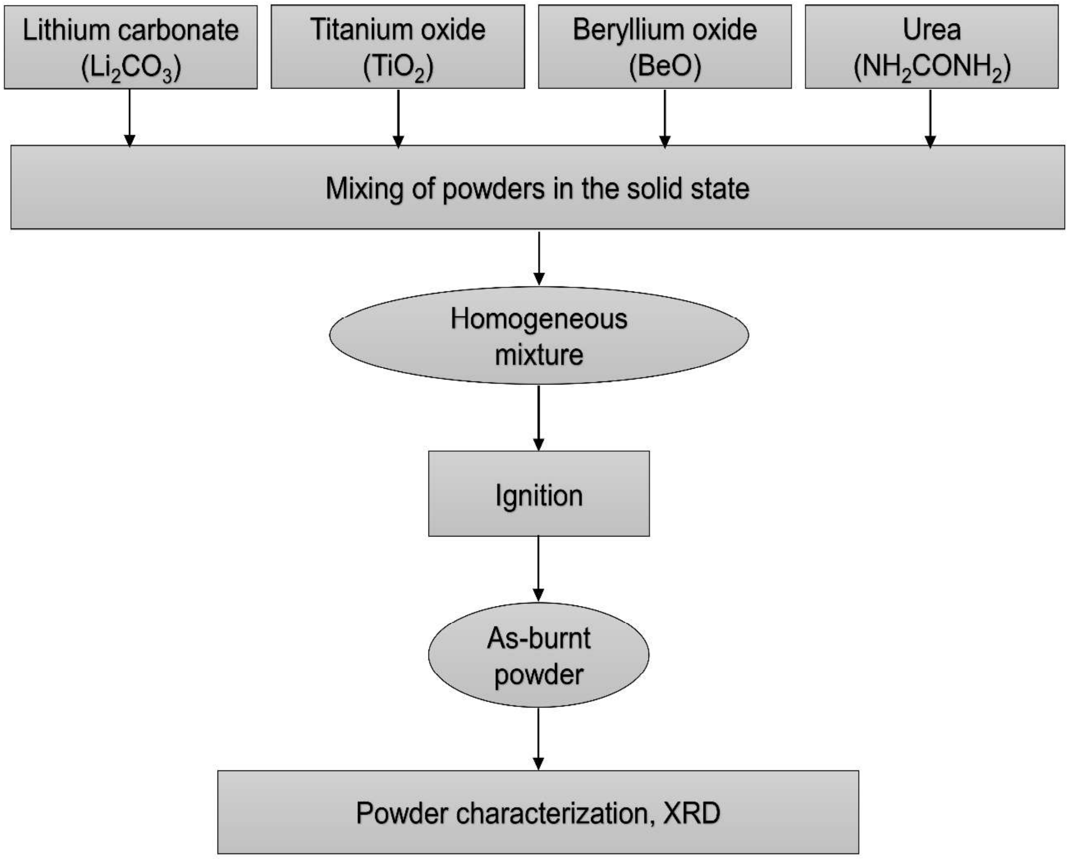

Figure 6.2 BeO doped Li_2TiO_3 powder synthesis process flow sheet

The starting materials were lithium carbonate (Li_2CO_3), titanium oxide (TiO_2), beryllium oxide (BeO) and urea (NH_2CONH_2). All chemicals with AR grade purity were purchased from Sigma-Aldrich and were used in synthesis process without further purification. For the preparation of pure Li_2TiO_3, stoichiometric proportions of Li_2CO_3 and TiO_2 were blended along with 25 wt % of urea using pestle and mortar in ethyl alcohol medium and the mixture was dried on hot plate. Subsequently, the dried powder was calcined at 700°C temperature for 3h duration at constant heating rate (10°C/min) in a muffle furnace (Nabertherm, Germany). Similarly, BeO doped Li_2TiO_3 samples with general composition expressed as $Li_{2(1-x)}Be_xTiO_3$ were prepared by mixing reagents in appropriate ratio followed by drying and calcination. The molar ratio of starting reagents (Li_2CO_3:TiO_2:BeO) was (2-2x):1:x (x=0.01 and 0.03).

6.2.2 Characterization

The crystallinity was examined using powder XRD patterns of Li_2TiO_3 with and without BeO doping recorded on a diffractometer (Proto AXRD, Canada) using Cu-Kα radiation (λ=1.54056 Å) as X-ray source. The microstructure of sintered pellets after dilatometry measurement was examined by a scanning electron microscope (SEM, Carl-Zeiss, Germany) operating at 20kV accelerating voltage. Pellets were sputter-coated with gold to prevent charging due to lack of electrical conductivity of the samples. The particle size of Li_2TiO_3 powder was analysed using a transmission electron microscope (TEM). The surface area of Li_2TiO_3 powder was determined by BET method using N_2 gas as an adsorbent.

6.2.3 Evaluation of sintering by dilatometry

The synthesised Li_2TiO_3 powders with and without BeO doping were pressed on a hydraulic press under pressure of about 300 MPa at room temperature using tungsten carbide (WC) die to fabricate pellets of dimension about 8mm diameter and 3-4mm thickness without addition of binder. These pellets were transferred in a Thermo-mechanical Analyser Instrument (Setaram, France) for dilatometry measurement. The dilatometric shrinkage of the pellets were measured as a function of temperature up to 1100°C, at heating rates of 10°C/min in oxygen atmosphere. The process flow sheet of powder consolidation and sintering is shown in **Figure 6.3**.

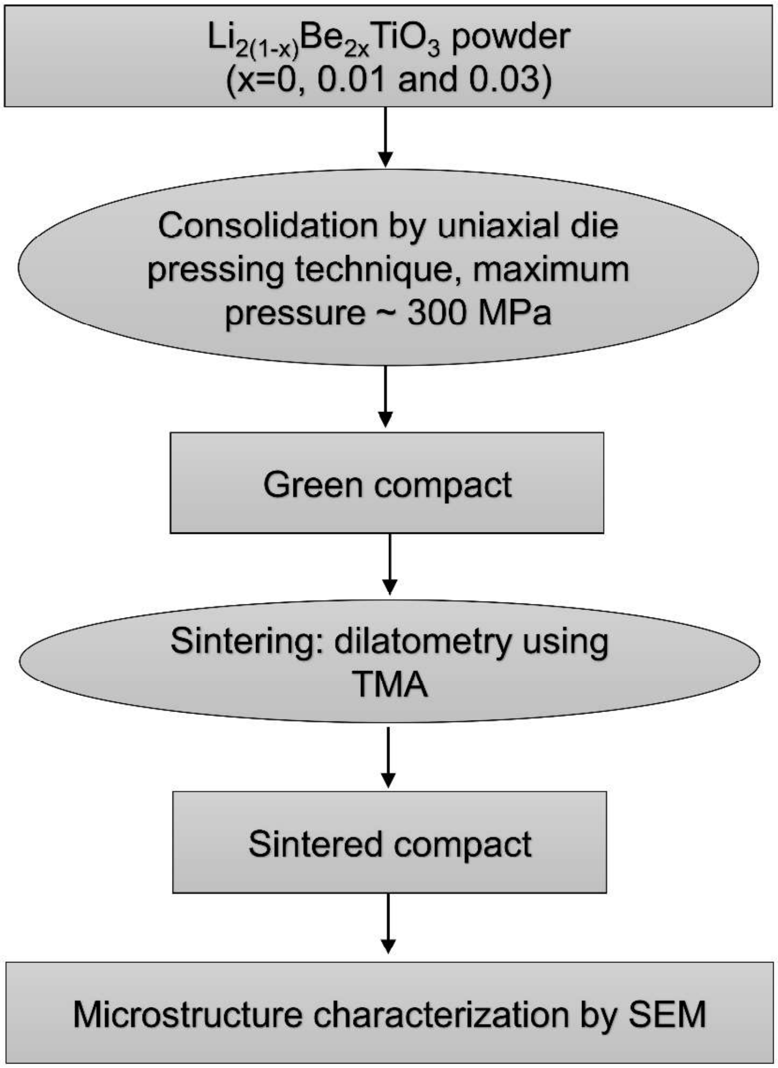

Figure 6.3 BeO doped Li_2TiO_3 powder consolidation and sintering process flow sheet

6.3 Result and discussion

6.3.1 Phase characterization of Li_2TiO_3

The XRD patterns of as-synthesized Li_2TiO_3 powders with and without BeO doping is depicted in **Figure 6.4**. Evidently, all XRD peaks match PDF card No. 033-0831 registered in Joint Committee on the Powder Diffraction Strands Card (JCPDS) which corresponds to the monoclinic crystal structure of Li_2TiO_3 nano-crystallites. It is to be noted that after doping with small amount of BeO (x=0.01, 0.03), any detectable change in XRD pattern of Li_2TiO_3 was not observed which indicates incorporation of BeO into crystal lattice of Li_2TiO_3 during the synthesis process.

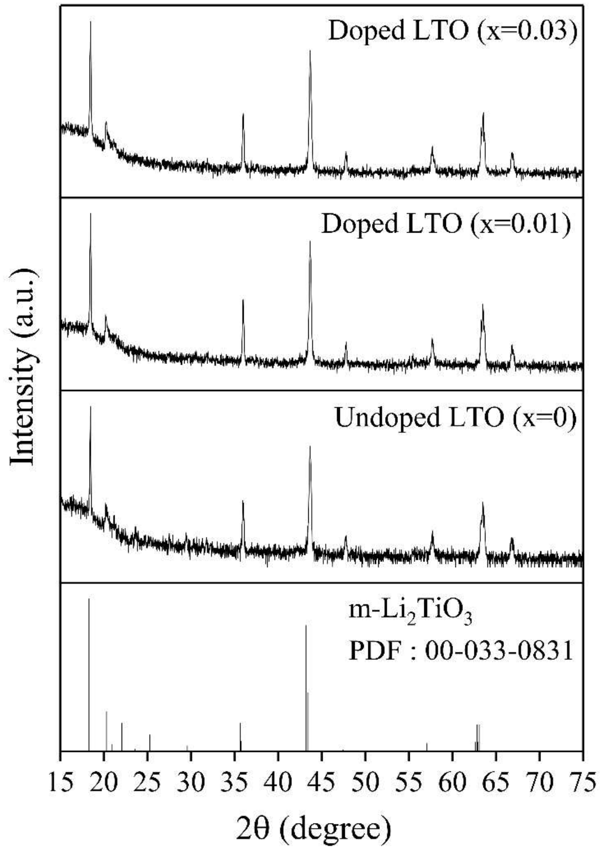

Figure 6.4 XRD patterns of as-synthesized un-doped and doped Li_2TiO_3

6.3.2 Characterization of powder morphology

The TEM image of Li_2TiO_3 powders are illustrated in **Figure 6.5**. Particle size distribution of Li_2TiO_3 was derived from TEM image which is expressed as number-frequency-histogram shown in **Figure 6.5**. Considerably broad particle size distribution of Li_2TiO_3 has been observed with particle size in the range of 50-350 nm.

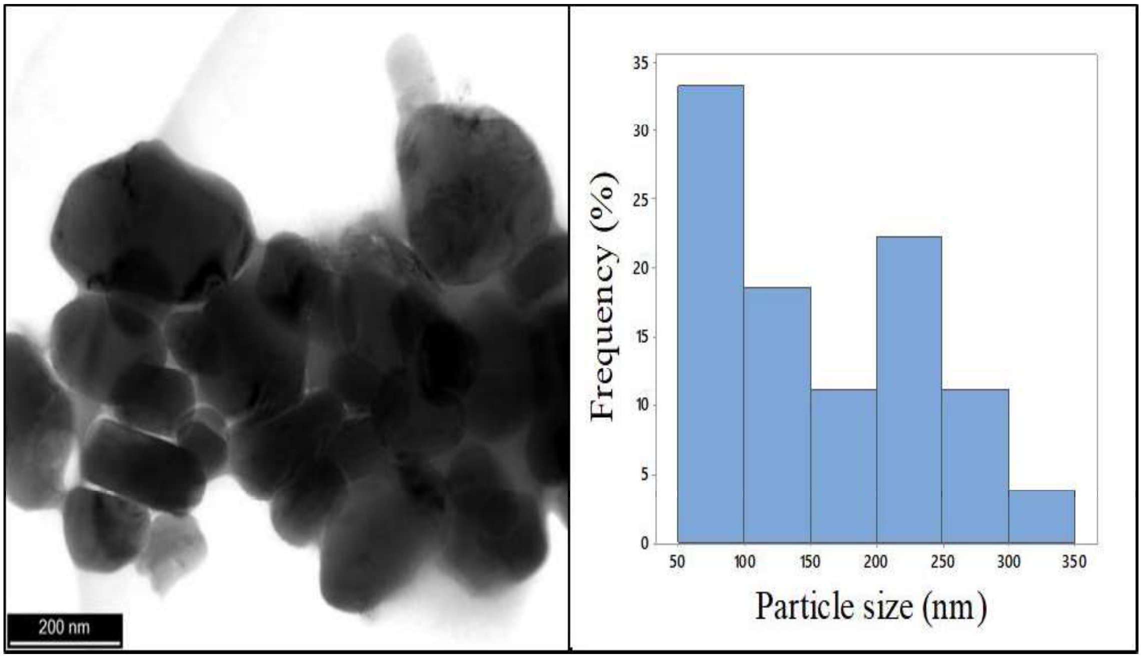

Figure 6.5 TEM micrograph and particle size distribution of un-doped Li_2TiO_3

The typical N_2 absorption-desorption isotherms of Li_2TiO_3 sample measured at liquid nitrogen temperature (78K) is depicted in **Figure 6.6**. From the N_2 static physisorption isotherm, the specific surface area of the sample was calculated invoking BET adsorption equation. The N_2 BET surface area of the sample was observed to be 14.43 m^2/g.

The as-synthesized Li_2TiO_3 powder was dark-brown in colour. This is because Li_2TiO_3 have some oxygen vacancies facilitated by urea as reducing agent and consequently some of the

Ti^{4+} ions are reduced to Ti^{3+} valence state (d^1 system) to maintain charge neutrality of the crystal and thereby imparts dark-brown colour to Li_2TiO_3 powder [133,157,201].

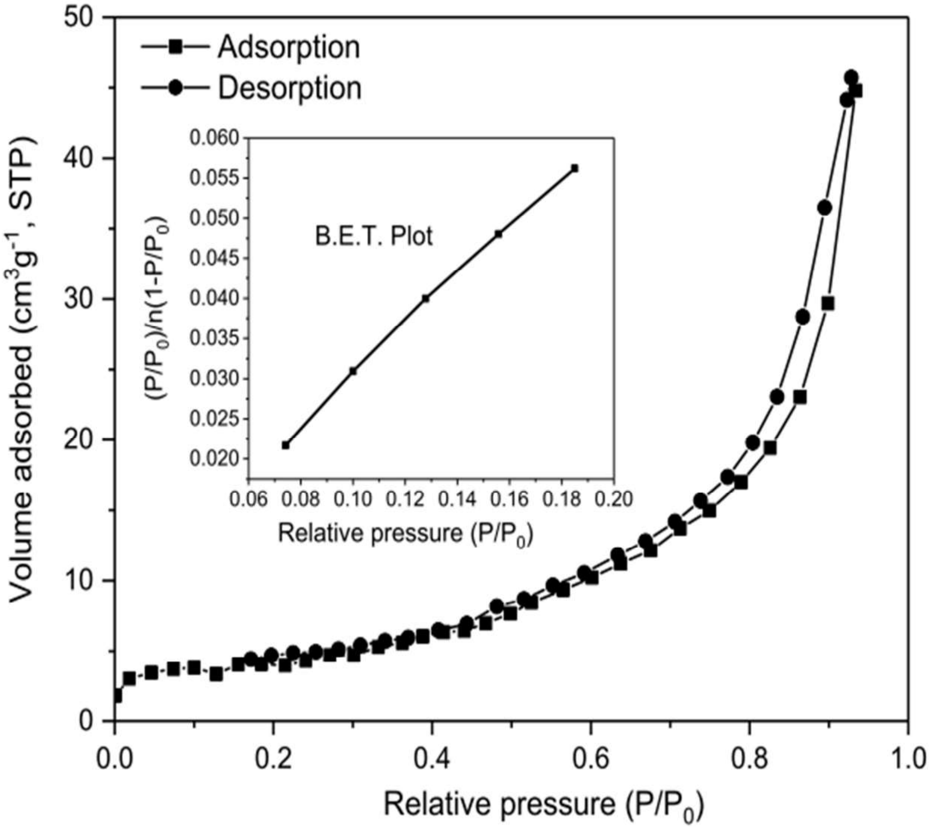

Figure 6.6 N_2 adsorption-desorption isotherm and BET plot of un-doped Li_2TiO_3

6.3.3 Analysis of dilatometric sintering behaviour

Dilatometry curve of as-synthesized un-doped as well as BeO doped Li_2TiO_3 measured up to 1100°C at a heating rate of 10°C/min in O_2 atmosphere is presented in **Figure 6.7**. The curve indicates percentage change in length of the pellet expressed as dL/L_0 (%) with increasing temperature, where Lo is initial length. Evidently, percentage change in length of the un-doped pellet is comprised of four distinct stages as shown in **Figure 6.7**. In stage-I (300-715°C), expansion of pellet was observed which is due to intrinsic thermal expansion of Li_2TiO_3. In stage-II (715-970°C), large shrinkage with maximum equals to around 7% was noticed as shown in **Figure 6.7**. Apparently, sintering mechanisms dominate over intrinsic thermal expansion in this stage which leads to shrinkage and thereby densification of the pellet.

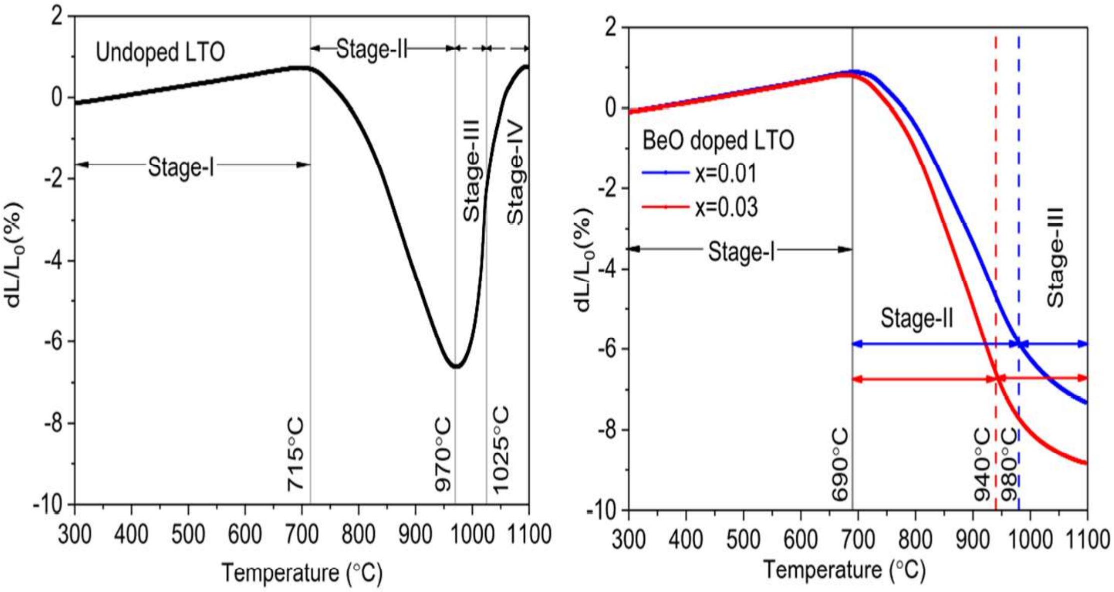

Figure 6.7 Dilatometry curve of un-doped and BeO doped (x=0.01&0.03) Li_2TiO_3 pellets

Sintering stage in un-doped Li_2TiO_3 commences at temperature as low as 715°C which implies excellent sinterability of Li_2TiO_3 powder. Abbasian et al., investigated sintering behaviour of Li_2TiO_3 powder with mean particle size 23μm by dilatometry and reported sintering temperature in the range of 882-1050°C [238,239]. It shows that sintering temperature was significantly reduced in present case. Reduction in sintering temperature can be attributed to smaller particle size of Li_2TiO_3 powder (mean ~ 0.16μm) (**Figure 6.5**) and oxygen vacancies in Li_2TiO_3. Small particle size, due to presence of large grain boundary volume fraction and short atomic diffusion pathways, as well as oxygen vacancies, both accelerate sintering mechanisms by facilitating atomic diffusion. Reduction in sintering temperature is significantly advantageous to effectively avoid problem of Li-sublimation and grain growth during sintering of Li_2TiO_3 powder. Surprisingly, during the stage-III (970-1025°C), the pellet expanded once again as evident from **Figure 6.7**. Normally, in this stage, the shrinkage is expected to attain plateau. In final stage-IV (1025-1100°C), pellet started shrinking once again which is obvious (**Figure 6.7**). In order to understand this anomalous expansion, XRD patterns of un-doped Li_2TiO_3 pellets before and after dilatometry test were compared as displayed in **Figure 6.8**.

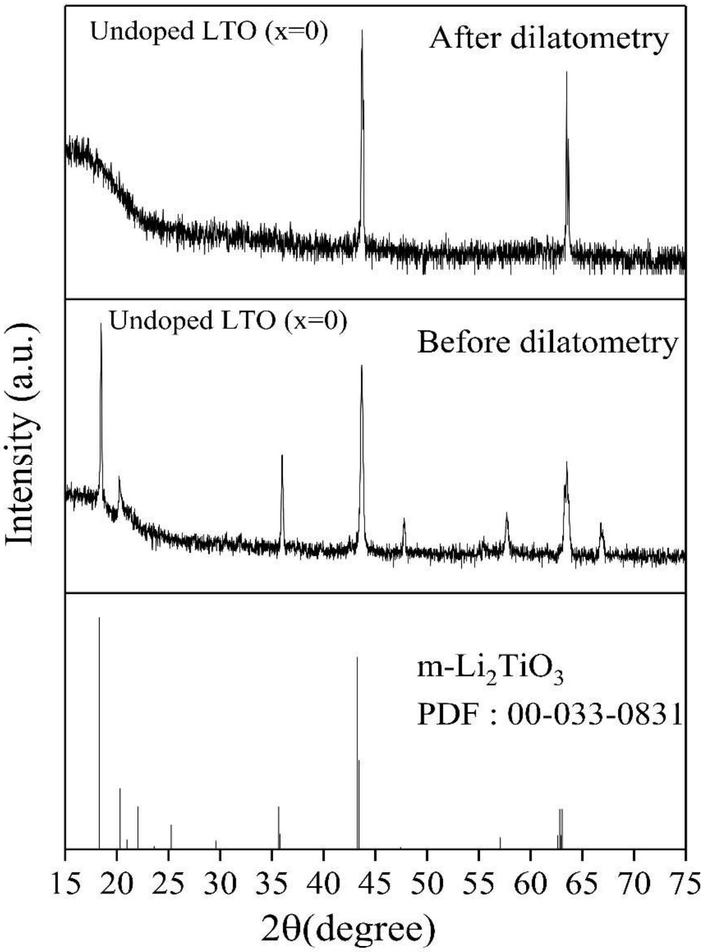

Figure 6.8 XRD patterns of un-doped Li_2TiO_3 before and after dilatometry test

Evidently, before dilatometry test, all XRD peaks of undoped Li_2TiO_3 matched pure phase monoclinic structure, however, post dilatometry test, XRD pattern matched PDF card No.

074-2257 which represents cubic crystal structure. Therefore, it can be inferred that anomalous expansion is due to monoclinic to cubic phase transformation. It is to be noted that this type of phase transformation in stoichiometric Li_2TiO_3 has been typically reported in temperature range 1150–1215°C while sintering in air [132,133,143,240]. However, in present study, the phase transformation temperature was observed close to 970°C which is considerably lower than the reported value. In order to gain more insight on this phase transformation, SEM images of surface of un-doped Li_2TiO_3 pellet after dilatometry test was captured at different magnifications as shown in **Figure 6.9**.

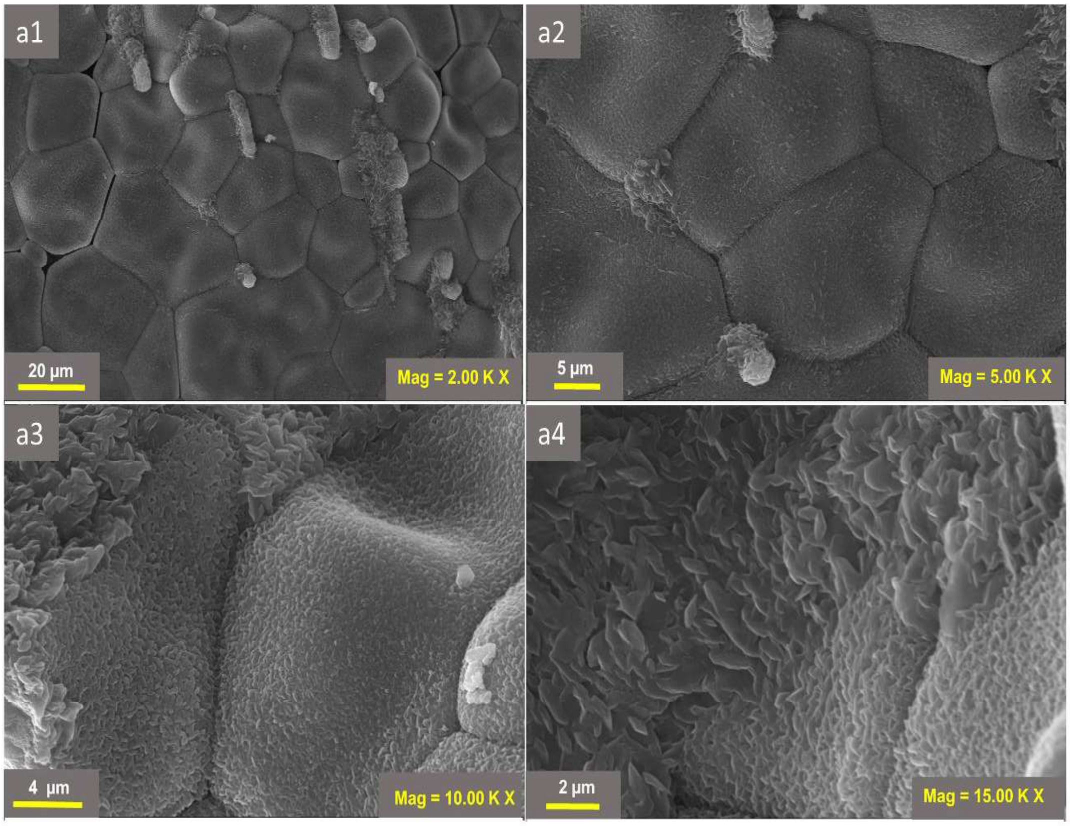

Figure 6.9 SEM images of un-doped Li_2TiO_3 pellet after dilatometry

Apparently, some of the grains are very large and some are comparatively small in size which indicates that rapid grain growth occurred during sintering of Li_2TiO_3. The grains around the grain boundary areas have completely different morphology than the bulk as shown **Figure 6.9 (a1-a3)**. It indicates that recrystallization of grains might have initiated from grain boundary areas and subsequently propagated throughout the volume as depicted in **Figure 6.9 (a4)**. Due to recrystallization process eventually a fine-grained microstructure (grain size ~2μm) was evolved as shown in **Figure 6.9 (a4)**. This type of monoclinic to cubic phase transformation was also reported in Li_2TiO_3 nanocrystallites synthesized by hydrothermal method at transformation temperature about 900°C [147,241]. In hydrothermally synthesized powder, due to very small particle size (~10nm), the role of high surface energy was assigned as main controlling factor for the phase transformation [241]. The role of particle size and surface energy on phase transformation of nanoparticles has been studied quite extensively. According to studies, phase transformations in nanocrystalline materials occur as a consequence of differences in surface energies between the polymorphs [242]. Generally, surface energy acts as main controlling factor in formation of thermodynamically metastable crystalline phases when particles are reduced below certain critical size. The critical size varies in very broad range (3-30 nm) as reported in the literature [243]. In present study, as Li_2TiO_3 particles are considerably larger than the critical size (**Figure 6.5**), the monoclinic to cubic phase transformation cannot be solely ascribed to surface energy. As already discussed in the previous section, oxygen vacancies are present in Li_2TiO_3 and therefore more plausible explanation relies on change in oxygen vacancy concentration with change in sintering atmosphere from ambient air to pure oxygen.

Dilatometry curve of BeO doped Li_2TiO_3 pellet is comprised of usual three distinct stages (stage-I stage-II and stage-III) as shown in **Figure 6.7**. The expansion of pellets (x=0.01and 0.03) in stage-I (300-690°C) is obvious due to intrinsic thermal expansion of Li_2TiO_3. In stage-II (690-980°C for x=0.01 and 690-940°C for x=0.03), sintering mechanisms become operative and consequently pellets underwent large shrinkage as shown in **Figure 6.7**. In stage-III (980-1100°C for x=0.01 and 940-1100°C for x=0.03), the grain growth mechanisms dominate over the densification and consequently shrinkage attained near saturation. Interestingly, anomalous expansion behaviour disappeared after doping Li_2TiO_3 powder with small quantity of BeO (x=0.01 and 0.03) as shown in **Figure 6.7**. In BeO doped Li_2TiO_3 (x=0.01 and 0.03), XRD patterns before and after dilatometry test as presented in **Figure 6.10** revealed that monoclinic to cubic phase transformation did not take place and consequently, anomalous expansion was not observed.

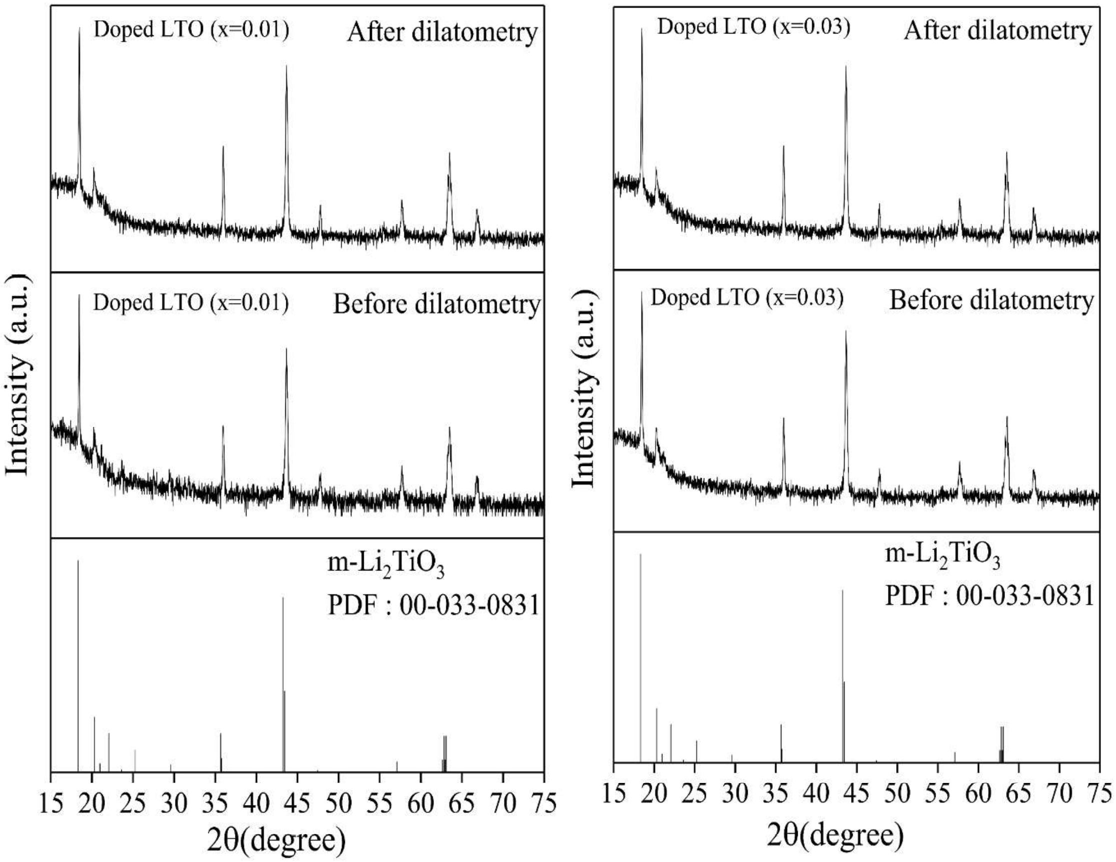

Figure 6.10 XRD patterns of BeO doped Li_2TiO_3 pellets before and after dilatometry

Figure 6.7 shows that the sinterability of Li_2TiO_3 powder has been improved after BeO doping which is characterized by reduction of sintering temperature and increase in shrinkage as compared to un-doped sample. The sinterability enhancement can be assigned to Li vacancies introduced into crystal lattice by aliovalent substitution of Li^+ by Be^{2+} which is beneficial to augment diffusion of Li. The suppression of monoclinic-to-cubic phase transformation after BeO doping can be assigned possibly to high charge-to-size ratio of Be^{2+} ion that facilitates formation of the stronger Be-O bonds and thereby stabilises the monoclinic structure. The stabilisation of monoclinic structure was also reported after small amount of MgO doping in Li_2TiO_3, however, at higher doping levels order-disorder phase transformation was observed [240]. In MgO doped Li_2TiO_3 powder, the sintering temperature was reported in the range of 850-1200°C which is considerably higher than the BeO doped Li_2TiO_3 [244]. The greatly improved sinterability of the Be doped Li_2TiO_3 breeder material would be probably helpful to circumvent Li sublimation, uncontrolled grain growth and improve release and inventory performance of the tritium.

6.4 Summary

Pure monoclinic phase Li_2TiO_3 powders with general composition expressed as $Li_{2(1-x)}Be_xTiO_3$ (x=0.01 and 0.03) using BeO as novel dopant were synthesized by urea assisted solid state method. As-synthesized un-doped Li_2TiO_3 powder exhibited excellent sinterability characterized by surprisingly low sintering onset temperature that is close to 715°C in O_2 atmosphere. Increasing sintering temperature resulted in an anomalous monoclinic-to-cubic phase transformation at temperature about 970°C which is significantly lower than reported transformation temperature (1150-1250°C). This phase transformation was suppressed in BeO doped Li_2TiO_3 powder. Moreover, sinterability of Li_2TiO_3 powder was augmented after doping with small amount of BeO. Reduction in sintering temperature has vital role in controlling Li sublimation and uncontrolled grain growth during fabrication of advance tritium breeder materials.

Chapter 7

Conclusion and future scope

Conclusion

The objective of the present thesis was to investigate the role of fine ceramic powders for improvement of the sinterability of Li-based ceramic tritium breeders (Li_2TiO_3, Li_2ZrO_3, and $LiAlO_2$). Due to the improved sinterability, Li-based ceramic can be sintered at relatively lower temperatures and short duration. Therefore, the economical production of sintered tritium breeders with the engineered microstructure (density and grain size) is possible without vaporization of Li.

The following conclusions have been drawn from the present work.

- ☐ The pure phase nanocrystalline Li_2TiO_3, Li_2ZrO_3, and $LiAlO_2$ powders were synthesized and characterized by various techniques.
- ☐ The pellet-shaped green compacts of Li_2TiO_3, Li_2ZrO_3, and $LiAlO_2$ with desired dimensions were made by consolidating the synthesized powders employing the isostatic hydraulic pressing method.
- ☐ The sintering behaviour of the Li_2TiO_3, Li_2ZrO_3, and $LiAlO_2$ green pellets, analysed by dilatometry, revealed the sintering temperature regimes of these ceramics.
- ☐ The isothermal sintering (conducted based on dilatometry data) disclosed the effect of sintering temperature on densification of Li_2TiO_3, Li_2ZrO_3, and $LiAlO_2$ green pellets and also established the appropriate sintering temperature of these ceramic tritium breeders.

- The high densification of Li_2TiO_3, Li_2ZrO_3, and $LiAlO_2$ green pellets observed at relatively low sintering temperature and short duration, indicated improved sinterability of these ceramic tritium breeders.
- Reduction in sintering temperature and time play a vital role in circumventing Li sublimation and uncontrolled grain growth during production of advance ceramic tritium breeder materials.
- The enhanced sinterability resulted in fine grain-sized microstructure with the uniform grain morphology in sintered Li_2TiO_3, Li_2ZrO_3, and $LiAlO_2$ pellets as confirmed by the SEM images of the fracture surface of the sintered pellets.
- The isothermal sintering of Li_2TiO_3 pellet at a temperature as low as 850°C resulted in a relative density close to 90%, which often considered sufficient for tritium breeder application. Further, an increase in sintering temperature to 950-1000°C resulted in a high relative density (~98%) of Li_2TiO_3 compact.
- The SEM images of the fracture surface depicted uniform grain morphology and small grain size (2-3 µm) in Li_2TiO_3 pellet sintered at 900 and 950°C. Increasing the sintering temperature above 950°C resulted in rapid grain growth without significant improvement in densification of the Li_2TiO_3 compact.
- The impedance analysis of sintered Li_2TiO_3 pellet at different temperatures revealed significant improvement in Li conductivity resulting from a decrease in grain and grain boundary resistance and thereby accelerating the intragranular and grain boundary diffusion processes. The improved Li conductivity indicated better tritium release property of sintered Li_2TiO_3 compact.
- The dilatometry analysis of Li_2ZrO_3 pellet revealed the onset of sintering at significantly low temperature (850-900°C) with peak around 1000°C.

- The isothermal sintering of Li_2ZrO_3 pellet at a temperature of 950°C resulted in a relative density of around 90%. Further, an increase in sintering temperature to 1000°C produced nearly full densification (97-98%) of the pellet.
- The SEM images of the fracture surface depicted uniform grain morphology and small grain size (1-2 μm) in Li_2ZrO_3 pellet sintered at 1000°C. Increasing the sintering temperature above 1000°C produced a rapid grain growth with a large number of the closed pores without significant improvement in densification of the pellet.
- The dilatometry analysis of $LiAlO_2$ pellet revealed the onset of sintering at significantly low temperature (800-900°C) with peak around 1000°C.
- The isothermal sintering of $LiAlO_2$ pellet at a temperature of 900°C produced a relative density close to 93%. Further, an increase in sintering temperature to 950-1000°C resulted in nearly full densification (97-98%) of the pellet.
- The SEM images of the fracture surface depicted uniform grain morphology and grain size of around 2-4μm in $LiAlO_2$ pellet sintered at 900 and 950°C. Further, an increase in sintering temperature above 950°C resulted in a rapid grain growth with large number of the closed pores without significant improvement in densification of the pellet.
- The chemical analysis by ICP-AES revealed Li content in the synthesized powders and the sintered Li_2TiO_3, Li_2ZrO_3, and $LiAlO_2$ pellets nearly close to the stoichiometric value, which confirmed no significant loss of Li during the synthesis of powders as well as sintering of the pellets.
- A novel BeO doped Li_2TiO_3 ceramic tritium breeder was synthesized by the solid-state combustion method employing urea as a fuel. The XRD analysis revealed doping of BeO in Li_2TiO_3.

- The pellet-shaped green compact of BeO doped Li_2TiO_3 was made by isostatic hydraulic pressing technique.
- The dilatometry analysis revealed, improvement in densification of Li_2TiO_3 pellet after BeO doping in comparison to the undoped sample.
- The dilatometry analysis revealed an anomalous monoclinic-to-cubic phase transformation in undoped Li_2TiO_3 at a sintering temperature of around 970°C, whereas the usual phase transformation temperature has been reported in the range of 1150-1250°C.
- The doping of BeO resulted in the suppression of the monoclinic-to-cubic phase transformation in Li_2TiO_3.
- The Li_2TiO_3, Li_2ZrO_3, and $LiAlO_2$ compacts prepared utilizing the fine ceramic powders synthesized in this work have achieved the desired densification (relative density: 85-90%) with small grain size (1-4 μm) at the sintering temperature < 1000°C without loss of Li.

Future scope

- Study of irradiation behaviour of the sintered Li_2TiO_3, Li_2ZrO_3, and $LiAlO_2$ compacts can be undertaken.
- Study of sintering kinetics and derivation of master sintering curves for Li-based nanoceramics
- Study on porous/cellular Li-based ceramic tritium breeding materials
- In-depth study of BeO doped Li based ceramics as an advance tritium breeder material can be undertaken.

References

[1] IEA - International Energy Agency, Redrawing the Energy-Climate Map: World Energy Outlook Special Report, (2013) 134.

[2] IEA, India 2020 Policy Energy Review, Www.Iea.Org. 4 (2020) 1–14.

[3] International Renewable Energy Agency (IRENA), Global Energy Transformation: A Roadmap to 2050, 2018.

[4] M. Höök, X. Tang, Depletion of fossil fuels and anthropogenic climate change-A review, Energy Policy. 52 (2013) 797–809.

[5] V. Krey, L. Clarke, Role of renewable energy in climate mitigation: A synthesis of recent scenarios, Clim. Policy. 11 (2011) 1131–1158.

[6] A. Mohan, The Future of Nuclear Energy in India, Obs. Res. Found. . (2016).

[7] A.M. Bradshaw, T. Hamacher, U. Fischer, Is nuclear fusion a sustainable energy form?, Fusion Eng. Des. 86 (2011) 2770–2773.

[8] C.L. Smith, The need for fusion, Fusion Eng. Des. 74 (2005) 3–8.

[9] R. Toschi, Nuclear fusion, an energy source, Fusion Eng. Des. 36 (1997) 1–8.

[10] P.S. Garry McCracken, Fusion The energy of the universe, Elsevier Academic Press 2012

[11] S.H. Mohr, G.M. Mudd, D. Giurco, Lithium resources and production: Critical assessment and global projections, Minerals. 2 (2012) 65–84.

[12] L. Kavanagh, J. Keohane, G.G. Cabellos, A. Lloyd, J. Cleary, Global lithium sources-industrial use and future in the electric vehicle industry: A review, Resources. 7

(2018).

[13] C. Grosjean, P. Herrera Miranda, M. Perrin, P. Poggi, Assessment of world lithium resources and consequences of their geographic distribution on the expected development of the electric vehicle industry, Renew. Sustain. Energy Rev. 16 (2012) 1735–1744.

[14] T. Tanabe, Tritium: Fuel of fusion reactors, Springer Japan 2017.

[15] T. Tanabe, Tritium fuel cycle in ITER and DEMO: Issues in handling large amount of fuel, J. Nucl. Mater. 438 (2013) S19–S26.

[16] Y. Katoh, L.L. Snead, C.H. Henager, T. Nozawa, T. Hinoki, A. Iveković, S. Novak, S.M. Gonzalez De Vicente, Current status and recent research achievements in SiC/SiC composites, J. Nucl. Mater. 455 (2014) 387–397.

[17] A.A.F. Tavassoli, E. Diegele, R. Lindau, N. Luzginova, H. Tanigawa, Current status and recent research achievements in ferritic/martensitic steels, J. Nucl. Mater. 455 (2014) 269–276.

[18] M. Victoria, N. Baluc, P. Spätig, Structural materials for fusion reactors, Nucl. Fusion. 41 (2001) 1047–1053.

[19] S. Banerjee, Overview of Indian activities on fusion reactor materials, J. Nucl. Mater. 455 (2014) 217–224.

[20] K. Ehrlich, Materials research towards a fusion reactor, Fusion Eng. Des. 56–57 (2001) 71–82.

[21] D. Clery, A Piece of the Sun: The Quest for Fusion Energy, Overlook Duckworth, 2013.

[22] Dstrozzi, File:Fusion rxnrate.svg - Wikimedia Commons, https://commons.wikimedia.org/w/index.php?curid=2351259.

[23] George H. Neilson, Magnetic fusion energy, From Experiments to Power Plants, Elsevier, 2016.

[24] J. D. Lawson, Some Criteria for a Power Producing Thermonuclear Reactor, Proceedings of the Physical Society, Section B 70 (1) (1955) 6–10

[25] H. Yamada, Fusion Energy, in: W.-Y. Chen, J. Seiner, T. Suzuki, M. Lackner (Eds.), Handb. Clim. Chang. Mitig., Springer US, New York, NY, 2012: pp. 1183–1215.

[26] What will ITER do ?, https://www.iter.org/sci/Goals..

[27] R. Aymar, - Overview of the ITER Project, in: T. Haruyama, T. Mitsui, K.B.T.-P. of the S.I.C.E.C.C.M.C. Yamafuji (Eds.), Elsevier Science, Oxford, 1997: pp. 53–59.

[28] Overview | ITER-India, (n.d.). https://www.iter-india.org/index.php/overview

[29] ITER EDA DOCUMENTATION SERIES NO. 22, International, International Thermonuclear Experimental Reactor (ITER), IAEA, (2001).

[30] https://www.iter.org/doc/all/content/com/gallery/media/6 - snapshots/flags jan 2019_3-small.jpg.

[31] G. Brumfiel, Fusion dreams delayed, Nature. 459 (2009) 488–489.

[32] M. Ni, Y. Wang, B. Yuan, J. Jiang, Y. Wu, Tritium supply assessment for ITER and DEMOnstration power plant, Fusion Eng. Des. 88 (2013) 2422–2426.

[33] R.J. Pearson, A.B. Antoniazzi, W.J. Nuttall, Tritium supply and use: a key issue for the development of nuclear fusion energy, Fusion Eng. Des. 136 (2018) 1140–1148.

[34] F. Mannone, Safety in Tritium Handling Technology, Springer, 1993.

[35] U.S.D. of Energy, Doe Handbook: Tritium Handling and Safe Storage, (2007).

[36] T.K. E. Proust, L. Anzidei, M. Dalle Donne, U. Fischer, Solid breeder blanket design and tritium breeding, 16 (1991) 73–84.

[37] ITER EDA DOCUMENTATION SERIES No. 24, ITER TECHNICAL BASIS, IAEA. (2018).

[38] N. Roux, C. Johnson, K. Noda, Properties and performance of tritium breeding ceramics, J. Nucl. Mater. 191–194 (1992) 15–22.

[39] A.. Raffray, M. Akiba, V. Chuyanov, L. Giancarli, S. Malang, Breeding blanket concepts for fusion and materials requirements, J. Nucl. Mater. 307–311 (2002) 21–30.

[40] T. Giegerich, C. Day, R. Knitter, N. Osman, Lithium enrichment issues in the sustainable supply chain of future fusion reactors, Kit. (2016) 1–21. https://nucleus.iaea.org/sites/fusionportal/Technical Meeting Proceedings/1st IAEA TM on Fusion Power Plant Safety/Presentations/Giegerich.pdf.

[41] W. Biel, Tritium Breeding and blanket technology, (2014) 1–24. https://www.dpg-physik.de/veranstaltungen/2014/biel2.pdf.

[42] M. Abdou, N.B. Morley, S. Smolentsev, A. Ying, S. Malang, A. Rowcliffe, M. Ulrickson, Blanket/first wall challenges and required R&D on the pathway to DEMO, Fusion Eng. Des. 100 (2015) 2–43.

[43] C.E. Johnson, Ceramic Breeder Materials, 17 (1991) 253–258.

[44] F.A. Hernández, P. Pereslavtsev, First principles review of options for tritium breeder and neutron multiplier materials for breeding blankets in fusion reactors, Fusion Eng. Des. 137 (2018) 243–256.

[45] N. Roux, G. Hollenberg, C. Johnson, K. N, R. Verrall, Fusion Engineering and Design Summary of experimental results for ceramic breeder materials, 27 (1995) 154–166.

[46] M.H.H. Kolb, K. Mukai, R. Knitter, T. Hoshino, Li_4SiO_4 based breeder ceramics with Li_2TiO_3, $LiAlO_2$ and $Li_XLa_YTiO_3$ additions, part I: Fabrication, Fusion Eng. Des. 115 (2017) 39–48.

[47] B. Rasneur, Tritium Breeding Material: γ-$LiAlO_2$, Fusion Technol. 8 (1985) 1909–1914.

[48] B. Rasneur, J. Mougin, N. Roux, Study of the thermomechanical and tritium release behaviour of Li_2ZrO_3 as tritium breeding ceramic for the European BIT blanket concept, J. Nucl. Mater. 212–215 (1994) 923–926.

[49] R. German, Sintering: From Empirical Observations to Scientific Principles, Elsevier Butterworth-Heinemann, 2014.

[50] W.D. Kingery, H.K. Bowen, D.R. Uhlmann, Introduction to Ceramics, 2nd edition, John Wiley & Sons, 1976.

[51] C. Barry Carter, M. Grant Norton, Ceramic materials: Science and engineering, Springer, 2007.

[52] Suk-Joong L.Kang, Sintering, Densification,Grain-growth, and Microstructure, Elsevier Butterworth-Heinemann, 2005.

[53] M.N. Rahaman, Ceramic processing and sintering, second edition, Marcel Dekker Inc., 2017.

[54] Mohamed N . Rahaman, Sintering of Ceramics, CRC Press Taylor & Francis Group 2007.

[55] M.J. Mayo, Processing of nanocrystalline ceramics from ultrafine particles, Int. Mater. Rev. 41 (1996) 85–115.

[56] M. Winterer, Nanocrystalline Ceramics: Synthesis and Structure, Springer-Verlag Berlin Heidelberg 2002.

[57] M.L. Panchula, J.Y. Ying, Synthesis and sintering of nanocrystalline alumina and aluminum nitride, Thesis, MIT, 1999.

[58] V.Y. Novikov, Impact of grain size on grain growth in nanomaterials, Mater. Lett. 132 (2014) 45–47.

[59] H. Gleiter, Nanostructured materials: basic concepts and microstructure, Acta Mater. 48 (2000) 1–29.

[60] K. Lu, Sintering of nanoceramics, Int. Mater. Rev. 53 (2008) 21–38.

[61] M.J. Mayo, Synthesis and applications of nanocrystalline ceramics, J. Mater. Chem. 19 (2009) 4673–4686.

[62] M.J. Mayo, M. Çiftçioglu, Issues in the Processing of Bulk Nanocrystalline Ceramics for Structural Applications, MRS Proc. 206 (1990) 545–550.

[63] M. Abdou, N.B. Morley, S. Smolentsev, A. Ying, S. Malang, A. Rowcliffe, M. Ulrickson, Blanket/first wall challenges and required R&D on the pathway to DEMO, Fusion Eng. Des. 100 (2015) 2–43.

[64] M. Nishikawa, T. Kinjyo, T. Ishizaka, S. Beloglazov, T. Takeishi, M. Enoeda, T. Tanifuji, Release behavior of bred tritium from LiAlO2, J. Nucl. Mater. 335 (2004) 70–76.

[65] G. Federici, A.R. Raffray, M.A. Abdou, Mistral: A comprehensive model for tritium

transport in lithium-base ceramics. Part I: Theory and description of model capabilities, J. Nucl. Mater. 173 (1990) 185–213.

[66] M. Nishikawa, T. Kinjyo, Y. Nishida, Chemical form of tritium released from solid breeder materials, J. Nucl. Mater. 325 (2004) 87–93.

[67] T. Kinjyo, M. Nishikawa, N. Yamashita, T. Koyama, T. Tanifuji, M. Enoeda, Chemical form of released tritium from solid breeder materials under the various purge gas conditions, Fusion Eng. Des. 82 (2007) 2147–2151.

[68] H.P. Paudel, Y.L. Lee, D.J. Senor, Y. Duan, Tritium Diffusion Pathways in γ-$LiAlO_2$ Pellets Used in TPBAR: A First-Principles Density Functional Theory Investigation, J. Phys. Chem. C. 122 (2018) 9755–9765.

[69] C. Alvani, S. Casadio, S. Casadio, Kinetics of tritium release from irradiated Li_2TiO_3 pebbles in out-of-pile TPD tests, Fusion Eng. Des. 69 (2003) 275–280.

[70] M. Kobayashi, Y. Oya, K. Okuno, Tritium trapping states induced by lithium-depletion in Li_2TiO_3, J. Nucl. Mater. 487 (2017) 84–90.

[71] F. Botter, D. Cherquitte, N. Roux, Out of Pile Tritium Release from various lithium materials, in: Fusion Technol. 1986, Pergamon, 1986: pp. 1537–1544.

[72] M. Smaihi, J.P. Boilot, F. Botter, J. Mougin, M.J. Boncoeur, Out-of-pile tritium extraction from lithium orthosilicate-based ceramics, J. Nucl. Mater. 185 (1991) 19–28.

[73] J.P. Kopasz, S.W. Tam, C.E. Johnson, Enhanced tritium transport and release by solids modification, J. Nucl. Mater. 179–181 (1991) 816–819.

[74] C. Alvani, P.L. Carconi, S. Casadio, M.R. Mancini, A. Moauro, Tritium Removal From $LiAlO_2$ and Li_2ZrO_3, in: C. Ferro, M. Gasparotto, H. Knoepfel (Eds.), Fusion

Technol. 1992, North-Holland, Oxford, 1993: pp. 1266–1270.

[75] M. Briec, F. Botter, J.J. Abassin, R. Benoit, P. Chenebault, M. Masson, B. Rasneur, P. Sciers, H. Werle, E. Roth, In and out-of-pile tritium extraction from samples of lithium aluminates, J. Nucl. Mater. 141–143 (1986) 357–363.

[76] F. Botter, S. Tistchenko, M. Briec, J.P. Kopasz, Progress in the knowledge of the mechanism of tritium release from lithium ceramics, Fusion Eng. Des. 17 (1991) 49–54.

[77] L. Debarberis, P. Moretto, In-pile tritium release rate limiting process study, Fusion Eng. Des. 23 (1993) 43–48.

[78] M. Briec, J.J. Abassin, M. Masson, E. Roth, P. Sciers, H. Werle, In-pile tritium extraction from samples of lithium aluminate, J. Nucl. Mater. 155–157 (1988) 549–552.

[79] F. Alessandrini, C. Alvani, S. Casadio, M.R. Mancini, C.A. Nannetti, In-situ tritium release (CORELLI-2 experiment) and ex-reactor ionic conductivity of substoichiometric $LiAlO_2$ breeder ceramics, J. Nucl. Mater. 224 (1995) 236–244.

[80] E. Carella, T. Hernández, The effect of ??-radiation in Li_4SiO_4 ceramic breeder blankets, Fusion Eng. Des. 90 (2015) 73–78.

[81] J.D. Lulewicz, N. Roux, G. Piazza, J. Reimann, J. Laan, Behaviour of Li_2ZrO_3 and Li_2TiO_3 pebbles relevant to their utilization as ceramic breeder for the HCPB blanket, J. Nucl. Mater. 283–287 (2000) 1361–1365.

[82] J. Charpin, F. Botter, M. Briec, B. Rasneur, E. Roth, N. Roux, J. Sannier, Investigation of γ lithium aluminate as tritium breeding material for a fusion reactor blanket, Fusion Eng. Des. 8 (1989) 407–413.

[83] F. Botter, B. Rasneur, E. Roth, Irradiation behaviour of a tritium breeding material, γ-$LiAlO_2$- results of two in-pile experiments: ALICE I and ALICE II, J. Nucl. Mater. 160 (1988) 48–57.

[84] X. Gao, X. Chen, M. Gu, C. Xiao, S. Peng, Fabrication and characterization of Li_4SiO_4 ceramic pebbles by wet method, J. Nucl. Mater. 424 (2012) 210–215.

[85] J.D. Lulewicz, N. Roux, First results of the investigation of Li_2ZrO_3 and Li_2TiO_3 pebbles, Fusion Eng. Des. 39–40 (1998) 745–750.

[86] M. Hong, Y. Zhang, Y. Mi, M. Xiang, Y. Zhang, Fabrication and characterization of Li_2TiO_3 core–shell pebbles with enhanced lithium density, J. Nucl. Mater. 445 (2014) 111–116.

[87] B. Rasneur, G. Thevenot, Y. Bouilloux, Irradiation behavior of $LiAlO_2$ and Li_2ZrO_3 ceramics in the ALICE 3 experiment, J. Nucl. Mater. 191–194 (1992) 243–247.

[88] G.W. Hollenberg, Fast neutron irradiation results on Li_2O, Li_4SiO_4, Li_2ZrO_3 and $LiAlO_2$, J. Nucl. Mater. 123 (1984) 896–900.

[89] D. Mandal, M.C. Jadeja, N.S. Ghuge, D. Sen, S. Mazumder, Effect of excess lithium on sintering behaviour of lithium-titanate pebbles: Modifications of microstructure and pore morphology, Fusion Eng. Des. 112 (2016) 520–526.

[90] T. Hoshino, F. Oikawa, Y. Natori, K. Kato, T. Sakka, M. Nakamura, K. Tatenuma, Trial synthesis of $Li_2Be_2O_3$ for high-functional tritium breeders, Fusion Eng. Des. 88 (2013) 2268–2271.

[91] M. Mazaheri, A.M. Zahedi, M. Haghighatzadeh, S.K. Sadrnezhaad, Sintering of titania nanoceramic: Densification and grain growth, Ceram. Int. 35 (2009) 685–691.

[92] W. Zhang, Q. Zhou, L. Xue, Y. Yan, Fabrication of Li_2TiO_3 pebbles with small grain

size via hydrothermal and improved dry-rolling methods, J. Nucl. Mater. 464 (2015) 389–393.

[93] B.M. Tripathi, T. Mohanty, D. Prakash, A.K. Tyagi, P.K. Sinha, Monoclinic β-Li_2TiO_3 nanocrystalline particles employing novel urea assisted solid state route: Synthesis, characterization and sintering behavior, J. Nucl. Mater. 490 (2017) 167–173.

[94] X. Wu, Z. Wen, X. Xu, Z. Gu, X. Xu, Optimization of a wet chemistry method for fabrication of Li_2TiO_3 pebbles, J. Nucl. Mater. 373 (2008) 206–211.

[95] T. Hoshino, F. Oikawa, Trial fabrication tests of advanced tritium breeder pebbles using sol–gel method, Fusion Eng. Des. 86 (2011) 2172–2175.

[96] K. Shin-mura, Y. Otani, S. Ogawa, E. Niwa, T. Hashimoto, T. Hoshino, K. Sasaki, Synthesis of high-purity Li_8ZrO_6 powder by solid state reaction under hydrogen atmosphere, Fusion Eng. Des. 109–111 (2016) 1739–1743.

[97] S. Ogawa, Y. Masuko, H. Kato, H. Yuyama, Y. Sakai, E. Niwa, T. Hashimoto, K. Mukai, T. Hosino, K. Sasaki, Li vaporization property of two-phase material of Li_2TiO_3 and Li_2SiO_3 for tritium breeder, Fusion Eng. Des. 98–99 (2015) 1859–1863.

[98] T. Hoshino, M. Yasumoto, K. Tsuchiya, K. Hayashi, H. Nishimura, A. Suzuki, T. Terai, Non-stoichiometory and vaporization characteristic of $Li_{2.1}TiO_{3.05}$ in hydrogen atmosphere, Fusion Eng. Des. 82 (2007) 2269–2273.

[99] K. Shin-mura, Y. Otani, S. Ogawa, T. Hoshino, K. Sasaki, Li vaporization properties of candidate materials for tritium breeder with high Li density, Fusion Eng. Des. 124 (2017) 762–766.

[100] M. Asano, Y. Kato, T. Harada, Y. Mizutani, Vaporization and thermochemical properties of Li_8ZrO_6 and comparison with other lithium-containing complex oxides, J.

Nucl. Mater. 230 (1996) 110–115.

[101] T. Hoshino, M. Yasumoto, K. Tsuchiya, K. Hayashi, Vapor species evolved from Li_2TiO_3 heated at high temperature under various conditions, Fusion Eng. Des. 81 (2006) 555–559.

[102] R. Ramaraghavulu, S. Buddhudu, G. Bhaskar Kumar, Analysis of structural and thermal properties of Li_2TiO_3 ceramic powders, Ceram. Int. 37 (2011) 1245–1249.

[103] G.B. Kumar, S. Buddhudu, Synthesis and emission analysis of RE^{3+} (Eu^{3+} or Dy^{3+}):Li_2TiO_3 ceramics, Ceram. Int. 35 (2009) 521–525.

[104] D. Sathiyamoorthy, S.J. Ghanwat, B.M. Tripathi, C. Danani, Novel mixed-oxide ceramic for neutron multiplication and tritium generation, J. Nucl. Mater. 417 (2011) 775–779.

[105] D. Mandal, M.R.K. Shenoi, S.K. Ghosh, Synthesis & fabrication of lithium-titanate pebbles for ITER breeding blanket by solid state reaction & spherodization, Fusion Eng. Des. 85 (2010) 819–823.

[106] D. Mandal, D. Sathiyamoorthy, V.G. Rao, Preparation and characterization of lithium–titanate pebbles by solid-state reaction extrusion and spherodization techniques for fusion reactor, Fusion Eng. Des. 87 (2012) 7–12.

[107] D. Mandal, Reaction Kinetics for the Synthesis of lithium titanate (Li_2TiO_3) By Solid State Reaction, 4 (2014) 59–66.

[108] S. Sonak, U. Jain, A.K. Sahu, S. Kumar, N. Krishnamurthy, Thermogravimetric analysis and kinetic study of formation of lithium titanate by solid state route, J. Nucl. Mater. 457 (2015) 88–93.

[109] T.V. Vittal Rao, Y.R. Bamankar, S.K. Mukerjee, S.K. Aggarwal, Preparation and

characterization of Li_2TiO_3 pebbles by internal gelation sol–gel process, J. Nucl. Mater. 426 (2012) 102–108.

[110] H. Pfeiffer, K.M. Knowles, Reaction mechanisms and kinetics of the synthesis and decomposition of lithium metazirconate through solid-state reaction, J. Eur. Ceram. Soc. 24 (2004) 2433–2443.

[111] J. Jimenez-Becerril, P. Bosch, S. Bulbulian, Synthesis and Characterization of γ-$LiAlO_2$, J. Nucl. Mater. 185 (1991) 304–307.

[112] F. Deganello, A.K. Tyagi, Solution combustion synthesis, energy and environment: Best parameters for better materials, Prog. Cryst. Growth Charact. Mater. 64 (2018) 23–61.

[113] A. Varma, A.S. Mukasyan, A.S. Rogachev, K. V. Manukyan, Solution Combustion Synthesis of Nanoscale Materials, Chem. Rev. 116 (2016) 14493–14586.

[114] A.S. Mukasyan, P. Dinka, Novel approaches to solution-combustion synthesis of nanomaterials, Int. J. Self-Propagating High-Temperature Synth. 16 (2007) 23–35.

[115] S.R. Jain, K.C. Adiga, V.R. Pai Verneker, A new approach to thermochemical calculations of condensed fuel-oxidizer mixtures, Combust. Flame. 40 (1981) 71–79.

[116] P.J. Haines, Principles of Thermal analysis and Calorimetry, The Royal Society of Chemistry, 2002.

[117] M. E. Brown, Handbook of Thermal Analysis and Calorimetry, Volume 1, Elsevier Science B.V., 1998.

[118] B.D. Cullity, Elements of X-ray Diffraction, Addison-Wesley, 1956.

[119] Joseph I. Goldstein, Harveg Yakowitz, Practical Scanning Electron Microscopy,

Plenum Press, New York , 1975.

[120] S. Lowell , J. E. Shields, M. A. Thomas, Q.M. Thommes, Characterization of Porous Solids and Powders: Surface Area, Pore Size and Density, Springer, 2004.

[121] M. Thommes, K. Kaneko, A. V. Neimark, J.P. Olivier, F. Rodriguez-Reinoso, J. Rouquerol, K.S.W. Sing, Physisorption of gases, with special reference to the evaluation of surface area and pore size distribution (IUPAC Technical Report), Pure Appl. Chem. 87 (2015) 1051–1069.

[122] J.R. Dean, Practical Inductively Coupled Plasma Spectrometry, 2nd ed, John Wiley & Sons, 2019.

[123] G.L. Moore, Introduction to Inductively Coupled Plasma Atomic Emission Spectrometry, Elsevier Science Publishers B.V., 1989.

[124] T.A. Ring, Fundamentals of Ceramic Powder Processing and Synthesis, Academic Press, 1996.

[125] M.E. Orazem, B. Tribollet, Electrochemical impedance spectroscopy, John Wiley & Sons, 2008.

[126] E. Barsoukov. J. R. Macdonald, Impedance Spectroscopy Theory, Experiment, and Applications, 2nd ed., John Wiley & Sons, 2013.

[127] K. Noda, Y. Ishii, H. Matsui, H. Ohno, H. Watanabe, A study of tritium behavior in lithium oxide by ion conductivity measurements, Fusion Eng. Des. 8 (1989) 329–333.

[128] M.M. Islam, T. Bredow, Lithium Diffusion Pathways in β-Li_2TiO_3: A Theoretical Study, J. Phys. Chem. C. 120 (2016) 7061–7066.

[129] F. Bianchini, H. Fjellvåg, P. Vajeeston, A first principle comparative study of the ionic

diffusivity in $LiAlO_2$ and $NaAlO_2$ polymorphs for solid-state battery applications, Phys. Chem. Chem. Phys. 20 (2018) 9824–9832.

[130] U. Dash, S. Sahoo, S.K.S. Parashar, P. Chaudhuri, Effect of Li^+ ion mobility on the grain boundary conductivity of Li_2TiO_3 nanoceramics, J. Adv. Ceram. 3 (2014) 98–108.

[131] X. Zhan, Y.T. Cheng, M. Shirpour, Nonstoichiometry and Li-ion transport in lithium zirconate: The role of oxygen vacancies, J. Am. Ceram. Soc. 101 (2018) 4053–4065.

[132] G. Izquierdo, A.R. West, Phase equilibria in the system Li_2O-TiO_2, Mater. Res. Bull. 15 (1980) 1655–1660.

[133] H. Kleykamp, Phase equilibria in the Li-Ti-O system and physical properties of Li_2TiO_3, Fusion Eng. Des. 61–62 (2002) 361–366.

[134] A. Chitnis, B. Chakraborty, B.M. Tripathi, A.K. Tyagi, N. Garg, High pressure stability of lithium metatitanate and metazirconate: Insight from experiments & ab-initio calculations, J. Nucl. Mater. 499 (2018) 334–343.

[135] C. Julien, Z. Stoynov, Materials for lithium-ion batteries, Springer, 2000.

[136] C.P. Sandhya, B. John, C. Gouri, Lithium titanate as anode material for lithium-ion cells: a review, Ionics, 20 (2014) 601–620.

[137] S. Wang, W. Quan, Z. Zhu, Y. Yang, Q. Liu, Y. Ren, X. Zhang, R. Xu, Y. Hong, Z. Zhang, K. Amine, Z. Tang, J. Lu, J. Li, Lithium titanate hydrates with superfast and stable cycling in lithium ion batteries, Nat. Commun. 8 (2017) 627.

[138] A. Lakshminarayana, M. Dhananjaya, N. Guruprakash, O. Hussain, A. Mauger, C. Julien, Li_2TiO_3/Graphene and Li_2TiO_3/CNT Composites as Anodes for High Power Li–Ion Batteries, Chemistry Select. 3 (2018) 9150–9158.

[139] J. Liu, X. Wei, F. Meng, Lithium Titanate-Based Lithium-Ion Batteries, in: Adv. Batter. Mater., John Wiley & Sons, Ltd, 2019: pp. 87–157.

[140] L. Youjie, R. Li, Y. Yang, Z. Li, Lithium titanate anode for high-performance lithium-ion batteries using octadecylamine and folic acid-functionalized graphene oxide for fabrication of ultrathin lithium titanate nanoflakes and modification of binder, New J. Chem. 42 (2018) 15097–15104.

[141] Y. Liu, W. Li, X. Zhou, An investigation of Li_2TiO_3–coke composite anode material for Li-ion batteries, RSC Adv., 9 (2019) 17835–17840.

[142] M.S. Whittingham, Lithium Batteries and Cathode Materials, Chem. Rev. 104 (2004) 4271–4302.

[143] M. Castellanos, A.R. West, Order-disorder phenomena in oxides with rock salt structures: the system Li_2TiO_3-MgO, J. Mater. Sci. 14 (1979) 450–454.

[144] M.D. Aguas, G.C. Coombe, I.P. Parkin, New solid state routes to lithium transition metal oxides via reactions with lithium oxide, Polyhedron. 17 (1998) 49–53.

[145] C.-L. Yu, K. Yanagisawa, S. Kamiya, T. Kozawa, T. Ueda, Monoclinic Li_2TiO_3 nano-particles via hydrothermal reaction: Processing and structure, Ceram. Int. 40 (2014) 1901–1908.

[146] X. Wu, Z. Wen, J. Han, X. Xu, B. Lin, Fabrication of Li_2TiO_3 pebbles by water-based sol-gel method, Fusion Eng. Des. 83 (2008) 112–116.

[147] A. Laumann, K.T. Fehr, M. Wachsmann, M. Holzapfel, B.B. Iversen, Metastable formation of low temperature cubic Li_2TiO_3 under hydrothermal conditions — Its stability and structural properties, Solid State Ionics. 181 (2010) 1525–1529.

[148] C.H. Jung, J.Y. Park, W.J. Kim, W.S. Ryu, S.J. Lee, Characterizations of Li_2TiO_3

prepared by a solution combustion synthesis and fabrication of spherical particles by dry-rolling granulation process, Fusion Eng. Des. 81 (2006) 1039–1044.

[149] Q. Zhou, L. Tao, Y. Gao, L. Xue, Y. Yan, Flash synthesis of Li_2TiO_3 powder by microwave-induced solution combustion, J. Nucl. Mater. 455 (2014) 101–105.

[150] Q. Zhou, Y. Mou, X. Ma, L. Xue, Y. Yan, Effect of fuel-to-oxidizer ratios on combustion mode and microstructure of Li_2TiO_3 nanoscale powders, J. Eur. Ceram. Soc. 34 (2014) 801–807.

[151] C.H. Jung, Sintering characterization of Li_2TiO_3 ceramic breeder powders prepared by the solution combustion synthesis process, J. Nucl. Mater. 341 (2005) 148–152.

[152] A. Sinha, S.R. Nair, P.K. Sinha, Single step synthesis of Li_2TiO_3 powder, J. Nucl. Mater. 399 (2010) 162–166.

[153] C. Suryanarayana, M. G. Norton, X-Ray Diffraction A Practical Approach, Springer, 1998.

[154] R. Padhy, N. Rao A., S.K.S. Parashar, K. Parashar, P. Chaudhuri, Sintering effect on electrical properties of Li_2TiO_3, Solid State Ionics. 256 (2014) 29–37.

[155] H. Ohno, S. Konishi, T. Nagasaki, T. Kurasawa, H. Katsuta, H. Watanabe, Correlation behavior of lithium and tritium in some solid breeder materials, J. Nucl. Mater. 133–134 (1985) 181–185.

[156] T. Fehr, E. Schmidbauer, Electrical conductivity of Li_2TiO_3 ceramics, Solid State Ionics. 178 (2007) 35–41.

[157] S.T. Murphy, N.D.M. Hine, Point defects and non-stoichiometry in Li_2TiO_3, Chem. Mater. 26 (2014) 1629–1638.

[158] U. Dash, S. Sahoo, P. Chaudhuri, S.K.S. Parashar, K. Parashar, Electrical properties of bulk and nano Li_2TiO_3 ceramics: A comparative study, J. Adv. Ceram. 3 (2014) 89–97.

[159] R. Xiong, J. Ida, Y.S. Lin, Kinetics of carbon dioxide sorption on potassium-doped lithium zirconate, Chem. Eng. Sci. 58 (2003) 4377–4385.

[160] Q. Xiao, Y. Liu, Y. Zhong, W. Zhu, A citrate sol-gel method to synthesize Li_2ZrO_3 nanocrystals with improved CO_2 capture properties, J. Mater. Chem. 21 (2011) 3838–3842.

[161] W. Yao, H. Zhang, S. Zhong, J. Li, L. Wang, Facile synthesis of Li_2ZrO_3-modified $LiNi_{0.5}Mn_{0.5}O_2$ cathode material from a mechanical milling route for lithium-ion batteries, J. Electroceramics. (2018) 3–10.

[162] J. Ichi Ida, R. Xiong, Y.S. Lin, Synthesis and CO_2 sorption properties of pure and modified lithium zirconate, Sep. Purif. Technol. 36 (2004) 41–51.

[163] E. Ochoa-ferna, Nanocrystalline Lithium Zirconate with Improved Kinetics for High-Temperature CO_2 Capture, (2006) 1383–1385.

[164] S. Dash, D.D. Sood, R. Prasad, Phase diagram and thermodynamic calculations of alkali and alkaline earth metal zirconates, J. Nucl. Mater. 228 (1996) 83–116.

[165] E. Ochoa-ferna, Synthesis and CO_2 Capture Properties of Nanocrystalline Lithium Zirconate, 2 (2006) 6037–6046.

[166] B. N. Nair, T. Yamaguchi, H. Kawamura, S.I. Nakao, K. Nakagawa, Processing of Lithium Zirconate for Applications in Carbon Dioxide Separation: Structure and Properties of the Powders, J. Am. Ceram. Soc. 87 (2008) 68–74.

[167] M. Khokhani, R.B. Khomane, B.D. Kulkarni, Sodium-doped lithium zirconate nano squares: Synthesis, characterization and applications for CO_2 sequestration, J. Sol-Gel

Sci. Technol. 61 (2012) 316–320.

[168] G.P. Wyers, E.H.P. Cordfunke, Phase relations in the system Li_2O-ZrO_2, J. Nucl. Mater. 168 (1989) 24–30.

[169] A. Skokan, Phase Stability Investigations in the Ceramic Breeder Systems Li_2O-Al_2O_3 and Li_2O-ZrO_2, Fusion Technol. 1990 (1991) 772–776.

[170] A. Kordatos, S.R.G. Christopoulos, N. Kelaidis, A. Chroneos, Defect processes in Li_2ZrO_3: insights from atomistic modelling, J. Mater. Sci. Mater. Electron. 28 (2017) 11789–11793.

[171] J.L. Hodeau, M. Marezio, A. Santoro, R.S. Roth, Neutron profile refinement of the structures of Li_2SnO_3 and Li_2ZrO_3, J. Solid State Chem. 45 (1982) 170–179.

[172] N. Roux, J.J. Abassin, M. Briec, D. Cruz, T. Flament, I. Schuster, Compatibility behavior of beryllium with $LiAlO_2$ and Li_2ZrO_3 ceramics, with 316L and 1.4914 steels in SIBELIUS, J. Nucl. Mater. 191–194 (1992) 168–172.

[173] R.E. Avila, L.A. Peña, J.C. Jiménez, Surface desorption and bulk diffusion models of tritium release from Li_2TiO_3 and Li_2ZrO_3 pebbles, J. Nucl. Mater. 405 (2010) 244–251.

[174] Y. Kawamura, M. Enoeda, K. Okuno, Isotope exchange reaction in Li_2ZrO_3 packed bed, Fusion Eng. Des. 39–40 (1998) 713–721.

[175] G.W. Hollenberg, R.C. Knight, P.J. Densley, L.A. Pember, C.E. Johnson, R.B. Poeppel, L. Yang, The FUBR-1B experiment - irradiation of lithium ceramics to high burnups under large temperature gradients, J. Nucl. Mater. 141–143 (1986) 271–274.

[176] J.G. Van Der Laan, H. Kawamura, N. Roux, D. Yamaki, Ceramic breeder research and development: Progress and focus, J. Nucl. Mater. 283 (2000) 99–109.

[177] J.M. Miller, R.A. Verrall, Performance of a Li_2ZrO_3 sphere-pac assembly in the CRITIC-II irradiation experiment, J. Nucl. Mater. 212–215 (1994) 897–901.

[178] H. Pfeiffer, Reaction mechanisms and kinetics of the synthesis and decomposition of lithium metazirconate through solid-state reaction, J. Eur. Ceram. Soc. 24 (2004) 2433–2443.

[179] N. Roux, J. Mougin, B. Rasneur, E. Proust, L. Giancarli, J.F. Salavy, Current material and design studies for the utilization of Li_2ZrO_3 in the BIT blanket concept, J. Nucl. Mater. 212–215 (1994) 862–867.

[180] X. Guo, L. Ding, J. Ren, H. Yang, Preparation and CO_2 capture properties of nanocrystalline Li_2ZrO_3 via an epoxide-mediated sol–gel process, J. Sol-Gel Sci. Technol. 81 (2016).

[181] K. Yuan, X. Jin, C. Xu, X. Wang, G. Zhang, Z. Yi, D. xu, Fabrication of dense and porous Li_2ZrO_3 nanofibers with electrospinning method, Appl. Phys. A. 124 (2018).

[182] S.Z. Kang, T. Wu, X. Li, J. Mu, Low temperature biomimetic synthesis of the Li_2ZrO_3 nanoparticles containing $Li_6Zr_2O_7$ and high temperature CO_2 capture, Mater. Lett. 64 (2010) 1404–1406.

[183] T. Ávalos-Rendón, J. Casa-Madrid, H. Pfeiffer, Thermochemical capture of carbon dioxide on lithium aluminates ($LiAlO_2$ and Li_5AlO_4): A new option for the CO_2 absorption, J. Phys. Chem. A. 113 (2009) 6919–6923.

[184] L. Zhou, H. Lin, B. Yi, Sintering behavior of porous α-lithium aluminate matrices in molten carbonate fuel cells at high temperature, J. Power Sources. 164 (2007) 24–32.

[185] L.L. Zhang, J.J. Chen, S. Cheng, H.F. Xiang, Enhanced electrochemical performances of $Li_{1.2}Ni_{0.2}Mn_{0.6}O_2$ cathode materials by coating $LiAlO_2$ for lithium-ion batteries,

Ceram. Int. 42 (2016) 1870–1878.

[186] D. Iadicicco, M. Vanazzi, F.G. Ferré, B. Paladino, S. Bassini, M. Utili, F. Di Fonzo, Multifunctional nanoceramic coatings for future generation nuclear systems, Fusion Eng. Des. 146 (2019) 1628–1632.

[187] W. Jiang, S.R. Spurgeon, Z. Zhu, X. Yu, K. Kruska, T. Wang, J. Gigax, L. Shao, D.J. Senor, Chemical imaging and diffusion of hydrogen and lithium in lithium aluminate, J. Nucl. Mater. 511 (2018) 1–10.

[188] W. Setyawan, D.J. Senor, R. Devanathan, Insights on Amorphization of Lithium Aluminate from Atomistic Simulation, J. Phys. Chem. C. 121 (2017) 7635–7642.

[189] F. Cheng, Y. Xin, Y. Huang, J. Chen, H. Zhou, X. Zhang, Enhanced electrochemical performances of 5 v spinel $LiMn_{1.58}Ni_{0.42}O_4$ cathode materials by coating with $LiAlO_2$, J. Power Sources. 239 (2013) 181–188.

[190] H. Cao, B. Xia, Y. Zhang, N. Xu, $LiAlO_2$-coated $LiCoO_2$ as cathode material for lithium ion batteries, Solid State Ionics. 176 (2005) 911–914.

[191] S. Terada, I. Nagashima, K. Higaki, Y. Ito, Stability of $LiAlO_2$ as electrolyte matrix for molten carbonate fuel cells, J. Power Sources. 75 (1998) 223–229.

[192] S. Mo, B. Zhang, K. Zhang, S. Li, F. Pan, $LiAl_5O_8$ as a potential coating material in lithium-ion batteries: A first principles study, Phys. Chem. Chem. Phys. 21 (2019) 13758–13765.

[193] E. Antolini, The stability of $LiAlO_2$ powders and electrolyte matrices in molten carbonate fuel cell environment, Ceram. Int. 39 (2013) 3463–3478.

[194] H.S. Kim, Y. Kim, S. Il Kim, S.W. Martin, Enhanced electrochemical properties of $LiNi_{1/3}Co_{1/3}Mn_{1/3}O_2$ cathode material by coating with $LiAlO_2$ nanoparticles, J. Power

Sources. 161 (2006) 623–627.

[195] D. Wiedemann, S. Nakhal, J. Rahn, E. Witt, M.M. Islam, S. Zander, P. Heitjans, H. Schmidt, T. Bredow, M. Wilkening, M. Lerch, Unravelling Ultraslow Lithium-Ion Diffusion in γ-$LiAlO_2$: Experiments with Tracers, Neutrons, and Charge Carriers, Chem. Mater. 28 (2016) 915–924.

[196] L. Lei, D. He, Y. Zou, W. Zhang, Z. Wang, M. Jiang, M. Du, Phase transitions of $LiAlO_2$ at high pressure and high temperature, J. Solid State Chem. 181 (2008) 1810–1815.

[197] S.J. Heo, R. Batra, R. Ramprasad, P. Singh, Crystal Morphology and Phase Transformation of $LiAlO_2$: Combined Experimental and First-Principles Studies, J. Phys. Chem. C. 122 (2018) 28797–28804.

[198] M.M. Islam, T. Bredow, Interstitial Lithium Diffusion Pathways in γ-$LiAlO_2$: A Computational Study, J. Phys. Chem. Lett. 6 (2015) 4622–4626.

[199] H. Tsuchihira, T. Oda, S. Tanaka, Displacement cascade simulation of $LiAlO_2$ using molecular dynamics, J. Nucl. Mater. 414 (2011) 44–52.

[200] M. Marezio, J. P. Remeika, High-Pressure Synthesis and Crystal Structure of α-$LiAlO_2$, J. Chem. Phys. 44 (1966).

[201] H. Tsuchihira, T. Oda, S. Tanaka, Modeling of influence of lithium vacancy on thermal conductivity in lithium aluminate, Fusion Eng. Des. 85 (2010) 1814–1818.

[202] Y.L. Lee, J. Holber, H.P. Paudel, D.C. Sorescu, D.J. Senor, Y. Duan, Density functional theory study of the point defect energetics in γ-$LiAlO_2$, Li_2ZrO_3 and Li_2 TiO_3 materials, J. Nucl. Mater. 511 (2018) 375–389.

[203] M. Marezio, The Crystal Structure and Anomalous Disperson of γ-$LiAlO_2$, Acta

Crystallogr. 19 (1965) 396–400.

[204] B. Singh, M.K. Gupta, R. Mittal, S.L. Chaplot, Phonons, phase transitions and thermal expansion in $LiAlO_2$: An: ab initio density functional study, Phys. Chem. Chem. Phys. 20 (2018) 12248–12259.

[205] X. Li, T. Kobayashi, F. Zhang, K. Kimoto, T. Sekine, A new high-pressure phase of $LiAlO_2$, J. Solid State Chem. 177 (2004) 1939–1943.

[206] W. Dienst, H. Zimmermann, Investigation of Mechanical Properties of Ceramic Breeder Materials, J. Nucl. Mater. 155 (1988) 476–479.

[207] J. Charpin, F. Botter, M. Briec, B. Rasneur, E. Roth, N. Roux, J. Sannier, Investigation of γ lithium aluminate as tritium breeding material for a fusion reactor blanket, Fusion Eng. Des. 8 (1989) 407–413.

[208] J. Lin, Z. Wen, X. Xu, Z. Gu, Processing and microstructure of γ-$LiAlO_2$ ceramics, Ceram. Int. 36 (2010) 2221–2225.

[209] B. Rasneur, Tritium Breeding MateriaL: γ-$LiAlO_2$., Fusion Technol. 8:1P2B (1985), 1909-1914.

[210] Z. Wen, Z. Gu, X. Xu, X. Zhu, Research on the preparation, electrical and mechanical properties of γ-$LiAlO_2$ ceramics, J. Nucl. Mater. 329–333 (2004) 1283–1286.

[211] J. Lin, Z. Wen, X. Xu, N. Li, S. Song, Characterization and improvement of water compatibility of γ-$LiAlO_2$ ceramic breeders, Fusion Eng. Des. 85 (2010) 1162–1166.

[212] H. Kleykamp, Enthalpy and heat capacity of $LiAlO_2$ between 298 and 1700 K by drop calorimetry, J. Nucl. Mater. 270 (1999) 372–375.

[213] A.K. Fischer, C.E. Johnson, Thermodynamic and kinetic observations on lialo2:

adsorption, dissolution, and evolution of water vapor, J. Nucl. Mater. 155–157 (1988) 466–470.

[214] J. Jiménez-Becerril, I. García-Sosa, Synthesis of lithium aluminate by thermal decomposition of a lithium dawsonite-type precursor, J. Ceram. Process. Res. 12 (2011) 52–56.

[215] D. Cruz, H.B. Ortiz-Oliveros, L.M. Pérez-Díaz, R.M. Flores-Espinosa, G. Rosano-Ortega, Modified combustion synthesis of γ-$LiAlO_2$ using metal oxides, Trans. Nonferrous Met. Soc. China, 28 (2018) 1793–1800.

[216] H. Wang, J. Zhao, Y. Luo, Fabrication of γ-$LiAlO_2$ spherical ceramics by a planet-type rotation process, J. Nucl. Mater. 208 (1994) 195–199.

[217] B. Schulz, H. Wedemeyer, Preparation, characterization and thermal diffusivity of γ-$LiAlO_2$, J. Nucl. Mater. 139 (1986) 35–41.

[218] H. Zuo, X. Tang, H. Zhang, Y. Lai, Y. Jing, H. Su, Low-dielectric-constant $LiAlO_2$ ceramics combined with LBSCA glass for LTCC applications, Ceram. Int. 43 (2017) 8951–8955.

[219] M. Asou, T. Terai, Y. Takahashi, Enthalpy and heat capacity of $LiAlO_2$ and Li_2SnO_3 from 300 to 1000 K, J. Nucl. Mater. 175 (1990) 42–46.

[220] V.P. Isupov, N. V. Eremina, Effect of mechanical activation of $Al(OH)_3$ on its reaction with Li_2CO_3, Inorg. Mater. 48 (2012) 918–924.

[221] M. Chatterjee, M.K. Naskar, Novel technique for the synthesis of lithium aluminate ($LiAlO_2$) powders from water-based sols, J. Mater. Sci. Lett. 22 (2003) 1747–1749.

[222] Z. Tang, L. Hu, Z. Zhang, J. Li, S. Luo, Hydrothermal synthesis of high surface area mesoporous lithium aluminate, Mater. Lett. 61 (2007) 570–573.

[223] L. Hu, B. Qiao, Z. Tang, Z. Zhang, Hydrothermal routes to various controllable morphologies of nanostructural lithium aluminate, Mater. Res. Bull. 42 (2007) 1407–1413.

[224] L. Hu, Z. Tang, Z. Zhang, Template-assisted synthesis of mesoporous $LiAlO_2$ hollow spheres with high surface area, Microporous Mesoporous Mater. 113 (2008) 41–46.

[225] O. Renoult, J.-P. Boilot, J.-P. Korb, D. Petit, M. Boncoeur, Sol-gel lithium aluminate ceramics and tritium extraction mechanisms, J. Nucl. Mater. 219 (1995) 233–239.

[226] F. Li, K. Hu, J. Li, D. Zhang, G. Chen, Combustion synthesis of γ-lithium aluminate by using various fuels, J. Nucl. Mater. 300 (2002) 82–88.

[227] R. Ianoş, I. Lazău, C. Păcurariu, Metal nitrate/fuel mixture reactivity and its influence on the solution combustion synthesis of γ-$LiAlO_2$, J. Therm. Anal. Calorim. 97 (2009) 209–214.

[228] X. Xu, Z. Wen, X. Wu, J. Lin, X. Wang, Rheology and chemorheology of aqueous γ-$LiAlO_2$ slurries for gel-casting, Ceram. Int. 35 (2009) 2191–2195.

[229] T.K. Basu, V.R. Nargundkar, P. Cloth, D. Filges, S. Taczanowski, Neutron Multiplication Studies in Beryllium for Fusion Reactor Blankets., Nucl Sci Eng. 70 (1979) 309–313.

[230] M. Mahdavi, E. Asadi, Estimates of Tritium Produced Ratio in the Blanket of Fusion Reactors, 2013 (2013) 8–11.

[231] L. Petrizzi, V. Rado, Neutronic performance of two European breeder-inside-tube (BIT) blankets for DEMO: the helium-cooled ceramic $LiAlO_2$ with Be multiplier and the water-cooled liquid $Li_{17}Pb$, Fusion Eng. Des. 28 (1995) 642–647.

[232] F. Cismondi, Basics of breeding blanket technology, KIT, Germany

https://staff.polito.it/roberto.zanino/sub1/teach_files/current_topics/lect_cismondi.pdf.

[233] J.P. Kopasz, C.E. Johnson, D.L. Baldwin, Performance of ceramic breeder materials in the SIBELIUS experiment, J. Nucl. Mater. 219 (1995) 259–264.

[234] P.F. Wambach, J.C. Laul, Beryllium health effects, exposure limits and regulatory requirements, J. Chem. Heal. Saf. 15 (2008) 5–12.

[235] K.A. Walsh, Beryllium Chemistry and Processing, edited by Edgar Edgar E. Vidal, Alfred Goldberg, Edward N.C. Dalder, David L. Olson, Brajendra Mishra, ASM International, 2009.

[236] D.D. Thorat, B.M. Tripathi, D. Sathiyamoorthy, Extraction of beryllium from Indian beryl by ammonium hydrofluoride, Hydrometallurgy. 109 (2011) 18–22.

[237] B.M. Tripathi, J. Prakash, D.D. Thorat, D. Sathiyamoorthy, Statistical Evaluation of Ammonium Hydrofluoride Process for Beryllium Extraction from Indian Beryl Ore, Powder Metall. Min. . 2 (2013) 4–7.

[238] A.R. Abbasian, M.R. Rahimipour, Z. Hamnabard, Initial sintering kinetics of lithium meta titanate at constant rates of heating, Iran. J. Mater. Sci. Eng. 10 (2013) 44–53.

[239] A.R. Abbasian, M.R. Rahimipour, Z. Hamnabard, Activation Energies for Initial and Intermediate Stage Sintering of Li_2TiO_3 Determined by a Two-Stage Master Sintering Curve Approach, Advances in Engineering Mechanics and Materials, 291-296, ISBN: 978-1-61804-241-5.

[240] L.C. Leu, J. Bian, D. Gout, S. Letourneau, R. Ubic, Order-disorder transition in the (1-x)Li_2TiO_3-xMgO system ($0 \leq x \leq 0.5$), RSC Adv. 2 (2012) 1598–1604.

[241] A.R. Abbasian, M.R. Rahimipour, Z. Hamnabard, Phase transformation during sintering of Li_2TiO_3 nanocrystallites synthesised by hydrothermal method, Micro Nano

Lett. 11 (2016) 822–824.

[242] B. Gilbert, H. Zhang, F. Huang, M.P. Finnegan, G.A. Waychunas, J.F. Banfield, Special phase transformation and crystal growth pathways observed in nanoparticles, Geochem. Trans. 4 (2003) 20–27.

[243] W. Zhang, Y. Xue, Q. Fu, Z. Cui, S. Wang, Size dependence of phase transition thermodynamics of nanoparticles: A theoretical and experimental study, Powder Technol. 308 (2017) 258–265.

[244] X. Wu, Z. Wen, X. Xu, J. Han, Synthesis and ionic conductivity of Mg-doped Li_2TiO_3, Solid State Ionics. 179 (2008) 1779–1782.